HABILITATIONSSCHRIFT

zur

Erlangung der Venia legendi

für das Fach Physik

der

Ruprecht-Karls-Universität

Heidelberg

vorgelegt von

Bernold Feuerstein

aus Bochum-Langendreer

2005

Dynamik kleiner Quantensysteme in intensiven Laserfeldern

Index

1.1 Einführung: Atome und Moleküle in intensiven Laserfeldern 9

1.2 Nichtsequentielle Doppel- und Mehrfachionisation von Atomen 12

1.2.1 Kinematik geladener Teilchen in intensiven Laserfeldern 12

1.2.2 Nichtsequentielle Doppelionisation von Neon: Rückstoßionenspektren 14

1.2.3 Nichtsequentielle Doppelionisation von Neon und Argon: Korrelierte Elektronenspektren 16

1.2.4 Nichtsequentielle Doppelionisation von Helium, Neon und Argon: Bedeutung der atomaren Struktur 20

1.2.5 Nichtsequentielle Mehrfachionisation 23

1.3 Theoretische Studien zur Wellenpaketspropagation 25

1.3.1 Berechnung von Fragment-Impulsverteilungen mit der Methode des ‚Virtuellen Detektors' 27

1.3.2 Fragmentation von H_2^+ im Laserfeld: Abhängigkeit vom Vibrations-. Anfangszustand. 28

1.3.3 Visualisierung der Wellenpaketsdynamik von D_2^+ mittels ultrakurzer Pulse 29

1.3.4 Ion-Atom-Stöße in elliptisch polarisierten Laserfeldern: zirkularer Dichroismus 31

1.4 Wellenpaketsdynamik von H_2^+ in ultrakurzen Laserpulsen 32

1.5 Ausblick: Pump-Probe-Experimente und laserassistierte Prozesse 35

Anhang I Vollständiges Schriftenverzeichnis 39

Fachzeitschriften und Konferenzberichte 41

Eingeladene Vorträge 46

Anhang II Auswahl der wichtigsten Publikationen 47

Momentum distributions of Ne^{n+} ions created by an intense ultrashort laser pulse [6]
R. Moshammer, B. Feuerstein, W. Schmitt, A. Dorn, C.D. Schröter, J. Ullrich, H. Rottke, C. Trump, M. Wittmann, G. Korn, K. Hoffmann and W. Sandner
Phys. Rev. Lett. ***84*** *(2000) 447*

Nonsequential multiple ionization in intense laser pulses: interpretation of ion momentum distributions within the classical 'rescattering' model [10]
B. Feuerstein, R. Moshammer and J. Ullrich
J. Phys. B ***33*** *(2000) L823*

Separation of recollision mechanisms in nonsequential strong-field double ionization of Ar: the role of excitation-tunneling [13]
B. Feuerstein, R. Moshammer, D. Fischer, A. Dorn, C.D. Schröter, J. Deipenwisch, C. Höhr, P. Neumayer, J. Ullrich, H. Rottke, C. Trump, M. Wittmann, G. Korn and W. Sandner
Phys. Rev. Lett. ***87*** *(2001) 043003*

Correlated two-electron dynamics in strong-field double ionization [17]
R. Moshammer, B. Feuerstein, J. R. Crespo Lopez-Urrutia, A. Dorn, D. Fischer, C.D. Schröter, W. Schmitt, J. Ullrich, H. Rottke, C. Trump, M. Wittmann, G. Korn, K. Hoffmann and W. Sandner
Phys. Rev. A ***65*** *(2002) 035401*

On the computation of momentum distributions within wave packet propagationcalculations [20]
B. Feuerstein and U. Thumm
J. Phys. B ***36*** *(2003) 707*

Strongly directed electron emission in non-sequential double ionization of Ne by intense laser pulses [21]
R. Moshammer, J. Ullrich, B. Feuerstein, D. Fischer, A. Dorn, C.D. Schroeter, J.R. Crespo Lopez-Urrutia, C. Hoehr, H. Rottke, C. Trump, M. Wittmann, G. Korn, K. Hoffmann and W. Sandner
J. Phys. B ***36*** *(2003) L113*

Fragmentation of H_2^+ in strong 800 nm laser pulses: initial vibrational state dependence [22]
B. Feuerstein and U. Thumm
Phys. Rev. A ***67*** *(2003) 043405*

Mapping of coherent and decohering nuclear wave packet dynamics in D_2^+ with ultrashort laser pulses [24]
B. Feuerstein and U. Thumm
Phys. Rev. A, ***67*** *(2003) 063408*

Atomic structure dependence of nonsequential double ionization of He, Ne and Ar in strong laser pulses [31]
V.L.B. de Jesus, B. Feuerstein, K. Zrost, D. Fischer, A. Rudenko, F. Afaneh, C.D. Schröter, R. Moshammer and J. Ullrich
J. Phys. B ***37*** *(2004) L161*

Circular dichroism in laser-assisted proton - hydrogen collisions [32]
T. Niederhausen, B. Feuerstein and U. Thumm
Phys. Rev. A ***70*** *(2004) 023408*

Fragmentation dynamics of molecular hydrogen in strong ultrashort laser pulses [37]
A. Rudenko, B. Feuerstein, K. Zrost, V.L.B. de Jesus, T. Ergler, C.D. Schröter, R. Moshammer and J. Ullrich
J. Phys. B ***38*** *(2005) 487*

1.1 Einführung: Atome und Moleküle in intensiven Laserfeldern

100 Jahre nach Albert Einsteins bahnbrechender Arbeit über den photoelektrischen Effekt ist die Wechselwirkung von Licht mit Materie immer noch Gegenstand aktueller Forschung. Ein wesentlicher Grund sind die enormen Fortschritte in der Lasertechnologie, welche die Erzeugung immer intensiverer und immer kürzerer Lichtpulse erlauben. Bei diesen hohen Intensitäten spielen nichtlineare Effekte, welche über den klassischen Photoeffekt hinausgehen, eine wesentliche Rolle (siehe Abb. 1).

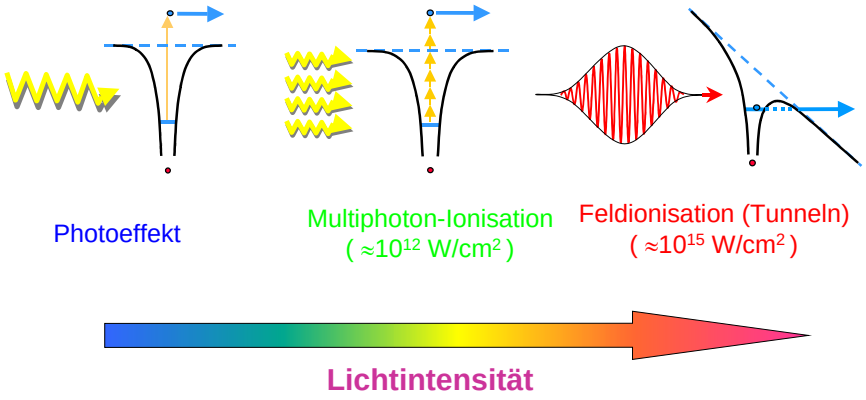

Abbildung 1. Vom Photoeffekt zur Tunnelionisation.

Schon 1931 veröffentlichte Maria Goeppert-Mayer eine Arbeit über Multiphotonenprozesse[1]. Später folgte eine Vielzahl von theoretischen und experimentellen Untersuchungen[2], in denen sich sowohl der Teilchen- (Multiphoton-Ionisation) als auch der klassische Wellencharakter (Feldionisation) manifestieren. Als recht erfolgreich in der Beschreibung von Elektronendynamik erwies sich das sogenannte "single active electron" (SAE) Modell, welches die beobachteten Raten für Einfachionisation gut wiedergeben konnte. Eine rege Diskussion der zugrunde liegenden Mechanismen löste vor gut 20 Jahren die Beobachtung aus, daß für niedrigere Intensitäten die Ausbeute an doppelt und mehrfach geladenen Ionen um mehrere Größenordnungen über den von dem SAE-Modell vorhergesagten Werten lag[3]. Hierbei wurde eine *sequentielle* Feldionisation angenommen und die beobachtete gravierende Diskrepanz als *nichtsequentielle* Doppel- bzw. Mehrfachionisation bezeichnet (Abb. 2). In den vergangenen Jahren hat sich das Verständnis dieser Prozesse dank moderner experimenteller Zugänge und neuer theoretischer Ansätze entscheidend verbessert, wozu nicht zuletzt auch die hier dargestellten Arbeiten entscheidend beigetragen haben[4].

Neben der atomaren Ionisation ist die Fragmentation von Molekülen (Ionisation, Dissoziation) in starken Laserfeldern ein ebenso aktueller Forschungsgegenstand. Der Laser hat dabei als extern steuerbares „Werkzeug" eine zentrale Bedeutung, was sich in vielfältiger Anwendung im Bereich der kohärenten Kontrolle zeigt. Daneben berührt die den betrachteten Prozessen zugrunde liegende Wellenpaketsdynamik fundamentale Fragestellungen in der Quantenmechanik, wie z.B. Dekohärenz, welche u.a. besonders relevant für mögliche Anwendungen (Quantencomputer, Kryptographie, Teleportation) sind.

---

[1] M. Goeppert-Mayer, *Ann. Phys. (Leipzig)* **9** (1931) 273.
[2] L. F. DiMauro and P. Agostini, *Adv. At. Mol. Opt. Phys.* **35** (1995) 79; M. Protopapas et al., *Phys. Rep.* **60** (1997) 389.
[3] A. L'Huiller et al., *Phys. Rev. A* **27** (1983) 2503.
[4] R. Dörner et al., *Adv. At. Mol. Opt. Phys.* **48** (2002) 1.

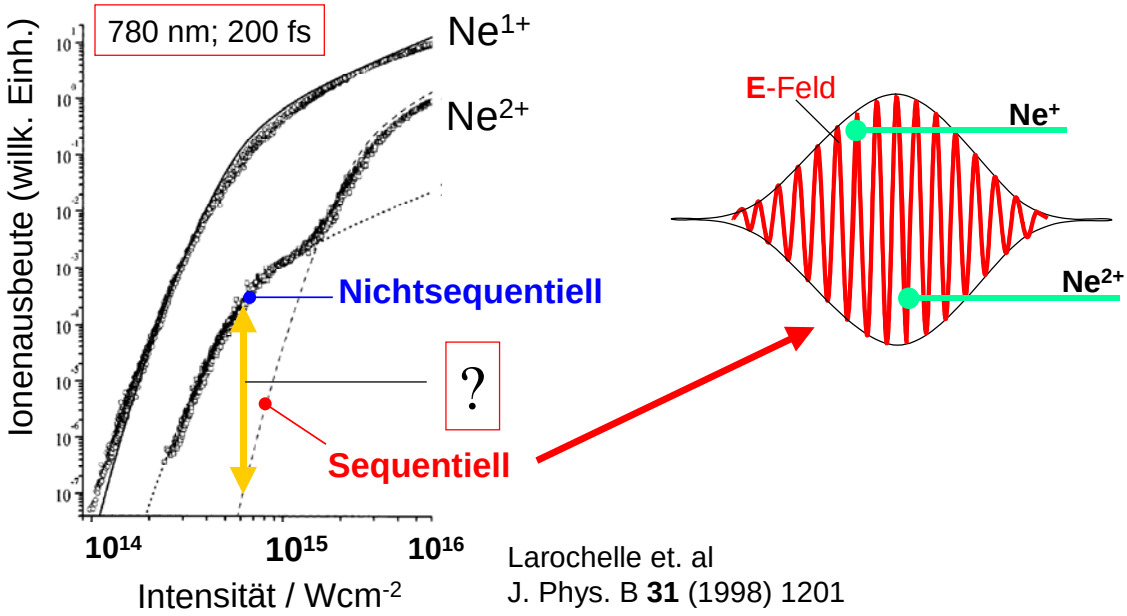

Abbildung 2. Ionenausbeuten für Einfach- und Doppelionisation von Neon in intensiven Laserpulsen.

Einen Schwerpunkt der Forschung bildet hier aufgrund seiner strukturellen Einfachheit H_2 bzw. D_2 und speziell seine ionische Form H_2^+ (D_2^+). Letzteres stellt das einfachste molekulare System überhaupt dar und ist durch einige spezifische Eigenschaften ausgezeichnet, die es zu einem idealen und vielfach untersuchten Modellsystem für die theoretische Beschreibung von Laser-Materie-Wechselwirkung machen[5]: Erstens ist nur der elektronische Grundzustand $1s\sigma_g$ gebunden, während alle angeregten Zustände repulsive Potentialkurven bilden, die zum $1/R$-Coulomb-Potential der beiden Protonen konvergieren (Abb. 3, R: internuklearer Abstand). Zweitens bedingt die Entartung der beiden untersten Zustände $1s\sigma_g$ und $2p\sigma_u$ bei großen Kernabständen in Gegenwart eines äußeren elektrischen Feldes ein großes Dipol-Übergangsmoment dieser Niveaus, welches wesentlich für die Kopplung des Systems an das Laserfeld und somit für die Fragmentationsdynamik ist. Drittens erlaubt die große Differenz der Ionisationspotentiale von H_2 (15,6 eV) und H_2^+ (30 eV) eine Behandlung der Fragmentation als Zwei-Stufen-Prozeß (Abb. 3): Beginnend mit neutralem H_2 wird in einem starken Laserfeld zunächst durch Feldionisation ein Elektron entfernt (1) und das so gebildete Molekülion erfährt nachfolgend weitere Fragmentationsprozesse.

Nach dem ersten Ionisationsschritt ist die so präparierte Kernwellenfunktion kein Eigenzustand zu der neuen Potentialkurve von H_2^+ und beginnt auf dieser als Wellenpaket zu propagieren. In Gegenwart des Laserfeldes kommt es zur Ausbildung von lichtinduzierten Potentialkurven (dressed states)[6], welche der Absorption einer diskreten Anzahl von Photonen entsprechen. Über vermiedene Kreuzungen öffnen sich dabei verschiedene Kanäle der Dissoziation (2), welche mit der Netto-Absorption von einem (1ω) bzw. zwei (2ω) Photonen verknüpft sind. Die Emission des zweiten Elektrons führt zur Coulomb-Explosion, welche im Prinzip auf zwei unterschiedlichen Wegen erreicht werden kann. Im Falle von Feldionisation spricht man von sequentieller Doppelionisation (3a), welche als Spezialfall des

[5] S. Chelkovski et al, *Phys. Rev. Lett.* **82** (1999) 3416.
[6] A.D. Bandrauk and M.L. Sink, *J. Chem. Phys.* **74** (1981) 1110.

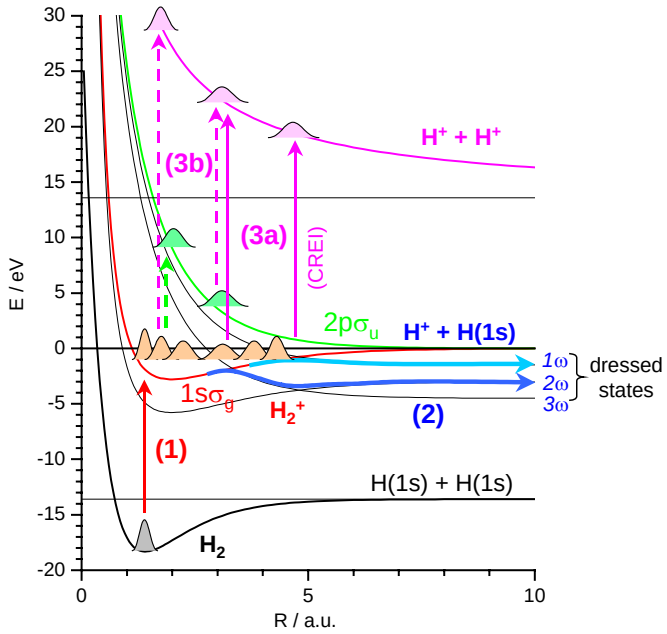

Abbildung 3. Fragmentationskanäle von H_2 im intensiven Laserfeld.

dissoziierenden Moleküls im Bereich von $R = 3$ bis 8 a.u.[7] eine stark erhöhte Ionisationswahrscheinlichkeit aufweist (Charge Resonance Enhanced Ionization, CREI)[8]. Im Falle linearer Polarisation kann das erste Elektron vom oszillierenden Feld zu seinem Mutterion zurückgetrieben werden und dieses entweder direkt durch Stoßionisation oder indirekt durch Stoßanregung mit nachfolgender Feldionisation des angeregten Elektrons weiter ionisieren (nichtsequentielle Doppelionisation, (3b))[9]. Als Konzept für zeitaufgelöste Studien wurde in neueren Arbeiten die Idee einer „molekularen Uhr" eingeführt[10], welche auf der kombinierten Wellenpaketsdynamik des emittierten Elektrons und der Kerne im oben geschilderten Rekollisions-Szenario für nichtsequentielle Doppelionisation beruht. Die Emission des ersten Elektrons setzt den Startzeitpunkt für die Propagation der Kerne, welche nach einer wohldefinierten Zeit durch die vom Rekollisionsprozeß induzierte Coulomb-Explosion gestoppt wird. Aus der kinetischen Energie der Fragmente kann nun der Kernabstand zum Zeitpunkt der Rekollision bestimmt werden, was im Prinzip eine Rekonstruktion des dynamischen Prozesses mit Attosekunden-Zeitauflösung erlaubt.

Für die Durchführung der hier beschriebenen Studien standen zunächst am Max-Born-Institut in Berlin-Adlershof und dann am MPI-K ein fs-Lasersystem zur Verfügung. Außerdem wurde erstmals ein hochauflösendes Reaktionsmikroskop [33] (Abb. 4) speziell für die Untersuchung der Wechselwirkung intensiver, ultrakurzer Laserpulse mit Atomen und Molekülen aufgebaut. Insbesondere die Verwendung von Vielfachkoinzidenztechniken hat, ähnlich wie zuvor schon in anderen Bereichen[11], zu entscheidenden Durchbrüchen im Verständnis der laserinduzierten Dynamik geführt. Neben zeitgleich durchgeführten

[7] Im folgenden werden vielfach atomare Einheiten (a.u.) verwendet. Länge: Bohrscher Radius a_0; Geschwindigkeit: 1/137 der Lichtgeschwindigkeit; Masse: Elektronenmasse; Energie: 27,2 eV (2 Rydberg); Zeit: 0,024 fs.
[8] T. Zuo and A. Bandrauk, *Phys. Rev. A* **52** (1995) R2511
[9] A. Staudte et al, *Phys. Rev. A* **65** (2002) 020703
[10] H. Niikura et al., *Nature* **417** (2002) 917.
[11] J. Ullrich et al., *Rep. Prog. Phys.* **66** (2003) 1463.

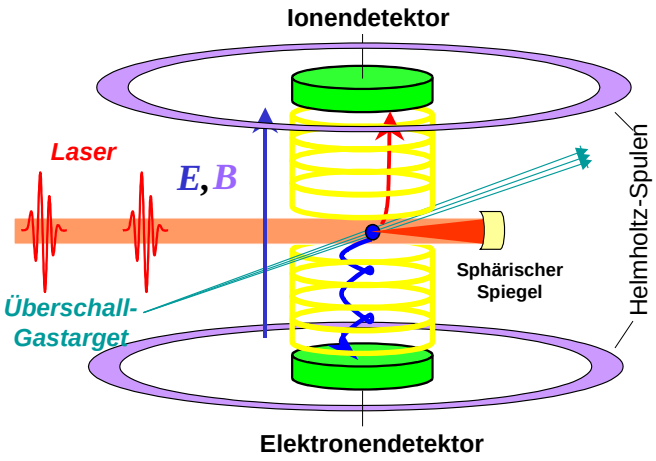

Abbildung 4. Schematischer Aufbau des Reaktionsmikroskops zur Untersuchung von laserinduzierten Prozessen (Ionisation, Fragmentation) in Atomen und Molekülen.

Pionierexperimenten der Universität Frankfurt werden Reaktionsmikroskope inzwischen weltweit an sechs führenden Labors verwendet bzw. befinden sich im Aufbau. In einer Ultrahochvakuum-Kammer ($2 \cdot 10^{-11}$ mbar) wird der Laserstrahl auf ein kollimiertes Überschallstrahl-Gastarget fokussiert. Bei einem Fokus-Durchmesser von 5 µm werden am MPI-K Intensitäten bis zu $5 \cdot 10^{16}$ W/cm^2 erreicht. Die im Quellvolumen erzeugten Reaktionsprodukte (Rückstoßionen, Elektronen) werden mit schwachen elektrischen (2 V/cm) und magnetischen (7 G) Feldern senkrecht zum Laserstrahl extrahiert und auf ortsempfindliche Detektoren abgebildet. Aus Ort und Flugzeit können die Impulskomponenten nach dem Stoß mit sehr hoher Auflösung (< 0,02 a.u.) und über einen großen Raumwinkelbereich (bis zu 4π) bestimmt werden. Der Ti:Saphir-Laser (795 nm Wellenlänge) erzeugt Pulse von 25 fs Dauer und einer Energie von bis zu 400 µJ bei einer Repititionsrate von 3 kHz. Zur Erzeugung ultrakurzer Pulse mit wenigen optischen Zyklen wird das Spektrum in einer gasgefüllten Hohlfaser verbreitert und die Pulse in einem Spiegel-Prismensystem auf 6 fs komprimiert[12]. Zum Zeitpunkt der hier durchgeführten Arbeiten konnten lediglich in ca. fünf Labors international solch kurze Pulsdauern realisiert werden.

1.2 Nichtsequentielle Doppel- und Mehrfachionisation von Atomen

1.2.1 Kinematik geladener Teilchen in intensiven Laserfeldern

Eine wichtige Grundlage zum Verständnis der nichtsequentiellen Doppel- und Mehrfachionisation von Atomen bildet die (klassische) Kinematik geladener Teilchen in einem intensiven Laserfeld. Daher sei diese der Interpretation der experimentellen Befunde vorangestellt. Für die betrachteten Intensitäten (10^{14} - 10^{15} W/cm^2) und Wellenlänge (795 nm) wird die Freisetzung von Elektronen im Bild der Feld- bzw. Tunnelionisation verstanden, wobei das Photonenfeld klassisch als elektrisches Feld[13] beschrieben wird. Auch in diesem Fall ist das elektrische Wechselfeld (optischer Zyklus: 2,7 fs) des Lasers quasistatisch auf der

[12] K. Zrost, *Dissertation*, Heidelberg 2005.
[13] Für Intensitäten unterhalb von 10^{16} W/cm^2 sind relativistische Effekte unbedeutend, so daß die magnetische Komponente vernachlässigt werden kann.

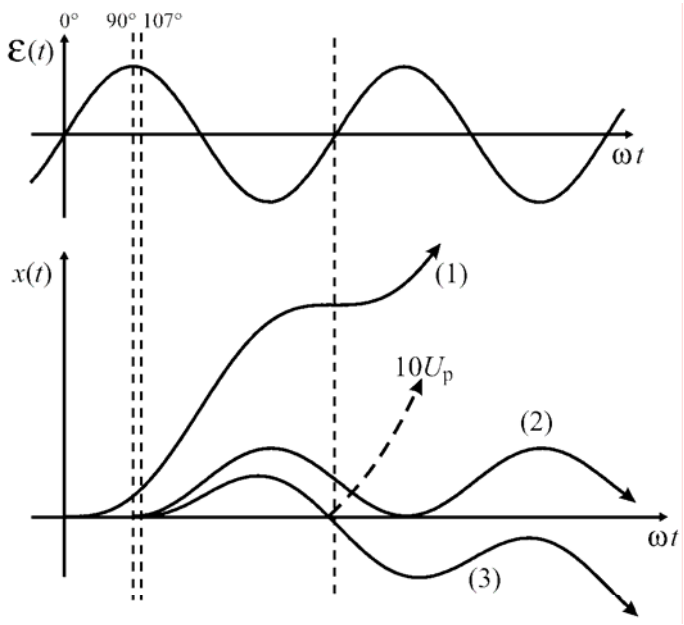

Abbildung 5. Schematische Darstellung exemplarischer Trajektorien eines geladenen Teilchens in einem Laserfeld für verschiedene Startphasen $\varphi_0 = \omega t_0$ [10]. (1): $\varphi_0 = 0°$, maximaler Driftimpuls; (2): $\varphi_0 = 180°$, Driftimpuls = 0; (3): $\varphi_0 = 107°$, Rekollision mit maximaler kinetischer Energie ($3{,}17U_p$). Elastische Rückstreuung von Elektronen zu diesem Zeitpunkt führt zu einer kinetischen Energie von $10U_p$ ("Cutoff" in ATI-Spektren)[14].

Zeitskala (10^{-18} s) des gebundenen Elektrons. Die Adiabasie wird durch den sog. Keldysh-Parameter[15] γ ausgedrückt. welcher durch das Verhältnis der charakteristischen Energien des gebundenen und freien Elektrons bestimmt ist:

$$\gamma = \sqrt{I_p/2U_p} \tag{1}$$

Hier ist I_p die Bindungsenergie (Ionisationspotential) und U_p die mittlere kinetische Energie (ponderomotives Potential, $U_p = I/4\omega^2$) des im Laserfeld (Intensität I, Frequenz ω) oszillierenden Elektrons. Für $\gamma < 1$ liegt Tunnelionisation vor. In diesem Fall ist die kinetische Energie unmittelbar nach dem Tunneln vernachlässigbar klein und als Anfangsbedingung für die Bewegung im Laserfeld kann ein ruhendes Teilchen angenommen werden. Die Lösung der klassischen Bewegungsgleichungen [10] für ein Teilchen der Ladung q im oszillierenden Feld

$$\mathcal{E}(t) = \mathcal{E}_0(t) \sin \omega t \tag{2}$$

eines linear polarisierten Laserpulses ergibt zwei Anteile – eine oszillierende Bewegung, welche nur während des Pulses auftritt und mit diesem abklingt und eine Driftbewegung, welche durch die Phase des Wechselfeldes zum Zeitpunkt der Ionisation t_0 bestimmt ist (siehe Abb. 6):

$$p(t_0) = \frac{q}{\omega} \mathcal{E}_0(t_0) \cos \omega t_0. \tag{3}$$

[14] G.G. Paulus et al, *J. Phys. B* **27** (2000) L703
[15] L.V. Keldysh, *Zh. Eksp. Teor. Fiz.* **47** (1964) 1945.

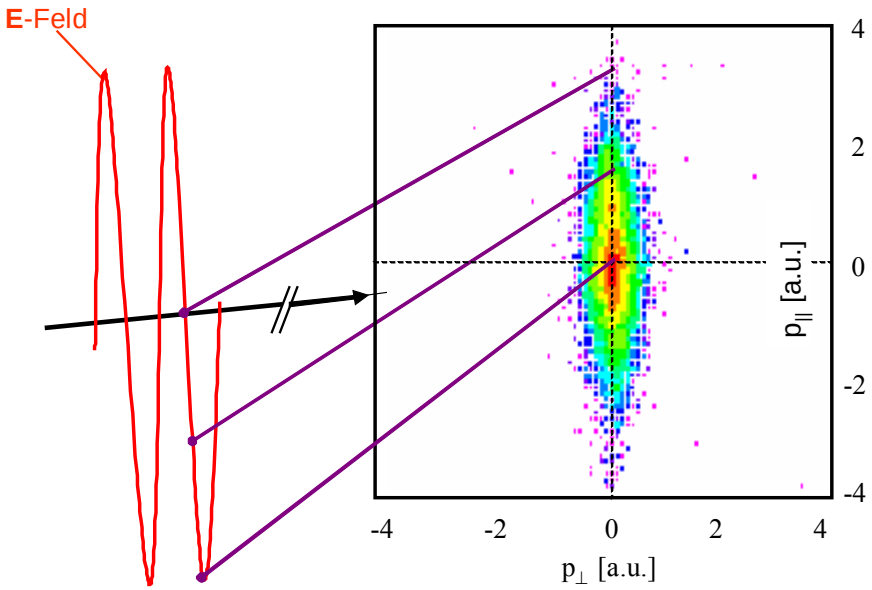

Abbildung 6. Zusammenhang der beobachteten Driftimpulse mit der Phase des Laserfeldes. Gezeigt ist ein Spektrum der Rückstoßionen für Einfachionisation von Neon bei einer Intensität von ca. $1 \cdot 10^{15}$ W/cm^2 [6].

Somit ist die beobachtete Impulskomponente (Driftimpuls) $p_\parallel$ parallel zur Richtung der Laserpolarisation direkt mit der Phase des Laserfeldes zur Zeit t_0 verknüpft. Der maximale Driftimpuls

$$p_{\max} = \frac{q}{\omega}\,\mathcal{E}_{\max} = 2\,q\sqrt{U_p} \qquad (4)$$

ergibt sich beim Start zu einem Nulldurchgang des Feldes, während für die an den Feldextrema beginnenden Trajektorien der Driftimpuls gleich Null ist. Da nun die Tunnelwahrscheinlichkeit exponentiell von der Feldstärke abhängt, folgt im SAE-Modell eine gaußartige Verteilung für $p_\parallel$, deren Maximum bei Null liegt[16] (siehe Abb. 6).

1.2.2 Nichtsequentielle Doppelionisation von Neon: Rückstoßionenspektren

Die ersten differentiellen Messungen zur nichtsequentiellen Doppel- und Mehrfachionisation von Neon wurden im Sommer 1999 in Zusammenarbeit mit dem Max-Born-Institut, Berlin-Adlershof (Gruppe Prof. Sandner) am dortigen Institut durchgeführt. Parallel dazu liefen Untersuchungen zur Doppelionisation von Helium einer Frankfurt-Marburger Kollaboration[17].

Die gemessenen Rückstoßionen-Impulsspektren für Neon sind in Abb. 7 dargestellt. Im Gegensatz zur Einfachionisation, welche die für das SAE-Modell erwartete Verteilung mit Maximum bei Null zeigt, ergibt sich für Ne^{2+} und Ne^{3+} eine gänzlich andere Form mit einem Doppelmaximum bei jeweils betragsmäßig recht hohen Impulsen, die zudem mit dem Ladungszustand skalieren. Die Intensität der Pulse von 30 fs Dauer lag jeweils bei ca.

[16] N.B. Delone and V.P. Krainov, *J. Opt. Soc. Am. B* **8** (1991) 1207.
[17] Th. Weber et al, *Phys. Rev. Lett.* **84** (2000) 443.

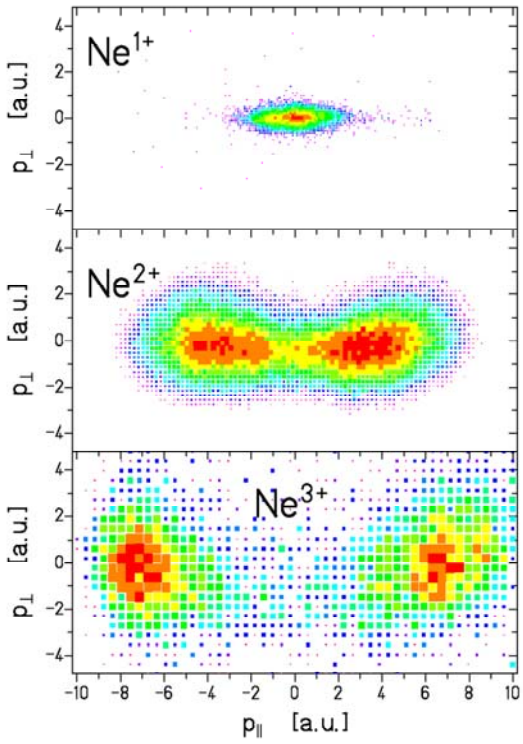

Abbildung 7. Zweidimensionale Spektren der Rückstoßionenimpulse parallel ($p_{\parallel}$) und senkrecht ($p_{\perp}$) zur Richtung der Laserpolarisation für Einfach-, Doppel-, und Dreifachionisation von Neon bei einer Intensität von ca. $1 \cdot 10^{15}$ W/cm^2 [6].

$1 \cdot 10^{15}$ W/cm^2. Unter den seinerzeit über mehr als ein Jahrzehnt hinweg kontrovers diskutierten Mechanismen der nichtsequentiellen Doppel- und Mehrfachionisation konnten somit jene ausgeschlossen werden, die eine "simultane" Freisetzung der Elektronen bei maximalem Feld annahmen (Shakeoff[18], kollektives Tunneln[19]), da diese eine ähnliche Form des Spektrums wie bei der Einfachionisation erwarten ließen. Hingegen lassen die hohen Driftimpulse auf eine sehr kleine Feldstärke zum Zeitpunkt der Doppel- bzw. Mehrfachionisation schließen, was eine Feldionisation praktisch ausschließt. Einzig das 1993 von Paul Corkum vorgeschlagene sog. Rekollisionsmodell[20] und das vorher in einem anderen Zusammenhang bereits diskutierte "antenna model"[21] erwiesen sich als konsistent mit diesem Befund. Die Propagation des Elektrons im Laserfeld wird dabei in der im vorigen Abschnitt ausgeführten Weise klassisch behandelt. Tunnelt das erste Elektron kurz nach dem Maximum des Feldes, so kann es vom oszillierenden Feld zu seinem Mutterion zurückgetrieben werden und durch Stoßionisation in einem (e,2e)-Prozeß ein oder mehrere Elektronen herausschlagen (Abb. 5). Dieses geschieht in der Nähe eines Nulldurchgangs des Feldes, so daß die zu diesem Zeitpunkt gebildeten, nun zweifach oder dreifach geladenen Ionen einen hohen Driftimpuls aufnehmen, der nach Gl. (4) proprotional zum Ladungszustand ist. Da bei optischen Wellenlängen der Impulsübertrag der Photonen vernachlässigt werden kann, ist der Impuls des Ions zu jedem Zeitpunkt gleich dem negativen Summenimpuls der freigesetzten Elektronen, der Gesamtimpuls aller Teilchen (von der geringen thermischen Bewegung des kalten Targets abgesehen) gleich Null (siehe Abb. 8). Der gemessene Impuls

[18] D.N. Fittinghoff et al., *Phys. Rev. Lett.* **69** (1992) 2642.
[19] U. Eichmann, *Phys. Rev. Lett.* **84** (2000) 3550.
[20] P.B. Corkum, *Phys. Rev. Lett.* **71** (1993) 1994.
[21] M.Y. Kuchiev, *Sov. Phys.-JETP Lett.* **45** (1987) 404.

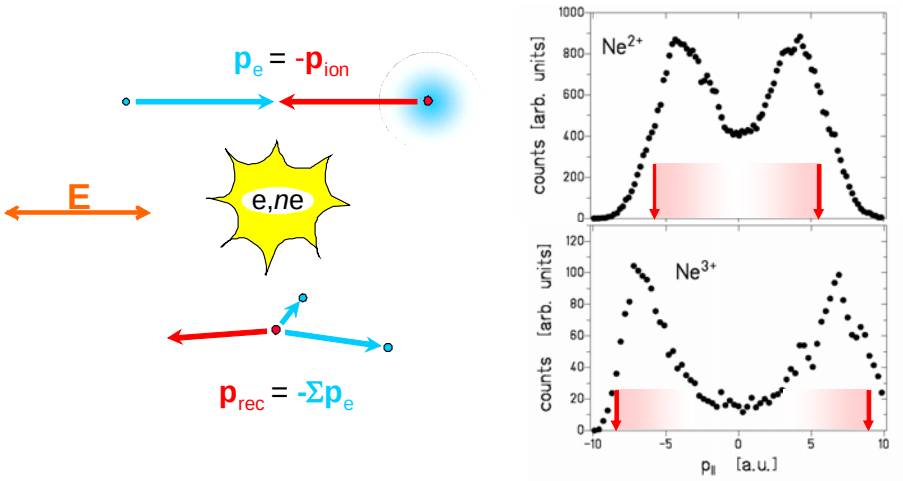

Abbildung 8. Impulsübertrag auf das Ion durch Rückstoß der nach der Stoßionisation auslaufenden Elektronen. Die Pfeile in den Spektren rechts geben den maximalen Driftimpuls an, siehe Gl. (4).

der Ionen ist die Summe aus dem Driftimpuls (für den Startzeitpunkt der Rekollision) und dem Rückstoßimpuls p_{rec} aus dem Stoßprozeß. Dieser Rückstoßimpuls ist dem Driftimpuls bei der (wahrscheinlicheren) Vorwärtsstreuung der Elektronen entgegengesetzt [6,10] und so erwartet man die Maxima der Impulsverteilung etwas unterhalb des maximalen Driftimpulses, was sehr gut mit dem experimentellen Befund übereinstimmt (schattierter Bereich innerhalb der Pfeile in den Spektren rechts in Abb. 8). Ein weiterer Grund für die Lage der Maxima innerhalb der maximalen Driftimpulse liegt darin, daß je nach Phasenlage der Tunnelionisation des ersten Elektrons auch kleinere Driftimpulse auftreten (siehe auch Fig. 4 in [6]).

Die Untersuchung von Neon an Stelle von Helium hatte meßtechnische Gründe, erwies sich aber im Nachhinein als Vorteil. Zum einen war diese Messung komplementär zur Arbeit der Frankfurt-Marburger Kollaboration, welche das von seiner Struktur her einfachere Helium betrachteten. Zum anderen erwies sich die Doppelstruktur der Spektren als deutlich ausgeprägter als im Falle von Helium (siehe auch Abschnitt 1.2.4) und die Ergebnisse für die Dreifachionisation ergaben ein zusätzliches sehr starkes Indiz für den Mechanismus der Rekollision. Technisch gesehen handelt es sich bei den hier diskutierten Arbeiten um die wohl erste Anwendung einer "Attosekunden-Streak-Kamera"[22], da die beobachteten Driftimpulse mit einer Zeitauflösung unterhalb einer Femtosekunde mit der Phase des Laserfeldes korreliert sind.

1.2.3 Nichtsequentielle Doppelionisation von Neon und Argon: Korrelierte Elektronenspektren

Zeigte sich schon die Doppelstruktur der Impulspektren für Helium[3] weniger deutlich ausgeprägt als für Neon, so galt dies noch mehr für Argon (Abb. 9), wie parallel Ergebnisse unserer und der Frankfurt-Marburger Gruppen zeigten, wobei auch die Intensitätsabhängigkeit der Rückstoßionenspektren untersucht wurde[23]. Dies ließ Zweifel an der Richtigkeit des Rekollisionsmodells aufkommen, obgleich theoretische Studien dieses im Prinzip stützten[24,25]. Bereichert wurde die experimentell verfügbare Information durch die

[22] Itatani et al., *Phys. Rev. Lett.* **88** (2002) 173903; M. Drescher et al., *Nature* **419** (2002) 803.
[23] Th. Weber et al., *Phys. Rev. Lett.* **84** (2000) 443.
[24] A. Becker and F.H.M. Faisal, *Phys. Rev. Lett.* **84** (2000) 3564; M. Lein et al., *Phys. Rev. Lett.* **85** (2000) 4707.

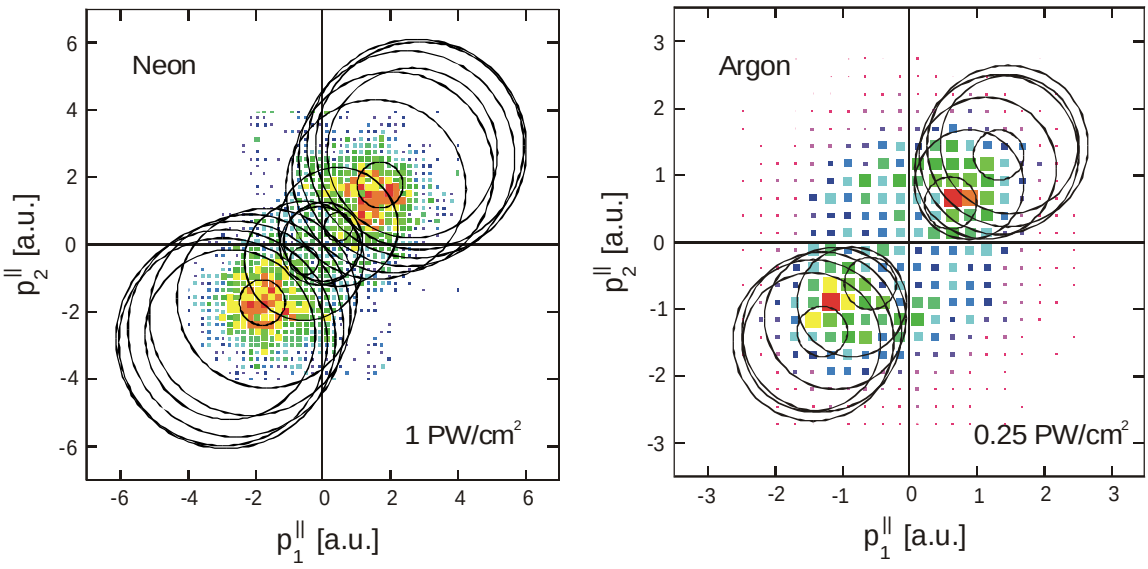

Abbildung 9. Korrelierte Spektren der Longitudinalimpulse (parallel zur Laserpolarisation) der emittierten Elektronen für nichtsequentielle Doppelionisation von Neon [21] und Argon [13].

erste koinzidente Messung der Impulse beider Elektronen für Doppelionisation von Argon[26], jedoch konnte noch keine umfassende und konsistente Interpretation gegeben werden. In Bezug auf die Auffüllung des „Tals“ zwischen den Maxima der Rückstoßimpulsspektren, also den Bereich um Impuls Null wurde ein weiterer Mechanismus innerhalb des Rekollisionsmodells diskutiert, nämlich die Elektronenstoßanregung bei der Rekollision mit nachfolgender Tunnelionisation des angeregten Elektrons (recollision-excitation plus subsequent field ionization (RESI))[9–27][10]. Ein Indiz ist die Tatsache, daß die Tunnelionisation vorzugsweise kleine Driftimpulse liefert. Um dieser Frage detaillierter nachzugehen, wurde eine kinematische Analyse eigener Daten zu den koinzident gemessenen Impulsen beider Elektronen vorgenommen. Wie im vorigen Abschnitt erwähnt, ist ja der Impuls des Ions gleich dem negativen Summenimpuls der emittierten Elektronen.

Abb. 9 zeigt die zweidimensionalen Spektren für die korrelierten Impulskomponenten der beiden Elektronen parallel zur Richtung der Laserpolarisation. Dabei entspricht der erste und dritte Quadrant einer Emission beider Elektronen in den gleichen Halbraum und der zweite bzw. vierte Quadrant einer Emission in entgegengesetzte Halbräume. Vergleicht man die Ergebnisse für Neon mit denen für Argon, so fällt im letzteren Fall die relativ stärkere Besetzung des zweiten und vierten Quadraten auf. Der Bildung des Summenimpulses, welcher betragsmäßig gleich dem Rückstoßionenimpuls ist, entspricht die Projektion des 2-D-Spektrums auf die Hauptdiagonale. Zwar finden sich entlang dieser in beiden Fällen die Maxima der 2-D-Verteilung, doch führen die zahlreichen Ereignisse im zweiten und vierten Quadranten bei Argon zu einer Auffüllung des Minimums im Spektrum der Rückstoßimpulse.

Die kinematische Analyse innerhalb des Rekollisionsmodells erlaubt nun, unter Berücksichtigung der Energie- und Impulserhaltung, Grenzen für die beobachteten Impulse anzugeben [13]. Der Vorteil einer solchen rein kinematischen Betrachtung liegt darin, daß sie keinerlei Kenntnis über die Details der Dynamik bedarf. Für den Fall einer direkten Stoßionisation (e,2e), ist der Rückstoßimpuls auf das Ion durch die Überschußenergie limitiert wie in Abb. 10 illustriert. Es ergeben sich Kreisflächen möglicher Impulsverteilungen

[25] R. Kopold et al., *Phys. Rev. Lett.* **85** (2000) 3781.
[26] Th. Weber et al., *Nature (London)* **405** (2000) 658.
[27] H. van der Hart, J. Phys. B **33** (2000) L699.

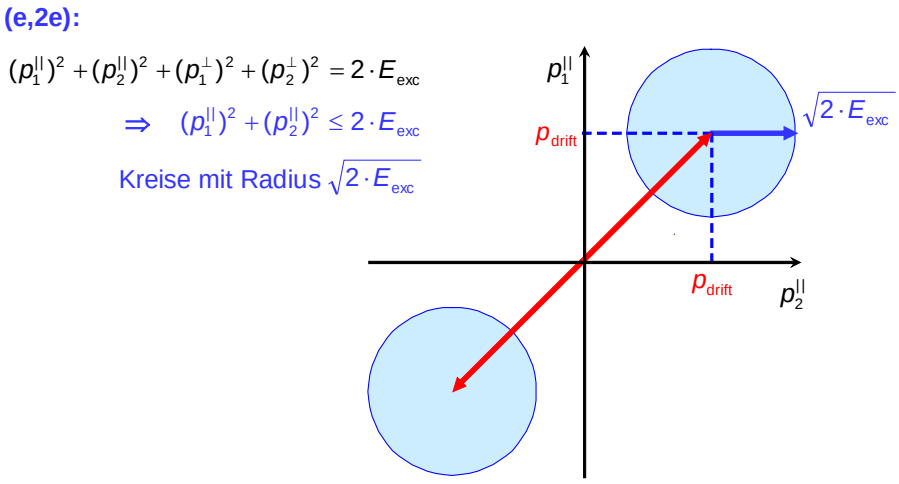

Abbildung 10. Kinematische Grenzen für die beobachteten Impulse der Elektronen nach dem Rekollisions-(e,2e)-Prozeß.

zwischen den beiden Elektronen, deren Radius proportional zur Quadratwurzel der Überschußenergie E_{exc} ist und deren Mittelpunkte um den Driftimpuls entlang der Hauptdiagonale vom Ursprung weg verschoben sind, da beide Elektronen nach dem Stoß den gleichen Driftimpuls aufnehmen. Der für einen (e,2e)-Prozeß kinematisch erlaubte Bereich ist nun durch die Union aller dieser Kreisflächen für sämtliche Startzeitpunkte des ersten, feldionisierten Elektrons gegeben. Eine repräsentative Auswahl dieser Kreise ist in Abb. 9 jeweils für Neon und Argon eingezeichnet. Im Fall von Neon [21] liegen fast alle Ereignisse innerhalb des für Stoßionisation kinematisch erlaubten Bereiches – dies ist demnach der dominierende Mechanismus. Hingegen zeigt das Resultat für Argon [13], daß ein Großteil der Daten nicht mit direkter Stoßionisation verträglich ist – dies betrifft vor allem den zweiten und vierten Quadranten. Dies legt nahe, daß es ein anderer, mutmaßlich der RESI-Mechanismus, entscheidend zu nichtsequentieller Doppelionisation beiträgt. Die zur vorigen Betrachtung analog ermittelten kinematischen Grenzen ergeben Rechtecke (Fig. 1b in [13]), keine Kreise, da nun beide Elektronen unabhängig voneinander emittiert werden: Das erste erfährt bei der Rekollision eine inelastische Streuung, das zweite wird sequentiell nach der Anregung durch Feldionisation freigesetzt. Der gesamte kinematisch erlaubte Bereich ist durch seinen kreuzförmigen Umriß als unterbrochene Linie in Abb. 11 dargestellt. Zur Verdeutlichung des Summenimpulses wurde das Diagramm gegenüber Abb. 9 um 45° gedreht. Es zeigt sich, daß die experimentell gefundenen Daten für Argon mit den nun durch den zweiten Mechanismus erweiterten kinematischen Grenzen vollständig abgedeckt werden. Mehr noch: Da für die betrachtete Intensität von $2{,}5 \cdot 10^{14}$ W/cm^2 sich die mit Stoßionisation verträglichen Bereiche hier auf den ersten und dritten Quadranten beschränken, war es unter der Annahme, daß sich die RESI-Ereignisse auf alle vier Quadranten gleichmäßig verteilen[28], erstmals möglich, beide Beiträge zu separieren [13]. Die Projektion der beiden Anteile auf die Hauptdiagonale ergibt das Spektrum der Rückstoßionen, welches in Abb. 11 oben dargestellt ist. Dabei entfallen ca. 3/4 Anteile auf den RESI-Mechanismus, welcher ein breites Maximum bei Impuls Null liefert, während sich für die verbleibenden Ereignisse die erwartete Doppelstruktur für den Fall der direkten Stoßionisation ergibt. Die beobachtete Häufung in der Nähe der Hauptdiagonalen [21] ist eine recht überraschende Tatsache, da für

[28] Dies ist dann gerechtfertigt, wenn die Lebensdauer der angeregten Zustände mindestens einen optischen Zyklus beträgt - siehe auch Abschnitt 1.2.4

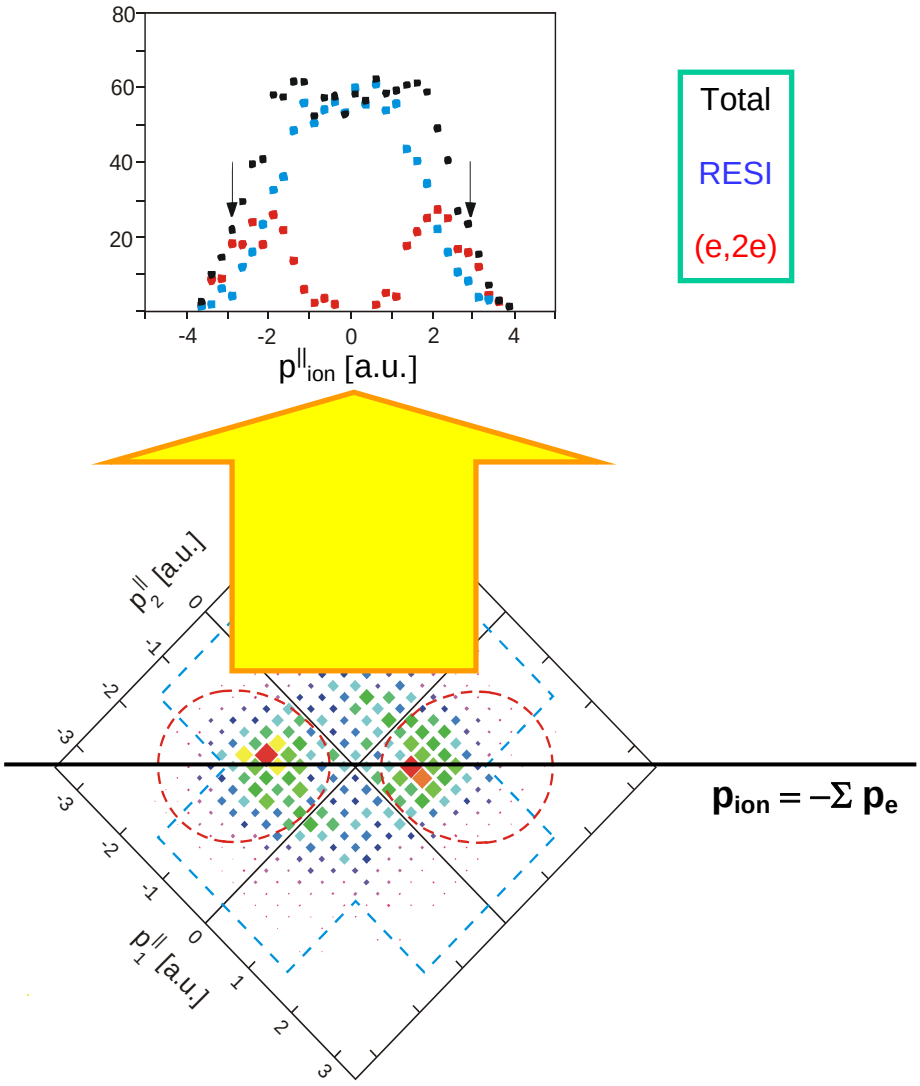

Abbildung 11. Korreliertes Spektrum der Longitudinalimpulse (parallel zur Laserpolarisation) der emittierten Elektronen für nichtsequentielle Doppelionisation von Argon (Intensität $2{,}5\cdot10^{14}$ W/cm^2). Kinematische Grenzen für die beobachteten Impulse der Elektronen nach dem Rekollisions-(e.2e)-(zwei Ovale) bzw. RESI-Modell (kreuzförmig). Die Projektion auf die Hauptdiagonale ergibt das Impulsspektrum der Ionen (obere Grafik), welches sich nach den (e,2e)- und RESI-Anteilen separieren läßt.

Stoßionisation mit schnellen Elektronen üblicherweise eine asymmetrische Aufteilung der Überschußenergie nach dem Stoß unter den emittierten Elektronen erfolgt, was zu einer Häufung abseits der Diagonalen, mehr zu den Achsen hin, führen sollte. Dies wird auch von Rechnungen, welche differentielle Querschnitte – allerdings unter Vernachlässigung des Laserfeldes in diesem Punkt – verwenden vorhergesagt[29]. Offenbar verhält sich die Dynamik der Stoßionisation in Gegenwart des Laserfeldes bzw. bei durch das Laserfeld induzierter Rekollision vollständig anders als aus Elektronenstoß-Experimenten bekannt, wo die elektrostatische Abstoßung der Elektronen imEndzustand eine wichtige Rolle spielt. Letztere manifestiert sich aber auch bei der Rekollision, wenn man zusätzlich den Transversalimpuls

[29] S.P. Goreslavskii et al., *Phys. Rev. A* **64** (2000) 053402.

(senkrecht zur Laserpolarisation) der Elektronen einschränkt, wie im Fall von Argon untersucht wurde [17]. Damit betrachtet man nur noch Elektronen, welche weitgehend parallel zum Laserfeld emittiert werden. Unter dieser Bedingung spaltet das Maximum in zwei symmetrische Gebiete abseits der Hauptdiagonalen auf. Dies ist offenbar eine direkte Folge der Elektronenabstoßung, welche eine Emission in die gleiche Raumrichtung unterdrückt. Solange aber der transversale Freiheitsgrad voll zur Verfügung steht, scheint das Laserfeld – im Gegensatz zum feldfreien Fall – eine symmetrische Aufteilung der Überschußenergie zu begünstigen. Eine definitive Erklärung hierfür liegt trotz einer Vielzahl von inzwischen erschienenen theoretischen Modellen leider mangels vollständig quantenmechanischer Rechnungen, welche den Einfluß des Laserfeldes auf die Stoßdynamik berücksichtigen, nicht vor. Dieser Umstand erhöht wiederum das Interesse am Studium laserassistierter Elektron-Atom-Stöße. Zur Zeit werden von verschiedener Seite erhebliche Anstrengungen unternommen, durch numerische Lösung der Schrödingergleichung im Laserfeld zu einem vollständigen Verständnis der Dynamik der Doppelionisation zu gelangen. Solche Rechnungen bewegen sich an der Grenze des mit moderner Computertechnologie machbaren.

1.2.4 Nichtsequentielle Doppelionisation von Helium, Neon und Argon: Bedeutung der atomaren Struktur

Aus dem schon diskutierten unterschiedlichen Verhalten von Neon und Argon erhebt sich die Frage nach dem Einfluß der atomaren Struktur auf die Dynamik nichtsequentieller Doppelionisation. Im SAE-Modell kommt diese (abgesehen von der Bindungsenergie) praktisch nicht vor, ja es wurde sogar teilweise die Ansicht vertreten, in Gegenwart starker Laserfelder würden sich alle Atome sehr ähnlich verhalten. Im Rekollisionsmodell hingegen spielen Elektronenstoßprozesse eine wesentliche Rolle; zudem ereignen sich diese zu Zeiten nahe der Nulldurchgänge des oszillierenden Feldes, so daß eine Abhängigkeit von der Atomstruktur nicht allzu überraschend erscheint. Ein wesentlicher Parameter für Stöße mit Elektronen ist deren anfängliche Energie. Bei der Rekollision ist die (klassisch betrachtet) maximale kinetische Energie proportional zur Intensität des Laserfeldes ($3{,}17U_\mathrm{p}$) und hängt zudem von der ursprünglichen Tunnelphase ab. Um die Energieabhängigkeit näher zu untersuchen, wurden die longitudinalen Impulsspektren der Ionen nach Doppelionisation systematisch bei verschiedenen Laserintensitäten (Pulsdauer 23 fs) für die Targets Helium, Neon und Argon vermessen [31]. Das Ergebnis ist in Abb. 12 zusammengestellt.

Da die Bestimmung der Laserintensität im Fokus allein aus der Geometrie und den Strahlparametern mit einem typischen Fehler von 30-50 % recht ungenau ist, wurde ein neues Verfahren der Intensitätskalibrierung angewendet. Hierzu wurde an das Elektronenspektrum für Einfachionisation von Neon eine theoretische Gaußverteilung[30] angepaßt. Mit dieser Methode konnte die absolute Intensität mit einer Genauigkeit von besser als 15 % bestimmt werden [31]. Die Intensitäten (Angaben jeweils oben links in Einheiten von 10^{15} W/cm^2) wurden so gewählt, daß die maximale Rekollisionsenergie in Einheiten des elementspezifischen Ionisationspotentials I_p der einfach geladenen Ionen etwa den gleichen Wert hat (kursive Zahlen oben rechts). Die schattierten Flächen geben die Bereiche an, in welchen die Maxima der Impulsverteilung für den (e,2e)-Mechanismus erwartet werden (siehe Abschnitt 1.2.2 und Abb. 8). Während die Verteilungen für Neon, abgesehen von der mit der Intensität wachsenden totalen Breite, immer die gleiche Gestalt haben, so zeigt sich

[30] N.B. Delone and V.P. Krainov, *Phys.-Usp.* **41** (1998) 469.

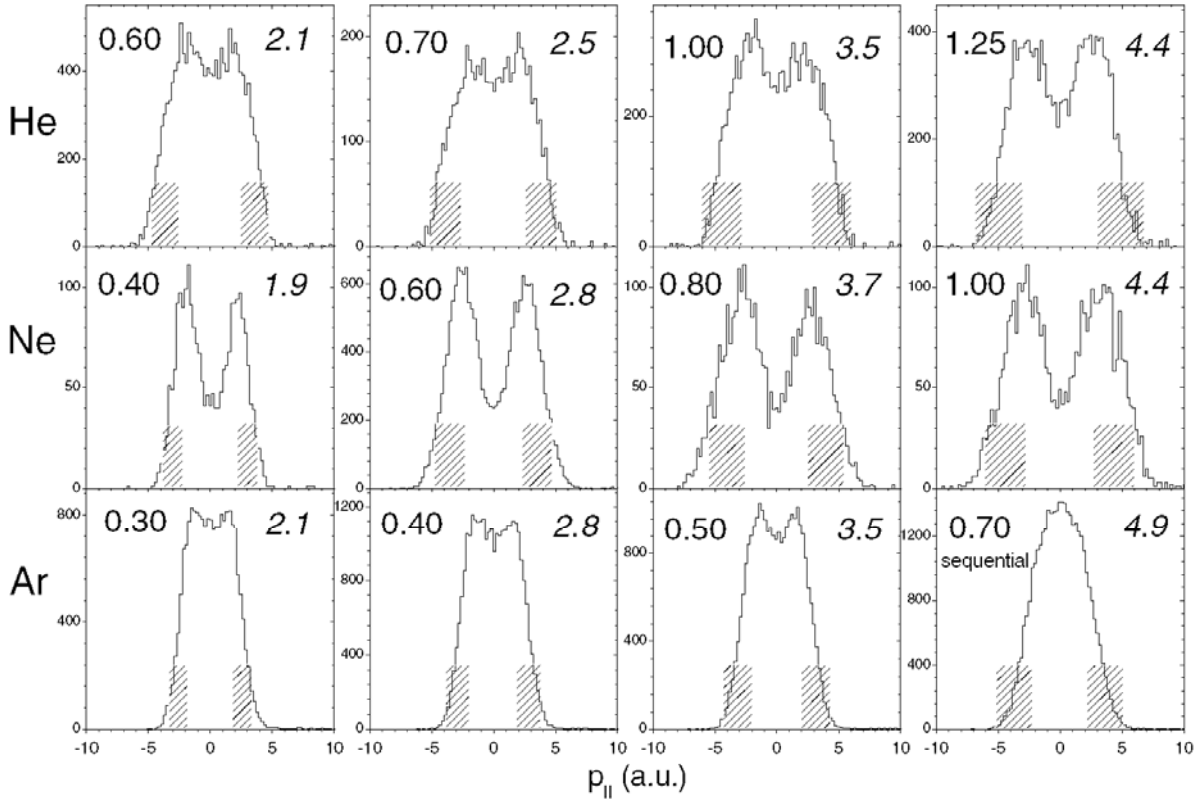

Abbildung 12. Spektren der Longitudinalimpulse für He^{2+}-, Ne^{2+}- und Ar^{2+}-Ionen [31]. Zum Vergleich sind jeweils die Spektren übereinander angeordnet, für welche die Rekollisionsenergie in Einheiten des Ionisationspotentials der einfach geladenen Ionen etwa den gleichen Wert hat (kursive Zahlen oben rechts). Die absolute Intensität in Einheiten von 10^{15} W/cm^2 ist oben links angegeben. In den schattierten Bereichen erwartet man die Maxima für den (e,2e)-Mechanismus.

für Helium zu niedrigeren Intensitäten hin die bereits für Argon beobachtete Auffüllung des Minimums um den Impuls Null. Der Übergang zu einer deutlichen Doppelstruktur wird bei Argon im Gegensatz zu Helium nicht mehr beobachtet, da oberhalb von $6 \cdot 10^{14}$ W/cm^2 bereits sequentielle Doppelionisation dominiert, welche von der Form des Spektrums her der Einfachionisation gleicht (Feldionisation für beide Elektronen).

Um das unterschiedliche Verhalten der drei Edelgase qualitativ zu verstehen, wurde eine einfache Modellrechnung für die relativen Anteile von RESI und (e,2e) vorgenommen. Zunächst wurden hierzu die (feldfreien) Wirkungsquerschnitte für Elektronenstoßanregung bzw. -ionisation mittels semiempirischer Formeln[31], die z.B. in der Astro- oder Plasmaphysik Verwendung finden, berechnet. Abb. 13 zeigt den Verlauf der Wirkungsquerschnitte als Funktion der Primärenergie der Elektronen in Einheiten des Ionisationspotentials. Schon hieraus wird deutlich, daß in Helium und vor allem in Argon die Querschnitte für Anregung gegenüber der Ionisation dominieren. Hinzu kommt das generell unterschiedliche Schwellenverhalten von Ionisation und Anregung: Die Ionisationsquerschnitte streben gegen Null, während die Querschnitte für Anregung schwellennah besonders hohe Werte annehmen. Die Bevorzugung der Anregung in Argon gegenüber Neon liegt in der atomaren Struktur begründet. In Ar^+ treten neben den Anregungen 3p → 4s und 3s → 3p insbesondere Übergänge 3p → 3d auf, welche durch den großen Überlapp der beteiligten Orbitale (gleiche Hauptquantenzahl) sehr hohe Oszillatorstärken aufweisen (Dipol-Riesenresonanzen in der

[31] H. van Regemorter, *Astrophys. J.* **136** (1962) 906; V.A. Bernshtam et al, *J. Phys. B* **33** (2000) 5025.

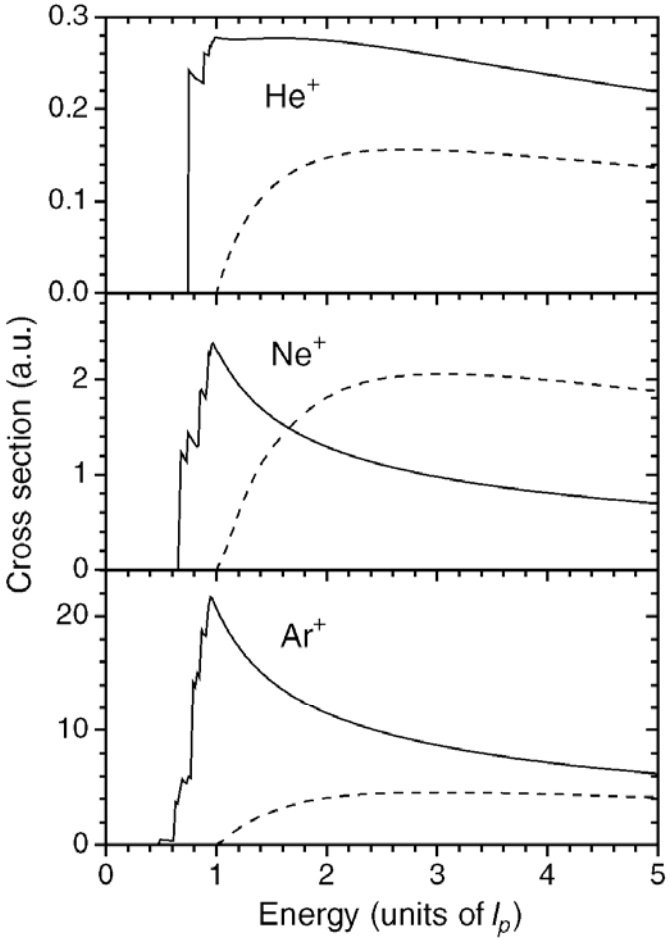

Abbildung 13. Wirkungsquerschnitte für Elektronenstoßanregung (durchgezogen) und -ionisation (gestrichelt) von He^+-, Ne^+- und Ar^+-Ionen [31] als Funktion der auf das Ionisationspotential normierten Primärenergie.

Photoabsorption)[32]. In Ne^+ dagegen findet man 2p → 3s, 2s → 2p und 2p → 3d, die Riesenresonanz tritt nicht auf. He^+ ist ein wasserstoffähnliches System mit einem hohen Entartungsgrad der angeregten Niveaus und als Folge dessen dominiert hier wiederum die Anregung. Um die relativen Beiträge $Y_{\mathrm{ion,exc}}$ der beiden Rekollisionsmechanismen zur nichtsequentiellen Doppelionisation zu berechnen, werden die Querschnitte, gewichtet mit der Tunnelwahrscheinlichkeit W_{ADK}, über alle möglichen Startzeiten t_0 innerhalb eines optischen Zyklus[33] gemittelt:

$$Y_{\mathrm{ion.exc}} = \int_{\pi/2}^{\pi} W_{\mathrm{ADK}}(t_0)\sigma_{\mathrm{ion.exc}}(E_{\mathrm{rec}}(t_0))\,\mathrm{d}(\omega t_0). \qquad (5)$$

Die Rekollisionsenergien E_{rec} ergeben sich dabei aus der klassischen Propagation des Elektrons im Laserfeld (siehe 1.2.1). Ferner wurde eine Absenkung der Potentialbarriere in Gegenwart eines endlichen Laserfeldes für die Stoßionisation berücksichtigt, was durch ein effektiv geringeres Ionisationspotential ausgedrückt werden kann[34] [25,31]. Abb. 14 zeigt für

[32] A. Hibbert and J.E. Hansen, *J. Phys. B* **27** (1994) 3325.
[33] Aus Symmetriegründen genügt es einen Viertelzyklus zu betrachten.
[34] H.W. van der Hart and K. Burnett, Phys. Rev. A **62** (2000) 013407.

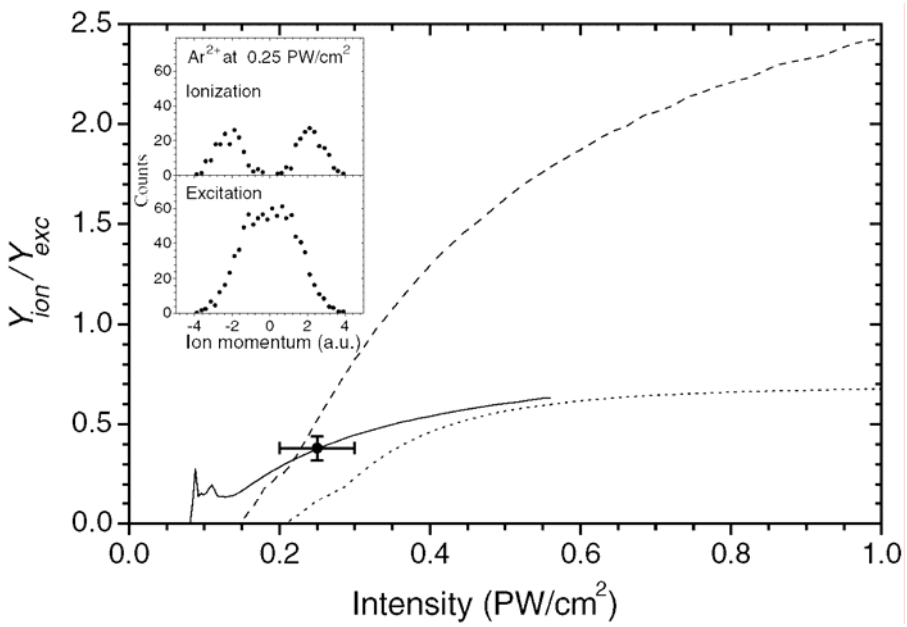

Abbildung 14. Modellierung der relativen Beiträge von RESI und (e,2e) zur nichtsequentiellen Doppelionisation von He (punktiert), Ne (gestrichelt) und Ar (durchgezogen) basierend auf den Wirkungsquerschnitten (Abb. 13). Eingetragen ist das experimentelle Resultat für Argon [13] (siehe Abschnitt 1.2.3).

He, Ne und Ar das Resultat für das Verhältnis Y_{ion}/Y_{exc} von RESI zu (e,2e) als Funktion der Laserintensität, wobei angenommen wird, daß alle angeregten Zustände vollständig feldionisiert werden. Wie anhand der Querschnitte (Abb. 13) zu erwarten, dominiert für Helium und Argon der RESI-, für Neon hingegen der (e,2e)-Mechanismus. Vergleicht man die Modellrechnung mit dem aus den kinematisch vollständigen Argon-Daten gewonnenen relativen Anteil [13], so ergibt sich eine recht gute Übereinstimmung, was durchaus überraschend ist, da das Modell starke Vereinfachungen beinhaltet und semiempirische feldfreie Querschnitte verwendet. Innerhalb dieser Betrachtung blieb die Frage nach der Lebensdauer der stoßangeregten Zustände in Gegenwart des Laserfeldes unberücksichtigt – hierauf wird im folgenden Abschnitt nochmals eingegangen.

1.2.5 Nichtsequentielle Mehrfachionisation

Im folgenden soll dargestellt werden, wie sich das Rekollisionsmodell auf die Mehrfachionisation verallgemeinern läßt. Der beobachtete Impuls eines *n*-fach geladenen Ions ist bis auf das Vorzeichen gleich dem Summenimpuls der emittierten Elektronen. Diese lassen sich nun danach unterscheiden, ob sie durch Feldionisation (e_T) oder in einem Rekollisionsprozeß (e_R) freigesetzt wurden [10, 35]:

$$p_{\text{ion}}^{(n)} = -\sum_{i=1}^{l} p_i(e_T) - \sum_{j=1}^{m} p_j(e_R), \qquad n = l + m. \tag{6}$$

Gemäß dem Rekollisionsmodell tragen zu signifikanten Driftimpulsen nur diejenigen Elektronen bei, welche einen Stoßprozeß mit dem Mutterion durchlaufen haben oder in einem solchen freigesetzt wurden. Die Driftimpulse von feldionisierten Elektronen hingegen fallen

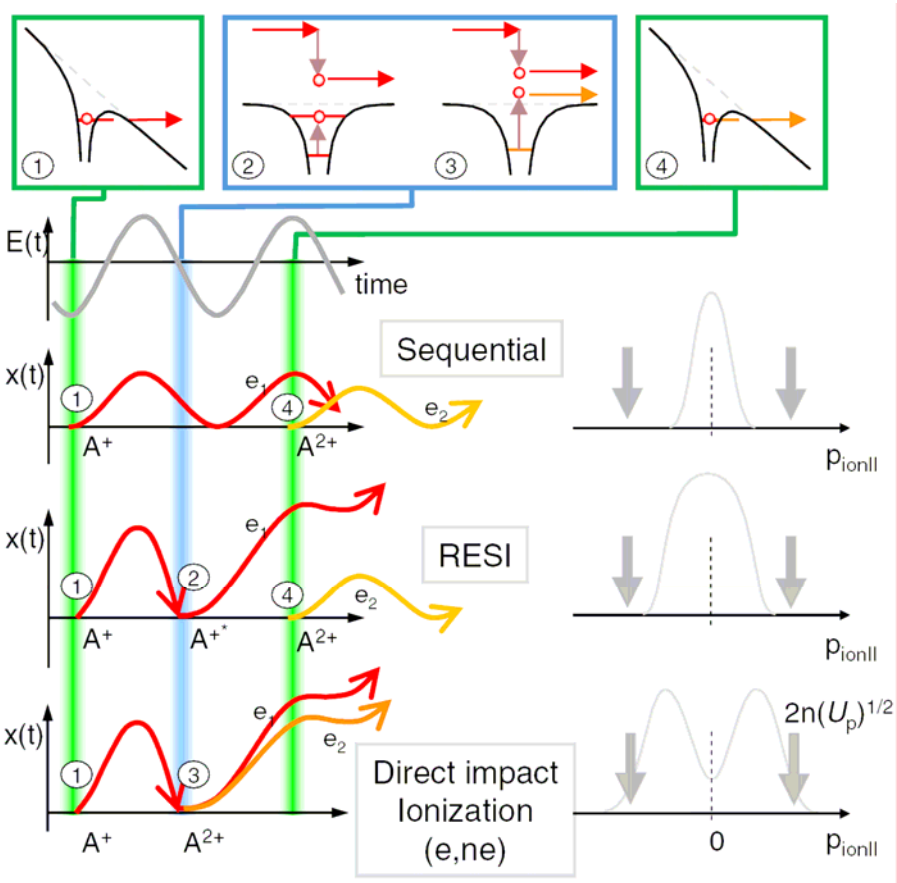

Abbildung 15. Übersicht der verschiedenen Mechanismen zur Doppel-(Mehrfach)ionisation in starken Laserfeldern und daraus resultierende (longitudinale) Impulsspektren der Ionen (aus [35]).

klein aus (siehe 1.2.1). Abb. 15 veranschaulicht dies noch einmal am Beispiel der Doppelionisation: Die schmalste Ionen-Impulsverteilung ergibt sich für sequentielle Feldionisation. Im Falle von RESI wird ein Elektron inelastisch gestreut, das andere tunnelt sequentiell – durch den Stoßprozeß erscheint die Impulsverteilung gegenüber dem rein sequentiellen Fall verbreitert. Im Falle von Rekollision mit Stoßionisation (e,2e) schließlich nehmen beide Elektronen einen recht hohen Driftimpuls auf. Die Breite der Impulsverteilung ist demnach im wesentlichen durch die Zahl *m* der gleichzeitig in einem Stoßprozeß freigesetzten Elektronen gegeben. Elektronen (*l*) aus reiner Feldionisation tragen demgegenüber nur unwesentlich zum Gesamtimpuls bei. Die maximale Breite zum Ladungszustand *n* findet sich demnach für einen reinen (e,*n*e)-Prozeß:

$$p_{\max} = 2n\sqrt{U_p} \tag{7}$$

Eine endliche Überschußenergie nach dem Stoß führt bei Vorwärtsemission der Elektronen zu einem etwas geringeren Endimpuls. Die Lage der Maxima der Impulsverteilung läßt sich unter Annahme eines minimalen Energieverlusts im Stoß daher dem folgenden kinematisch bevorzugten Bereich zuordnen [10]:

$$2n\sqrt{U_p} - \sqrt{2\,[3.17\,U_p - I_p(1 \to n)]} \leqslant p_{\parallel}^{n+} \leqslant 2n\sqrt{U_p}. \tag{8}$$

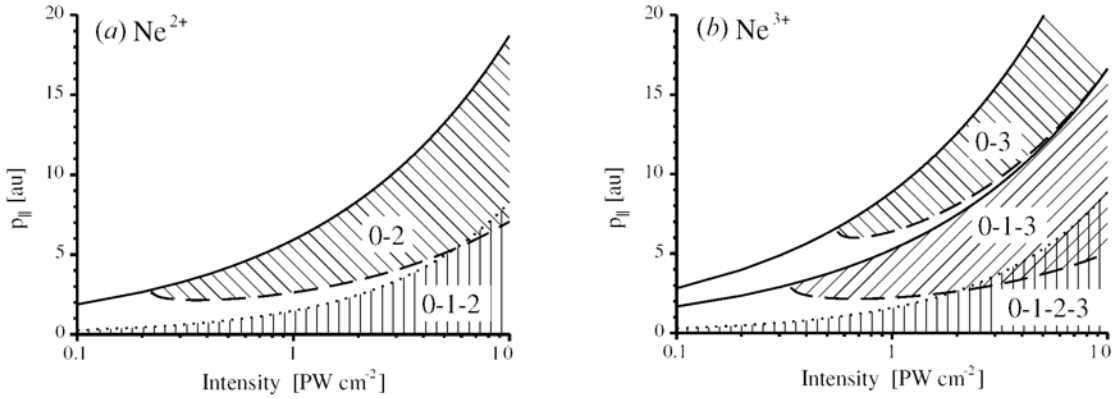

Abbildung 16. Kinematisch bevorzugte Bereiche (schraffiert) für Doppel-und Dreifachionisation von Neon in linear polarisierten Laserpulsen [10]. Rein sequentiell: (0-1-2) bzw. (0-1-2-3); rein nichtsequentiell: (0-2) bzw. (0-3); kombiniert sequentiell-nichtsequentieller Fall: (0-1-3).

Hier ist $I_p(1 \rightarrow n)$ die Ionisationsschwelle für den (e,*n*e)-Prozeß. Neben einem reinen (e,*n*e)-Prozeß sind aber auch Kombinationen von sequentieller und nichtsequentieller Ionisation möglich. Im Falle von RESI folgt der Anregung eine Feldionisation. Auch ist bei höheren Intensitäten eine stufenweise sequentielle Ionisation bis zu einem Ladungszustand *l* sequentielle Feldionisation denkbar, gefolgt von einer Rekollision mit einem (e,(*m*–1)e)-Prozeß. Dieser kombinierte Mechanismus wird dann dominieren, wenn die sequentielle Ionisation bis zum Ladungszustand *l* sättigt. Die kinematisch bevorzugten Bereiche sind in Abb. 16 als Funktion der Laserintensität für die Doppel- und Dreifachionisation von Neon dargestellt [10]. Als typischer Impuls für die rein sequentielle Ionisation (0-1-2) bzw. (0-1-2-3) wurde die Halbwertsbreite der Impulsverteilung für Tunnelionisation gewählt. Für rein nichtsequentielle Doppel- (0-2) bzw. Dreifachionisation (0-3) ergibt sich die aus Gl. (8) folgende Kinematik und für den kombinierten Pfad (0-1-3) ergeben sich nach Gl. (6) entsprechend kleinere Impulse. In neueren Experimenten stellte sich heraus, daß für Neon bis zum Ladungszustand 4 der rein nichtsequentielle (e,*n*e)-Mechanismus dominiert, während im Fall von Argon dieser gar nicht beobachtet wird und statt dessen die kombinierten Pfade bevorzugt werden [35,38,39].

Betrachtet man die Intensitätsabhängigkeit der Ionenausbeuten, so dominiert zunächst der rein nichtsequentielle Mechanismus. Bei sehr hohen Intensitäten erfolgt die Mehrfachionisation rein sequentiell. In einem Übergangsbereich sind die kombinierten Ionisationspfade zu erwarten. Durch die unterschiedliche Kinematik ergibt sich für das Spektrum dreifach geladener Ionen qualitativ die in Abb. 17 skizzierte Entwicklung [10].

1.3 Theoretische Studien zur Wellenpaketspropagation

Thema dieses Forschungsprojektes, welches im Rahmen eines DFG-Forschungsstipendiums an der Kansas State University durchgeführt wurde, war die Untersuchung des Einflusses starker Laserfelder auf den Einfang und die Emission von Elektronen in atomaren Stößen. Diese Thematik ist in das umfassendere Gebiet der laserassistierten atomaren Stöße (und Halbstöße) einzuordnen. Aufgrund erheblicher experimenteller Schwierigkeiten war und ist der Erkenntnisstand hier weitgehend auf die Theorie beschränkt, wobei bisher auch nur wenige Arbeiten vorliegen[35]. Es ist aber damit zu rechnen, daß weiterer Fortschritt in der

[35] T. Kirchner, *Phys. Rev. Lett.* **89** (2002) 093203.

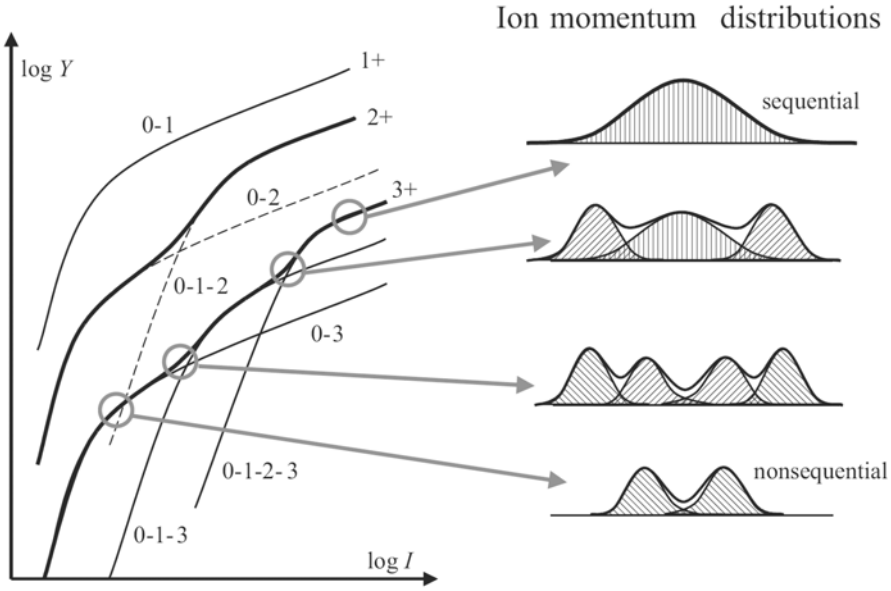

Abbildung 17. Schematisches Diagramm für den Intensitätsverlauf der Ionenausbeuten für einfache, doppelte und mehrfache Ionisation von Atomen in linear polarisierten Laserpulsen. Rechts ist die qualitative Entwicklung der Ionenspektren für Dreifachionisation von rein nichtsequentieller zu rein sequentieller Ionisation skizziert (aus [10]).

Lasertechnologie in Kombination mit effizienteren Untersuchungsmethoden atomarer Stoßprozesse in Kürze auch dieses Gebiet für das Experiment erschließt. Die besondere Schwierigkeit liegt darin, das Interaktionsvolumen möglichst gleichmäßig räumlich und zeitlich mit einem hinreichend starken Laserfeld zu überlagern. Dies setzt einen gepulsten Betrieb sowohl des Lasers als auch des Projektilstrahls sowie eine sehr gute Fokussierung beider Strahlen voraus. Die wenigen bisher vorgenommenen experimentellen Untersuchungen konzentrierten sich auf elastische und inelastische (Anregung) Streuung von Elektronen, also gebundene Systeme, und waren auf niedrige Laserintensitäten (perturbativer Bereich) beschränkt[36,37]. Daher war ein erster Teil des Vorhabens als Machbarkeitsstudie ausgelegt. Hierbei sollte in einem vereinfachten Modell die zeitliche Entwicklung des Elektronenzustands während eines Stoßprozesses unter Einwirkung des Laserfeldes betrachtet werden.

Aufgrund der inhaltlichen Nähe zum beantragten Vorhaben (im Sinne eines Halbstoßes) und der Aktualität der Fragestellung – u.a. von Seiten des Experiments vor Ort in Kansas und nicht zuletzt motiviert durch zukünftige Experimente in Heidelberg – wurde zunächst die Fragmentation (Dissoziation und Coulomb-Explosion) von H_2^+ behandelt. Dies ist unter anderem deswegen von besonderem Interesse, als daß durch die Kopplung des Elektrons an das Laserfeld eine zusätzliche elektronische Zeitskala (fs) auftritt, die nicht mehr kurz gegenüber der Kernbewegung (ebenfalls fs-Skala) ist, was einen Zusammenbruch der Born-Oppenheimer-Näherung bedeutet. Der erste Teil der Arbeit war mehr technisch orientiert. Hier wurde nach Wegen gesucht, die Fragment-Impulsverteilungen möglichst effizient aus den Propagationsrechnungen zu extrahieren [20]. Daneben wurde untersucht, wie die Eigenschaften des dreidimensionalen (3D) Moleküls (Potentialkurven) möglichst gut in einem kollinearen Modell mit jeweils einer Dimension für Elektronen- und Kernbewegung (parallel zur Laser-Polarisationsrichtung) reproduziert werden können. Dieses verbesserte Modell war dann Grundlage für Rechnungen zur Fragmentationsdynamik von H_2^+ in einem intensiven

[36] N.J. Mason, *Rep. Prog. Phys.* **56** (1993) 1275.
[37] C. Höhr et al., *Phys. Rev. Lett.* **94** (2005) 153201.

Laserpuls, wobei speziell die Abhängigkeit der Fragmentationskanäle Dissoziation und Coulomb-Explosion vom Vibrations-Anfangszustand und der Laserintensität untersucht wurde [22]. In einem dritten Schritt wurde diese Studie, welche ein statistisches Gemisch von Vibrationsniveaus – wie es in einem Molekülionenstrahl vorliegt – betrachtet, auf Pump-Probe-Szenarien mit zwei ultrakurzen (< 10 fs) Laserpulsen erweitert. Hierbei wird durch den ersten Puls eine kohärente Überlagerung von Vibrationsniveaus präpariert, welche vermöge der auf fs genau kontrollierbaren Verzögerung vom zweiten Puls zeitaufgelöst abgefragt wird. Über die Coulomb-Explosions-Spektren der Fragmente kann die zeitabhängige Elektronendichteverteilung rekonstruiert werden, was einen direkten Zugang zur Wellenpaketsdynamik erlaubt [24]. Auch ist die Messung von Dekohärenzzeiten und somit die Kopplung an mögliche weitere Freiheitsgrade auf einer fs- bis ps-Zeitskala mit dieser Methode denkbar.

Im vierten Teil wurde das bisher betrachtete Halbstoß-Szenario (laserinduzierte Molekül-Fragmentation) auf laserassistierte Ion-Atom-Stöße übertragen. Konkret wurde das Stoßsystem Proton-Wasserstoff betrachtet, wobei das Projektil auf einer geradlinigen, klassischen Trajektorie mit Stoßparameter b geführt wird. Die Elektronenbewegung bleibt in diesem Modell auf zwei Dimensionen (Streuebene) beschränkt. Berechnet wurden die Einfangs- und Ionisationswahrscheinlichkeiten $P_{\mathrm{cap}}(b)$, $P_{\mathrm{ion}}(b)$ als Funktion des Stoßparameters in Abhängigkeit von der Projektilgeschwindigkeit und den Laserparametern Frequenz, Intensität und Polarisation. Bei letzterer wird im allgemeinen Fall elliptischer Polarisation angenommen, daß die Polarisationsellipse in der Streuebene liegt. Die Rechnungen ergaben einen deutlichen zirkularen Dichroismus beim Einfang in langsamen Proton-Wasserstoff-Stößen unter Einfluß eines zirkular polarisierten Laserfeldes.

Bei allen hier vorgestellten Propagationsrechnungen wurde die zeitabhängige Schrödinger-Gleichung auf einem Gitter numerisch mit der Crank-Nicholson-Split-Operator-Methode[38] gelöst.

1.3.1 Berechnung von Fragment-Impulsverteilungen mit der Methode des ‚Virtuellen Detektors'

Wellenpaket-Propagationsrechnungen werden üblicherweise im Ortsraum auf einem numerischen Gitter durchgeführt. Ein Problem dabei ist die Behandlung der Wellenfunktion am Rand des Gitters. Um hier unphysikalische Reflexionen zu vermeiden kann man entweder das Gitter genügend groß wählen, was aber oft an die Grenzen der verfügbaren Rechnerleistung stößt, oder vor dem Rand einen ‚Absorber' plazieren, einen Bereich mit einem optischen (imaginären) Potential, welches das Wellenpaket wegdämpft, bevor es den Rand des Gitters erreicht. Damit geht aber auch der für den Vergleich mit experimentellen Impulsverteilungen von Fragmenten wichtige Kontinuumsanteil der Wellenfunktion verloren. Eine Standardmethode zur Extraktion von Impulsverteilungen aus der Wellenfunktion im Ortsraum ist die Fourier-Transformation in den Impulsraum. Dabei muß aber der gebundene Anteil der Wellenfunktion vom Anteil im Kontinuum separiert sein. Propagiert man nun die Wellenfunktion genügend lang, wird zwar eine räumliche Trennung dieser Anteile erfolgen, der Kontinuumsanteil aber aufgrund der Dispersion der Wellenpakete einen sehr großen Raumbereich einnehmen, wodurch sich sowohl der numerische Aufwand der Propagation als solcher wie auch der Fourier-Transformation stark erhöht. Es ist nun zur Bestimmung von Reaktionsraten üblich, den ausgehenden Fluß vor dem Rand des Gitters (Absorbers) zu erfassen, welcher als Wahrscheinlichkeitsstromdichte ein Maß für die Fragmentationsrate

[38] W.H. Press, S.A. Teukolsky, W.T. Vetterling, and B.F. Flannery, *Numerical Recipes* (Cambridge University Press, Cambridge, 1992), p. 842.

(Ionisation, Dissoziation) ist. Die Idee war nun, aus der Zeitabhängigkeit der Wellenfunktion an einem festen Ort (vor dem Absorber) auf die Impulsverteilung zurückzuschließen. Dies ist gewissermaßen komplementär zur Fourier-Transformation, wo zu einem festen Zeitpunkt (am Ende der Propagation) die in der räumlichen Verteilung enthaltene Information genutzt wird. Vorteil der neuen Methode ist, daß das Wellenpaket ohne Verlust an Information absorbiert werden kann. Dadurch kann das numerische Gitter im Vergleich zur Methode der Fourier-Transformation wesentlich kleiner gehalten werden.

Die Berechnung der Impulsverteilung gestaltet sich wie folgt: Zu jedem Zeitschritt wird unmittelbar vor dem Absorber der Gradient der Phase der Wellenfunktion bestimmt, welcher als lokaler Impuls interpretiert werden kann. Diese Impulse werden in ein Histogramm einsortiert, welches schließlich die gesuchte Impulsverteilung ergibt. Da das Verfahren zu einem gewissen Grade einem Flugzeitspektrometer ähnelt, wurde hierfür die Bezeichnung ‚Virtueller Detektor' gewählt. In der Publikation [20] ist dieses Verfahren näher beschrieben. Neben zwei numerischen Beispielen für Molekül-Dissoziation und Photoionisation eines Modellatoms in einem intensiven Laserpuls wird am Beispiel eines Gaußschen Wellenpakets die Methode analytisch demonstriert und die numerische Konvergenz für dieses Beispiel getestet. Gegenüber konventioneller Fourier-Transformation kann leicht eine Größenordnung an Rechenzeit gespart werden. Die Methode des ‚Virtuellen Detektors' wurde in den Arbeiten zur Dissoziation und Coulomb-Explosion von H_2^+ in intensiven Laserpulsen zur Berechnung der Fragment-Impulsverteilungen verwendet.

1.3.2. Fragmentation von H_2^+ im Laserfeld: Abhängigkeit vom Vibrations-Anfangszustand.

Die Fragmentationsdynamik des H_2^+-Molekülions in intensiven Laserpulsen wird im wesentlichen durch die beiden tiefsten elektronischen Zustände $1s\,\sigma_g$ und $2p\,\sigma_u$ bestimmt (siehe auch Abschnitt 1.1). Für große internukleare Abstände sind diese Zustände entartet, weshalb die elektronische Wellenfunktion hier durch eine Überlagerung von $1s\,\sigma_g$ und $2p\,\sigma_u$ beschrieben wird. Dies entspricht anschaulich der Lokalisierung der Elektronenwolke an einem der beiden Kerne, also dem asymptotischen Zustand Proton plus Wasserstoffatom. Weiter folgt hieraus ein linear mit R wachsendes Dipolmoment, welches eine starke Kopplung an das Laserfeld bedeutet. Das Molekülion im Laserfeld kann durch lichtinduzierte Potentialkurven beschrieben werden, welche der Absorption von 0,1,2,3 ... usw. Photonen entsprechen (siehe Abb. 3). Mit wachsender Laserintensität kommt es zur Ausbildung vermiedener Kreuzungen, welche die Dissoziationsdynamik (1-Photon-Absorption sowie 3-Photonen-Absorption mit 1-Photon-Reemission) bestimmen. Zudem kommt es im Bereich der Kreuzungen zum oben erwähnten CREI-Prozeß.

Zunächst wurde das Ziel verfolgt, die ‚wahre' Form der Potentialkurven (in drei Dimensionen) in dem benutzten eindimensionalen Modell möglichst gut zu reproduzieren. Hierzu wurde das üblicherweise verwendete ‚Softcore'-Coulomb-Potential modifiziert und mittels einer R-abhängigen Abschirmfunktion eine exakte Anpassung an die ‚reale' ($1s\,\sigma_g$)-Kurve sowie eine hinreichend gute Wiedergabe der ($2p\,\sigma_u$)-Kurve erzielt (Fig. 1 aus [22]). Auf der Grundlage dieses verbesserten Modells wurde mittels Wellenpaket-Propagation die Fragmentation von H_2^+ in Abhängigkeit vom Vibrations-Anfangszustand und der Intensität untersucht und dabei sowohl die zeitabhängigen Raten als auch die Impulsverteilungen der Kerne für Dissoziation und Coulomb-Explosion berechnet. Im Intensitätsbereich um 0,1 PW/cm^2 kommt es zu einer Konkurrenz der beiden Fragmentationskanäle Dissoziation und Coulomb-Explosion, die im Detail vom anfänglichen Vibrationszustand bestimmt wird (Fig. 7

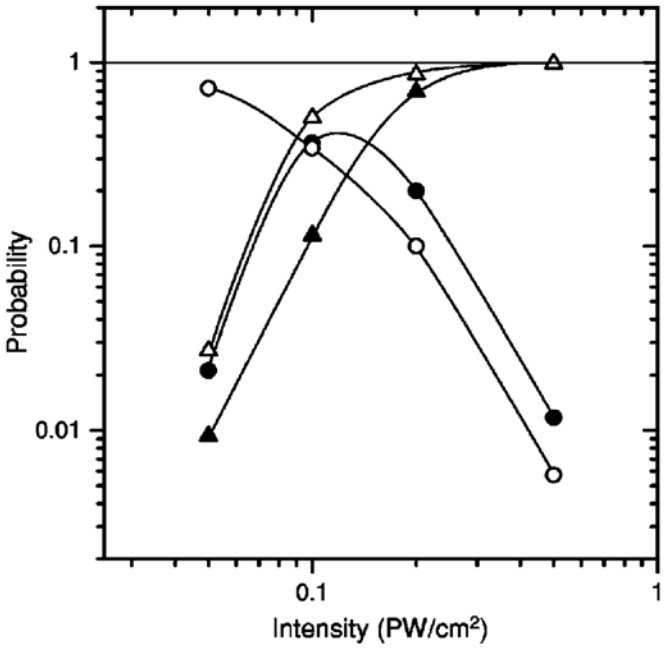

Abbildung 18. Wahrscheinlichkeiten für Dissoziation (Kreise) und Coulomb-Explosion (Dreiecke) von H_2^+ in 25-fs-Laserpulsen (800 nm) als Funktion der Laserintensität für die Vibrationszustände $v = 3$ (gefüllte Symbole) und $v = 6$ (offene Symbole) [22].

aus [22]). Zusätzlich macht sich noch ein Schwelleneffekt bemerkbar, da die Zustände $v = 0 – 5$ nur über den 3-Photonen-Kanal dissoziieren können. Für höhere Vibrationsniveaus stehen dagegen beide Kanäle offen, was sich in einer unterschiedlichen Intensitätsabhängigkeit niederschlägt, wie in Abb. 18 am Beispiel von $v = 3$ bzw. $v = 6$ demonstriert.

1.3.3 Visualisierung der Wellenpaketsdynamik von D_2^+ mittels ultrakurzer Pulse

Wie in der Einleitung schon erwähnt, wurde bei der überwiegenden Mehrheit der experimentellen Untersuchungen das neutrale Molekül als Target verwendet. Bei den verwendeten Pulslängen (50 – 150 fs) laufen Produktion und Fragmentation der Molekülionen innerhalb dieser Zeitskala ab, die oberhalb der typischen Vibrationsperiode von H_2^+ (14 fs) liegt. Somit ist das zeitliche Verhalten des Molekülions nicht direkt beobachtbar. Bei jedem einzelnen Ionisationsprozeß von H_2 (welcher schnell gegenüber der Kernbewegung geschieht) wird die Kernwellenfunktion auf die Potentialfläche von H_2^+ projiziert (Franck-Condon-Übergang). Dieses Wellenpaket kann nun in dem neuen Potential, zu dem es kein Eigenzustand ist, als Superposition der Eigenzustände von H_2^+ beschrieben werden. Ein kleinerer Teil hat einen Überlapp mit dem Kontinuum und dissoziiert folglich, der größere Teil vollführt eine kohärente gebundene Bewegung (siehe z.B. Fig. 2 aus [20]). Beschreibt man dieses Wellenpaket mit einer Dichtematrix (Gln. (1-3) aus [24]), so geben die Nicht-Diagonalelemente die Zeitabhängigkeit an, während es sich bei den konstanten Diagonalelementen um die bekannten Franck-Condon-Überlappfaktoren handelt. Ist nun der Zeitpunkt zwischen der Präparation des Wellenpakets (Ionisation von H_2) und einer weiteren Wechselwirkung (z.B. Fragmentation) nicht genau definiert, kann nur ein Zeitmittel der Dichtematrix beobachtet werden. Insbesondere verschwinden bei Mittelung über einen Zeitraum, der lang gegenüber der Zeitskala der Kernbewegung ist, die Nicht-

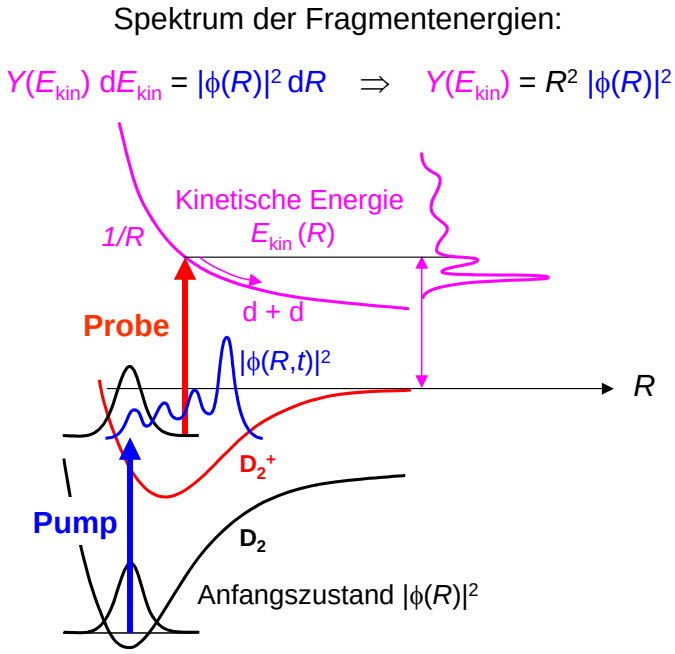

Abbildung 19. Skizze zur Visualisierung von Wellenpaketsdynamik mittels Spektroskopie der Fragmente nach Coulomb-Explosion im Probepuls.

Diagonalelemente und es verbleibt lediglich eine inkohärente Franck-Condon-Verteilung, also ein statistisches Gemisch. Dies gilt z.B. für aus einer Ionenquelle extrahierte Molekülionen[39], da die Zeitdifferenz zwischen Ionisation und Wechselwirkung mit dem Laserpuls in der Größenordnung von µs schwankt.

Einen Ausweg stellen Pump-Probe-Experimente mit zwei definiert zeitlich verzögerten Laserpulsen dar. Eine erste solche Studie zur Fragmentation von D_2^+ wurde vor einigen Jahren mit Pulslängen von 80 fs durchgeführt[40]. Trotz der hier noch beschränkten Zeitauflösung konnte eine von der Verzögerung abhängige Struktur in den Fragmentationsspektren beobachtet werden, welche als verzögerte Ionisation des auslaufenden Dissoziations-Wellenpakets gedeutet wurde, wobei die Coulomb-Energie mit zunehmendem Abstand der Fragmente, d.h. mit wachsender Verzögerung, abnimmt. Es gelang, ein solches Verhalten anhand der numerischen Wellenpaket-Propagation qualitativ zu reproduzieren (Fig. 1 u. 2 aus [24]). Mit ultrakurzen Pulsen (< 10 fs) sollte es ferner möglich sein, auch die Bewegung gebundener Zustände zeitlich aufgelöst zu verfolgen. Hierzu wurden Modellrechnungen für zwei intensive (1-2 PW/cm^2) Pulse von 5 fs Dauer vorgenommen. Dabei ionisiert der erste (Pump)-Puls D_2 mit einer Effizienz von nahe 100 % innerhalb von 1-2 fs, ohne jedoch das so erzeugte D_2^+-Molekülion zu zerstören, was erst durch den Einsatz genügend kurzer Pulse möglich wird. Die so präparierte kohärente Superposition von gebundenen Vibrationsniveaus wird mit dem zweiten (Probe-)Puls abgefragt, wobei das zweite Elektron ionisiert wird. Dabei kann aus der Coulomb-Energie der Fragmente der Kernabstand und somit das Betragsquadrat der Kernwellenfunktion rekonstruiert werden[41] (Abb. 19). Aufgrund der Anharmonizität des Molekülpotentials sind die Vibrationsniveaus nicht äquidistant. Dies führt zu einer komplizierten Zeitentwicklung des gebundenen

[39] K. Sändig, H. Figger and T.W. Hänsch, Phys. Rev. Lett. **85** (2000) 4876; I.D. Williams *et al.*, J. Phys. B **33** (2000) 2743.
[40] C. Trump, H. Rottke and W. Sandner, *Phys. Rev. A* **59** (1999) 2858.
[41] S. Chelkowski et al., *Phys. Rev. Lett.* **82** (1999) 3416; S. Chelkowski and A.D. Bandrauk, *Phys. Rev. A* **65** (2002) 023403.

Wellenpakets, welche durch ein periodisches, von Interferenzstrukturen überlagertes Zerfließen und Wiederherstellen (‚Revival') des Wellenpakets gekennzeichnet ist (siehe Fig. 3 u. 4 aus [24]). Eine solche (partielle) Wiederkehr tritt nach ca. 580 fs auf (siehe auch Abschnitt 1.4.2).

Eine interessante Fragestellung ist, wie lange die Kohärenz eines Quantensystems erhalten bleibt. Koppelt das System an weitere (viele) Freiheitsgrade oder gar an ein Wärmebad, so gehen die festen Phasenbeziehungen in der Dichtematrix (Gl. (2) aus [24]) verloren. Dieses als Dekohärenz bezeichnete Phänomen ist von großer Bedeutung sowohl für die Grundlagen der Quantenmechanik (Theorie des Meßprozesses) als auch für deren Anwendungen (Quantencomputer). Wird z.B. die in Fig. 3 aus [24] gezeigte Wellenpaketsdynamik durch Dekohärenz irreversibel gestört, so verschwindet die Zeitabhängigkeit der rekonstruierten Aufenthaltswahrscheinlichkeiten (Fig. 4 aus [24]) nach einer bestimmten, charakteristischen Dekohärenzzeit. Statt dessen beobachtet man nunmehr eine zeitunabhängige, inkohärente Franck-Condon-Verteilung.

1.3.4. Ion-Atom-Stöße in elliptisch polarisierten Laserfeldern: Zirkularer Dichroismus

Die oben betrachtete Molekülfragmentation kann als Halbstoß aufgefaßt werden. Der Übergang zu atomaren Stößen (Proton auf atomaren Wasserstoff) wurde hier so realisiert, daß das Projektil mit der Geschwindigkeit v_p auf einer geradlinigen klassischen Trajektorie mit Stoßparameter b geführt wird. Die Wellenpaketpropagation für das Elektron wurde dabei auf einem zweidimensionalen Gitter vorgenommen, welches die Streuebene definiert, welche gleichzeitig die Polarisationsellipse des Laserfeldes enthält (siehe Abb. 20).

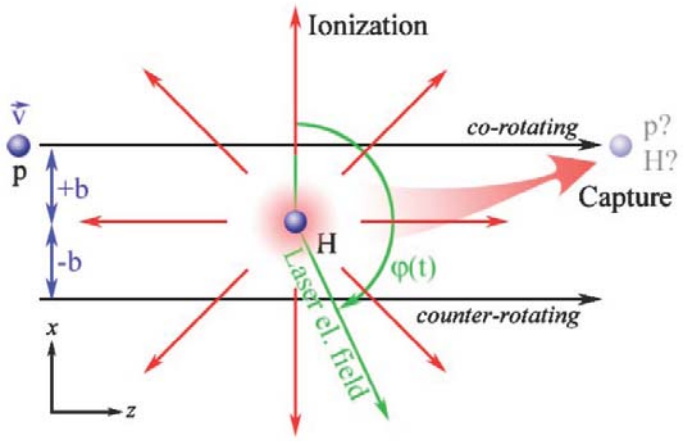

Abbildung 20. Veranschaulichung der Kollision des auf einer geraden Linie geführten Protons (Stoßparameter b und Geschwindigkeit v) mit einem atomaren Wasserstoff-Target in einem zirkular polarisierten Laserfeld [32]. Der rotierende Feldvektor bricht die azimutale Symmetrie: Für positive b folgt das Projektil dem Feldvektor (korotierender Fall), für negative b bewegen sich Projektil und Feldvektor gegenläufig (kontrarotierender Fall). Die absolute Phase φ(t) des Laserfeldes ist bezogen auf den Zeitpunkt der nächsten Annäherung von Projektil und Target definiert.

Anschaulich werden die deutlichsten Effekte für langsame ($v_p < 1$ a.u.) Stöße erwartet, wo die typische Stoßzeit $t = b/v_p$ in der Größenordnung der Oszillationszeit (fs) des Laserfeldes liegt. In diesem Geschwindigkeitsbereich ist der Elektroneneinfang der dominierende Prozeß, Ionisation ist von stark untergeordneter Bedeutung. Interessant ist nun wie und unter welchen Bedingungen ein äußeres Laserfeld die Elektronendynamik – evtl. sogar kontrollierbar –

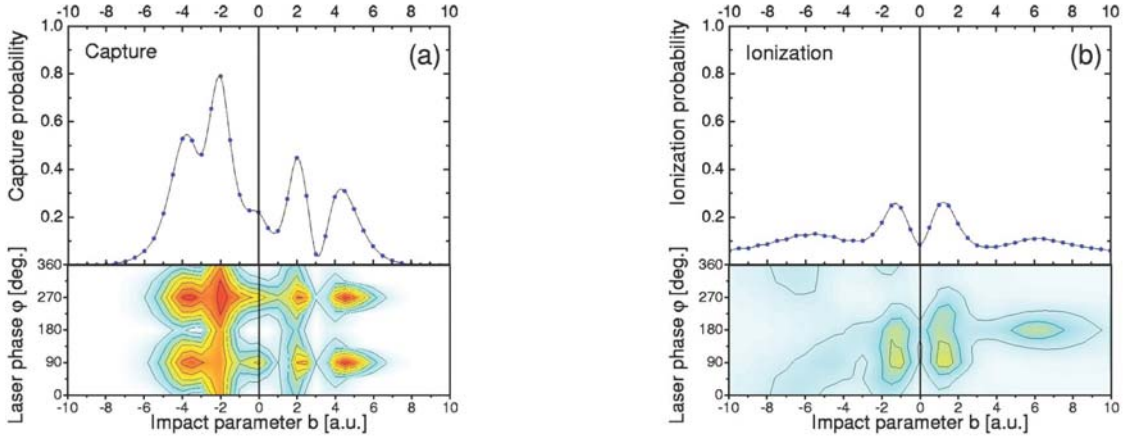

Abbildung 21. Elektroneneinfang und Ionisation im laserassistierten Stoß von Protonen (1,21 keV) mit atomarem Wasserstoff [32]. Die Intensität des zirkular polarisierten Lasers beträgt $5 \cdot 10^{14}$ W/cm^2. Die Konturplots zeigen die Einfangs- bzw. Ionisationswahrscheinlichkeit als Funktion des Stoßparameters *b* und der Laserphase φ zum Zeitpunkt der nächsten Annäherung von Projektil und Target.

beeinflußt. Als einfachste differentielle Observable kommen die stoßparameterabhängige Einfangs- und Ionisationswahrscheinlichkeiten $P_{cap}(b)$, $P_{ion}(b)$ in Betracht.

Abb. 21 zeigt ein ausgewähltes Resultat (aus [32]) für die stoßparameterabhängige Wahrscheinlichkeit für Elektroneneinfang und für Ionisation für laserassistierte Stöße von Protonen mit atomarem Wasserstoff. Die Energie der Protonen beträgt 1,21 keV und die Intensität des zirkular polarisierten Lasers $5 \cdot 10^{14}$ W/cm^2. Die Frequenz liegt mit 1064 nm im nahen Infrarot (Nd:YAG-Laser). Es ergibt sich eine links/rechts-Asymmetrie, welche für den Einfang gegenüber der Ionisation aber stärker ausgeprägt ist. Eine wichtige Größe ist die phasengemittelte Einfangs- bzw. Ionisationswahrscheinlichkeit (obere Grafiken), da die Phase des Laserfeldes nach derzeitigem Ermessen in einem Experiment nicht mit dem Stoß synchronisierbar ist. Für den Einfang bleibt auch nach der Mittelung eine deutliche Asymmetrie (zirkularer Dichroismus) übrig, während sich für die Ionisation ein nahezu symmetrisches Bild ergibt. Interessant ist aber die Tatsache, daß die betrachtete Laserintensität nicht ausreicht das Target zu ionisieren, so daß man in beiden nicht kombinierten Fällen (nur Stoß bzw. nur Laser) eine vernachlässigbare Ionisationswahrscheinlichkeit erhält. Es handelt sich somit um einen echten laserassistierten Prozeß. Beide Effekte (Asymmetrie und stark erhöhte Ionisationsraten) sollten experimentell relativ leicht zugängliche Meßgrößen sein, falls die o.g. technischen Schwierigkeiten überwunden werden.

1.4 Wellenpaketsdynamik von H_2^+ in ultrakurzen Laserpulsen

Als Vorstudie zu Pump-Probe-Experimenten zur Visualisierung der Wellenpaketsdynamik (siehe Abschnitt 1.3.3) wurde das Verhalten von H_2^+ in einzelnen Laserpulsen für verschiedene Pulsdauern und Intensitäten untersucht [37]. Abb. 22 zeigt die Flugzeitspektren der Rückstoßionen aus der Ionisation von H_2 bzw. nachfolgender Fragmentation für verschiedene Intensitäten und Pulslängen für lineare Laserpolarisation, welche hier parallel zur Flugzeitachse des Spektrometers ist. Bei der intensiven Linie rechts handelt es sich um die einfach ionisierten Molekülionen (H_2^+). In der nahezu spiegelsymmetrischen Struktur links davon finden sich Protonen aus der Dissoziation bzw. Coulomb-Explosion (CE) von H_2^+. Dabei entspricht die Mitte der Struktur Ionen mit Longitudinalimpuls Null. Ionen, deren

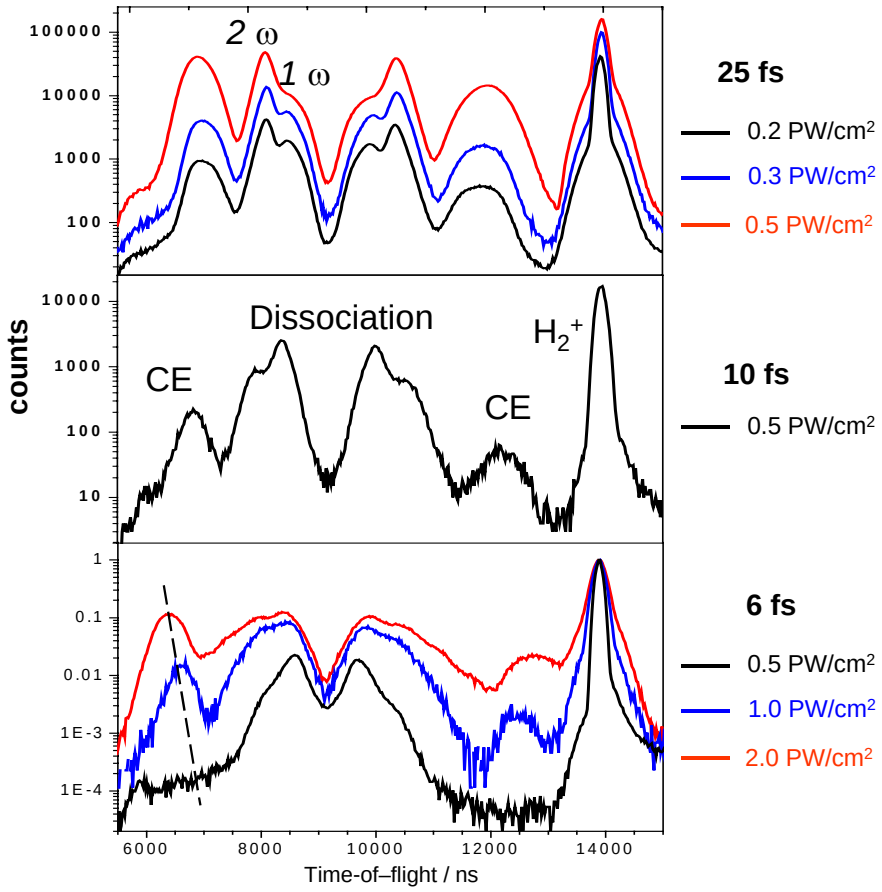

Abbildung 22. Flugzeitspektren der Fragmente von molekularem Wasserstoff in linear polarisierten Laserpulsen. Die Laserpolarisation ist parallel zur Flugzeitachse des Spektrometers (Abb. 4).

Impulsvektor auf den Detektor zu gerichtet ist, haben kürzere Flugzeiten als im umgekehrten Fall, weshalb die einzeln Fragmentationskanäle jeweils doppelt erscheinen. Mit zunehmender Intensität ist die Doppelionisation (CREI, siehe Abschnitt 1.1) stärker ausgeprägt, während sie mit abnehmender Pulsdauer stark unterdrückt wird (vergleiche die Spektren bei gleicher Intensität (0,5 PW/cm^2). Zugleich kehrt sich das Verzweigungsverhältnis der beiden Dissoziationskanäle (1ω und 2ω) um und die zugehörigen Linien verbreitern sich. Erhöht man hingegen die Intensität bei ultrakurzen (6 fs) Pulsen, so erscheint wiederum eine Struktur, welche durch Koinzidenzmessungen als Doppelionisation identifiziert werden kann [37], nun aber bei etwas höherer kinetischer Energie, wie auch Abb. 22 demonstriert. Dabei verschiebt sich die Struktur mit wachsender Intensität weiter zu höheren Energien (Pfeile in Abb. 23, gestrichelte Linie unten in Abb. 22). Dieses Verhalten kann – wie auch das Verschwinden von CREI – auf die Wellenpaketsbewegung in H_2^+ zurückgeführt werden. Bei sehr kurzen Pulsen bleibt nicht genügend Zeit zur Propagation vom Gleichgewichtsabstand von H_2 (1,4 a.u., siehe Abb. 3) in den CREI-Bereich (3–8 a.u.) hinein. Statt dessen kann aber bei hinreichend hoher Intensität H_2^+ sequentiell weiter ionisiert werden (CREI ist letztlich nur ein Spezialfall sequentieller Ionisation). Da die Ionisationswahrscheinlichkeit mit dem internuklearen Abstand *R* stark anwächst, wird mit wachsender Intensität der Pulse immer mehr auch der Bereich kleinerer *R* erfaßt, was zu höherer Energie der Coulomb-Explosions-Fragmente führt. Dieses Verhalten wird auch durch neuere Modellrechnungen reproduziert[42].

[42] X.M. Tong and C.D. Lin, *Phys. Rev.* A **70** (2004) 023406.

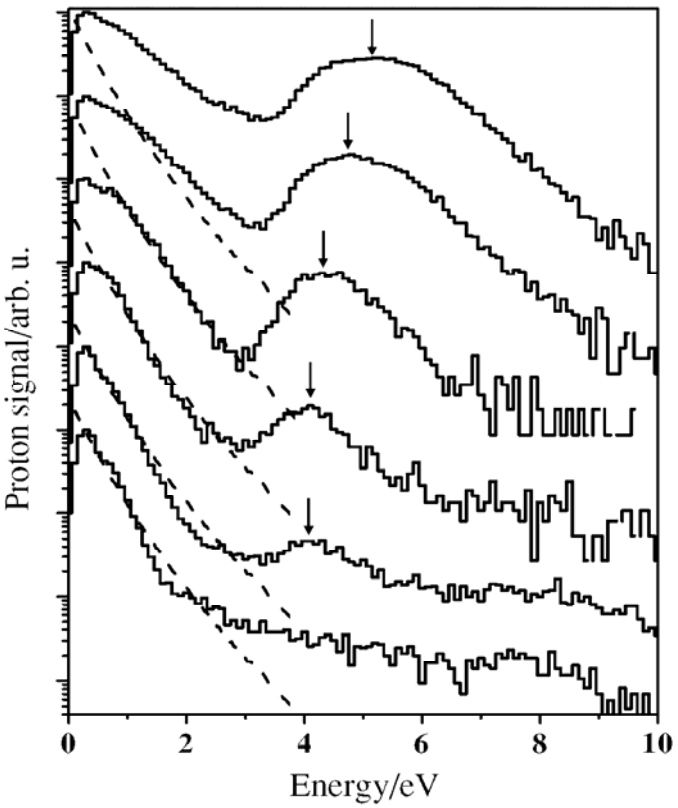

Abbildung 23. Spektren der Fragmentenergien nach Dissoziation bzw. Coulomb-Explosion (Pfeile) von H_2^+ in ultrakurzen Laserpulsen (6 fs) [37]. Der Übersichtlichkeit halber sind die einzelnen Spektren vertikal gegeneinander verschoben. Die Intensitäten von unten nach oben in PW/cm^2: 0,2 - 0,3 - 0,5 - 0,8 - 1,4 - 2,0. Gestrichelte Linien: theoretische Franck-Condon-Verteilung.

Die Form des Spektrums der Dissoziationsfragmente (links in Abb. 23) in ultrakurzen Pulsen ist mit einer Franck-Condon-Verteilung (gestrichelte Kurven) verglichen, welche sich im Grenzfall einer instantanen Ionisation in einem deltaförmigen Puls ergeben sollte [20]. Die beste Übereinstimmung findet sich dabei für mittlere Intensitäten um 0,8 PW/cm^2. Bei höheren Intensitäten ist die Näherung einer gegenüber der Zeitskala der Kernbewegung vernachlässigbar kurzen Pulsdauer zunehmend schlechter erfüllt, da die effektive Pulsdauer innerhalb welcher Ionisation bzw. Dissoziation auftreten kann wächst. Hinzu treten störende Vor- und Nachpulse[43]. Für niedrigere Intensitäten zeigt sich ein Mangel an höher energetischen Dissoziationsfragmenten. Dies kann mit der Tatsache erklärt werden, daß sich auf Grund der stark mit R wachsenden Ionisationswahrscheinlichkeit von H_2 weniger hoch angeregte Vibrationsniveaus besetzt werden[44], was auch die Anregung in das Dissoziationskontinuum betrifft.

Für lineare Polarisation tritt auch nichtsequentielle Doppelionisation auf. Da dies innerhalb eines optischen Zyklus geschieht, finden sich hier auch die höchsten Fragmentenergien (Schulter links in Abb. 22 bzw. rechts in Abb. 23). Vergleicht man die Spektren der longitudinalen Summenimpulse der beiden Protonen, welche dem Rückstoßionenimpuls bei nichtsequentieller Doppelionisation von Atomen entspricht, für den Rekollisionsmechanismus mit denen aus dem (sequentiellen) CREI-Bereich (Abb. 24), so

[43] Die Fragmentationsdynamik von H_2^+ zeigt sich als sehr empfindlich gegenüber der Pulsform und kann daher zur Pulsdiagnostik verwendet werden – für eine detailliertere Diskussion siehe [37].
[44] X. Urbain et al., *Phys. Rev. Lett.* **92** (2004) 163004.

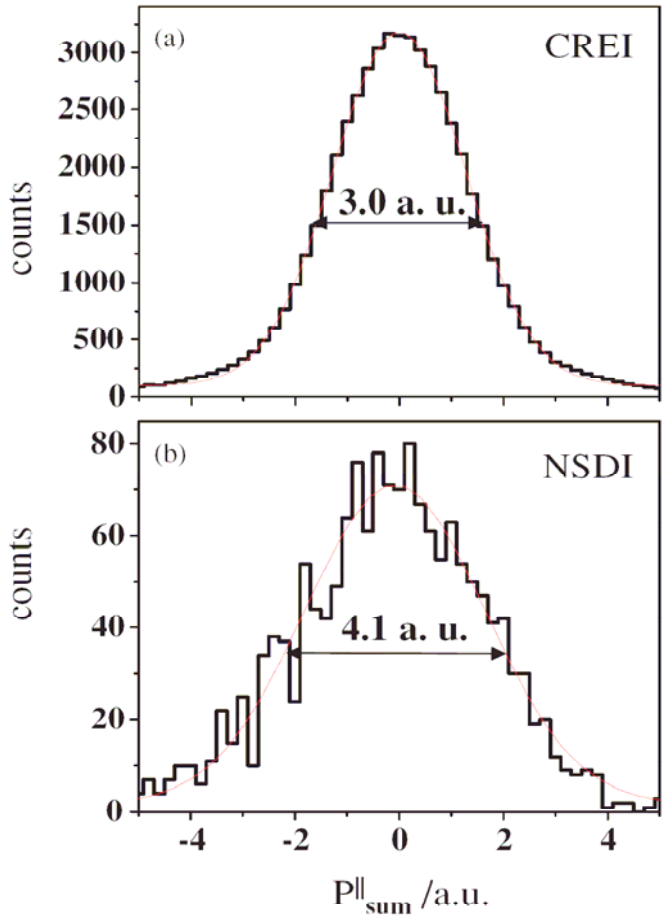

Abbildung 24. Spektren des longitudinalen Summenimpulses beider Protonen nach sequentieller (a) und nichtsequentieller (b) Doppelionisation von H_2 in linear polarisierten Laserpulsen [37]. Pulsdauer 25 fs, Intensität 0,5 PW/cm^2.

ergibt sich eine signifikant breitere Verteilung, wie sie von Atomen her bekannt ist (siehe Abschnitt 1.2). Es ist aber keine Doppelstruktur zu beobachten, was auf eine Dominanz des RESI-Mechanismus hindeutet. Diese Interpretation wird auch von der Theorie gestützt[45].

1.5 Ausblick: Pump-Probe-Experimente und laserassistierte Prozesse

Die Manipulation und möglicherweise die Kontrolle ultraschneller Dynamik von Mehrteilchen-Quantensystemen ist ein junges und hochaktuelles Gebiet innerhalb der Atom-, Molekül- und Optischen Physik, welches Elemente der Stoßphysik mit solchen der Quantenoptik verbindet und durch den Einsatz innovativer Techniken (Präparation von Quantenzuständen, Manipulation der Dynamik, kinematisch vollständige Experimente) ein hohes Entwicklungspotential aufweist. Gleichzeitig besteht interdisziplinär ein starker Bezug zur Physikalischen Chemie. Aus diesem Kontext ergeben sich zentrale Fragestellungen, z.B. Kontrolle von Wellenpaketsdynamik über Potentialbarrieren, laserinduzierte Fragmentation sowie lasermodifizierte Stöße und chemische Prozesse. Ziel zukünftiger Untersuchungen ist es, diese Fragestellungen in kinematisch vollständigen Experimenten zu beleuchten, wobei sowohl die Anfangszustands-Präparation als auch die Manipulation der Dynamik weitere wichtige Aspekte darstellen. Hier kommt dem Laser als „Werkzeug" eine zentrale Bedeutung

[45] X.M. Tong et al., *Phys. Rev. A* **68** (2003) 043412.

zu. Mein besonderes Interesse finden die thematisch verwandten Gebiete der laserinduzierten Fragmentation (Halbstöße) kleiner Moleküle sowie der laserassistierten atomare Stöße.

Erste Pump-Probe-Experimente – noch mit 25 fs Pulsdauer – ermöglichten bereits die Visualisierung dissoziierender Wellenpakete und über die Kontrolle der Interferenz zweier überlappender Pump-Probe-Pulse eine Manipulation der Fragmentationsdynamik [41]. Um auch die Wellenpaketsdynamik gebundener Zustände des Wasserstoffmolekülions zu visualisieren, ist eine weitere Reduzierung der „Belichtungszeit“ notwendig. Derzeit wird die Wellenpaketdynamik von H_2^+ und D_2^+ zeitaufgelöst mit ultrakurzen (7 fs) Pump-Probe-Pulsen untersucht, wobei die Modellrechnung [24] bestätigt werden konnte (siehe Abb. 25).

In der Verbindung koinzidenter hochaufgelöster Spektrometrie der Elektronen und Fragmente mit Pump-Probe-Techniken ultrakurzer (6-7 fs) Laserpulse wird experimentelles Neuland betreten und die Wellenpaketdynamik leichter Moleküle erstmals beobachtbar. Dies gilt noch mehr für das Studium laserassistierter Stöße, welche sich bislang dem experimentellen Zugang weitgehend verschlossen. Einen Ausweg bieten neuartige Laser-Ionenquellen zur Erzeugung gepulster energiescharfer Ionenstrahlen mit kleiner Emittanz in Verbindung mit einem Reaktionsmikroskop, was letztlich die technische Basis für eine breite Klasse zukünftiger, innovativer Experimente darstellt.

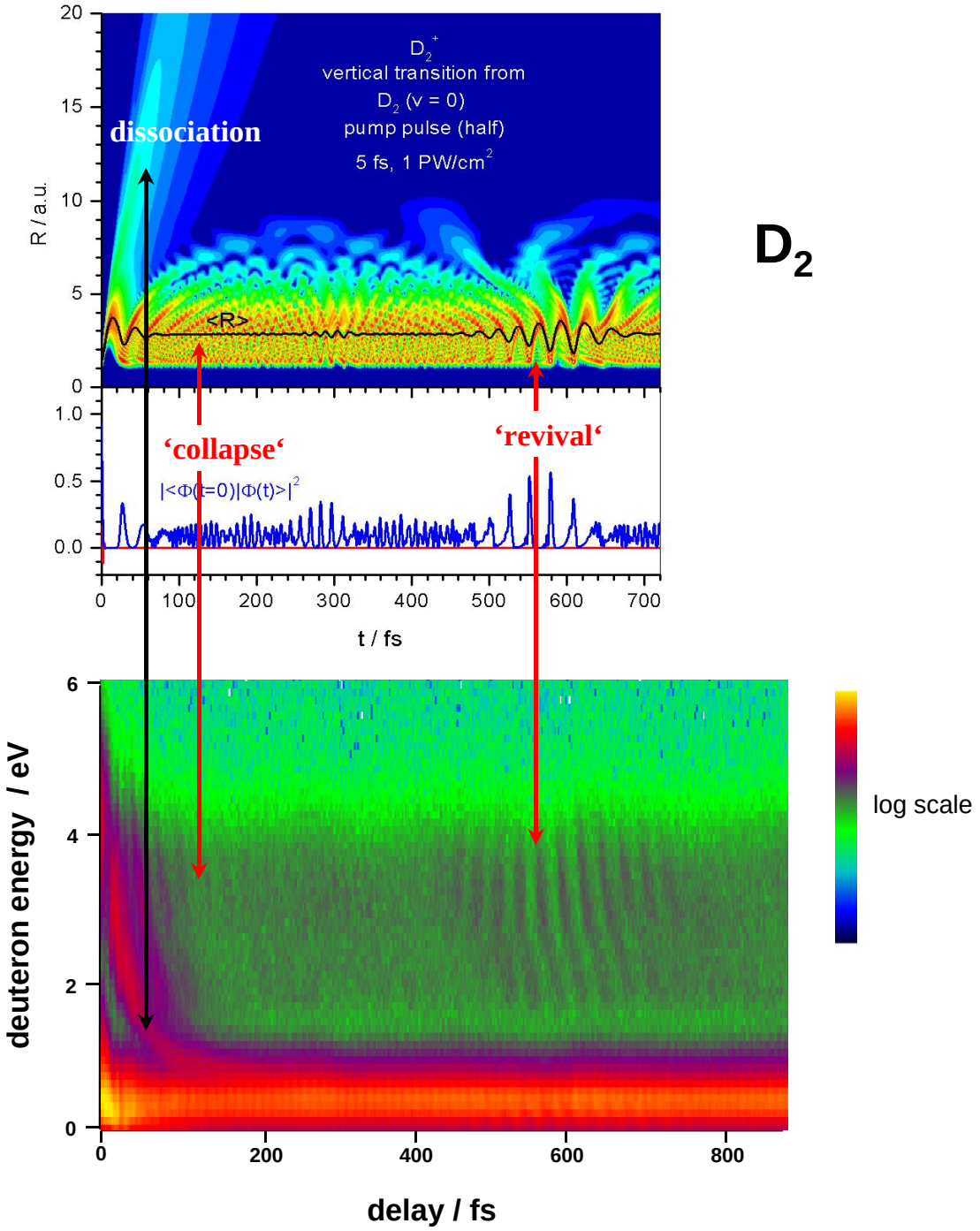

Abbildung 25. Wellenpaketsdynamik von D_2^+ nach Ionisation von D_2 in einem ultrakurzen (7 fs) Laserpuls. Oben: Modellrechnung [24] für die Wahrscheinlichkeitsdichte, die Kerne im Abstand R zu finden, als Funktion der Zeit nach dem Pump-Laserpuls. Die Bewegung im anharmonischen Molekülpotential führt zu einem "Kollaps" des Wellenpakets, welches sich nach einer gewissen Zeit regeneriert ("Revival") - siehe auch die Autokorrelationsfunktion (blaue Kurve). Unten: Experimentell wird die Wellenpaketsdynamik zeitaufgelöst über Coulomb-Explosion im Probe-Puls visualisiert (siehe Abb. 19). Im entsprechenden Spektrum zeigen sich (invertiert) die Strukturen, wie sie von der Modellrechnung vorhergesagt sind. Deutlich erkennbar ist ferner die Bewegung dissoziierender Molekülfragmente, wie sie schon mit 25-fs-Pulsen beobachtet wurde [41].

Anhang I

Vollständiges Schriftenverzeichnis

Fachzeitschriften und Konferenzberichte

[1] **The Giessen atomic beam source**
G. Clausnitzer, R. Baumann, B. Feuerstein, H.P. Flierl, M. Horoi, G. Keil, M. Mildner, D. Ochs. E. Pfaff, M. Preiss
*AIP Conference Proceedings **293** (1994) 76*

[2] **Electron impact excitation cross sections of sodium $2p^5 3s^2\ ^2P$ autoionizing state from threshold to 1.5 keV**
B. Feuerstein, A.N. Grum-Grzhimailo and W. Mehlhorn
*J. Phys. B **31** (1998) 593*

[3] **Alignment of the Na* $2p^5 3s^2\ ^2P_{3/2}$ autoionizing state excited by electron impact: experiment and theory**
B. Feuerstein , A.N. Grum-Grzhimailo, K. Bartschat and W. Mehlhorn
*J. Phys. B **32** (1999) 3727*

[4] **Near-threshold structures in electron-collision-induced alignment of core-excited atomic states**
A.N. Grum-Grzhimailo, K. Bartschat, B. Feuerstein and W. Mehlhorn
*Phys. Rev. A **60** (1999) R1751*

[5] **Electron-impact excitation cross sections of K*($3p^5 4s^2\ ^2P_{3/2}$,$^2P_{1/2}$) autoionizing states: strong fine-structure dependence near threshold**
B. Feuerstein, A.N. Grum-Grzhimailo and W. Mehlhorn
*J. Phys. B **32** (1999) 4547*

[6] **Momentum distributions of Ne^{n+} ions created by an intense ultrashort laser pulse**
R. Moshammer, B. Feuerstein, W. Schmitt, A. Dorn, C.D. Schröter, J. Ullrich, H. Rottke, C. Trump, M. Wittmann, G. Korn, K. Hoffmann and W. Sandner
*Phys. Rev. Lett. **84** (2000) 447*

[7] **Electron correlations observed through intensity interferometry**
M. Schulz, R. Moshammer, W. Schmitt, H. Kollmus, B. Feuerstein, R. Mann, S. Hagmann and J. Ullrich
*Phys. Rev. Lett. **84** (2000) 863*

[8] **Cross sections of $3p^{-1}$ diagram and satellite Auger states in atomic calcium for electron impact**
B. Feuerstein, O.I. Zatsarinny and W. Mehlhorn
*J. Phys. B **33** (2000) 1237*

[9] **First results from the Freiburg electron beam ion trap FreEBIT**
J.R. Crespo Lopez-Urrutia, B. Bapat, B. Feuerstein, A. Werdich and J. Ullrich
*Hyperfine Interactions **127** (2000) 497*

[10] **Nonsequential multiple ionization in intense laser pulses: interpretation of ion momentum distributions within the classical 'rescattering' model**
B. Feuerstein, R. Moshammer and J. Ullrich
*J. Phys. B **33** (2000) L823*

[11] **Strong-field non-sequential ionization: The vector momentum distribution of multiply charged Ne ions**
H. Rottke, C. Trump, M. Wittmann, G. Korn, W. Becker, K. Hoffmann, W. Sandner, R. Moshammer, B. Feuerstein, W. Schmitt, A. Dorn, C.D. Schröter and J. Ullrich
*AIP Conference Proceedings **525** (2000) 285*

[12] **Non-sequential double ionization of Ne in intense laser pulses: a coincidence experiment**
R. Moshammer, B. Feuerstein, D. Fischer, A. Dorn, C.D. Schröter, J. Deipenwisch, J.R. Crespo Lopez-Urrutia, C. Höhr, P. Neumayer and J. Ullrich
*Optics Express **8** (2001) 358*

[13] **Separation of recollision mechanisms in nonsequential strong-field double ionization of Ar: the role of excitation-tunneling**
B. Feuerstein, R. Moshammer, D. Fischer, A. Dorn, C.D. Schröter, J. Deipenwisch, C. Höhr, P. Neumayer, J. Ullrich, H. Rottke, C. Trump, M. Wittmann, G. Korn and W. Sandner
*Phys. Rev. Lett. **87** (2001) 043003*

[14] **Electron correlations observed through intensity interferometry: study of model initial state wavefunctions**
B. Feuerstein, M. Schulz, R. Moshammer and J. Ullrich
*Physica Scripta **T92** (2001) 447*

[15] **Post-collision interaction after inner-shell ionization by electron impact: the shape of Auger lines**
W. Kuhn, B. Feuerstein and W. Mehlhorn
*J. Phys. B **34** (2001) 2835*

[16] **State-resolved measurements of single-electron capture in slow Ne^{7+}- and Ne^{8+}-helium collisions**
D. Fischer, B. Feuerstein, R.D. DuBois, R. Moshammer, J.R. Crespo López-Urrutia, I. Draganic, H. Lörch, A.N. Perumal and J. Ullrich
*J. Phys. B **35** (2002) 1369*

[17] **Correlated two-electron dynamics in strong-field double ionization**
R. Moshammer, B. Feuerstein, J. R. Crespo Lopez-Urrutia, A. Dorn, D. Fischer, C.D. Schröter, W. Schmitt, J. Ullrich, H. Rottke, C. Trump, M. Wittmann, G. Korn, K. Hoffmann and W. Sandner
*Phys. Rev. A **65** (2002) 035401*

[18] **Coincident Fragment Detection in Strong Field Photoionization and Dissociation of H_2**
H. Rottke, C. Trump, M. Wittmann, G. Korn, W. Sandner, R. Moshammer, A. Dorn, C.D. Schröter, D. Fischer, J. R. Crespo Lopez-Urrutia, P. Neumayer, J. Deipenwisch, C. Höhr, B. Feuerstein and J. Ullrich
Phys. Rev. Lett. ***89*** *(2002) 013001*

[19] **Double ionization in strong laser fields**
R. Dörner, Th. Weber, M. Weckenbrock, A. Staudte, S. Kammer, H. Schmidt-Böcking, H. Rottke, R. Moshammer, B. Feuerstein and J. Ullrich
Photonic, electronic and atomic collisions, XXII Int. Conf. Santa Fe (NM), ed. J. Burgdörfer et al, Rinton Press (2002)

[20] **On the computation of momentum distributions within wave packet propagation calculations**
B. Feuerstein and U. Thumm
J. Phys. B ***36*** *(2003) 707*

[21] **Strongly directed electron emission in non-sequential double ionization of Ne by intense laser pulses**
R. Moshammer, J. Ullrich, B. Feuerstein, D. Fischer, A. Dorn, C.D. Schroeter, J.R. Crespo Lopez-Urrutia, C. Hoehr, H. Rottke, C. Trump, M. Wittmann, G. Korn, K. Hoffmann and W. Sandner
J. Phys. B ***36*** *(2003) L113*

[22] **Fragmentation of H_2^+ in strong 800 nm laser pulses: initial vibrational state dependence**
B. Feuerstein and U. Thumm
Phys. Rev. A ***67*** *(2003) 043405*

[23] **Projectile charge-sign dependence of four-particle dynamics in helium double ionization**
D. Fischer, R. Moshammer, A. Dorn, J.R. Crespo López-Urrutia, B. Feuerstein, C. Höhr, C.D. Schröter, S. Hagmann, H. Kollmus, R. Mann, B. Bapat and J. Ullrich
Phys. Rev. Lett. ***90*** *(2003) 243201*

[24] **Mapping of coherent and decohering nuclear wave packet dynamics in D_2^+ with ultrashort laser pulses**
B. Feuerstein and U. Thumm
Phys. Rev. A, ***67*** *(2003) 063408*

[25] **Laser-induced non-sequential double ionization investigated at and below the threshold for electron impact ionisation**
E. Eremina, H. Rottke, W. Sandner, A. Dreischuh, F. Lindner, F. Grasbon, G.G. Paulus, H. Walther, R. Moshammer, B. Feuerstein and J. Ullrich
J. Phys. B ***36*** *(2003) 3269*

[26] **Rescattering of ultralow-energy electrons for single ionization of Ne in the tunneling regime**
R. Moshammer, J. Ullrich, B. Feuerstein, D. Fischer, A. Dorn, C. D. Schröter, J. R. Crespo Lopez-Urrutia, C. Hoehr, H. Rottke, C. Trump, M. Wittmann, G. Korn and W. Sandner
Phys. Rev. Lett. ***91*** *(2003) 113002*

[27] **Physics with Highly-Charged Ions in an EBIT**
J.R. Crespo López-Urrutia, B. Bapat, B. Feuerstein, D. Fischer, H. Lörch, R. Moshammer and J. Ullrich
Hyperfine Interactions ***146*** *(2003) 109*

[28] **Subshell-resolved measurements of single-electron capture in slow Ne^{7+}-helium collisions**
D. Fischer, B. Feuerstein, R. Moshammer, J.R. Crespo López-Urrutia, I. Draganic, H. Lörch, A.N. Perumal, J. Ullrich and R.D. DuBois
Hyperfine Interactions ***146*** *(2003) 177*

[29] **Multiple Ionization of Atoms in Intense Laser Fields**
A. Rudenko, C.D. Schröter, R. Moshammer, K. Zrost, V.L.B. de Jesus, B. Feuerstein, D. Fischer, T. Ferger and J. Ullrich
AIP Conference Proceedings ***697*** *(2003) 13*

[30] **Double ionization of helium by impact of particles with positive and negative charge**
A. Rudenko, C.D. Schröter, R. Moshammer, K. Zrost, V.L.B. de Jesus, B. Feuerstein, D. Fischer, T. Ferger and J. Ullrich
AIP Conference Proceedings ***697*** *(2003) 65*

[31] **Atomic structure dependence of nonsequential double ionization of He, Ne and Ar in strong laser pulses**
V.L.B. de Jesus, B. Feuerstein, K. Zrost, D. Fischer, A. Rudenko, F. Afaneh, C.D. Schröter, R. Moshammer and J. Ullrich
J. Phys. B ***37*** *(2004) L161*

[32] **Circular dichroism in laser-assisted proton - hydrogen collisions**
T. Niederhausen, B. Feuerstein and U. Thumm
Phys. Rev. A ***70*** *(2004) 023408*

[33] **Reaction microscopes applied to study atomic and molecular fragmentation in intense laser fields: non-sequential double ionization of helium**
V.L.B. de Jesus, A. Rudenko, B. Feuerstein, K. Zrost, C.D. Schröter, R. Moshammer and J. Ullrich
J. Elec. Spec. ***141*** *(2004) 127*

[34] **Resonant Structures in the Low-Energy Electron Continuum for Single Ionization of Atoms in the Tunneling Regime**
A. Rudenko, K. Zrost, C.D. Schröter, V.L.B. de Jesus, B. Feuerstein, R. Moshammer and J. Ullrich
J. Phys. B ***37*** *(2004) L407*

[35] **Correlated multi-electron dynamics in ultrafast laser pulse - atom interactions**
A. Rudenko, K. Zrost, B. Feuerstein, V.L.B. de Jesus, C.D. Schröter, R. Moshammer and J. Ullrich
Phys. Rev. Lett. ***93*** *(2004) 253001*

[36] **Assessing a tornado climatology from global tornado intensity distributions**
B. Feuerstein, N. Dotzek and J. Grieser
Journal of Climate ***18*** *(2005) 585*

[37] **Fragmentation dynamics of molecular hydrogen in strong ultrashort laser pulses**
A. Rudenko, B. Feuerstein, K. Zrost, V.L.B. de Jesus, T. Ergler, C.D. Schröter, R. Moshammer and J. Ullrich
J. Phys. B ***38*** *(2005) 487*

[38] **Multiple ionization in strong fields**
A. Rudenko, R. Moshammer, C.D. Schröter, K. Zrost, B. Feuerstein, V.L.B. de Jesus, and J. Ullrich
Inst. Phys. Conf. Ser.No. 183 (2005) 93

[39] **Multiple ionization of atoms by 25 and 7 fs laser pulses**
A. Rudenko, B. Feuerstein, K. Zrost, V.L.B. de Jesus, C.D. Schröter, R. Moshammer and J. Ullrich
Ultrafast Phenomena XIV, Springer Series in Chem. Phys. ***79*** *(2005) 894*

[40] **Coulomb singularity in the transverse momentum distribution for strong-field single ionization**
A. Rudenko, K. Zrost, Th. Ergler, A.B. Voitkiv, B. Najjari, V.L.B. de Jesus, B. Feuerstein C.D. Schröter, R. Moshammer and J. Ullrich
J. Phys. B ***38*** *(2005) L191*

[41] **Time-resolved imaging and manipulation of H_2 fragmentation in intense laser fields**
Th. Ergler, A. Rudenko, B. Feuerstein K. Zrost, C.D. Schröter, R. Moshammer and J. Ullrich
Phys. Rev. Lett. ***95*** *(2005) 093001*

[42] **Observational evidence for exponential tornado intensity distributions over specific kinetic energy**
N. Dotzek, M.V. Kurgansky, J.Grieser, B. Feuerstein and P. Névir
Geophys. Res. Lett., submitted

Eingeladene Vorträge

[T1] **Nonsequential multiple ionization in intense laser pulses: Interpretation of Ne^{n+} ion momentum distributions within a classical "rescattering model"**
International Workshop on Atomic Systems in Extreme Fields, Dresden (27.3.2000)

[T2] **Recollision mechanisms in nonsequential strong-field double ionization of neon and argon: the role of (e,2e) and excitation-tunneling**
Seminar, Department of Theoretical and Computational Physics, Queen's University Belfast (1.5.2001)

[T3] **State-resolved single electron capture in slow Ne^{7+}- and Ne^{8+}- He collisions**
XVII ISIAC, Ensenada, Mexico (26.7.2001)

[T4] **Wenn das Elektron zum Bumerang wird: Mehrfachionisation in starken Laserpulsen**
Seminar des SFB 276, Fakultät für Physik, Universität Freiburg (21.11.2001)

[T5] **Mapping of wave packet dynamics of H_2^+ using ultrashort pump-probe laser pulses**
Bothe-Kolloquium, Max-Planck-Institut für Kernphysik, Heidelberg (26.6.2002)

[T6] **Few-body quantum dynamics in strong fields: From "simple" single ionisation to exploding molecular clocks**
Atomic Physics Seminar, Department of Physics, Kansas State University, Manhattan (KS), USA (30.4.2004)

[T7] **Wave packet dynamics of H_2^+ in ultrashort laser pulses**
329th WE Heraeus Seminar, Physikzentrum Bad Honnef, Germany (26.6.2004)

[T8] **Skywarn Deutschland e.V.: present status and perspectives**
Tornado Forecasting Workshop, DWD - Deutscher Wetterdienst, Langen, Germany (24.2.2005)

Anhang II

Auswahl der wichtigsten Publikationen

Momentum Distributions of Ne^{n+} Ions Created by an Intense Ultrashort Laser Pulse

R. Moshammer,[1,*] B. Feuerstein,[1] W. Schmitt,[1,2] A. Dorn,[1] C. D. Schröter,[1] and J. Ullrich[1]
[1]*Universität Freiburg, Hermann-Herder Strasse 3, D-79104 Freiburg, Germany*
[2]*Gesellschaft für Schwerionenforschung, D-64220 Darmstadt, Germany*

H. Rottke,[3] C. Trump,[3] M. Wittmann,[3] G. Korn,[3] K. Hoffmann,[3] and W. Sandner[3,4]
[3]*Max-Born-Institut, Rudower Chaussee 6, D-12489 Berlin, Germany*
[4]*Technische Universität Berlin, Hardenbergstrasse 36, D-10623 Berlin, Germany*
(Received 24 August 1999)

Vector momentum distributions of Ne^{n+} ($n = 1, 2, 3$) ions created by 30 fs, $\approx$1 PW/cm^2 laser pulses at 795 nm have been measured using recoil-ion momentum spectroscopy. Distinct maxima along the light polarization axis are observed at 4.0 and 7.5 a.u. for Ne^{2+} and Ne^{3+} production, respectively. Hence, mechanisms based on an instantaneous release of two (or more) electrons can be ruled out as a dominant contribution to nonsequential strong-field multiple ionization. The positions of the maxima are in accord with kinematical constraints set by the classical "rescattering model."

PACS numbers: 32.80.Rm, 31.90.+s, 32.80.Fb

In the past, a profound understanding of nonlinear physics leading to single ionization and high harmonic generation has been achieved within a single active electron (SAE) model. Contrarily, the observation of surprisingly large yields of multiply charged ions emerging from the interaction of intense laser fields with single atoms has been the subject of controversial debate since the first experimental evidence was reported about 15 years ago [1]. Even recent precision measurements (see, e.g., [2–4]) could not unambiguously clarify the mechanisms of enhanced multiple ionization. The prediction of multiple ionization yields within SAE, assuming sequential ionization of independent electrons, fails by many orders of magnitude (for an overview, see [5]). While there is common agreement that the correlated electron-electron dynamics is responsible for the observed discrepancy [6], the "nonsequential" (NS) mechanisms leading to the enhanced yields remained unclear and are under lively discussion (see, e.g., [7,8]). Up to now, this debate was solely based on total multiple ionization rate measurements.

In essence, three dynamic mechanisms have been proposed for NS double ionization: First, when one electron is rapidly removed in the laser field the remaining electron cannot adiabatically readjust to the ionic potential and is instantaneously "shaken off" into the continuum [2]. This mechanism is known to dominate double ionization of helium after absorption of single photons with energies beyond 1 keV [9]. Second, a "rescattering" process was proposed [10] within a semiclassical model where the second electron is ionized $(e, 2e)$ in a collision with the first electron hitting its parent ion after free propagation during about half an optical cycle in the external laser field. This process is also immanent to many-body intense-field S-matrix calculations [11] which are in excellent agreement with experimental data. Rescattering in a generalized view has been shown to play an important role for NS ionization in SAE calculations where the e-e Coulomb interaction has been approximately incorporated [7]. Third, and most recently, collective multielectron tunneling has been considered in detail but found to be quantitatively too weak. A semiempirical expression resembling a tunneling formula has been found that is in good overall agreement with measured multiple ionization rates [12]. A conclusion that "tunneling is responsible for NS double ionization" has been drawn from the measured ratios of double to single ionization yields over a large range of laser intensities [3].

In this Letter, we present first differential experimental data on double and triple ionization of neon in ultrashort (30 fs FWHM) laser pulses at intensities ($\approx$1 PW/cm^2) where NS multiple ionization dominates but saturation is not yet reached. Cold target recoil-ion momentum spectroscopy (COLTRIMS) [13] has been used to measure the momentum vectors $\vec{p}_{\mathrm{ion}}$ of ejected $Ne^{(1-3)+}$ ions. In the limit of negligibly small momentum transfer by the absorbed photons ($p_\gamma < 0.05$ a.u.) and for short laser pulses (no ponderomotive acceleration of electrons) $\vec{p}_{\mathrm{ion}}$ reflects the sum momentum of emitted electrons $\vec{p}_{\mathrm{ion}} = -\sum \vec{p}_e$. Thus, the ion momentum distributions are a sensitive measure of the many-electron dynamics. We demonstrate that each proposed multiple ionization mechanism leads to distinct momentum patterns of the ions. The comparison with the observed distributions gives, for the first time, decisive information about the importance of different mechanisms.

The experiment was performed at the Max Born Institute using light pulses of a Kerr-lens mode locked Ti:sapphire laser at 795 nm wavelength amplified to pulse energies of up to 600 μJ at 1 kHz repetition rate. The light pulses of 30 fs (FWHM) were focused by a lens ($f = 260$ mm) to a spot of 30 μm (FWHM) diameter into an ultrahigh vacuum chamber (5×10^{-11} torr) reaching pulse peak intensities up to 1.8 PW/cm^2. Intensity fluctuations monitored during the experiment

were kept below 5%. To verify the intensity calculated from the beam parameters we measured Ne^{1+} momentum distributions for circularly polarized light at different intensities. An annular momentum distribution was observed with a diameter which is in accordance with previous measurements of electron energy distributions and theoretical models [14].

At its focus the laser beam was crossed by a low-density (10^8 atoms/cm^3) supersonic jet of Ne atoms. The jet was formed by expanding Ne gas at a pressure of 5 bar through a cooled (LN_2 temperature) 10 μm nozzle. After expansion, the beam was collimated over a total length of 2 m to a diameter of 2 mm at the interaction point. Ions created in the focus were extracted by a weak homogeneous electric field of 1 V/cm. After acceleration over 10 cm and passing a field free drift tube of 20 cm length they were recorded by a two dimensional position sensitive multichannel plate detector (0.1 mm position resolution). From the time of flight the charge state of the ion and its momentum component in the direction of extraction is obtained, the two other components are calculated from the position on the detector. Thus, COLTRIMS yields the charge state and the momentum vector of each single ion with an actual resolution in any direction of $\Delta p_{x,y,z} \leq 0.2$ a.u. (limited mainly by the temperature of the gas jet) and a solid angle for acceptance of 4π for all ions with momenta below $|\vec{p}_{\mathrm{ion}}| \leq 10$ a.u. Only the salient points of recoil-ion spectroscopy are given here; details can be found in Ref. [13].

In Fig. 1 the momentum distributions of Ne^{1+} ions parallel ($P_\parallel$) and perpendicular ($P_\perp$) to the polarization axis are shown for linearly polarized light. The laser intensity of 1.3 PW/cm^2 corresponds to a Keldysh parameter [15] of $\gamma = 0.35$ indicating that the production of singly charged ions mainly occurs via tunnel ionization. In this case most of the ions are "born" at a time when the electric field maximizes. For linear polarization the electric field can be written as $\vec{E}(t) = \vec{E}_o(t)\sin(\omega t)$. Assuming that an ion is created with charge state q and zero initial momentum at a time t_o the final ionic drift momentum strongly depends on the phase $\phi = \omega t_0$ as

$$p(t_0) = \frac{q}{\omega} E_0(t_0)\cos(\omega t_0)\,. \qquad (1)$$

Thus, the final ion momentum distribution contains information about the phase ϕ when ionization occurs. It follows from Eq. (1) that ions created at $\phi = 90°$ (i.e., at maximum field strengths where the tunneling probability maximizes) gain zero drift momentum and, hence, the final momentum distribution peaks at zero. Our experimental results are in nice agreement with a simple expression for electron momentum distributions derived by Delone and Krainov [14] on the basis of tunnel ionization (Fig. 1). Thus, as expected, the Ne^{1+} momentum spectra are well understood in terms of tunnel ionization at the

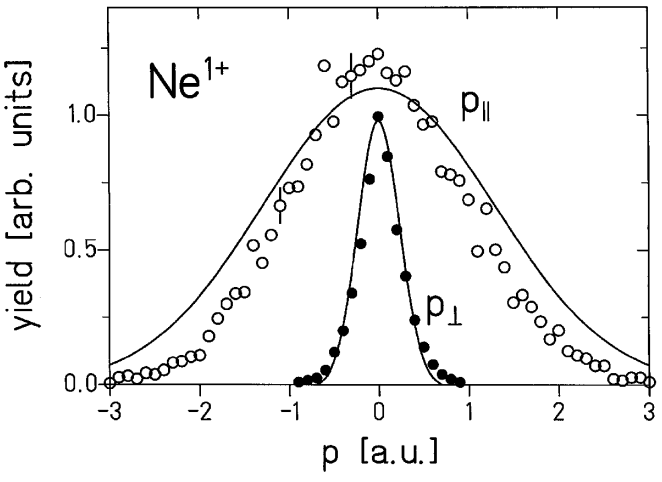

FIG. 1. Momentum distributions parallel ($p_\parallel$) and perpendicular ($p_\perp$) to the polarization axis of Ne^{1+} ions created by 30 fs linearly polarized 795 nm laser pulses at a peak intensity of 1.3 PW/cm^2 (solid line: theoretical results according to [14]).

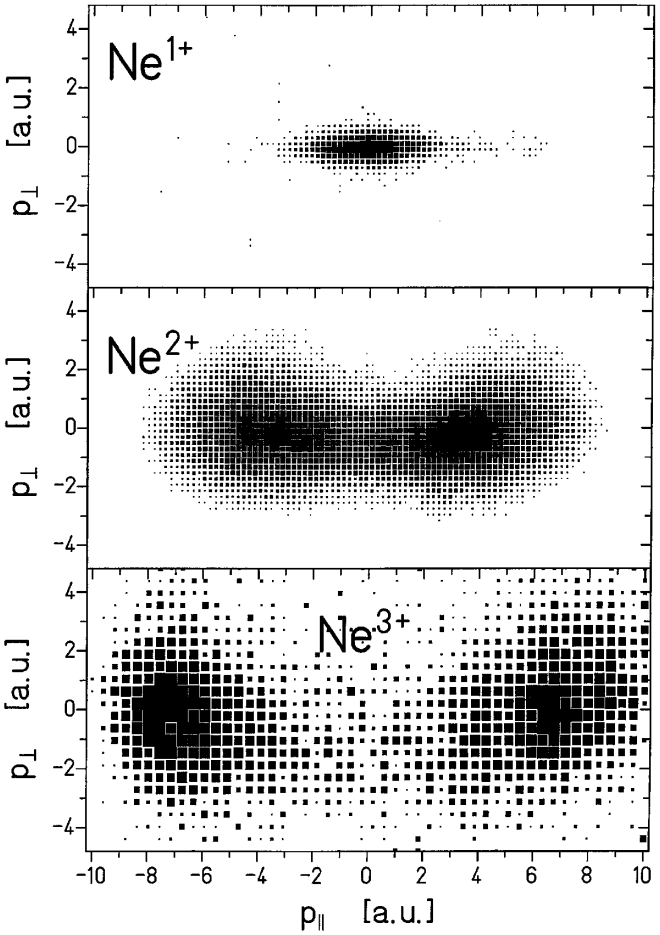

FIG. 2. Two-dimensional momentum distributions ($p_\parallel$, $p_\perp$) of Ne^{n+} ions at peak intensities of 1.3 PW/cm^2 (Ne^{1+}, Ne^{2+}) and 1.5 PW/cm^2 (Ne^{3+}). The distributions are integrated over the third Cartesian coordinate.

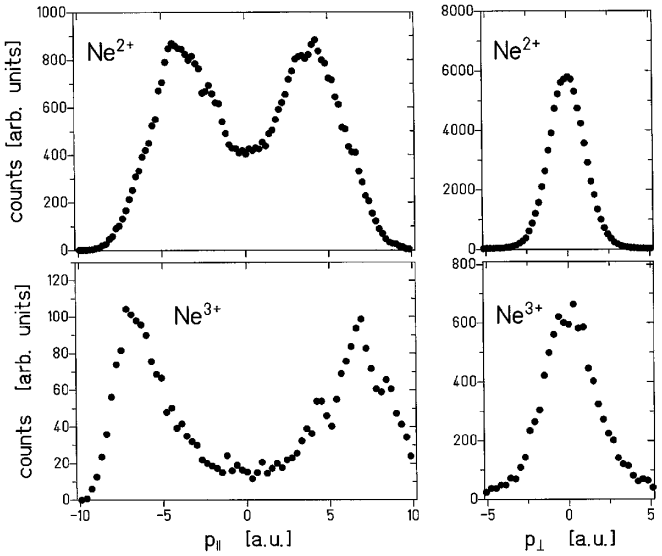

FIG. 3. Projections of the momentum distributions of Fig. 2 onto the axis parallel ($p_\parallel$) and perpendicular ($p_\perp$) to the polarization direction for Ne^{2+} and Ne^{3+}.

present intensity and the agreement confirms the approximation that the ion balances the electron momenta.

As mentioned before, different NS multiple ionization mechanisms result in specific ion momentum distributions. The "collective tunneling" mechanism [12] should lead to a momentum distribution concentrated around zero as discussed before for single ionization [see Eq. (1)]. This follows also for the proposed "shake-off" mechanism [2]. In both cases, the two electrons are released "simultaneously" close to the maximum field strength, i.e., around $\phi = 90°$ where the tunneling probability maximizes. In contrast to these instantaneous double (multiple) ionization processes a stepwise ionization by inelastic rescattering of the first electron leads to substantially different final momenta. The second or more electrons are ionized when the first electron revisits the parent ion, which occurs most likely at a phase when the electric field strength is close to zero. This results in a large final drift momentum according to Eq. (1). In addition, a certain momentum can be transferred to the ion in this ionizing (e, ne) collision.

The experimental two-dimensional ($p_\parallel$, $p_\perp$) momentum distributions for Ne^{n+} ions are shown in Fig. 2. In striking contrast to Ne^+ the distributions for Ne^{2+} and Ne^{3+} exhibit a minimum at $p_\parallel = 0$ and symmetric wings peaking at 4 and 7.5 a.u., respectively. Thus, any instantaneous process leading to double or triple ionization can be excluded as a dominant contribution to multiple ionization under the present conditions. Hence, rescattering appears to be the most appropriate model.

In the following, we will give a qualitative interpretation of our experimental results using a two-step model for double and triple ionization based on inelastic ionizing collisions of the rescattered first electron [10]: First, at a time t_0 single ionization occurs via tunneling. Depending on the phase $\phi = \omega t_0$ the first electron may return back at a time t_1 leading to doubly or triply charged ion via an $(e, 2e)$ or $(e, 3e)$ process, respectively. Considering the kinematical conditions for the inelastic rescattering the final longitudinal momentum of the ion is given by

$$p_{n+}(t_0) = p_{1+}(t_1) + \Delta p + p_{n+}^{\mathrm{drift}}(t_1), \qquad n = 2, 3, \tag{2}$$

where $p_{1+}(t_1)$ is the momentum of the singly charged ion [which balances the momentum $p_e(t_1)$ of the rescattered electron] at time t_1 (it should be noted that t_1 is a function of the initial phase ωt_0). The second term denotes the momentum Δp transferred to the ion in the (e, ne) process, and $p_{n+}^{\mathrm{drift}}(t_1)$ is the final drift momentum an ion with charge state $q = n$ (created with zero initial momentum) accumulates.

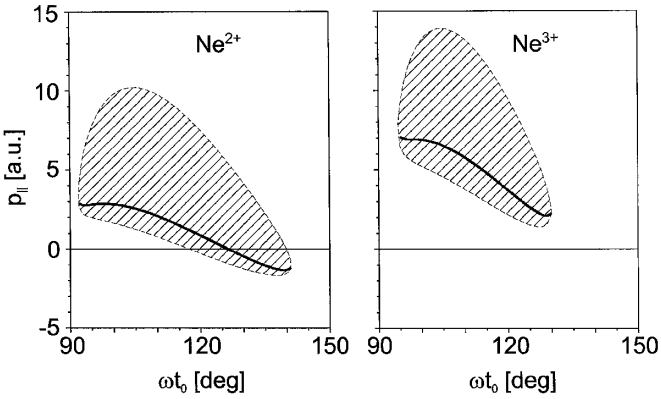

FIG. 4. Within a classical rescattering model kinematically allowed regions of final longitudinal ion momenta (hatched areas) as a function of the phase $\phi = \omega t_0$ where initial single ionization occurs. The solid line is a reasonable likely phase dependence (see text). Intensities are the same as in Fig. 2.

The kinematics of the inelastic (e, ne) collision with an ionization potential I_p sets well-defined constraints for the longitudinal momentum transfer $\Delta p^{\min,\max} = p_e(t_1) \mp n \cdot \sqrt{(1/n)[p_e^2(t_1) - 2I_p]}$ and therefore defines via Eq. (2) a lower and upper limit of possible final longitudinal momenta of created ions as a function of the phase $\phi = \omega t_0$ when the first electron was ionized. This kinematically allowed region is displayed in Fig. 4 in addition with a reasonable likely phase dependence (solid line in Fig. 4) assuming minimal energy loss of the first electron scattered in the forward direction. Since single ionization by tunneling preferentially occurs near $\phi = 90°$ we expect favored ion momenta of 3–4 a.u. for Ne^{2+} and of 7–8 a.u. for Ne^{3+}, respectively, in close overall agreement with the experiment. A detailed description of momentum distributions within the classical rescattering model will be published in a forthcoming paper.

In conclusion, as a result of the measured momentum distributions for multiply charged Ne ions we are able to rule out several mechanisms proposed to explain nonsequential ionization in intense light pulses. Only the kinematics of the rescattering mechanism is in accordance with

the present experimental data. Upon inelastic scattering at the first return of the tunnel ionized first electron to the core a second and even two electrons can be removed from Ne^+ by electron impact ionization. In the future, kinematically complete experiments similar to those performed for ion, electron, and single photon impact [13] are planned using combined recoil-ion and many-electron momentum spectroscopy [16].

The experiments were supported by the Leibniz-Program of the Deutsche Forschungsgemeinschaft DFG. Support from GSI is gratefully acknowledged. We would like to thank W. Becker, M. Doerr, and R. Dörner for fruitful discussions.

*Email: Moshammer@physik.uni-freiburg.de

[1] A. L'Huiller *et al.,* Phys. Rev. A **27**, 2503 (1983).
[2] D. N. Fittinghoff *et al.,* Phys. Rev. Lett. **69**, 2642 (1992).
[3] B. Walker *et al.,* Phys. Rev. Lett. **73**, 1227 (1994).
[4] S. Larochelle, A. Talebpour, and S. L. Chin, J. Phys. B **31**, 1201 (1998).
[5] L. F. DiMauro and P. Agostini, Adv. At. Mol. Opt. Phys. **35**, 79 (1995).
[6] W.-C. Liu *et al.,* Phys. Rev. Lett. **83**, 520 (1999).
[7] J. B. Watson *et al.,* Phys. Rev. Lett. **78**, 1884 (1997).
[8] B. Sheehy *et al.,* Phys. Rev. A **58**, 3942 (1998).
[9] V. Schmidt, *Electron Spectrometry of Atoms using Synchrotron Radiation* (Cambridge University Press, Cambridge, England, 1997).
[10] P. B. Corkum, Phys. Rev. Lett. **71**, 1994 (1993); K. C. Kulander, J. Cooper, and K. J. Schafer, Phys. Rev. A **51**, 561 (1995).
[11] A. Becker and F. H. M. Faisal, J. Phys. B **29**, L197 (1996); F. H. M. Faisal and A. Becker, Laser Phys. **7**, 684 (1997).
[12] U. Eichmann *et al.* (to be published).
[13] J. Ullrich *et al.,* J. Phys. B **30**, 2917 (1997), topical review.
[14] N. B. Delone and V. P. Krainov, J. Opt. Soc. Am. B **8**, 1207 (1991).
[15] L. V. Keldysh, Zh. Eksp. Teor. Fiz. **47**, 1945 (1964).
[16] R. Moshammer *et al.,* Nucl. Instrum. Methods Phys. Res., Sect. B **108**, 425 (1996).

J. Phys. B: At. Mol. Opt. Phys. **33** (2000) L823–L830. Printed in the UK PII: S0953-4075(00)16615-5

LETTER TO THE EDITOR

Nonsequential multiple ionization in intense laser pulses: interpretation of ion momentum distributions within the classical 'rescattering' model

B Feuerstein, R Moshammer and J Ullrich
Fakultät für Physik, Universität Freiburg, D-79104 Freiburg, Germany

Received 24 August 2000, in final form 28 September 2000

Abstract. The classical 'rescattering' model is used to give an interpretation of ion momentum distributions for multiple ionization of atoms in intense fs laser pulses. Kinematical constraints for the ion momenta derived from simple classical considerations reproduce the positions of the maxima observed in experimental momentum distributions of Ne^{2+} and Ne^{3+} ions. Based on these constraints we present a first prediction on the principle structure of differential ion momentum distributions for multiple ionization. We show that different ionization channels can be characterized by their kinematics, leading to specific ion momentum distributions. A qualitative analysis of the intensity dependence is also given.

The physics of double and multiple ionization of atoms in strong fs laser pulses has been the subject of vivid discussion since the first observation of surprisingly high ion yields more than 15 years ago [1]. Single ionization is quantitatively well understood within the 'single active electron' (SAE) model which also holds for double and multiple ionization at intensities above $\simeq$ 1 PW cm^{-2}, where the atom is ionized sequentially during the laser pulse by individual single ionization events. The model of 'sequential' double (or multiple) ionization fails at lower intensities where the predicted ion yields are several orders of magnitude weaker than the experimental values. This discrepancy was the origin of a controversial debate on the mechanisms leading to the enhanced ionization rates. There is general agreement that a 'nonsequential' ionization mechanism (in contrast to the sequential ionization at high intensities) has to imply the correlated dynamics of two (or more) electrons in the strong laser field. However, the nature of this mechanism was not clear as far as the discussion was based only on total ion yields, i.e. integral observables.

In essence, three mechanisms have been proposed for nonsequential double ionization. First, within the 'sudden approximation', when one electron is rapidly removed in the laser field, the remaining electron can be instantaneously 'shaken off' into the continuum due to a finite overlap of its initial (bound) and final (continuum) state wavefunction [2]. Second, a classical 'rescattering' model was proposed [3, 4] in which the first ionized electron freely propagates during about half an optical laser cycle. Under certain conditions it is then 'rescattered' to its parent ion causing double or n-fold ionization in an (e, ne) collision. It should be noted that this process is also immanent to many-body intense-field S-matrix calculations [5, 6] which are in good agreement with experimental data. Third, and most recently, a 'collective multi-electron tunnelling' mechanism has been considered [7] which, however, was found to be quantitatively too weak. Both 'shake-off' as well as the 'collective tunnelling' yield an instantaneous emission of the electrons whereas in the 'rescattering' model the second electron is emitted after the classical recurrence time of the first electron. Thus, this difference

0953-4075/00/210823+08$30.00

in the kinematics should manifest itself in differential observables, e.g. in the momentum distributions of various fragments.

Recent experiments in helium [8], neon [9] and argon [10] succeeded in measuring the momentum distributions of singly, doubly and triply charged ions at laser intensities where nonsequential ionization dominates the total yield. In addition, and most recently, coincident momentum distributions of two electrons have been determined for double ionization of argon [11]. In [9] it was shown that mechanisms based on an instantaneous release of two (or more) electrons can be ruled out as a dominant contribution to nonsequential strong-field multiple ionization. This follows from the fact that a simultaneous electron emission leads to an ion momentum distribution along the laser polarization axis which peaks at zero momentum. In contrast, the observed distributions in the nonsequential regime exhibit distinct maxima at nonzero values [8,9]. For Ne^{2+} and Ne^{3+} ions the positions of these maxima are in accord with kinematical constraints set by the classical 'rescattering' model [9].

The purpose of this letter is to give a more detailed description of these kinematical constraints with the extension to different ionization channels for n-fold ($n > 2$) ionization. For instance, triple ionization can occur via three different ionization channels: First, purely nonsequential ionization (0–3), second, a two-step sequential–nonsequential ionization where two electrons tunnel sequentially and the third electron is emitted in a nonsequential process (0–1–3). The other two-step (nonsequential–sequential) channel with a nonsequential first ionization step (0–2–3) is not considered here since it does not contribute significantly to the total ion yield. Third, purely sequential ionization might occur, which will be denoted (0–1–2–3). In a recent theoretical work on strong-field multiple ionization of the noble gases [12] these various decay channels have been taken into account in the S-matrix approach. The results agree remarkably well with experimental total ion yields over the entire intensity range and reproduce the observed 'knee' structures.

In this letter we will give a first prediction on the principle structure of differential ion momentum distributions for multiple ionization based on simple classical considerations. It will be shown that the ionization channels mentioned above, each of which dominates the ion yield at a specific intensity range, can be characterized by the kinematical constraints for the ion momenta. By comparison with (future) experimental results this should give a deeper insight into the mechanisms leading to strong-field multiple ionization. The kinematical constraints will be derived within the classical rescattering model. First, we will consider the motion of a single charged particle in a linearly polarized laser field which is given by the oscillating electric field vector $\mathcal{E}(t) = \mathcal{E}_0(t) \sin \omega t$ with an envelope function $\mathcal{E}_0(t)$. Since the magnetic field can be neglected for the intensity range considered here, we have a one-dimensional motion along the laser polarization axis (x-axis). The integration of the equation of motion $F(t) = q\,\mathcal{E}(t) = m\,\ddot{x}$ leads to the momentum $p(t, t_0)$ of the particle (charge q, mass m) at time t depending on the starting time t_0:

$$p(t,t_0) = \int_{t_0}^{t} F(t')\,\mathrm{d}t' = q\int_{t_0}^{t} \mathcal{E}_0(t')\sin\omega t'\,\mathrm{d}t' \tag{1}$$

$$= -\frac{q}{\omega}\left[\mathcal{E}_0(t')\cos\omega t'\right]_{t_0}^{t} + \frac{q}{\omega}\int_{t_0}^{t} \dot{\mathcal{E}}_0(t')\cos\omega t'\,\mathrm{d}t'$$

$$\approx -\frac{q}{\omega}\left[\mathcal{E}_0(t')\cos\omega t'\right]_{t_0}^{t} + \frac{q}{\omega}\frac{\mathcal{E}_{\max}}{\tau\omega}\left[\sin\omega t'\right]_{t_0}^{t}.$$

In the second step we used the estimation $\dot{\mathcal{E}}_0 \approx \mathcal{E}_{\max}/\tau$, where $\mathcal{E}_{\max}$ is the maximum field during the laser pulse. If the duration τ of the pulse is long compared to the oscillation period

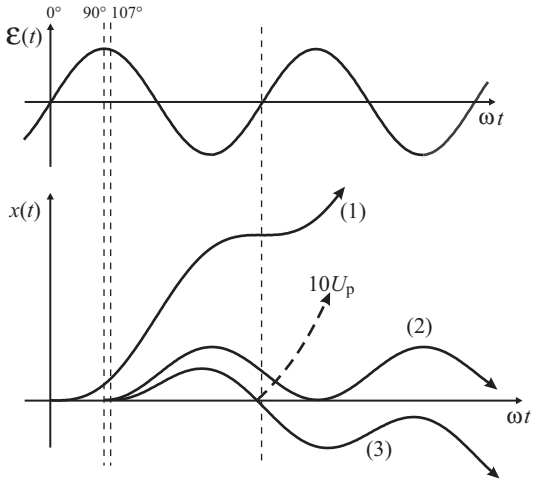

Figure 1. Sketch of the motion $x(t)$ of an electron in a linearly polarized laser field $\mathcal{E}(t) \propto \sin \omega t$. Exemplary trajectories are shown for three different phases $\phi_0 = \omega t_0$ at which the initial single ionization occurs. Curve (1): $\phi_0 = 0°$, no rescattering. Curve (2): $\phi_0 = 90°$, the electron reaches its parent ion, but with zero kinetic energy. Curve (3): $\phi_0 \approx 107°$, the electron hits its parent ion with maximal kinetic energy of $3.17\,U_\mathrm{p}$; elastic backscattering at this point leads to the 'cut-off' electron energy of $10\,U_\mathrm{p}$ [14].

$(\tau\omega \gg 1)$† the second term can be neglected yielding

$$p(t, t_0) = -\frac{q}{\omega}\left[\mathcal{E}_0(t)\cos\omega t - \mathcal{E}_0(t_0)\cos\omega t_0\right]. \tag{2}$$

Here, the first term describes the oscillatory motion in the alternating field and the second term corresponds to a drift momentum which depends on the phase ωt_0 when the charged particle was 'born'. As the laser pulse passes by, the oscillatory motion vanishes with $\mathcal{E}_0(t)$ and the final drift momentum remains $(t \to \infty,\ \mathcal{E}_0(t) \to 0)$

$$p(t_0) = \frac{q}{\omega}\,\mathcal{E}_0(t_0)\cos\omega t_0. \tag{3}$$

Thus, the maximal drift momentum of a charged particle created in a laser pulse takes the form

$$p_\mathrm{max} = \frac{q}{\omega}\,\mathcal{E}_\mathrm{max} = 2\,q\sqrt{U_\mathrm{p}} \tag{4}$$

where $U_\mathrm{p} = \mathcal{E}^2/4\omega^2$ is the 'ponderomotive potential' which reflects the mean quiver energy of a charged particle in the laser field. Assuming that an ion is created with charge state q and zero initial momentum at time t_0 the final ion momentum distribution contains information about the phase ωt_0 when the ionization occurs (see equation (3)). Ions created at $\omega t_0 = 90°$, where the field strength is maximal and tunnel ionization is most probable, gain zero drift momentum‡ and, hence, the final momentum distribution peaks at zero. This is well known for single ionization in the 'tunnelling regime' [13]. The same holds for sequential multiple ionization because it is a sequence of single tunnel ionization steps [10].

Large final momenta for multiply charged ions are observed when the ion gets its final charge state close to a zero crossing of the oscillating field. This can be understood within the classical rescattering model. Figure 1 illustrates the motion of an electron in the laser field

† In recent experiments [8–10] $\tau\omega$ was of the order of 70–450.

‡ Except for the small contribution of the second term in (1) which is of the order of $\sqrt{2\,U_\mathrm{p}}/\tau\omega$.

for three different phases $\phi_0 = \omega t_0$ where the single ionization occurs via tunnelling (this means zero initial momentum). At $\phi_0 = 0^\circ$ (or 180°, zero crossing) the electron acquires the maximal drift momentum and escapes from the atom without rescattering (curve (1)), whereas at $\phi_0 = 90^\circ$ (or 270°, maximal field strength) the electron gets zero drift momentum and it returns back to the ion with zero kinetic energy (curve (2)). Only within the phase ranges $90^\circ < \phi_0 < 180^\circ$ and $270^\circ < \phi_0 < 360^\circ$, can the electron hit its parent ion with finite kinetic energy. The maximal and the most likely electron velocity at the classical recurrence time t_1 corresponds to an kinetic energy of approximately $3.17\,U_\mathrm{p}$ (see figure 1 of [3]). The corresponding phase of the initial tunnel ionization is around 107° (287°) and the electron passes its parent ion close to a zero crossing of the oscillating field (curve (3) in figure 1). Now, the electron can undergo an elastic† or inelastic scattering process. An (e, ne) collision at this point results in a large final drift momentum of the ion according to equation (3). It should be noted that in the limit of small momentum transfer by the absorbed photons ($p_\gamma < 0.05$ au for a Ti:sapphire laser) and short laser pulses (no ponderomotive acceleration of the electrons) the ion momentum $\vec{p}_\mathrm{ion}$ reflects the sum momentum of the emitted electrons: $\vec{p}_\mathrm{ion} = -\sum \vec{p}_\mathrm{e}$.

In order to obtain kinematical constraints for the final ion momentum distributions the momentum exchange during the (e, ne) collision has to be taken into account. In the case of purely nonsequential ionization the momentum of the incoming electron balances the momentum of the singly charged ion:

$$\vec{p}_\mathrm{ion}^{\,1+} = -\vec{p}_\mathrm{e}. \tag{5}$$

Directly after the collision, the momentum of the n-fold charged ion is equal to the recoil momentum $\Delta\vec{p}_\mathrm{rec}$ due to the (e, ne) process. The latter reflects the sum momentum of the n outgoing electrons:

$$\vec{p}_\mathrm{ion}^{\,n+} = \Delta\vec{p}_\mathrm{rec} = -\sum_{i=1}^{n} \vec{p}_{\mathrm{e}_i}. \tag{6}$$

Finally, the ion acquires the drift momentum according to equation (3) which leads to a final momentum $\vec{p}_\mathrm{ion}^{\,n+}(t_0) = \Delta\vec{p}_\mathrm{rec}(t_1, t_0) + \vec{p}_\mathrm{drift}^{\,n+}(t_1, t_0)$. Note that the recurrence time t_1 depends implicitly on the phase ωt_0 at which the initial single ionization occurs.The recoil momentum is limited by the excess energy E_exc, i.e. the kinetic energy of the rescattered electron minus the sum of the binding energies of n ionized electrons in an (e, ne) event. This leads to the following kinematical constraints for the ion momentum parallel ($\parallel$) and perpendicular ($\perp$) to the polarization direction:

$$p_\parallel^{n+}(t_0)_\mathrm{min}^\mathrm{max} = p_\mathrm{drift}^{n+}(t_1, t_0) \pm \sqrt{2\,n\,E_\mathrm{exc}(t_1, t_0)}, \tag{7}$$

$$|p_\perp^{n+}(t_0)| \leqslant \sqrt{2\,n\,E_\mathrm{exc}(t_1, t_0)}. \tag{8}$$

The kinematically allowed regions of final parallel ion momenta as a function of the phase ωt_0 according to equation (7) are shown in figure 4 of [9].

In the following we will discuss the kinematics for the general case of combined sequential–nonsequential multiple ionization with the emphasis on the intensity dependence. For the sake of simplicity we will only consider the most probable kinetic energy of the rescattered electron of $3.17\,U_\mathrm{p}$ and the maximal drift momentum of $2\,n\sqrt{U_\mathrm{p}}$ (equation (4)). Assuming that small recoil momenta are favoured in the (e, ne) collision, which is well justified by various measurements (see e.g. [15]), one obtains from equation (7) for the most probable

† If the electron is elastically backscattered (broken curve in figure 1) it gains a large final kinetic energy of up to $10U_\mathrm{p}$ [14] which corresponds to the well-known 'cut-off' energy in electron spectra following strong-field single ionization.

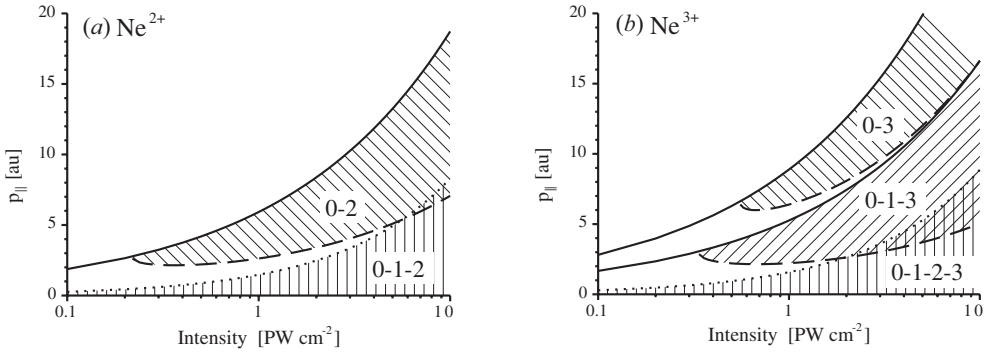

Figure 2. Kinematically favoured regions (hatched areas) of final longitudinal momenta for (*a*) Ne^{2+} and (*b*) Ne^{3+} ions as a function of the laser intensity for different ionization channels: nonsequential ionization (0–2),(0–3); sequential ionization (0–1–2),(0–1–2–3); combined sequential–nonsequential ionization (0–1–3). The solid curves give the ion momenta for zero recoil momentum $\Delta p_{\rm rec}$ in the (e, *n*e) collision. For nonsequential ionization (0–2),(0–3) this is the drift momentum $2n\sqrt{U_{\rm p}}$ of an *n*-fold charged ion. The lower limit (broken curves) corresponds to a minimal energy loss of the first electron scattered in the forward direction. The half width of the momentum distribution for sequential ionization is given by the dotted curves.

final ion momentum:

$$2\,n\sqrt{U_{\rm p}} - \sqrt{2\,[3.17\,U_{\rm p} - I_{\rm p}(1 \to n)]} \leqslant p_{\parallel}^{n+} \leqslant 2\,n\sqrt{U_{\rm p}}. \tag{9}$$

Here, $I_{\rm p}(1 \to n)$ is the ionization potential. The lower limit corresponds to a minimal energy loss of the first electron scattered in the forward direction. For multiple ionization of neon at an intensity of $\simeq 1$ PW cm^{-2} we get $p_{\parallel}^{2+} \simeq 3$–6 au and $p_{\parallel}^{3+} \simeq 6$–9 au, respectively, which is in good accord with the observed maxima of the corresponding ion momentum distributions [9]. Recent *S*-matrix calculations [16] for the momentum distributions of recoil ions from laser-induced nonsequential double ionization of He reproduced the double-hump structure along the polarization axis. Moreover, a cutoff formula for the ion momentum was found which is similar to the upper limit in equation (7). In a combined sequential–nonsequential ionization channel, first the atom is ionized sequentially into charge state *m* followed by an (e, $[n-m+1]$e) collision creating the *n*-fold charged ion. Now, the momentum $\vec{p}_{\rm e}$ of the incoming electron does not balance the momentum of the *m*-fold charged ion due to the $(m-1)$ other electrons which were created in sequential processes and do not take part in the collision. Thus, for the momentum of the *n*-fold charged ion directly after the (e , $[n-m+1]$e) collision we find $\vec{p}_{\rm ion}^{\,n+} = (1-m)\vec{p}_{\rm e} + \Delta\vec{p}_{\rm rec}$. Analogous to equation (9) the most probable final ion momenta parallel to the polarization direction can be estimated by

$$2\,n\sqrt{U_{\rm p}} - (m-1)\sqrt{2\cdot 3.17\,U_{\rm p}} - \sqrt{2\,E_{\rm exc}} \leqslant p_{\parallel}^{n+} \leqslant 2\,n\sqrt{U_{\rm p}} - (m-1)\sqrt{2\cdot 3.17\,U_{\rm p}} \tag{10}$$

with $E_{\rm exc} = 3.17\,U_{\rm p} - I_{\rm p}(m \to n)$.

Figure 2(*a*) illustrates the kinematically favoured momentum range (in atomic units) for nonsequential (0–2) and sequential (0–1–2) double ionization of neon as a function of the laser intensity. For sequential ionization the half width of the momentum distribution is shown as a dotted curve. This width is calculated by convolution of the two single ionization momentum distributions according to [13]. The classical rescattering model predicts a 'threshold intensity' where the kinematically allowed momentum range shrinks to zero. At this intensity the maximal kinetic energy of the returning electron is equal to the ionization potential. Below the threshold intensity the classical model fails to explain the observed

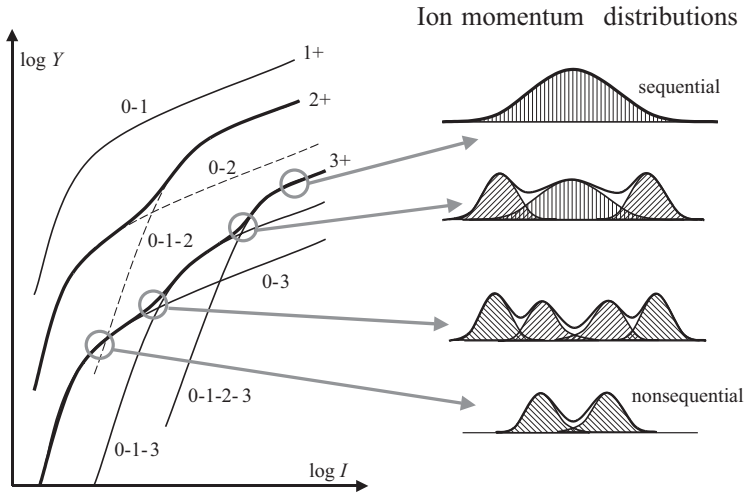

Figure 3. Schematic diagram of the ion yield Y for single, double and triple ionization in an intense linearly polarized laser field as a function of the laser intensity I. A qualitative evolution for the momentum distributions of triply charged ions is shown on the right. The contributions of the different ionization channels are indicated by the hatched areas: \\\\\, nonsequential ionization (0–3); / / / / /, combined sequential–nonsequential ionization (0–1–3); | | | | |, sequential ionization (0–1–2–3).

multiple ionization yields which do not indicate any threshold effect. The only classically allowed ion momentum at threshold is the drift momentum $2n\sqrt{U_p}$, whereas at higher intensities the kinematically favoured momentum range lies below this value. In figure 2(*b*) the kinematically favoured regions are shown for triple ionization of neon. The three ionization channels, purely nonsequential (0–3), combined sequential-nonsequential (0–1–3) and purely sequential (0–1–2–3) ionization can be characterized by their specific momentum distributions. Maxima at finite momenta are predicted for the channels (0–3) and (0–1–3) whereas the channel (0–1–2–3) peaks at zero. Here, analogous to double ionization, the dotted curve gives the half width of a convolution of three single ionization momentum distributions.

Based on this kinematical analysis we are able to predict the general intensity dependence of the shape of momentum distributions for triply charged ions created in a strong laser pulse. The ion momentum distribution consists of portions from the different ionization channels. Since their relative contributions to the total ion yield are strongly intensity-dependent, the shape of the momentum distribution will change as we go from the nonsequential regime to the sequential regime. Figure 3 illustrates this behaviour in a qualitative way. The left part of the figure shows a schematic diagram of the ion yield Y as a function of the laser intensity I. On the right, four exemplary momentum distributions of triply charged ions are given schematically. At low intensities, purely nonsequential (0–3) triple ionization dominates the total ion yield leading to the well-known double-hump shape of the momentum distribution. At intensities above the first 'knee' in the total ion yield, the combined sequential–nonsequential channel (0–1–3) starts to exceed the (0–3) channel leading to a momentum distribution which may exhibit up to four maxima since both channels are of the same magnitude. However, the width of the individual maxima cannot be predicted on the basis of purely classical considerations and, hence, this structure may be washed out. As the intensity increases further, the (0–3) contribution vanishes relative to the other channels. Above the second 'knee' the purely sequential channel (0–1–2–3) exceeds the (0–1–3) channel and a corresponding maximum

appears at zero momentum. Finally, in the purely sequential regime the momentum distribution is dominated by the (0–1–2–3) channel with a single maximum at zero momentum. Up to now only the momentum distribution of Ne^{3+} has been measured in the (0–3) regime [9]. How the shape of the momentum distribution evolves quantitatively with increasing intensity is not known, since no experimental or theoretical data are available at the moment. The momentum distributions should depend strongly on the cross section of the (e, *n*e) collision as well as on the division of the excess energy between the ejected electrons.

Finally, we will discuss the limits of the classical rescattering model. One important point is the existence of a threshold intensity which has not been observed experimentally. This limitation is a result of the classical treatment of the laser field in combination with tunnel ionization, i.e. the assumption that the electron appears in the continuum for single ionization with zero initial momentum. In a quantum-mechanical description (e.g. as in [5]) the absorption of a corresponding number of photons by the first ionized electron provides the energy needed for double (or multiple) ionization. This demonstrates nicely the transition from the classical-field regime to the multi-photon regime with decreasing intensity and it explains the ion yield below the threshold which is out of the scope of the classical model. In this context the relevance of target excitation also has to be mentioned, since the rescattering mechanism can also lead to exited target states which are then sequentially field-ionized. Another limitation of a simple classical model is the fact that no details of an (e, *n*e) process in the presence of a laser field are included except the kinematical constraints which are simply based on the conservation of energy and momentum. Nevertheless, the classical rescattering model allows us to understand the observed ion momentum distributions and is strongly supported by recent time-dependent quantum calculations [17, 18].

To conclude, we have used the classical rescattering model to obtain kinematical constraints for ion momentum distributions following *multiple* ionization of atoms by intense laser fields. It is shown that different ionization channels (nonsequential, sequential and combinations of them) can be characterized by the kinematical constraints for the ion momenta. For nonsequential production of Ne^{2+} and Ne^{3+} ions at an intensity of $\simeq$ 1 PW cm^{-2} these constraints reproduce positions of the maxima observed in previous experimental momentum distributions. At higher intensities the contribution of more than one multiple ionization channel may lead to more complex ion momentum distributions. A comparison of this prediction with experiment and more sophisticated theories has to wait for future investigations in this field. We hope that this work based on a very simple model will stimulate further experimental and theoretical studies on the intensity dependence of strong-field multiple ionization.

This work was supported by the Leibniz-Programm of the Deutsche Forschungsgemeinschaft. We would like to thank W Becker and R Kopold for fruitful discussions.

References

[1] L'Huillier A, L'Lompre A, Mainfray G and Manus C 1983 *Phys. Rev.* A **27** 2503
[2] Fittinghoff D N, Bolton P R, Chang B and Kulander K D 1992 *Phys. Rev. Lett.* **69** 2642
[3] Corkum P B 1993 *Phys. Rev. Lett.* **71** 1994
[4] Kulander K C, Cooper J and Schafer K J 1995 *Phys. Rev.* A **51** 561
[5] Becker A and Faisal F H M 1996 *J. Phys. B: At. Mol. Opt. Phys.* **29** L197
[6] Becker A and Faisal F H M 1999 *Phys. Rev.* A **59** R3182 and references therein
[7] Eichmann U, Dörr M, Maeda H, Becker W and Sandner W 2000 *Phys. Rev. Lett.* **84** 3550
[8] Weber Th, Weckenbrock M, Staudte A, Spielberger L, Jagutzki O, Mergel V, Urbasch G, Vollmer M, Giessen H and Dörner R 2000 *Phys. Rev. Lett.* **84** 443

[9] Moshammer R, Feuerstein B, Schmitt W, Dorn A, Schröter C D, Ullrich J, Rottke H, Trump C, Wittmann M, Korn G, Hoffmann K and Sandner W 2000 *Phys. Rev. Lett.* **84** 447
[10] Weber Th, Weckenbrock M, Staudte A, Spielberger L, Jagutzki O, Mergel V, Afaneh F, Urbasch G, Vollmer M, Giessen H and Dörner R 2000 *J. Phys. B: At. Mol. Opt. Phys.* **33** L127
[11] Weber Th *et al* 2000 *Nature* **405** 658
[12] Becker A and Faisal F H M 1999 *J. Phys. B: At. Mol. Opt. Phys.* **32** L335
[13] Delone N B and Krainov V P 1991 *J. Opt. Soc. Am.* B **8** 1207
[14] Paulus G G, Becker W, Nicklich W and Walther H 1994 *J. Phys. B: At. Mol. Opt. Phys.* **27** L703
[15] Ehrhardt H, Jung K, Knoth G and Schlemmer P 1986 *Z. Phys.* D **1** 3
[16] Becker A and Faisal F H M 2000 *Phys. Rev. Lett.* **84** 3546
[17] Lein M, Gross E K U and Engel V 2000 *J. Phys. B: At. Mol. Opt. Phys.* **33** 433
[18] Dörr 2000 *Opt. Express* **6** 111

Separation of Recollision Mechanisms in Nonsequential Strong Field Double Ionization of Ar: The Role of Excitation Tunneling

B. Feuerstein,[1] R. Moshammer,[1,2] D. Fischer,[1] A. Dorn,[2] C. D. Schröter,[2] J. Deipenwisch,[1]
J. R. Crespo Lopez-Urrutia,[1] C. Höhr,[1] P. Neumayer,[3] J. Ullrich,[1,2]
H. Rottke,[4] C. Trump,[4] M. Wittmann,[4] G. Korn,[4] and W. Sandner[4]

[1]*Universität Freiburg, Hermann-Herder-Strasse 3, D-79104 Freiburg, Germany*
[2]*Max-Planck-Institut für Kernphysik, Saupfercheckweg 1, D-69117 Heidelberg, Germany*
[3]*Gesellschaft für Schwerionenforschung (GSI), D-64291 Darmstadt, Germany*
[4]*Max-Born-Institut, Max-Born-Strasse 2a, D-12489 Berlin, Germany*

(Received 5 April 2001; published 9 July 2001)

Vector momentum distributions of two electrons created in double ionization of Ar by 25 fs, 0.25 PW/cm^2 laser pulses at 795 nm have been measured using a "reaction microscope." At this intensity, where nonsequential ionization dominates, distinct correlation patterns are observed in the two-electron momentum distributions. A kinematical analysis of these spectra within the classical "recollision model" revealed an $(e, 2e)$-like process and excitation with subsequent tunneling of the second electron as two different ionization mechanisms. This allows a qualitative separation of the two mechanisms demonstrating that excitation-tunneling is the dominant contribution to the total double ionization yield.

DOI: 10.1103/PhysRevLett.87.043003 PACS numbers: 32.80.Rm, 31.90.+s, 32.80.Fb

Since the first observation of surprisingly high ion yields in double and multiple ionization in strong, linearly polarized laser pulses more than 15 years ago [1] many-electron dynamics in intense laser fields has been the subject of a large number of theoretical and experimental investigations (for a review, see [2]). Considering that theoretical predictions based on the "single active electron" model, assuming sequential ionization of independent electrons, fail by many orders of magnitude, it was agreed that a "nonsequential" (NS) ionization mechanism has to incorporate the correlated dynamics of two (or more) electrons in the strong laser field.

Experimental imaging techniques [3], combined with recent progress in laser development, succeeded in measuring momentum distributions of multiply charged ions for He [4], Ne [5], and Ar [6]. It was shown that mechanisms based on an instantaneous release of two (or more) electrons at a phase where the field maximizes, such as "shakeoff" [7] or "collective tunneling" [8], can be ruled out as a dominant contribution to NS double ionization. Whereas these processes lead to an ion momentum distribution along the laser polarization axis peaking at zero, the observed spectra exhibit distinct maxima at nonzero momenta [4,5]. The positions of these maxima are in accord with kinematical constraints set by the classical "rescattering model" [5,9] which was originally proposed by Corkum [10] eight years ago. In this model the first ionized electron is driven back by the oscillating laser field to its parent ion causing the ionization of a second electron in an $(e, 2e)$-like process. The experimental results settled the controversial debate on the mechanisms responsible for NS multiple ionization and stimulated a series of theoretical papers [11–14], which all include the $(e, 2e)$ recollision mechanism and, thus, support the widely accepted evidence that rescattering dominates multiple ionization in the intensity regimes investigated.

Since ion momentum distributions alone do not give complete information on the $(e, 2e)$ process during recollision, the interest focused on the correlation of the electrons emitted by an atom in the strong laser field. Very recently, coincident momentum distributions of two electrons have been determined for double ionization of Ar [15]. The investigation of strong-field double ionization of argon is of special interest because a systematic experimental study of the intensity dependence of the ion momentum distributions along the laser polarization axis for an intensity range from 0.2 to 2 PW/cm^2 [6] revealed distinct differences in the shape of these distributions compared to theoretical predictions either based on simple classical considerations [9] or on recent quasiclassical calculations [11,13]. Instead of a double-peak structure which should become more pronounced with decreasing laser intensity the observed distributions show only one broad peak around zero momentum. A similar behavior was found for He [4].

The observation that the minimum between the two peaks is filled with decreasing laser intensity is closely related to the question of a threshold intensity where the maximum kinetic energy of the rescattered electron becomes equal to the ionization potential of the singly charged ion. Experimentally, no such threshold effect has ever been observed. In contrast to a classical approach the quantum-mechanical description avoids the problem of a threshold intensity: the absorption of a corresponding number of photons by the first ionized electron provides the energy needed for double ionization. Indeed, a "sawtooth structure" appears in the calculated ion momentum distributions at intensities below the classical threshold (Fig. 2 of [13]) which reflects the discrete energy transfer

from the laser field to the atom and demonstrates nicely the transition from the classical-field regime to the multiphoton domain. It has been pointed out repeatedly [9,13,15] that electron impact excitation during the recollision with subsequent electric field (tunnel) ionization of the excited electron may also contribute significantly to double ionization. This has been already demonstrated for He in a recent semiquantitative calculation [16]. Because of its sequential nature the excitation-tunneling mechanism tends to fill up the minimum in the momentum distribution.

In order to clarify this question we present a detailed kinematical analysis on the correlated electron momenta for argon double ionization at an intensity of 0.25 PW/cm^2. It will be demonstrated that a kinematically complete experiment allows one to identify and separate contributions from two types of recollision mechanisms—$(e,2e)$ and excitation tunneling.

The experiments were performed at the Max-Born-Institut in Berlin using pulses of a Kerr-lens mode locked Ti:sapphire laser at 795 nm wavelength amplified to pulse energies up to 500 μJ at 1 kHz repetition rate. The width of the amplified pulses was 25 fs.

Focused by a spherical on-axis mirror ($f = 100$ mm) to a spot size of 10 μm diameter (FWHM) in an ultrahigh vacuum chamber (7×10^{-11} mbar), it was possible to achieve pulse peak intensities of up to 25 PW/cm^2. Intensity fluctuations were controlled throughout the experiment and kept below 5%. The laser beam was focused on a low-density (10^8 atoms/cm^3) supersonic Ar jet which was collimated to a rectangular shape of 0.2×4 mm^2 at the focal spot. The wide side of the jet was oriented perpendicular with respect to the laser beam thus yielding an overlap volume between laser beam and Ar jet of 200 μm length and 10 μm diameter.

Vector momenta of ions and electrons emerging from the source volume were recorded using a "reaction microscope" which has been described in detail before [17]. All electrons with transverse energies below 30 eV and longitudinal energies below 15 eV were detected with 4π solid angle of acceptance. The ion momentum resolution along the jet expansion axis was limited by the internal jet temperature to 0.3 a.u. Transverse to the jet axis a resolution of 0.1 a.u. was achieved due to collimation of the atomic beam. In order to ensure that electrons and ions detected in each laser shot emerged from the same atom, the target and rest gas densities had to be low enough to have less than one ionization event per laser pulse occurring.

The final momentum $\vec{p}_{\mathrm{final}}$ of an electron emitted from an atom in a strong, linearly polarized laser pulse is the sum of the drift momentum $\vec{p}_{\mathrm{drift}}$ due to the acceleration in the field and the initial momentum $\vec{p}_{\mathrm{initial}}(t_1)$ of the electron starting at time t_1. The drift momentum depends on the phase $\phi = \omega t_1$ where the electron was born in the oscillating electric field $\vec{E}(t) = \vec{E}_0(t)\sin(\omega t)$ through $\vec{p}_{\mathrm{drift}} = \omega^{-1}\vec{E}_0(t_1)\cos(\omega t_1)$. After an $(e,2e)$ process during recollision both electrons receive the same drift momentum. The initial momenta $\vec{p}^{\,(1)}_{\mathrm{initial}}$, $\vec{p}^{\,(2)}_{\mathrm{initial}}$ of the two electrons depend on the dynamical parameters of the $(e,2e)$ process itself, i.e., on the excess energy of the recolliding electron, energy sharing, and the emission angles. Thus, the $(e,2e)$ final two-particle momentum state just after the recollision is simply shifted by $\vec{p}_{\mathrm{drift}}$ for each of the electrons yielding the finally observed correlated two electron momentum patterns. Since only the momentum components $p_1^{\parallel}$, $p_2^{\parallel}$ parallel to the polarization direction are affected by acceleration in the laser field, the perpendicular components $p_1^{\perp}$, $p_2^{\perp}$ remain unchanged directly reflecting the $(e,2e)$ dynamics. This also holds true for the momentum difference $\vec{p}_- = \vec{p}_1 - \vec{p}_2$ since the identical drift momenta cancel each other [15].

We now consider the correlated electron momentum spectra for the parallel component. Because of energy conservation we get for a given phase ωt_1 as kinematically allowed regions two circles with radius $\sqrt{2E_{\mathrm{exc}}}$ centered on the diagonal with equal drift momenta $\vec{p}_{\mathrm{drift}}(t_1)$ as illustrated in Fig. 1(a). Here, E_{exc} is the excess energy of the $(e,2e)$ process. Superposition of the circles for all phases where the energy of the recolliding electron exceeds the ionization potential of the singly charged ion leads to the kinematical constraints for the $(e,2e)$ reaction (solid line in Fig. 2). This classical domain has been found also in a recent quasiclassical calculation by Goreslavski and Popruzhenko [11].

In Fig. 2 the parallel momentum correlation spectrum is presented for electron pairs emitted from an Ar atom during a 0.25 PW/cm^2 laser pulse. The large portion of events outside the $(e,2e)$-allowed regime now leads us to the excitation-tunneling model. Again, the observed electron momenta consist of the drift momentum and the initial momentum but, in contrast, now the electrons start at different times t_1 (recollision) and t_2 (tunneling) and, thus, gain different drift momenta. The first, recolliding electron excites its parent ion yielding an initial momentum $|\vec{p}_1(t_1)| = \sqrt{2E_{\mathrm{exc}}}$. The second, excited electron subsequently tunnels at a time t_2 and receives only drift momentum since the initial momentum for tunneling can be neglected.

Based on this scenario we can now derive the kinematical constraints for the correlated parallel electron momenta. For a given phase ωt_1 the final momentum of the recolliding electron is restricted by $p_{\mathrm{drift}}(\omega t_1) - \sqrt{2E_{\mathrm{exc}}(t_1)} \le p^{\parallel}_{\mathrm{final}}(t_1) \le p_{\mathrm{drift}}(\omega t_1) + \sqrt{2E_{\mathrm{exc}}(t_1)}$, whereas the momentum of the second, tunneling electron is limited by $p^{\parallel}_{\mathrm{final}}(t_1) \le p^{\mathrm{max}}_{\mathrm{drift}} = 2\sqrt{U_P}$ with an expected maximum at $p^{\parallel}_{\mathrm{final}} = 0$. Here, $U_P = I/4\omega^2$ is the ponderomotive potential which corresponds to the mean quiver energy of an electron in the laser field with intensity I. The kinematically allowed region [shown in Fig. 1(b)] now has a rectangular shape and occurs fourfold due to the two half cycles of the laser field yielding opposite drift

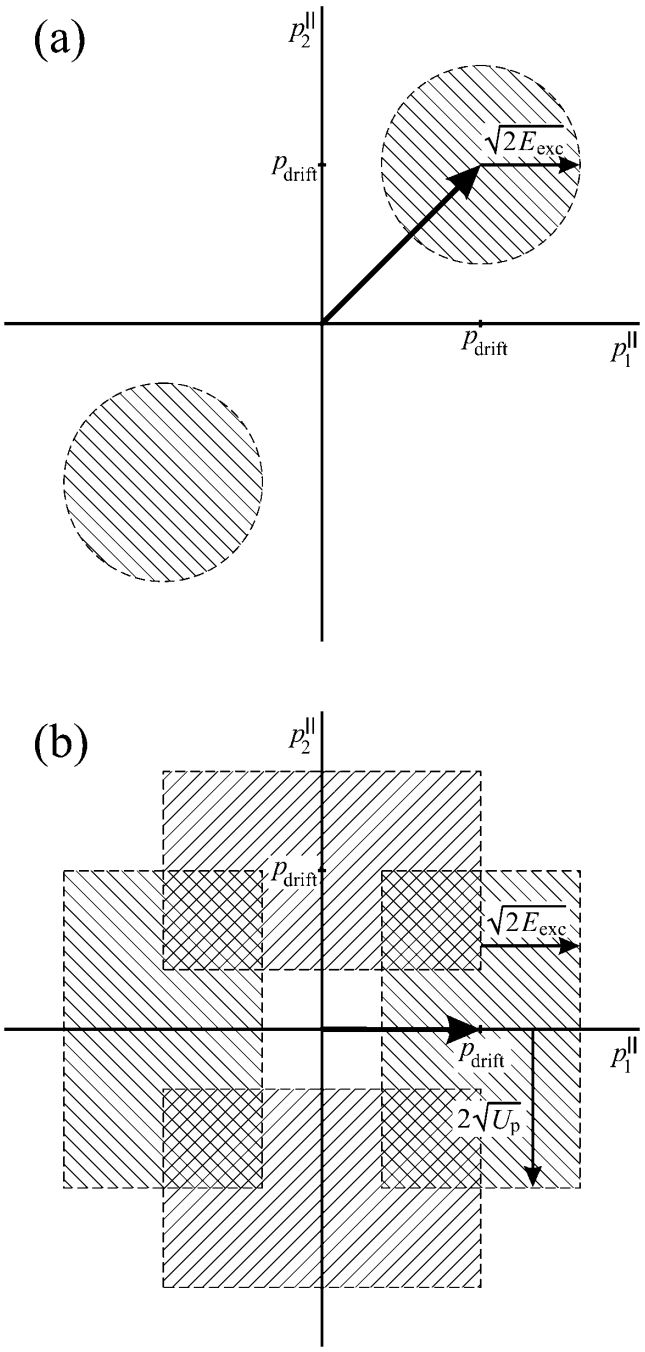

FIG. 1. Kinematically allowed regions (shaded areas) for the correlated electron momentum components $p_1^{\parallel}$, $p_2^{\parallel}$ parallel to the laser polarization axis. (a) Recollision $(e, 2e)$ process. (b) Recollision excitation with subsequent tunneling. See text for details.

momenta and due to the indistinguishability of the electrons. Superposition of these areas for all phases where the recollision energy exceeds the necessary excitation energy gives the total kinematically allowed region for the excitation-tunneling mechanism. Figure 2 illustrates that these kinematical constraints (dashed line) are in excellent accord with the experimental data. Of special interest is the symmetry of the correlation patterns for the two double

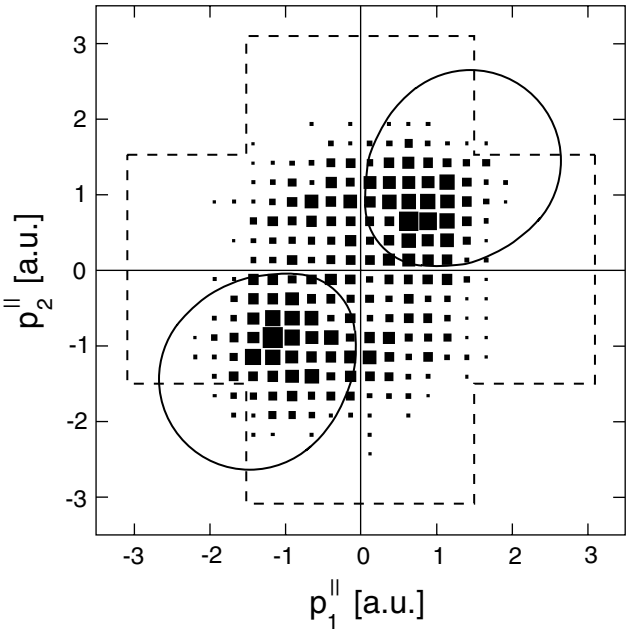

FIG. 2. Correlated electron momentum spectrum of two electrons emitted from Ar atoms at 0.25 PW/cm^2 for the parallel components $p_1^{\parallel}$, $p_2^{\parallel}$. The superposition of the kinematical constraints for all phases is shown for the recollision $(e, 2e)$ process (solid line) and for recollision excitation with subsequent tunneling (dashed line), respectively.

ionization mechanisms. Because of the fact that the electrons cannot be distinguished and the laser field defines only an alignment but not an orientation the correlation pattern for $p_1^{\parallel}$, $p_2^{\parallel}$ is symmetric with respect to both diagonals. In the case of the excitation-tunneling mechanism an additional symmetry with respect to the coordinate axes occurs because of the subsequent, independent emission of the electrons. For the $(e, 2e)$ mechanism this symmetry is broken due to the fact that both electrons acquire the same drift momentum.

Now, we discuss the filling of the "valley" in the ion momentum distribution parallel to the laser polarization direction. In the $p_1^{\parallel}$, $p_2^{\parallel}$ correlation spectrum the events due to the $(e, 2e)$ process are found only in the first and third quadrants. Based on the symmetry discussed above it is possible to obtain the full correlation pattern for the excitation-tunneling mechanism from the data in the second and fourth quadrants. This allows us to separate both mechanisms by subtracting the corresponding number of excitation-tunneling events from the measured number of all events in the first and third quadrants. Projection of the correlation pattern on the main diagonal gives the distribution for the parallel sum momentum $p_+^{\parallel} = p_1^{\parallel} + p_2^{\parallel}$, which reflects the parallel momentum spectrum of the doubly charged ions. Figure 3 shows these spectra separately for the different mechanisms. The $(e, 2e)$ process alone now leads to two clearly separated maxima close to the ion drift momentum of $4\sqrt{U_P}$, which is indicated

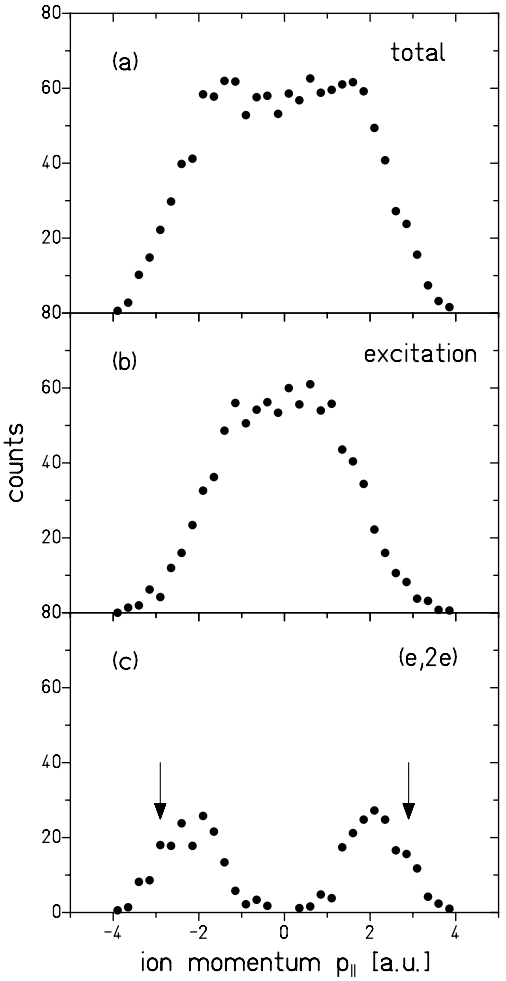

FIG. 3. Separation of the contributions of recollision ionization and excitation to the ion momentum distributions parallel to the laser polarization axis. Total ion momentum spectrum (a), recollision excitation with subsequent tunneling (b), and recollision $(e, 2e)$ process (c). The drift momentum $4\sqrt{U_P}$ for doubly charged ions is indicated by the arrows.

by the arrows. This is in good accord with our previous predictions based on simple classical considerations [9], as well as with recent quasiclassical calculations [11,13]. The second (excitation-tunneling) mechanism gives a single peak around zero momentum which dominates the total ion yield. Thus, the valley between the $(e, 2e)$ peaks is filled leading to the observed broad structure in the ion momentum distribution.

Finally, one may ask why the excitation mechanism in Ar at 0.25 PW/cm^2 is much more pronounced compared to Ne at 1.0 PW/cm^2 [5]. The reason may be twofold. First, the intensity normalized to the ionization potential is lower for Ar^+ ($I_P = 1.01$ a.u.) than for Ne^+ ($I_P = 1.51$ a.u.). Thus, the phase range where the recollision energy exceeds I_P is reduced for Ar. Moreover, excitation and ionization by electron impact differ in their behavior at low impact energies. Whereas the ionization cross section approaches zero at threshold excitation may become increasingly probable. Second, $3p$-$3d$ excitations occur in Ar with large cross sections which are missing in Ne. The so-called "collapse" of the $3d$ orbital gives rise to large overlap with the $3p$ orbital yielding in very strong $3p$-$3d$ transitions which exceed the oscillator strength of $3p$-$4s$ transitions by a factor of 4 [18].

In conclusion, using a kinematical analysis of two-electron momentum correlation patterns for nonsequential double ionization of Ar in 0.25 PW/cm^2 laser pulses we are able to separate two different double ionization mechanisms. Both are based on the recollision of the first ionized electron with its parent ion core. In addition to the $(e, 2e)$ mechanism we identified excitation of the parent ion during the recollision with subsequent tunnel ionization of the excited electron as a second, dominant mechanism. This model explains the shape of observed ion momentum distributions and demonstrates the importance of excitation tunneling for nonsequential double ionization of Ar.

The experiments were supported by the Leibniz-Program of the Deutsche Forschungsgemeinschaft DFG. Support from GSI is gratefully acknowledged. We thank R. Dörner and W. Becker for fruitful discussions.

[1] A. L'Huiller, A. L'Lompre, G. Mainfray, and C. Manus, Phys. Rev. A **27**, 2503 (1983).
[2] L. F. DiMauro and P. Agostini, Adv. At. Mol. Opt. Phys. **35**, 79 (1995).
[3] J. Ullrich *et al.,* J. Phys. B **30**, 2917 (1997); R. Dörner *et al.,* Phys. Rep. **330**, 96 (2000).
[4] Th. Weber *et al.,* Phys. Rev. Lett. **84**, 443 (2000).
[5] R. Moshammer *et al.,* Phys. Rev. Lett. **84**, 447 (2000).
[6] Th. Weber *et al.,* J. Phys. B **33**, L127 (2000).
[7] D. N. Fittinghoff, P. R. Bolton, B. Chang, and K. C. Kulander, Phys. Rev. Lett. **69**, 2642 (1992).
[8] U. Eichmann *et al.,* Phys. Rev. Lett. **84**, 3550 (2000).
[9] B. Feuerstein, R. Moshammer, and J. Ullrich, J. Phys. B **33**, L823 (2000).
[10] P. B. Corkum, Phys. Rev. Lett. **71**, 1994 (1993).
[11] S. P. Goreslavski and S. V. Popruzhenko, Opt. Express **8**, 395 (2001).
[12] A. Becker and F. H. M. Faisal, Phys. Rev. Lett. **84**, 3564 (2000).
[13] R. Kopold, W. Becker, H. Rottke, and W. Sandner, Phys. Rev. Lett. **85**, 3781 (2000).
[14] M. Lein, E. K. U. Gross, and V. Engel, Phys. Rev. Lett. **85**, 4707 (2000).
[15] Th. Weber *et al.,* Nature (London) **405**, 658 (2000).
[16] H. van der Hart, J. Phys. B **33**, L699 (2000).
[17] R. Moshammer *et al.,* Nucl. Instrum. Methods Phys. Res., Sect. B **108**, 425 (1996).
[18] A. Hibbert and J. E. Hansen, J. Phys. B **27**, 3325 (1994).

Correlated two-electron dynamics in strong-field double ionization

R. Moshammer,[1,*] B. Feuerstein,[2] J. Crespo López-Urrutia,[1] J. Deipenwisch,[1] A. Dorn,[1] D. Fischer,[1] C. Höhr,[1] P. Neumayer,[3] C. D. Schröter,[1] J. Ullrich,[1] H. Rottke,[4] C. Trump,[4] M. Wittmann,[4] G. Korn,[4] and W. Sandner[4]

[1]*Max-Planck-Institut für Kernphysik, Saupfercheckweg 1, D-67119 Heidelberg, Germany*

[2]*Universität Freiburg, Hermann-Herder Strasse 3, D-79104 Freiburg, Germany*

[3]*Gesellschaft für Schwerionenforschung GSI, D-64291 Darmstadt, Germany*

[4]*Max-Born-Institut, Max-Born-Strasse 2a, D-12489 Berlin, Germany*

(Received 08 October 2001; published 11 February 2002)

Vector momenta of electrons and ions have been measured for strong-field (25 fs, 0.25 to 1.0 PW/cm^2) double ionization of Ar using a ''reaction microscope.'' Correlated two-electron momentum distributions along the field direction ($P_{1\|}, P_{2\|}$) are explored at different transverse momenta $P_{1\perp}$ of one of the electrons. Whereas a distinct ($P_{1\|}, P_{2\|}$) correlation, strongly varying with $P_{1\perp}$ is observed for nonsequential double ionization at small light intensity, only a weak, but still significant correlation is found at large intensity where sequential ionization dominates.

DOI: 10.1103/PhysRevA.65.035401 PACS number(s): 32.80.Rm, 31.90.+s, 32.80.Fb

A profound knowledge of many-electron dynamics in intense, femtosecond laser fields interacting with single atoms or molecules is basic and indispensable for our understanding of laser-matter interactions in general and, thus, for a large variety of present and future application. Among them are high-order harmonic generation, acceleration of electrons and ions, strong-field induced fusion or the realization of intense table-top x-ray sources. Theoretically, this requires a consistent quantum description of the time-dependent correlated motion of several electrons in the combined fields of the laser light and of the ionic core on a subfemtosecond time scale, i.e., for times that are short compared to one optical cycle of a typical laser pulse. Experimentally, the ultimate goal would be to trace the electronic dynamics on such short time scales, which has not been feasible up to now, leaving this domain completely unexplored.

The development of multielectron-ion imaging techniques [1] and their successful combination with femtosecond laser systems with kilohertz pulse-repetition rates enabled first single-differential measurements on strong-field multiple ionization of He [2,3], Ne [4], Ar [5], and Xe [6]. Surprisingly, the determination of ion recoil momenta alone already settled a 15-yr controversial debate on the mechanisms responsible for nonsequential (NS) double ionization and stimulated a series of theoretical papers: Only the ''rescattering model'' proposed by Corkum [7] eight years ago was found to be kinematically consistent with experimental-ion momentum distributions [4,8]. Recent theoretical *S*-matrix results [9–12], various numerical time-dependent two-electron quantum calculations [13,14] as well as predictions based on classical dynamics [15] all obtain the experimentally observed, characteristic double-peak structure in the recoil-ion momentum along the polarization direction $P_{R\|}$. Thus, they all provide strong evidence that rescattering dominantly contributes to NS multiple ionization in the intensity-regimes investigated.

Though being generally accepted that rescattering is the leading mechanism at intermediate intensities, the various calculations strongly disagree among each other in predicting the details of the underlying dynamics, i.e., of the electron-impact-ionization $(e,2e)$ kinematics in the presence of the field. Moreover, none of them is in quantitative agreement with first experimental results for argon double ionization [16]. Here, the correlated electron-momentum distributions along the field direction of the linear polarized light were found to be strongly peaked for emission of the two electrons in the same direction with a significant contribution of back-to-back scattered electrons.

Whereas all three-dimensional (3D) *S*-matrix calculations [10–12] do predict the unidirectional emission of the electrons at moderate light intensities, none of them can account for back-to-back ejection of the two electrons [16]. Moreover, even the details for unidirectionally emitted electrons differ strongly in the various 3D models. One of them, based on a Coulomb form factor for the $(e,2e)$ scattering process, predicts strongly asymmetric energy (momentum) sharing between the two electrons [10,12]. The other one, assuming a hard-core contact potential for the electron-electron interaction, on the other hand yields symmetric longitudinal momentum sharing [11,13].

Thus, in essence, though rescattering as being the trigger for multiple NS double ionization seems to be out of question, the details of the electron-scattering dynamics, i.e., of the $(e,2e)$ kinematics in the presence of the electric field are far from being well understood and remain the subject of intense debate.

In a previous paper [17] we have shown for 0.25 PW/cm^2, 25-fs light pulses interacting with an argon target, that back-to-back emitted electrons may consistently be interpreted as being due to excitation during rescattering [18] at a phase where the electric field is small with subsequent and independent field (tunnel) ionization of the second electron. Within the assumptions of the model [classical $(e,2e)$ dynamics without energy exchange with the light wave during recollision] both processes may be separated experimentally,

*Email address: R.Moshammer@mpi-hd.mpg.de

leaving us now with the question on the correlated dynamics of unidirectionally emitted electrons.

In this paper, we present differential experimental information on correlated electron-momentum spectra in the longitudinal direction for unidirectionally emitted electrons as a function of one-electron's transverse momentum, shedding light on the details of the correlated electronic motion in the field and providing benchmark data for theory. Strong effects are observed in that an asymmetric sharing of the longitudinal momenta is favored if the transverse momentum space is restricted. Surprisingly, a weak though significant correlation is also found at an increased light intensity where sequential double ionization is expected to dominate. Recently, similar results were reported by Weckenbrock *et al.* for 150-fs laser pulses [20].

The experiments were performed at the Max-Born-Institut in Berlin using a Kerr-lens mode-locked Ti sapphire laser at 795-nm central wavelength. The laser pulses were amplified at 1 kHz repetition rate up to pulse energies of 500 μJ and focused by an on-axis spherical mirror ($f=100$ mm) to a spot of ≈ 10 μm diameter (full width at half maximum) within an ultrahigh vacuum chamber (base pressure less than 7×10^{-11} mbar). The pulse peak intensity was adjusted in the range between 0.25 and 1.0 PW/cm^2. Intensity fluctuations were controlled throughout the experiment and kept below 5%.

The laser beam was focused on a low density (10^8 atom/cm^3) supersonic gas jet formed by expanding Ar at a stagnation pressure of 5 bar through a cooled, 10-μm-diam nozzle. The beam was collimated over a total path of 2 m to a rectangular shape of 0.2×4 mm^2 at the focal spot, oriented with the broad side perpendicular to the laser beam. This yielded an overlap volume between laser beam and argon jet of 200 μm in length and 10 μm in diameter.

Vector momenta of ions and electrons emerging from the source volume were recorded using a ''reaction microscope'' that has been described in detail before [19]. Low-energy ions and electrons are accelerated in opposite directions by a 1-V/cm electric field applied perpendicular with respect to the propagation directions of the laser as well as the atomic beam and parallel to the laser-polarization direction. The transverse motion of the electrons is confined by an additional homogeneous solenoidal magnetic field. In this way all electrons with transverse energies smaller than 50 eV and longitudinal energies below 15 eV are guided onto a 75-mm-diam two-dimensional position-sensitive microchannel plate detector placed 20 cm away from the reaction volume. From the measured absolute positions and flight times the ion and electron trajectories are reconstructed and their initial momenta are calculated. For the electrons a momentum resolution in transverse and longitudinal directions of 0.05 a.u. is achieved. The ion-momentum resolution in the direction of the jet expansion is limited by the internal jet temperature to 0.3 a.u. Transverse to the jet expansion a resolution of 0.1 a.u. is achieved due to collimation of the jet.

In Fig. 1 the correlated two-electron longitudinal momentum spectrum is shown for argon double ionization at a power density of 0.25 PW/cm^2, where nonsequential ionization dominates. In this plot, which has been published before

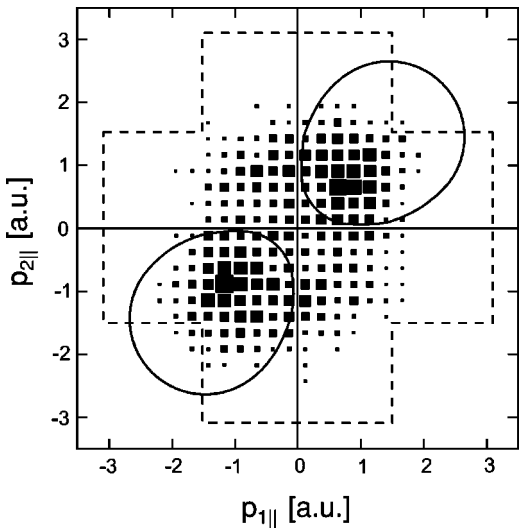

FIG. 1. Longitudinal momentum of electron one ($P_{1\|}$) versus that of electron two ($P_{2\|}$) for Ar double ionization by 25-fs laser pulses at a peak intensity of 0.25 PW/cm^2. Box sizes correspond to the intensity on a linear scale between zero and maximum intensity. Full line: borderline for (e,2e) kinematics. Dashed line: borderline for excitation-tunneling events (see also Ref. [17]).

[17], the longitudinal electron momenta are presented without any further restriction on the other momentum components. As discussed, a significant correlation is observed: Preferentially the two electrons are emitted into the same direction having both either positive or, equivalently, negative momenta of similar magnitude. Here, at relatively low light intensity, a kinematical analysis within the conditions described in Ref. [17] demonstrated, that events due to (e,2e) ionization during rescattering are exclusively restricted to unidirectional emission of the two electrons into the area surrounded by the solid line. Excitation during rescattering followed by tunnel ionization of the second electron, instead, allow for two-electron momenta inside the area indicated by the broken lines.

In order to explore the electronic motion during rescattering in more detail we have plotted the correlated electron momenta for unidirectional emission, where the (e,2e) events occur, under the additional condition that the transverse momentum of one electron ($P_{1\perp}$) is either larger or smaller than 0.5 a.u. (Fig. 2). This splits the total number of events into two contributions of about identical size.

Distinct differences are found. If the transverse momentum of electron ''one'' is large $P_{1\perp}\geqslant0.5$ a.u., the correlation in the longitudinal electronic motion becomes even more pronounced [Fig. 2(a)]. Unequal momentum sharing is widely suppressed and the electrons most likely emerge with quite similar final momenta along the diagonal in the two-dimensional plot. Therefore, both electrons must have been created with similar or very small momentum components $P_{1\|}$,$P_{2\|}$ at the same phase in the light wave and, thus, have received similar drift momenta after their creation.

This tendency might be understood within the rescattering model assuming energy conservation $P_{1\|}^2+P_{2\|}^2+P_{1\perp}^2+P_{1\perp}^2=2(E_0-I_p)$ during recollision (E_0: energy of the returning

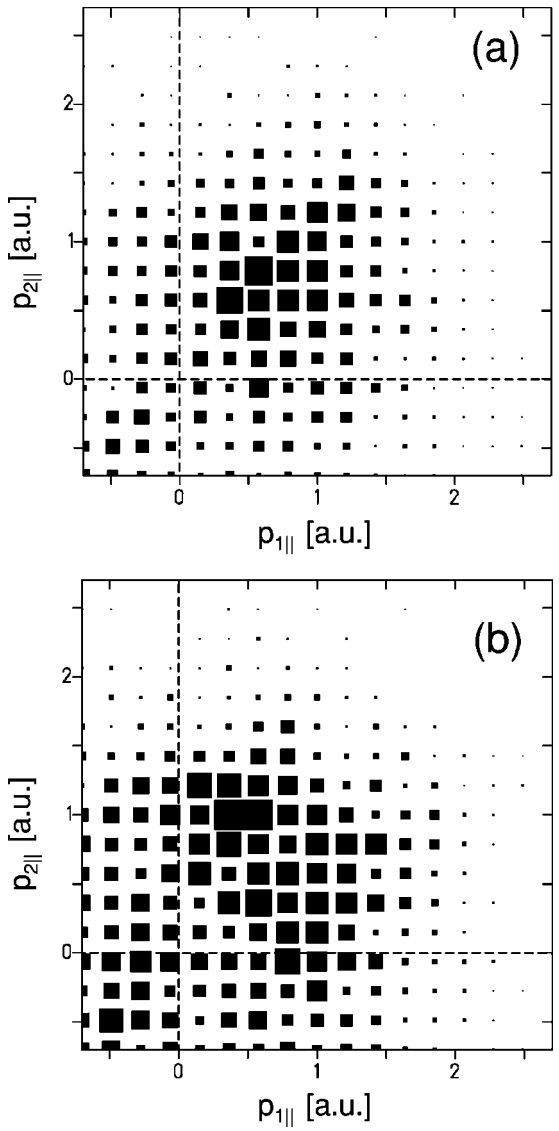

FIG. 2. Enlarged view of the uppermost right-hand part of Fig. 1 with additional conditions on the transverse momentum of electron "one:" (a) $P_{1\perp} \geqslant 0.5$ a.u. and (b) $P_{1\perp} \leqslant 0.5$ a.u.

electron; $I_p = 27.62$ eV: ionization potential of Ar). In a field-free $(e,2e)$ collision at moderate E_0, "binary collisions" between the electrons would dominate for significant transverse momentum transfer to one of them ($P_{1\perp} \geqslant 0.5$ a.u.), leaving the second one with a similar $P_{2\perp} \geqslant 0.5$ a.u. Consequently, this reduces the kinematically allowed regime for the longitudinal momenta from $P_{1\|}^2 + P_{2\|}^2 = 2(E_0 - I_p) = 1.47$ a.u. for $P_{1\perp} = P_{2\perp} = 0$ at maximum $E_0 = 3.17U_p$ to $P_{1\|}^2 + P_{2\|}^2 \leqslant 0.97$ a.u. for $P_{1\perp}$, $P_{2\perp} \geqslant 0.5$ a.u. (U_P is the ponderomotive potential). Thus, a significantly reduced, still quite large momentum spread between the two electrons in the longitudinal direction remains possible and asymmetric sharing is expected from field-free $(e,2e)$ dynamics. This is definitely not observed experimentally [Fig. 2(a)]. Assuming further that $P_{1\|}^2 \approx P_{2\|}^2$, which might be justified at small excess energies, finally leads to similar longitudinal electron momenta of less than 0.7 a.u., Depending on

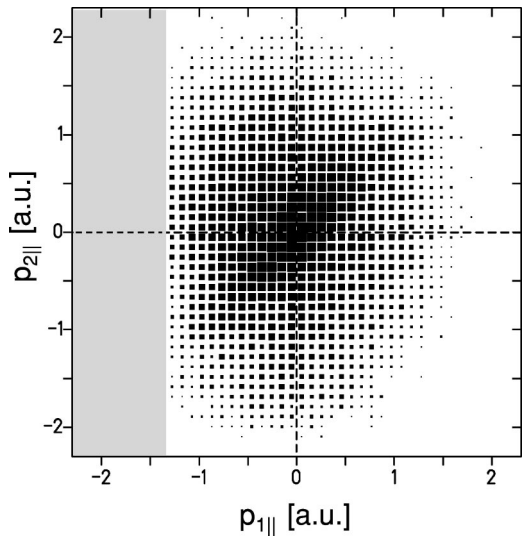

FIG. 3. Same as Fig. 1 for an intensity of 1.0 PW/cm^2. Shaded area indicates a region of no acceptance for electron "one."

the recollision phase in the oscillating field, both electrons would then acquire nearly identical drift momenta of less than 1.5 a.u. each, in qualitative agreement with the experimental data.

Obviously, the Coulomb repulsion between the two electrons in the longitudinal direction is strongly suppressed and quite similar momenta do occur if comparably large relative momenta of the electrons in the second, i.e., in the transverse dimension, are admitted. Thus, one-dimensional calculations will never be able to give longitudinal momentum distributions in agreement with the experimental data. In essence, they predict zero intensity for equal momentum sharing, i.e., along the diagonals in Figs. 1 and 2 at a light intensity comparable with the one used here [13,14]. Clearly, the deficiency of such models lies in their reduced dimensionality resulting in a strong overestimation of the electron-electron repulsion. As a consequence, equal longitudinal electron momenta are strictly forbidden if they are created in a rescattering event at identical phase.

If small transverse momenta of electron "one" $P_{1\perp} \leqslant 0.5$ a.u. are selected instead, i.e., if the two-electron phase space in the second dimension is reduced, the $(P_{1\|}, P_{2\|})$ pattern changes significantly [Fig. 2(b)]. Unequal momentum sharing is strongly favored now, with typical momenta around 1 a.u. for one and 0.5 a.u. for the other electron. This behavior is well known from field-free $(e,2e)$ dynamics, where unequal energy sharing dominantly contributes to the cross section at small scattering angles of the projectile electron. In the rescattering scenario, the impinging electron is little deflected and only looses a small part of its longitudinal momentum in the $(e,2e)$ collision, producing a low-energy secondary electron. Thus, directly after recollision, the start momenta of both electrons are very different, resulting in a most likely asymmetric momentum sharing in the final state.

Basically, such a behavior has been theoretically predicted for Argon at identical light intensity within an *S*-matrix approach using a Coulomb form factor to describe the $(e,2e)$ collision [10,12]. It is not consistent, however, with the re-

sults of similar calculations using a hard-core potential [11,12]. Moreover, since the momentum space is reduced in the transverse direction, Coulomb repulsion between the two electrons after recollision, which is not included in any of the 3D calculations [10,12], is expected to reduce events with similar longitudinal momenta. Reduction of the transverse momentum of one of the electrons essentially limits its motion in this direction, making the electron propagation ''one-dimensional'' with increased importance of the electron-electron repulsion in the longitudinal direction. Thus, it is no surprise that the two-electron momentum distribution is now in better qualitative agreement with results of one-dimensional calculations.

Finally, two-electron spectra have been investigated in Fig. 3 at a high peak intensity of 1 PW/cm^2 where sequential electric-field (tunnel) ionization is expected to be the dominant mechanism. We cannot completely exclude possible volume effects, but any contribution from regions with lower intensities should result in the appearance of a structure similar to that of Fig. 1, namely, two well-separated maxima in the momentum pattern. For sequential and therefore noncorrelated electron emission one would expect a spherically symmetric two-electron momentum distribution. Surprisingly, more events appear along the diagonal line indicating that some correlation is left. Both electrons are preferentially emitted into the same direction for small longitudinal-momentum components, i.e., for electrons that have been created close to the maxima of the oscillating electric field. Such a pattern might be expected if two electrons either leave by tunneling (sequential or collective) or by ''shake-off'' during the same cycle of the laser pulse.

In summary, we have presented differential correlated two-electron longitudinal-momentum spectra for different transverse momenta of one of the electrons. It has been demonstrated that our experimental data can help to distinguish between predictions of different calculations, thus, serving as benchmark data for theory.

The experiments were supported by the Deutsche Forschungsgemeinschaft (DFG, RO 1929) and by the Leibniz-Program of the DFG. Support from GSI, Darmstadt, is gratefully acknowledged. The MPI (former Freiburg) group would like to thank the MBI for their hospitality.

[1] R. Dörner *et al.*, Phys. Rep. **330**, 96 (2000).
[2] T. Weber *et al.*, Phys. Rev. Lett. **84**, 443 (2000).
[3] R. Lafon *et al.*, Phys. Rev. Lett. **86**, 2762 (2001).
[4] R. Moshammer *et al.*, Phys. Rev. Lett. **84**, 447 (2000).
[5] T. Weber *et al.*, J. Phys. B **33**, L127 (2000).
[6] B. Witzel, N. A. Papadogiannis, and D. Charalambidis, Phys. Rev. Lett. **85**, 2268 (2000).
[7] P. B. Corkum, Phys. Rev. Lett. **71**, 1994 (1993).
[8] B. Feuerstein, R. Moshammer, and J. Ullrich, J. Phys. B **33**, L823 (2000).
[9] A. Becker and F. H. M. Faisal, Phys. Rev. Lett. **84**, 3546 (2000).
[10] S. V. Popruzhenko and S. P. Goreslavskii, J. Phys. B **34**, L239 (2001); Opt. Express **8**, 395 (2001).
[11] R. Kopold *et al.*, Phys. Rev. Lett. **85**, 3781 (2000).
[12] R. Kopold, S. V. Popruzhenko, S. P. Goreslavskii, and W. Becker, Phys. Rev. A **64**, 053402 (2001).
[13] M. Lein, E. K. U. Gross, and V. Engel, J. Phys. B **33**, 433 (2000).
[14] M. Lein, E. K. U. Gross, and V. Engel, Phys. Rev. Lett. **85**, 4707 (2000).
[15] B. Eckhardt and K. Sacha, Phys. Scr. **T90**, 185 (2001).
[16] T. Weber *et al.*, Nature (London) **405**, 658 (2000).
[17] B. Feuerstein *et al.*, Phys. Rev. Lett. (to be published).
[18] H. van der Hart, J. Phys. B **33**, L655 (2000).
[19] R. Moshammer *et al.*, Nucl. Instrum. Methods Phys. Res. B **108**, 425 (1996).
[20] M. Weckenbrock *et al.*, J. Phys. B **34**, L449 (2001).

INSTITUTE OF PHYSICS PUBLISHING JOURNAL OF PHYSICS B: ATOMIC, MOLECULAR AND OPTICAL PHYSICS

J. Phys. B: At. Mol. Opt. Phys. **36** (2003) 707–716 PII: S0953-4075(03)56589-0

On the computation of momentum distributions within wavepacket propagation calculations

Bernold Feuerstein and Uwe Thumm

Department of Physics, Kansas State University, Manhattan, KS 66506, USA

Received 28 October 2002
Published 4 February 2003
Online at stacks.iop.org/JPhysB/36/707

Abstract

We present a new method to extract momentum distributions from time-dependent wavepacket calculations. In contrast to established Fourier transformation of the spatial wavepacket at a fixed time, the proposed 'virtual detector' method examines the time dependence of the wavepacket at a fixed position. In first applications to the ionization of model atoms and the dissociation of H_2^+, we find a significant reduction of computing time and are able to extract reliable fragment momentum distributions by using a comparatively small spatial numerical grid for the time-dependent wavefunction.

1. Introduction

Numerical wavefunction propagation for solving the time-dependent Schrödinger equation has been used extensively in order to describe the dynamics of strongly perturbed systems (Hermann and Fleck 1988, Kosloff 1994, Borisov *et al* 1999, Thumm 2002). Especially in the area of laser–matter interactions at high intensities, this method is currently applied to photoionization and photodissociation of few-particle systems such as the helium atom or small molecules, where the low or reduced dimensionality of the problem makes time-dependent calculations of this type feasible (Kulander *et al* 1996, Walsh *et al* 1998, Liu *et al* 2000, Lein *et al* 2000, Parker *et al* 2001, Bandrauk and Chelkowski 2001). Usually, the propagation is carried out in coordinate space and yields integral information about the considered process, e.g. total dissociation or ionization rates. However, if one desires to compare the calculation to differential experimental data such as momentum or kinetic energy distributions of the fragments, one has to extract these distributions from the outgoing wavepackets. A well established method is Fourier transformation (FT) which projects the wavefunction onto momentum eigenfunctions at a fixed time. The finite width of the momentum distributions gives rise to a significant dispersion of the wavepackets in coordinate space. Thus, a large numerical grid and long propagation times are required to get the full momentum information and to make the Fourier integrals converge. This becomes a serious computing time problem for systems of higher dimensionality. If the asymptotic behaviour of the continuum wavefunction

is analytically known, this problem can be avoided. Using analytical propagation for the asymptotic part of the wavefunction, the size of the numerical grid can be kept rather small (Keller 1995).

In this paper, we propose a new method to extract momentum distributions without propagation of the wavepacket over a large numerical grid. Here, the time dependence of the wavepacket at a *fixed* position is the source of the momentum information. Due to the analogy of this procedure to an experimental situation, we call this the 'virtual detector' (VD) method. The paper is structured as follows. After the general formulation, we demonstrate this method analytically as well as numerically for Gaussian wavepackets in one dimension. Next, we give numerical examples for the one-dimensional (1D) dissociation of H_2^+ following a Franck–Condon transition from the H_2 ground state and for the strong-field ionization of a 1D model hydrogen atom. We use atomic units throughout this paper, unless indicated otherwise.

2. General formulation of the 'virtual detector' method

The principles of quantum mechanics tell us that the wavefunction in any representation contains complete information about the considered system. As an example, the momentum distribution of a wavepacket Ψ is given by

$$|\Phi(\boldsymbol{k})|^2 = \left| (2\pi)^{-3/2} \int \Psi(\boldsymbol{r}) \exp(-\mathrm{i}\boldsymbol{k}\boldsymbol{r})\, \mathrm{d}\boldsymbol{r} \right|^2, \tag{1}$$

i.e. by FT of the wavepacket's coordinate space representation $\Psi(\boldsymbol{r})$. Thus, the momentum information is based on the global behaviour of Ψ in coordinate space. In many applications, transition rates which are related to the motion of wavepackets in coordinate space like ionization and dissociation (Kulander *et al* 1996, Chelkowski *et al* 1996, Dundas *et al* 1999) or reactive scattering (Neuhauser 1992) have been derived from the outgoing flux of the wavepacket through a given surface. The time-integrated flux corresponds to the probability of the corresponding ionization, dissociation or reaction channel. Using absorbing walls, comparatively small numerical grids can be used and, thus, the computing time can be significantly reduced. Here, we wish to extract information about the momentum distribution from the *time dependence* of an outgoing wavepacket at a *fixed position* in coordinate space. The input for FT is the *spatial dependence* of the wavefunction at a *fixed time*, i.e. the end of the propagation.

For the following considerations, we rewrite the wavefunction in the form

$$\Psi(\boldsymbol{r}, t) = A(\boldsymbol{r}, t) \exp(\mathrm{i}\phi(\boldsymbol{r}, t)) \tag{2}$$

with a real, time-dependent amplitude $A(\boldsymbol{r}, t)$ and a real, time-dependent phase $\phi(\boldsymbol{r}, t)$. At a given position $\boldsymbol{r}_\mathrm{d}$, $\phi(\boldsymbol{r}, t)$ contains information about the momentum distribution. To reveal this information, we consider the current density $\boldsymbol{j}$ at $\boldsymbol{r}_\mathrm{d}$ of outgoing particles with mass μ,

$$\boldsymbol{j}(\boldsymbol{r}_\mathrm{d}, t) = \frac{\rho(\boldsymbol{r}_\mathrm{d}, t)}{\mu} \nabla\phi(\boldsymbol{r}_\mathrm{d}, t) \qquad \text{with } \rho(\boldsymbol{r}_\mathrm{d}, t) = |A(\boldsymbol{r}_\mathrm{d}, t)|^2. \tag{3}$$

The (probability) current density can be interpreted as the product of the probability density ρ and a 'local' velocity $\boldsymbol{v}$ at position $\boldsymbol{r}_\mathrm{d}$ which corresponds to the momentum

$$\boldsymbol{k}(\boldsymbol{r}_\mathrm{d}, t) = \mu\boldsymbol{v} = \nabla\phi(\boldsymbol{r}_\mathrm{d}, t). \tag{4}$$

The simplest example is an outgoing monochromatic plane wave $\Psi(\boldsymbol{r}, t) = (2\pi)^{-3/2} \exp[\mathrm{i}(\boldsymbol{k}\boldsymbol{r} - \omega t)]$ where the phase gradient is directly related to the momentum $\boldsymbol{k}$. Similar to an experimental time-of-flight set-up, we now have to apply a 'binning' or 'histogramming' procedure in order to derive the momentum distribution $\mathrm{d}N/\mathrm{d}k$. In order

to keep this formulation transparent, we consider here the 1D case. Having the VD located at x_d, for each time t, we get the momentum $k(x_\mathrm{d}, t)$. After time integration, the probability for finding the number of 'events' ΔN with momenta k within a small interval Δk around a momentum value k_j is given by

$$\Delta N(k_j) = \Delta k \int_0^\infty \mathrm{d}t\; j(x_\mathrm{d}, t) \begin{cases} 1 & \text{for } k \in \left[k_j - \frac{\Delta k}{2}, k_j + \frac{\Delta k}{2}\right] \\ 0 & \text{else.} \end{cases} \tag{5}$$

In the limit of an infinitesimal interval length $\mathrm{d}k$, the 'box' distribution in (5) becomes a δ distribution,

$$\left.\frac{\mathrm{d}N}{\mathrm{d}k}\right|_{k'} = \int_0^\infty \mathrm{d}t\; j(x_\mathrm{d}, t)\delta(k' - k(x_\mathrm{d}, t)). \tag{6}$$

The implicit time dependence of the argument of the δ distribution can be transformed into an explicit time dependence according to

$$\left.\frac{\mathrm{d}N}{\mathrm{d}k}\right|_{k'} = \sum_m \int_0^\infty \mathrm{d}t\; j(x_\mathrm{d}, t) \frac{\delta(t - t_\mathrm{m})}{|\frac{\mathrm{d}k}{\mathrm{d}t}(t_\mathrm{m})|} \qquad t_\mathrm{m} : k(t_\mathrm{m}) = k' \tag{7}$$

$$= \frac{j(x_\mathrm{d}, t(k'))}{|\frac{\mathrm{d}k}{\mathrm{d}t}(t(k'))|}. \tag{8}$$

Equation (7) can be reduced to (8) if $j(x_\mathrm{d}, t)$ has dominant contributions only for sufficiently large t. This applies in the example below (section 3.1), where $k(t)$ is a monotonous function in t and the argument of the δ distribution in (6) has only one zero.

The VD method can be extended to higher-dimensional calculations. In this case, the detector becomes a (hyper)surface the flux through which is given according to (3) by the current density at all points $\boldsymbol{r}_\mathrm{d}$ on this surface. The momentum spectra for all points, integrated over the entire (hyper)surface, yield the final momentum spectrum. The choice of the surface depends on the physical problem and the range of momentum components of interest. In the following two sections 3.1 and 3.2, we will test this technique for a moving Gaussian wavepacket in one dimension.

3. Simple test: momentum distribution for a moving Gaussian wavepacket

3.1. Analytical result

The Gaussian wavepacket is prepared at time $t = 0$, centred at $x = 0$ with an initial width Γ and an initial (average) momentum k_0,

$$G(x, t = 0) = \left(\frac{1}{\sqrt{\Gamma}\pi^{1/4}}\right) \exp\left(-\frac{x^2}{2\Gamma^2}\right) \exp(\mathrm{i}k_0 x). \tag{9}$$

The momentum representation of this wavepacket

$$M(k) = \frac{1}{\sqrt{2\pi}} \int_{-\infty}^\infty G(x, t = 0) \exp(-\mathrm{i}kx)\, \mathrm{d}x = \frac{\sqrt{\Gamma}}{\pi^{1/4}} \exp\left(-\frac{1}{2}(k_0 - k)^2\Gamma^2\right) \tag{10}$$

leads to the time-dependent, freely propagating wavepacket in coordinate space

$$G(x, t) = \frac{1}{\sqrt{2\pi}} \int_{-\infty}^\infty M(k) \exp\left(\mathrm{i}\left(kx - \frac{1}{2}k^2 t/\mu\right)\right) \mathrm{d}k$$

$$= \frac{1}{\pi^{1/4}} \sqrt{\frac{\Gamma}{\Gamma^2 + \mathrm{i}t/\mu}} \exp\left(-\frac{(x - \mathrm{i}k_0\Gamma^2)^2}{2(\Gamma^2 + \mathrm{i}t/\mu)}\right) \exp\left(-\frac{1}{2}k_0^2\Gamma^2\right). \tag{11}$$

In order to derive the phase gradient, we rewrite $G(x,t)$ in the form $A(x,t)\exp(\mathrm{i}\phi(x,t))$ with the real, time-dependent amplitude

$$A(x,t) = \frac{\sqrt{\Gamma}}{\sqrt[4]{\pi(\Gamma^4 + t^2/\mu^2)}} \exp\left(-\frac{\Gamma^2(x - k_0 t/\mu)^2}{2(\Gamma^4 + t^2/\mu^2)}\right), \tag{12}$$

and a real, time-dependent phase

$$\phi(x,t) = \frac{\Gamma^4 k_0(x - \frac{1}{2}k_0^2 t/\mu) + \frac{1}{2}x^2 t/\mu}{\Gamma^4 + t^2/\mu^2} + \theta(t). \tag{13}$$

The additional global phase $\theta(t)$ is not of interest, since it does not affect the phase gradient. According to (3), (4), we find the 'local' momentum at position x_d:

$$k(x_\mathrm{d},t) = \frac{\partial}{\partial x}\bigg|_{x=x_\mathrm{d}} \phi(x,t) = \frac{\Gamma^4 k_0 + x_\mathrm{d} t/\mu}{\Gamma^4 + t^2/\mu^2} = \mu v \tag{14}$$

$$\approx \mu x_\mathrm{d}/t \qquad (x_\mathrm{d} t/\mu \gg \Gamma^4 k_0, t^2/\mu^2 \gg \Gamma^4), \tag{15}$$

and the outgoing current

$$j(x_\mathrm{d},t) = \rho(x_\mathrm{d},t)k/\mu = |A(x_\mathrm{d},t)|^2 k/\mu = \frac{\Gamma}{\sqrt{\pi(\Gamma^4 + t^2/\mu^2)}} \exp\left(-\frac{\Gamma^2(x_\mathrm{d} - k_0 t/\mu)^2}{\Gamma^4 + t^2/\mu^2}\right)\frac{k}{\mu}. \tag{16}$$

Note, that for the 1D case considered here, there is no need to distinguish between current and current density. Provided that the approximation given above is valid, equation (15) is directly related to a time-of-flight measurement in an experiment with a particle detector placed at position x_d, and the label 'VD method' appears appropriate. However, we note that this analogy with the experiment is limited and possibly misleading, since a real 'measurement' of the momentum at a fixed position would violate the uncertainty principle. Nevertheless, the phase gradient is related to the momentum distribution. Physically, (13)–(15) show that the leading edge of the Gaussian wavepacket is moving faster than the remaining part, corresponding to normal dispersion.

For sufficiently large t (15) holds and we can use the approximation (8). With $j(x_\mathrm{d},t)$ from (16) and using $t(k) \approx \mu x_\mathrm{d}/k$ (15) we finally obtain

$$\frac{\mathrm{d}N}{\mathrm{d}k} = \frac{\Gamma}{\sqrt{\pi(\Gamma^4 + x_\mathrm{d}^2/k^2)}} \exp\left(-\frac{\Gamma^2(x_\mathrm{d} - k_0 x_\mathrm{d}/k)^2}{\Gamma^4 + x_\mathrm{d}^2/k^2}\right)\frac{x_\mathrm{d}}{k} \tag{17}$$

$$\approx \frac{\Gamma}{\sqrt{\pi}} \exp(-\Gamma^2(k - k_0)^2) = |M(k)|^2 \qquad (x_\mathrm{d}^2/k^2 = t^2/\mu^2 \gg \Gamma^4), \tag{18}$$

which is the momentum distribution of the wavepacket (see (10)). The conditions (15), (18) mean that the momentum components of $\Psi(x,t)$ which have the same initial phase at $t = 0$ (9) are dephasing due to the dispersion relation in (11), $E_\mathrm{kin} = \frac{1}{2}k^2/\mu$. According to (14), $k(t)$ is equal to k_0 for very small t and exhibits a maximum before it reaches the asymptotic $1/t$ behaviour.

3.2. Numerical result

Let us now consider the numerical test of the VD method for the Gaussian wavepacket. Here, as well as for the other examples in section 4, we use the Crank–Nicholson propagation scheme which provides unconditional numerical stability. The momentum spectra are generated as

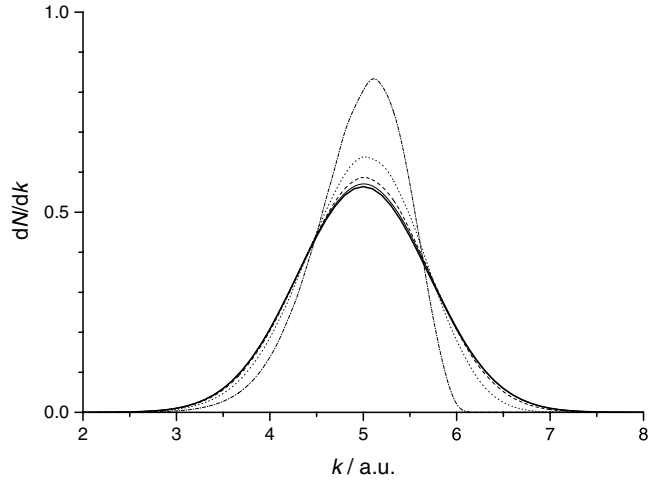

Figure 1. Convergence behaviour of the VD method for a moving Gaussian wavepacket. The exact analytical momentum distribution (10) is given by the thick solid curve. The numerical momentum spectrum is shown for different positions x_d of the VD: — · —, $x_d = 5$; · · · · · ·, $x_d = 10$; - - - -, $x_d = 20$; ——, $x_d = 50$.

follows. For each time step t_i the phase gradient of the wavepacket at the position x_d of the VD is calculated using a five point formula. According to (5) and (14), the momenta $k_i = k(t_i) = \partial/\partial x[\phi(x, t_i)]_{x_d}$ and $\Delta N/\Delta k(k_i)$ are combined to a histogram. This procedure ensures correct normalization, i.e. the integrated momentum distribution gives the total yield in the corresponding fragmentation channel. Figure 1 shows the convergence behaviour of the VD method with increasing x_d, i.e. the transition from (14) to (15) and (17) to (18), respectively. In the present example we use a Gaussian wavepacket initially centred at $x = 0$ with $\Gamma = 1$, $k_0 = 5$, $\mu = 1$. The propagation was performed up to $t = 25$ with time intervals $\Delta t = 10^{-3}$ on a numerical grid which extends from $x = -20$ to 280 with a grid spacing of $\Delta x = 0.05$. The numerically derived momentum distribution converges quickly towards the analytical result $|M(k)|^2$ as x_d increases from 5 to 50. Once convergence is reached, the numerical distribution no longer depends on x_d (see (18)). The smaller width of the numerical momentum distributions for values of x_d that are smaller than required by approximation (15) is caused by the 'soliton-like' behaviour of the wavepacket at small t. In this case we find $k(x_d, t) \approx k_0$ which leads to an (unphysical) δ distribution $\Delta N/\Delta k \approx \delta(k_0)$. Once the dispersion-induced broadening of the wavepacket becomes large compared to the initial width Γ, the numerical momentum distribution also broadens and converges to the analytical result.

4. Numerical applications of the 'virtual detector' method

4.1. Momentum distribution of dissociating H_2^+

As a first application, we study dissociation of the H_2^+ molecule following (fast) single ionization of H_2. The stationary ground state ($v = 0$) nuclear wavefunction of the neutral H_2 molecule is promoted via a vertical (Franck–Condon) transition onto the potential curve of the H_2^+ molecular ion. In our simulation this is achieved by propagating the $v = 0$ state of H_2 on the potential curve of H_2^+ in the electronic ground state. Since the electronic ground state potential curves for H_2 and H_2^+ differ in equilibrium distance and width (Huber and Herzberg 1979),

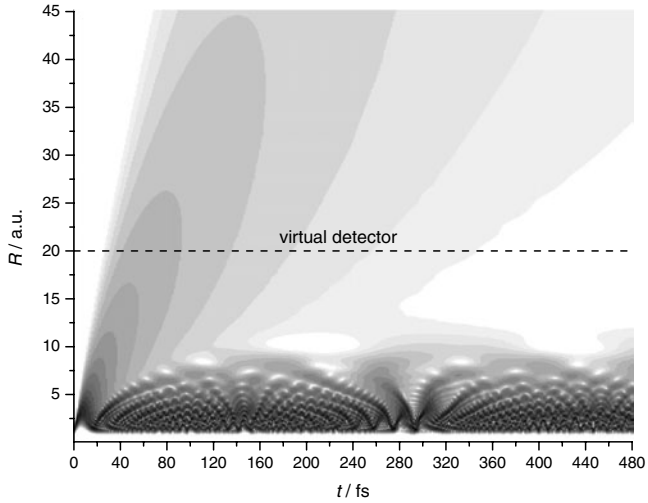

Figure 2. Wavepacket dynamics of H_2^+ following a Franck–Condon transition from the H_2 vibrational ground state. The time evolution of the probability density is shown as a contour plot on a logarithmic grey scale (R: internuclear distance). The position $R_d = 20$ of the VD is indicated by the dashed line. Note the revival of the bound part of the wavepacket at $t = 275$ fs.

the wavefunction becomes a non-stationary wavepacket leading to a *coherent* superposition of many (bound) vibrational states of H_2^+ as well as to dissociation. For comparison, the momentum distribution of the dissociative part of the wavefunction will here be calculated by using (a) standard FT (equation (1)) and (b) the VD method. The 1D numerical grid for the internuclear distance R extends from $R = 0.05$ to 500 with a grid spacing of $\Delta R = 0.05$. The propagation was carried out until $t_{max} = 2 \times 10^4$ (480 fs) with intervals $\Delta t = 1$.

Figure 2 shows the time evolution of the probability density as a contour plot on a logarithmic grey scale. The FT needs to be taken only for the dissociating part of the wavepacket. Thus, one has to wait until the wavepacket has left the region of bound states, which are localized at $R < 15$. By the time the slowest dissociation components have left that region, the fastest components already reach distances of $R = 420$ which defines a minimum size of the array needed for the FT (figure 3). The sharp cutoff of the wavefront at $R = 420$ is caused by the finite grid spacing which supports free propagation of momentum components up to $k_{max} \approx 1/\Delta R = 20$ according to Nyquist's criterion. The corresponding maximum velocity $v_{max} = k_{max}/\mu = 20/918 = 2.18 \times 10^{-2}$ gives the position of the wavefront at the end of the propagation at time t_{max} at $R_{max} = 435$ which is close to the cutoff in figure 3. In contrast to FT, a VD located at $R_d = 20$ requires a much smaller numerical grid extending only to $R = 30$. This includes an absorber located between $R = 20$ and 30, which is adjusted to prevent reflections of the wavepacket at the boundary of the numerical grid. We implemented this absorber as a fourth-order optical potential $V_{opt} = 0.05(R - 20)^4$ starting at $R = 20$. We also checked the convergence by comparing the numerical momentum spectra for $R_d = 20$ and 40 which show no significant difference. This demonstrates the efficiency of the VD method which reduces the computation time in the present example by more than an order of magnitude. A comparison of the FT result for the fragment momentum spectrum dN/dk with the VD method is given in figure 4. Both results agree very well except for the small superimposed oscillations which are caused by the finite grid size (for the FT) and by the finite number of time steps which causes a statistical error in the VD method. The statistical error can be reduced either by using smaller time steps Δt or by using a set of VDs which extends

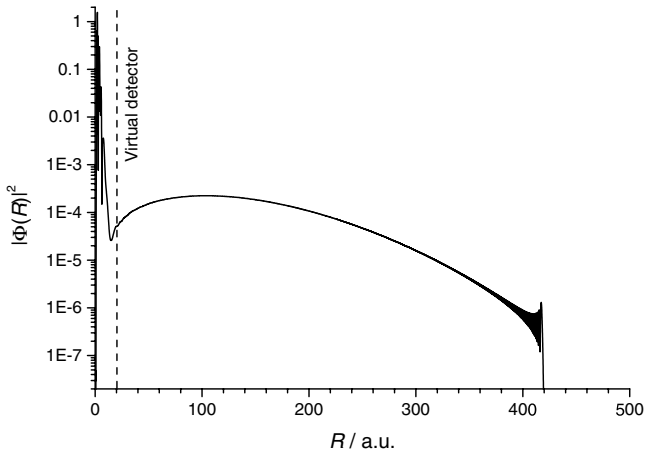

Figure 3. Snapshot (log scale) of the 1D probability density for the H_2^+ nuclei (see also figure 2) as a function of the internuclear distance R at $t = 480$ fs. The bound part of the wavepacket is localized at $R \leqslant 15$, whereas the dissociative part has already spread from $R = 15$ to 420. The position $R_d = 20$ of the VD is indicated by the dashed line. Note the sharp cutoff of the wavefront at $R = 420$ due to the the finite grid spacing ($\Delta R = 0.05$).

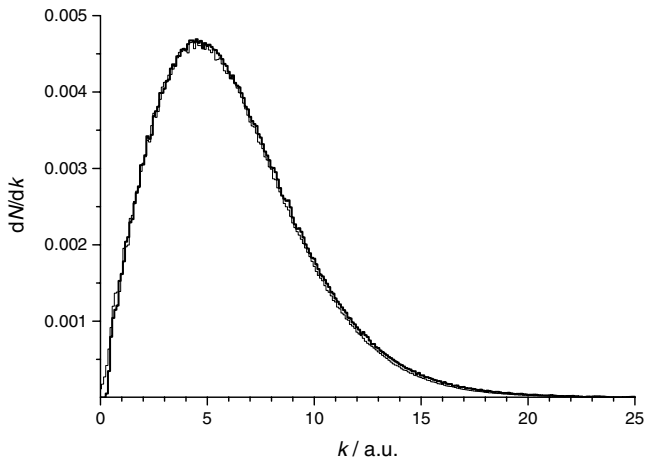

Figure 4. Momentum spectrum for dissociation of H_2^+ following a Franck–Condon transition from the H_2 vibrational ground state. Thick solid curve: VD method; thin solid curve: FT result.

over a finite array of grid points. The latter method was found to be much more effective with respect to computation time, since it only requires the calculation of the phase gradient at a set of fixed positions x_d. The time propagation is a matrix operation on the entire numerical grid and, thus, reduction of Δt is much more time consuming.

4.2. Quiver motion of an electron ionized by a strong laser field

In the second numerical example, we examine the strong-field ionization of a 1D model hydrogen atom, in particular, the effect of the quiver motion of the electron on the momentum distribution. The mean quiver energy of an electron in the presence of the laser of electric field strength $\mathcal{E}$ and frequency ω is expressed in terms of the 'ponderomotive energy' $U_p = \mathcal{E}^2/4\omega^2$.

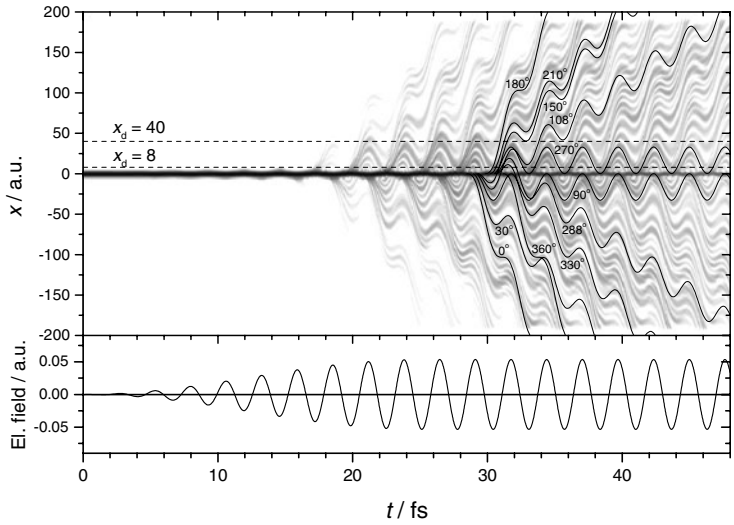

Figure 5. Strong-field ionization of a 1D model hydrogen atom by a 0.1 PW cm^{-2} intensity, 800 nm CW laser (with 25 fs ramp): contour plot (logarithmic grey scale) of the time evolution of the electron probability density. The positions of the VD are indicated by the broken lines. Selected classical trajectories starting within one optical cycle are shown as solid curves. The labels give the corresponding phases relative to the $\sin(\omega t)$ CW laser electric field.

The electron–nucleus interaction of the atom is modelled by a soft-core Coulomb potential (Su and Eberly 1991) $-1/\sqrt{x^2+a^2}$ where the parameter $a = 1.4$ is adjusted to the ionization potential of hydrogen. The 1D grid extends from $x = -200$ to 200 with a grid spacing of $\Delta x = 0.2$. Fourth-order optical potential absorbers were used covering the first and last 100 grid points.

The quiver motion may lead (depending on the phase of the laser field, when the electron was ionized) to a rescattering of the electron (Corkum 1993, Paulus *et al* 1994, Kulander *et al* 1995, Feuerstein *et al* 2000). Figure 5 shows the time-dependent electron probability density for the 1D model hydrogen atom interacting with a CW 800 nm laser at 0.1 PW cm^{-2} with a 25 fs $\sin^2$ ramp. For the propagation, 1100 time steps were used per optical cycle. Interestingly, the outgoing electron 'jets' exhibit a structure similar to classical electron trajectories in a laser field (see, e.g., figure 1 in Feuerstein *et al* 2000). For comparison, we show selected classical trajectories starting within one optical cycle for different phases of the oscillating laser field ($\sin(\omega t)$). Rescattering occurs for phases $90° \leqslant \omega t < 180°$ and $270° \leqslant \omega t < 360°$, respectively. The VD method allows us to extract the (not directly observable) momenta of the quiver motion. In order to demonstrate the effect of the quiver motion, we consider the momentum distributions derived for two different positions of the VD. In the first case, the VD is placed at a distance $x_\mathrm{d} = 8$ from the atomic nucleus. This distance is smaller than the classical quiver amplitude $x_\mathrm{q} = \mathcal{E}/\omega^2 = 5.3 \times 10^{-2}/0.057^2 = 16.4$, but lies outside the region with significant density of bound states which would otherwise disturb the spectrum. At this position close to the nucleus, rescattering events influence the momentum distribution (solid curve in figure 6). Negative momenta (note that $x_\mathrm{d} > 0$) are observed with a cutoff close to the classical maximal recollision momentum (Corkum 1993) $k_\mathrm{rec} = -\sqrt{2 \times 3.17 U_\mathrm{p}} = -1.2$.

If the VD is placed at $x_\mathrm{d} = 40$ we exclude negative drift momenta, since only the corresponding classical trajectories starting at $90° < \omega t < 270°$ reach the VD. Thus, the momentum distribution is shifted towards positive momenta (the dashed curve in figure 6)

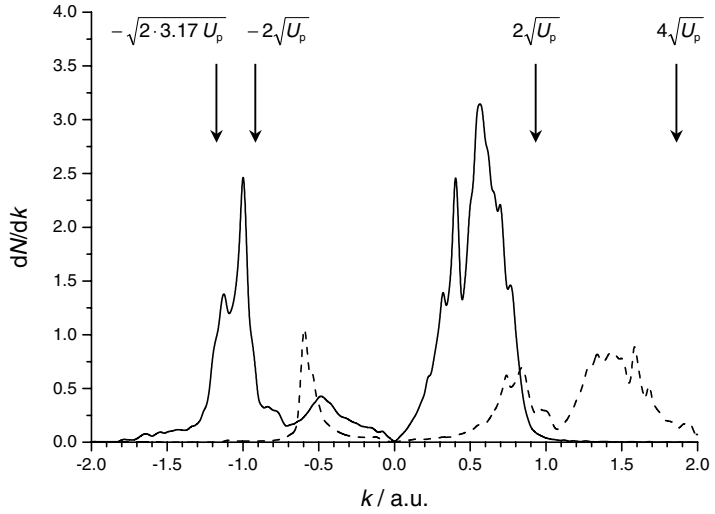

Figure 6. Momentum distributions for an electron after strong-field ionization of a 1D model hydrogen atom. Laser parameters: 0.1 PW cm^{-2} intensity, 800 nm wavelength, CW with a 25 fs ramp. The VD is placed at $x_d = 8$ (solid curve) and $x_d = 40$ (dashed curve), respectively. Typical momenta for an electron in a laser field are indicated by arrows (also see the text).

and extends up to the upper limit for the classical motion of an electron in a strong laser field $k_{max} = 4\sqrt{U_p} = 1.9$. Here, the drift and quiver momenta (the maximum value of both being $2\sqrt{U_p} = 0.95$) add up constructively. We note that the asymmetry of both spectra shown in figure 6 with respect to $k = 0$ is not caused by an absolute phase effect, but rather by the fact that we considered only one direction, i.e. we used only one VD. Absolute phase effects are negligible in this example since the laser field is turned on sufficiently slowly and, at 0.1 PW cm^{-2}, the ionization rate is relatively small, i.e. the ionization occurs over many optical cycles without depletion of the bound states. A VD placed at $-x_d$ would yield a mirror image of the corresponding momentum distribution. Thus, the sum of the spectra for VDs placed at x_d and $-x_d$ will give a symmetric spectrum since absolute phase effects are negligible.

5. Conclusion

In this paper we proposed a new method to extract momentum and kinetic energy distributions from time-dependent wavepacket propagation calculations. Compared to the established FT method which uses the spatial dependence of the wavepacket at a fixed time, this new VD method examines the time-dependent behaviour of the wavepacket at a fixed position x_d. Thus, the size of the spatial array needed to extract the momentum spectrum can be reduced significantly. As a test, for 1D Gaussian wavepackets, the equivalence with FT was shown analytically. In numerical examples we demonstrate that compared to FT, the computation time can be reduced by more than a factor of ten. In addition to being faster than the FT method, the use of the VD method provides momentum information that is not otherwise available, as shown in our example for the quiver motion of an electron ionized by a strong laser field.

Acknowledgments

This work was supported in part by the National Science Foundation (grant no PHY-0071035) and the Division of Chemical Sciences, Office of Basic Energy Sciences, Office of Energy

Research, US Department of Energy. BF acknowledges the financial support in the form of a Research Scholarship provided by the Deutsche Forschungsgemeinschaft.

References

Bandrauk A D and Chelkowski S 2001 *Phys. Rev. Lett.* **87** 273004
Borisov A G, Kazansky A K and Gauyacq J P 1999 *Phys. Rev.* B **59** 10935
Chelkowski S, Conjusteau A, Zuo T and Bandrauk A D 1996 *Phys. Rev.* A **54** 3235
Corkum P B 1993 *Phys. Rev. Lett.* **71** 1994
Dundas D, Taylor K T, Parker J S and Smyth E S 1999 *J. Phys. B: At. Mol. Opt. Phys.* **32** L231
Feuerstein B, Moshammer R and Ullrich J 2000 *J. Phys. B: At. Mol. Opt. Phys.* **33** L823
Hermann M R and Fleck Jr J A 1988 *Phys. Rev.* A **38** 6000
Huber K P and Herzberg G 1979 *Molecular Structure and Molecular Spectra IV. Constants of Diatomic Molecules* (New York: Van Nostrand-Reinhold)
Keller A 1995 *Phys. Rev.* A **52** 1450
Kosloff R 1994 *Annu. Rev. Phys. Chem.* **45** 145
Kulander K C, Cooper J and Schafer K J 1995 *Phys. Rev.* A **51** 561
Kulander K C, Mies F H and Schafer K J 1996 *Phys. Rev.* A **53** 2562
Lein M, Gross E K U and Engel V 2000 *J. Phys. B: At. Mol. Opt. Phys.* **33** 433
Liu W C, Eberly J H, Haan S L and Grobe R 2000 *Phys. Rev. Lett.* **83** 520
Neuhauser D 1992 *Chem. Phys. Lett.* **200** 173
Parker J S, Moore L R, Merhag K J, Dundas D and Taylor K T 2001 *J. Phys. B: At. Mol. Opt. Phys.* **34** L69
Paulus G G, Becker W, Nicklich W and Walther H 1994 *J. Phys. B: At. Mol. Opt. Phys.* **27** L703
Su Q and Eberly J H 1991 *Phys. Rev.* A **44** 5997
Thumm U 2002 *22nd Int. Conf. on the Physics of Photonic, Electronic and Atomic Collisions (Santa Fe, NM)* ed S Datz *et al* (Princeton, NJ: Rinton Press) p 592 Book of invited papers
Walsh T D G, Ilkov F A, Chin S L, Châteauneuf F, Nguyen-Dang T T, Chelkowski S, Bandrauk A D and Atabek O 1998 *Phys. Rev.* A **58** 3922

INSTITUTE OF PHYSICS PUBLISHING JOURNAL OF PHYSICS B: ATOMIC, MOLECULAR AND OPTICAL PHYSICS

J. Phys. B: At. Mol. Opt. Phys. **36** (2003) L113–L119 PII: S0953-4075(03)57905-6

LETTER TO THE EDITOR

Strongly directed electron emission in non-sequential double ionization of Ne by intense laser pulses

R Moshammer[1], J Ullrich[1], B Feuerstein[1], D Fischer[1], A Dorn[1], C D Schröter[1], J R Crespo López-Urrutia[1], C Höhr[1], H Rottke[2], C Trump[2], M Wittmann[2], G Korn[2], K Hoffmann[2] and W Sandner[2]

[1] Max-Planck-Institut für Kernphysik, Saupfercheckweg 1, D-67119 Heidelberg, Germany
[2] Max-Born-Institut, Max-Born-Strasse 2a, D-12489 Berlin, Germany

E-mail: R.Moshammer@mpi-hd.mpg.de

Received 20 December 2002
Published 4 March 2003
Online at stacks.iop.org/JPhysB/36/L113

Abstract

Double ionization of Ne by 25 fs, 1.0 PW cm^{-2} laser pulses has been explored in a kinematically complete experiment using a 'reaction microscope'. Electrons are found to be emitted into a narrow cone along the laser polarization (ε), much more confined than for single ionization, with a broad maximum in their energy distribution along ε. Correlated momentum spectra show both electrons being ejected into the same hemisphere, in sharp contrast to predictions based on field-free (e, 2e) recollision dynamics, but in overall agreement with recent semiclassical calculations for He.

Double ionization of atoms is one of the most fundamental processes when intense laser fields interact with matter, and, at the same time, one of the most challenging problems in atomic physics, theoretically as well as experimentally. Whereas single ionization is well understood in the framework of the 'single active electron model' (SAE), the measured yields of double ionization exceed those theoretically expected assuming a sequence of individual and independent single-ionization events by many orders of magnitudes at an intermediate intensity regime. Undoubtedly, this 'non-sequential' (NS) contribution to double ionization is a consequence of the electron–electron interaction. The underlying mechanism, however, remained unclear for many years (for reviews see [1, 2]).

Only recently, a new generation of differential measurements [3, 4], along with various quantum [5–10] as well as classical calculations [11, 12], provided convincing evidence that the so-called 'rescattering' or recollision scenario—one of the three NS double-ionization pathways (beyond collective tunnelling and shake-off) which have been proposed in the past—is the dominating mechanism. Here, one electron is ionized via tunnelling, accelerated in the oscillating laser field and, under certain conditions, driven back to its parent ion knocking out another electron. It was demonstrated that the kinematics of this dynamical process is the only one that leads to recoil-ion momentum distributions with a 'double-hump' structure as observed

in the experiments [13]. Even before, results of experiments on harmonic generation [1] and, in particular, the disappearance of NS ionization when circularly polarized light is used [14] were strongly in favour of the rescattering model. Thus, it is generally accepted at present that rescattering is the dominant NS double-ionization mechanism in an intermediate intensity regime. On the other hand, however, the underlying dynamics during recollision, i.e. the electron impact ionization (e, 2e) dynamics in the presence of the laser field, its intensity or pulse-time dependence, is far from being understood.

Consequently, a series of recent experiments have addressed this question on different levels of sophistication. Ratios of double to single ionization and electron energy distributions for double ionization (partly integrated over emission angles for low electron energies) have been reported [15–18] along with experiments where one momentum component of one emerging electron was measured in coincidence with the full momentum vector of the recoiling target ion, providing information about the correlated momenta of both emitted electrons along the laser polarization direction [19, 20]. Here, for NS double ionization of Ar by 0.38 and 0.2 PW cm^{-2}, 780 nm pulses at a pulse length of 220 and 25 fs, respectively, detailed information on the momentum sharing between both ejected electrons was obtained, which sensitively depends on the recollision dynamics. In both experiments, the two electrons were found to be predominantly emitted into the same hemisphere in agreement with the kinematical constraints set by the classical rescattering model. In addition, however, a considerable fraction was observed to be emitted back-to-back, which has been interpreted as being due to excitation during rescattering [20] with subsequent and independent field (tunnel) ionization of the second electron. Measuring in addition the transverse momentum of one of the electrons, the recollision dynamics was explored in even more detail. Setting severe constraints on the transverse motion of the electrons, signatures of the final-state repulsion between the two emitted electrons along the polarization direction were observed [21, 22].

For lighter target atoms, where excitation can be expected to be less important and, thus, the recollision dynamics should be less obscured by the target electronic structure, no experimental data on correlated electron emission for strong-field double ionization have been reported up to now because of enormous experimental complications. Here, the comparison with theory, completely neglecting any influence of the atomic structure, should become much more reliable. Quantum mechanical *S*-matrix calculations [8] indeed predict the correlated electron momentum distributions to depend sensitively on the details of the recollision process: different approximations used to account for the electron–electron correlation in double ionization of Ne led to completely different two-electron momentum patterns. If a simplified contact potential is applied to describe the interaction between the colliding electrons, they both appear with similar momenta along the polarization direction in the final state. In contrast, if a more realistic Coulomb form factor is used a quite asymmetric electron momentum sharing is predicted. Applying a three-dimensional semiclassical model Fu *et al* [12] have obtained a quite symmetric momentum sharing for 1 PW cm^{-2} pulses interacting with He atoms with both electrons having most likely similar or even equal momenta along the polarization direction. Fully quantum-mechanical theoretical treatments solving the three-dimensional Schrödinger equation [9] are only feasible at higher photon frequencies with present computer capabilities. Hence, the correlated two-electron dynamics in the presence of the laser field occurring during rescattering essentially remained in the dark.

Here we present highly differential information on strong-field (1 PW cm^{-2}) NS double ionization of Ne, obtained in a kinematically complete experiment with a reaction microscope. Energy- and angle-resolved electron spectra, covering the major part of the final-state momentum space, are presented in addition to two-electron momentum distributions along the polarization direction (ε). Electrons are found to be strongly directed along ε with similar

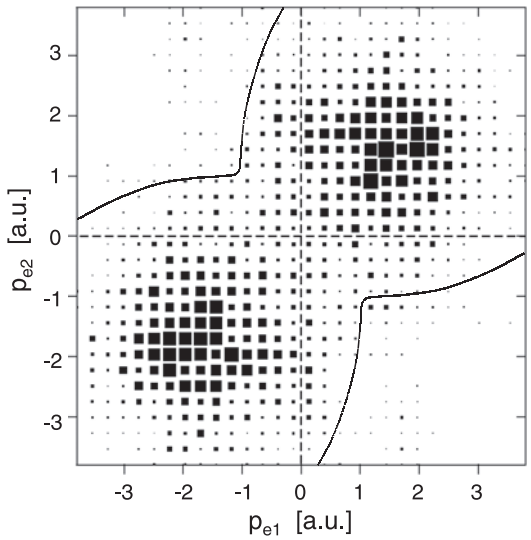

Figure 1. Correlated two-electron momentum distributions along the laser polarization axis for electrons ejected in double ionization of Ne by 25 fs, linearly polarized, 800 nm laser pulses at a peak intensity of 1.0 PW cm^{-2}. The data are integrated over the momentum components perpendicular to the polarization. The full curves denote the upper limit of correlated electron momenta compatible with the classical rescattering model. The z axis is on a logarithmic scale with box sizes corresponding to the respective intensity.

momenta, in contrast to field-free (e, 2e) recollision kinematics [8] but in qualitative agreement with classical predictions [12]. Back-to-back emission of both electrons is extremely unlikely for Ne in sharp contrast to the Ar results.

The experiment was performed at the Max Born Institute in Berlin using a Kerr-lens mode-locked Ti:sapphire laser at 800 nm wavelength with a repetition rate of 1 kHz. By focusing the 25 fs (FWHM) light pulses onto a spot of 10 μm (FWHM) diameter in an ultrahigh vacuum chamber (2×10^{-11} Torr), pulse peak intensities of 1.0 PW cm^{-2} were reached. At its focus the laser beam was crossed by a well collimated low-density (10^8 atoms cm^{-3}) supersonic Ne jet, resulting in an interaction volume of 50 μm length and 10 μm diameter. Using a reaction microscope, which has been described in detail in [2, 20, 22], the ionic charge as well as the coincident momentum vectors of both ions and electrons were recorded with a momentum resolution of $\Delta p \approx 0.1$ au. Intensity fluctuations were monitored during the experiment and kept below 5%. The stability of all experimentally relevant parameters was maintained throughout the beam-time of several days.

In figure 1 the longitudinal momentum (i.e. the component along the laser polarization axis) of one electron is plotted versus that of the other electron without any restriction on their transverse momenta. A strongly correlated electron motion is observed in a way that both electrons are preferentially emitted into the same hemisphere with very similar momenta. Differing from all previous results for Ar targets [19–22], back-to-back-emission is essentially absent, i.e. only a few events are observed where both electrons escape in opposite directions, confirming the expectation that recollisional excitation and subsequent field ionization is less important for lighter targets. Moreover, one might now inspect whether the measured distribution is compatible with the recollision kinematics (see also [20]). For a certain tunnelling phase of the first electron ωt_0, recollision happens at a well defined recollision

energy E^{recoll} and phase ωt_1. The latter results in well defined and equal drift momenta of both electrons $p_e^{drift}(\omega t_1)$ after the collision. In addition, they can share the excess energy $E^{ex} = E^{recoll} - I_P$ (I_P: ionization potential). Neglecting the transverse energies of the electrons, which will be shown to be small, energy conservation $p_{e1\parallel}^2 + p_{e2\parallel}^2 = 2E^{ex}$ during rescattering yields a circle with radius $\sqrt{2E^{ex}}$ around the points $(\pm p_{e1}^{drift}(\omega t_1), \pm p_{e2}^{drift}(\omega t_1))$ as maximum drift momentum combinations. Considering all phases, the full curves in figure 1 are obtained, indicating the classical boundary for rescattering. The comparison with experimental data impressively shows that nearly all events are within these boundaries.

While practically all events are compatible with the kinematical boundaries for recollision the correlation pattern itself, however, with many electrons of quite similar longitudinal momenta is in contradiction with predictions based on field-free electron-impact (e, 2e) ionization dynamics, which becomes actually more obvious at higher intensities [8]. In accordance with the fact that unequal energy sharing between projectile and ionized electron is by far the most likely configuration in field-free (e, 2e) at not too low impact energy, unequal final momenta are also predicted for NS double ionization in laser fields, in striking contrast to the experimental results. Several other predictions, using a hard core form factor for the electron collision [8] or solving the one-dimensional time-dependent Schrödinger equation with correlated electrons, are in poor agreement with experiment. Only recent semiclassical calculations [12] were able to predict a similar pattern as observed. There, the first electron is set free with a velocity distribution following from tunnelling theory and propagated classically in the combined fields of the laser and ionic core. The remaining He^+ ion is also modelled classically, with the electron in a micro-canonical distribution in the intermediate state. Thus, within the classical approximation, all interactions are correctly taken into account in all three dimensions.

To further elucidate electron emission in NS double ionization of Ne, electron energy distributions are shown in figure 2 for single as well as double ionization integrated over all emission angles. At the present laser intensity of 1.0 PW cm^{-2} the Keldysh parameter [23] is $\gamma = 0.30$, indicating that single ionization mainly proceeds via tunnelling [24]. Since tunnelling ionization is most likely close to the maximum of the electric field $\vec{F}(t) = \vec{F}_0(t) \cdot \sin(\omega t)$ the final drift momentum $p^{drift}(t_0) = 1/\omega \cdot F_0(t_0)\cos(\omega t_0)$ is typically small. Thus, structureless electron spectra are expected, peaked at low kinetic energies in agreement with experiment.

In comparison, the electron energy distribution in coincidence with double ionization is significantly less steep, extending to much higher energies. Similar observations have been reported recently for emission along the polarization axis for Xe, Ar and He targets [15–17]. Larger electron energies are in qualitative agreement with the rescattering scenario, since recollision most likely happens at a phase close to a zero crossing of the oscillating electric field. Hence, both electrons accumulate large drift momenta or, equivalently, large final kinetic energies of up to $E_{max} = F_0^2/(2\omega^2) = 2U_P = 120$ eV for the present laser intensity. Obviously, inspecting doubly differential energy spectra for different emission angles ϑ with respect to the polarization in figure 3, this value sets an upper limit for the electron energies for emission along ε. Here the differences in the spectra between single and double ionization are even more significant: whereas the distribution strongly peaks at small energies for Ne^{1+} production, a broad maximum around 30 eV is observed for double ionization. Such a behaviour has not been observed in the previous measurements [15–17].

In contrast to the very different energy distributions for single and double ionization the electron angular distributions integrated over all electron energies are very similar, as illustrated in figure 4. In both cases, as might have been expected from the drift motion,

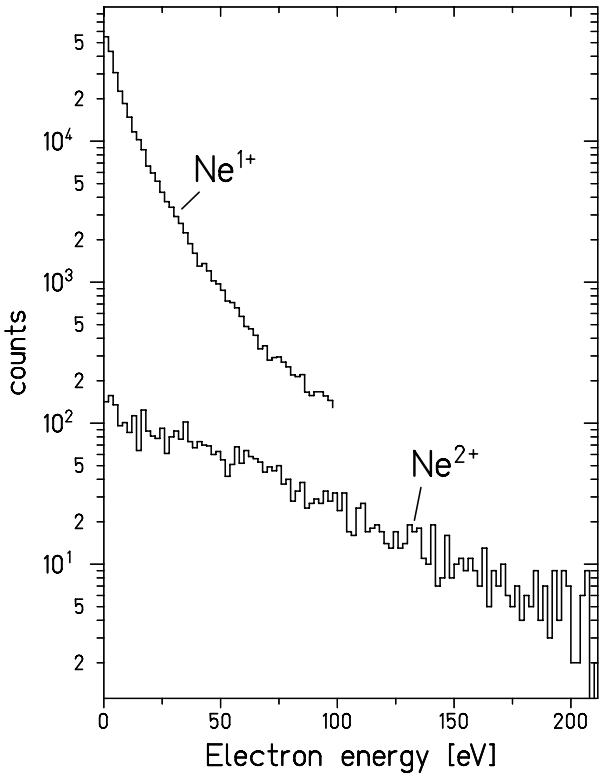

Figure 2. Electron energy distributions integrated over all emission angles for single and double ionization of Ne for the same laser parameters as in figure 1. In the case of double ionization the distribution of one (typical) of the two electrons is shown. The Ne^{2+} counts have to be divided by a factor of 10 to recover the experimental double- to single ionization ratio.

electrons are preferentially emitted along the polarization axis. Most surprisingly however, the angular distribution is significantly narrower for double ionization, intuitively contradicting the recollision scenario: during the (e, 2e)-like rescattering event the returning projectile electron, as well as the ionized electron, can gain considerable momenta in the transverse direction of up to $p_{\perp}^{max} < \sqrt{2(3.17U_P - I_p)}$ which, for the present laser intensity, can be as large as the maximum drift momentum of $2\sqrt{U_P}$. Hence, a substantial broadening of the angular emission would be expected and even electron emission angles of up to $\vartheta = 45^{\circ}$ might occur.

Staying within the recollision scenario, the sharply peaked angular distribution for electron emission in double ionization necessarily leads to the conclusion that large transverse electron momenta are unlikely to appear. Obviously, the dominant contribution to NS double ionization of Ne comes from nonviolent, soft (e, 2e) collisions with small energy and momentum transfers between the colliding partners, where the external field substantially assists in overcoming the binding energy of the second electron, i.e. at a most likely recollision phase where the field is not zero. Then, the ponderomotive force, acting along the polarization axis, dictates the emission characteristics of electrons being 'just' promoted into the continuum during recollision, resulting in a strongly directed, jet-like electron ejection with very similar longitudinal momenta, significantly below the maximum drift momentum. Such an interpretation is supported by recent measurements at laser intensities below the classical threshold for (e, 2e) during recollision, where the double-hump structure for Ne is still observed [25].

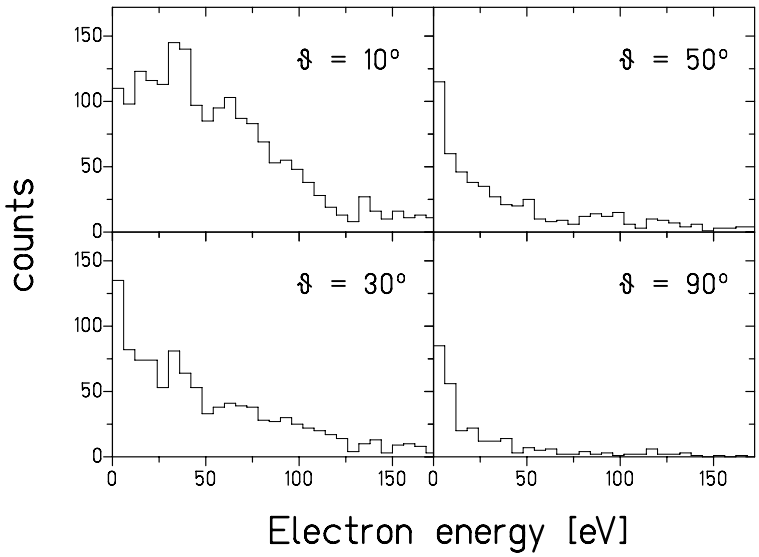

Figure 3. Electron energy distributions for fixed emission angles ϑ (integrated over $\Delta\vartheta = \pm 5°$) with respect to the polarization axis for double ionization of Ne. The distribution of one (typical) of the two electrons is shown.

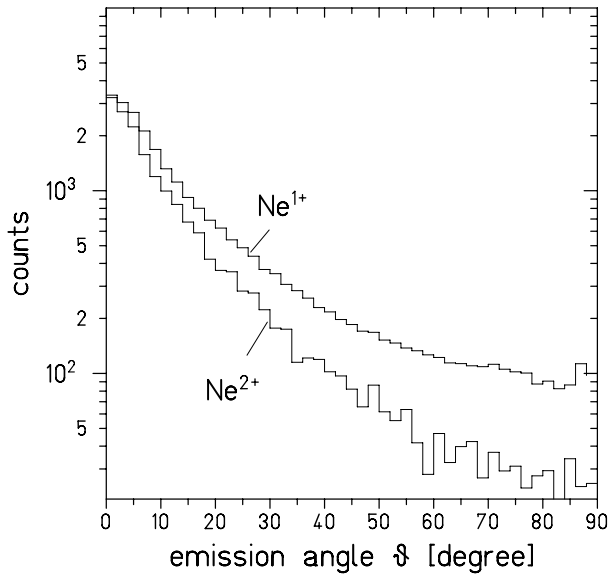

Figure 4. Angular distributions of electrons ejected in single and double ionization of Ne. The number of registered electrons per solid angle $\sin\vartheta\ \mathrm{d}\vartheta$ is plotted versus ϑ. Intensities are the same as in figure 1.

In summary, the first kinematically complete experimental data on NS double ionization in intense laser pulses have been presented. Strongly directed and correlated jet-like electron emission was observed. Even though the experimental data are in accordance with the kinematics of the rescattering mechanism, the attempt to interpret the data based on the well

known dynamics of field-free electron impact ionization fails. On the contrary, one is led to the conclusion that the laser field is crucially required to obtain double ionization: at a phase where the field is not zero, low-energy electrons are created during recollision whose kinematics is then dictated by the external field.

The experiments were supported by the Deutsche Forschungsgemeinschaft (DFG, RO 1929) and the Leibniz-Program of DFG. Support from GSI is gratefully acknowledged. We are grateful to R Dörner and W Becker for numerous discussions.

References

[1] Protopapas M, Keitel C H and Knight P L 1997 *Rep. Prog. Phys.* **60** 389
[2] Dörner R *et al* 2002 *Adv. At. Mol. Opt. Phys.* **48** 1
[3] Weber Th *et al* 2000 *Phys. Rev. Lett.* **84** 443
[4] Moshammer R *et al* 2000 *Phys. Rev. Lett.* **84** 447
[5] Becker A and Faisal F H M 2000 *Phys. Rev. Lett.* **84** 3546
[6] Lein M, Gross E K U and Engel V 2000 *Phys. Rev. Lett.* **85** 4707
[7] Haan S L *et al* 2000 *Opt. Express* **7** 29
[8] Goreslavskii S P, Popruzhenko S V, Kopold R and Becker W 2000 *Phys. Rev.* A **64** 053402
[9] Parker J S *et al* 2001 *J. Phys. B: At. Mol. Opt. Phys.* **33** L691
Parker J S *et al* 2001 *J. Phys. B: At. Mol. Opt. Phys.* **34** L69
[10] Kopold R *et al* 2000 *Phys. Rev. Lett.* **85** 3781
[11] Sacha K and Eckhard B 2001 *Phys. Rev.* A **63** 043414
[12] Fu L B, Liu J and Chen S G 2002 *Phys. Rev.* A **65** 021406
[13] Feuerstein B, Moshammer R and Ullrich J 2001 *J. Phys. B: At. Mol. Opt. Phys.* **33** L823
[14] Fittinghoff D N *et al* 1994 *Phys. Rev.* A **49** 2174
[15] Witzel B, Papadogiannis N A and Charalambidis D 2000 *Phys. Rev. Lett.* **85** 2268
[16] Peterson E R and Bucksbaum P H 2001 *Phys. Rev.* A **64** 053405
[17] Lafon R *et al* 2001 *Phys. Rev. Lett.* **86** 2762
[18] Bhardwaj V R *et al* 2001 *Phys. Rev. Lett.* **86** 3522
[19] Weber Th *et al* 2000 *Nature* **404** 608
[20] Feuerstein B *et al* 2001 *Phys. Rev. Lett.* **87** 043003-1
[21] Weckenbrock M *et al* 2001 *J. Phys. B: At. Mol. Opt. Phys.* **34** L449
[22] Moshammer R *et al* 2001 *Phys. Rev.* A **65** 035401
[23] Keldysh L V 1964 *Zh. Eksp. Teor. Fiz.* **47** 1945
[24] Delone N B and Krainov V P 1998 *Phys.–Usp.* **41** 469
[25] Eremina E *et al* 2002 *Phys. Rev. Lett.* submitted

Fragmentation of H_2^+ in strong 800-nm laser pulses: Initial-vibrational-state dependence

Bernold Feuerstein* and Uwe Thumm†
Department of Physics, Kansas State University, Manhattan, Kansas 66506
(Received 17 December 2002; published 15 April 2003)

The fragmentation of the H_2^+ molecular ion in 25-fs, 800-nm laser pulses in the intensity range 0.05–0.5 P W/cm^2 is investigated by means of wave-packet propagation calculations. We use a collinear reduced-dimensionality model that represents both the nuclear and electronic motion by one degree of freedom including non-Born-Oppenheimer couplings. In order to reproduce accurately the properties of the ''real'' three-dimensional molecule, we introduce a modified ''soft-core'' Coulomb potential with a softening function that depends on the internuclear distance. The analysis of the calculated flux of the outgoing wave packets allows us to obtain fragmentation probabilities and kinetic-energy spectra. Our results show that the relative probabilities for dissociation and Coulomb explosion depend critically on the initial vibrational state of the molecular ion.

DOI: 10.1103/PhysRevA.67.043405 PACS number(s): 33.80.Rv, 33.90.+h, 42.50.Hz

I. INTRODUCTION

This simplest molecule, the hydrogen molecular ion, is of fundamental interest in atomic and molecular physics. It constitutes a bound three-body Coulomb system which, in contrast to its atomic counterparts, the negative hydrogen ion and the helium atom, exhibits (if we neglect rotation) two time scales, the fast electronic motion (as scale) and the vibrational motion of the nuclei [femtosecond (fs) scale]. The interaction of this smallest molecule with strong fs laser pulses is of particular interest, since the pulse duration is comparable to the vibrational period (14 fs for H_2^+ in the vibrational ground state). Further, from a theoretical point of view, the simple structure of H_2^+ allows for a numerical solution of the time-dependent Schrödinger equation within reduced dimensionality models by using, e.g., standard Crank-Nicholson split-operator propagation techniques [1–7].

Interacting with a strong, linearly polarized laser field, H_2^+ exhibits two fragmentation channels, dissociation

$$H_2^+ + n\hbar\omega \rightarrow p + H, \tag{1}$$

and Coulomb explosion (CE)

$$H_2^+ + n'\hbar\omega \rightarrow p + p + e^-. \tag{2}$$

The fragmentation of H_2^+ in strong laser fields has been considered in numerous theoretical investigations emphasizing the influence of the two-center nature of the electronic potential on strong-field ionization [3,4,8–15]. Here, the laser-induced coupling of the lowest electronic states $1s\sigma_g$ and $2p\sigma_u$ results in a localization of the electron near one of the nuclei. The electron cloud oscillates between the nuclei and gives rise to dissociation of the molecule and to ''charge resonance enhanced ionization'' (CREI) at intermediate internuclear distances R between 5 and 10 a.u. [4,8,9].

Experimentally, the situation is more challenging since mostly neutral H_2 targets are available [16–22], such that the production and fragmentation of the molecular ion occur in the same laser pulse and are difficult to separate. It was shown that for 50-fs pulses, saturation of H_2^+ is never reached at any intensity [19]. Hence, there is a growing interest in molecular ions as targets which have been investigated in two recent experiments [23,24]. In this work, we consider the vibrational-state dependence of the fragmentation yields for the processes (1) and (2). The experimental data of Posthumus *et al.* [19] show that there is competition of dissociation and CREI for intensities around 10^{14} W/cm^2. We use wave-packet propagation calculations in a collinear 2×1D (one-dimensional) model to derive dissociation and CE probabilities and the corresponding kinetic-energy spectra for the fragments.

This paper is structured as follows. First, in Sec. II, we describe our theoretical model with emphasis on the effects of the reduced dimensionality on the potential curves of H_2^+. This section includes a discussion of the properties of the widely used ''soft-core'' (SC) Coulomb potential [25] for the electron-nucleus interaction (Sec. II A). In Sec. II B, we present an improved SC Coulomb potential which allows the exact reproduction of the 3D ground-state potential curve of H_2^+. Next, we provide kinetic-energy spectra by applying the recently proposed ''virtual detector'' method [26] to the laser-induced fragmentation of H_2^+. We present and discus the numerical results for the vibrational-state dependence of the fragmentation dynamics including the intensity dependence for two selected vibrational states (Sec. III). Our concluding remarks follow in Sec. IV. Atomic units are used throughout this paper, unless otherwise indicated.

II. THEORETICAL MODEL

For linearly polarized nonrelativistic laser fields considered here, only the coordinates parallel to the electric-field vector play an important role. Thus, in order to keep the computational effort at a reasonable level, we describe the molecular ion in a collinear model. This reduced-dimensionality model includes two coordinates, the elec-

*Electronic address: feuerstb@mpi-hd.mpg.de
†Electronic address: thumm@phys.ksu.edu

tronic coordinate z relative to the center of mass of the nuclei and the internuclear distance R. The model-inherent alignment of the molecule along the polarization axis is not a serious problem, since in a kinematically complete experiment fragmentation along this axis can be selected. We note that the model includes non-Born-Oppenheimer couplings between the electronic and nuclear motion. The solution of the time-dependent Schrödinger equation is formally given by the propagation of the initial wave function,

$$\Psi(z,R,t)=\exp\left[-i\int_0^t dt'\,\mathcal{H}(z,R,t')\right]\Psi(z,R,t=0) \quad (3)$$

with the Hamiltonian

$$\mathcal{H}(z,R,t)=\mathcal{T}_R+V_{nn}(R)+\mathcal{H}_{el}, \quad (4a)$$

$$\mathcal{H}_{el}=\mathcal{T}_z+V_{en}(z,R)+F(t)z. \quad (4b)$$

$\mathcal{T}_R$ and $\mathcal{T}_z$ are the kinetic-energy operators for the electronic and the nuclear motion. $V_{nn}(R)=1/R$ is the internuclear Coulomb potential and $V_{en}(z,R)$ the two-center Coulomb potential for the electron-nucleus interaction. The interaction of the electric component $F(t)$ of the laser field with the electron is given in dipole approximation in the length gauge. The propagation (3) is carried out numerically on a grid using the Crank-Nicholson split-operator method which provides unconditional numerical stability [27]. Here, for each time step Δt, the wave function at time $t+\Delta t$ is recursively given by

$$\Psi(t+\Delta t)=\exp[-\tfrac{1}{2}i\mathcal{T}_R\Delta t]\exp[-i(V_{nn}+\mathcal{H}_{el})\Delta t]\times\exp[-\tfrac{1}{2}i\mathcal{T}_R\Delta t]\Psi(t)+O(\Delta t^3). \quad (5)$$

In order to avoid the singularity of the Coulomb potential in 1D calculations, usually a SC Coulomb potential is introduced [3,25].

A. Soft-core Coulomb potential for H_2^+

Before we discus the application of the SC potential to the H_2^+ molecular ion, we briefly consider its basic properties. The SC Coulomb potential is given by

$$V_{\mathrm{SC}}(z)=\frac{-Q}{\sqrt{z^2+a^2}}. \quad (6)$$

Q describes the (effective) nuclear charge of the atom/ion, and a is a ''softening'' parameter which removes the singularity at $z=0$. For large z, this looks like a Coulomb potential $-Q/z$ whereas the behavior for small z resembles a harmonic-oscillator potential

$$V_{\mathrm{SC}}(z)=-Q/a+Qz^2/(2a^2)+O(z^3). \quad (7)$$

The parameter a can be adjusted in order to reproduce the correct ground-state energy. In principle, one could also change the parameter Q. However, this would lead to an unphysical asymptotic behavior of the potential, and Q would differ from the asymptotic charge seen by the electron at large distances z. For one-electron systems, such as hydrogenlike ions, it turns out that for each value of Q the parameter a has to be adjusted separately in order to reproduce the correct binding energy of the ground state.

In the case of H_2^+, the two-center potential requires a continuous adjustment of a while the internuclear distance R is changed. The two limiting cases are $R=0$ (He atom, $a=0.709$) and $R\to\infty$ (H atom, $a=1.415$). In their previous work, Kulander, Mies, and Schafer [3] suggested a softening function $a(R)$, but did not use it for their calculations. Instead, they keep $a=1$ fixed for all internuclear distances. They compare the basic properties of their 1D model molecule with known 3D results for the shape of the two lowest electronic state ($1s\sigma_g$ and $2p\sigma_u$) potential curves and the dipole matrix element $d_{ug}=\langle 2p\sigma_u|z|1s\sigma_g\rangle$ coupling these states. It has been shown [4,8,9] that these two states and their coupling are most important for the dynamics of H_2^+ in strong laser fields. The degeneracy of $1s\sigma_g$ and $2p\sigma_u$ electronic states enables charge localization at one nucleus and results in a diverging dipole moment which increases linearly with R. The shape of the potential curves also affects the positions of (avoided) crossings of the different $n\omega$ Floquet channels, corresponding to a net absorption of $n=1$, 2, or 3) photons [16]. Figure 1(a) shows these 1D dressed potential curves for a fixed softening parameter $a=1$ in comparison with the result of a full 3D calculation. We find the $1s\sigma_g$ curve in the 1D model from Ref. [3] shifted to larger R by 30% in the equilibrium distance whereas the $2p\sigma_u$ curves show a better overall agreement of the 1D and 3D calculations. The larger equilibrium distance R_0 in Kulander's model is crucial, since the ionization probability depends critically on the position of R_0 relative to the curve crossings. A comparison of the model molecular properties with the corresponding exact 3D values is given in Table I. The anharmonicity constant $\omega_e x_e$ is obtained by fitting the lowest vibrational energies in the $1s\sigma_g$ potential curve to the expression $E_v=\omega_e(v+\frac{1}{2})-\omega_e x_e(v+\frac{1}{2})^2$. Figure 2 shows the 1D and 3D values for the coupling dipole moment d_{ug} of the lowest electronic states as a function of R.

B. Improved soft-core Coulomb potential for H_2^+

Based on the idea of Kulander, Mies, and Schafer [3] to use a softening function $a(R)$, we now attempt to find a more realistic 1D model. The SC Coulomb potential (7) behaves like a harmonic-oscillator potential for small z. The parameter a determines simultaneously the depth $-Q/a$ and width of the potential. The width is proportional to $a/\sqrt{Q}$, i.e., it is given by the prefactor Q/a^2 of the quadratic term. Our idea is now to control depth and width of the SC Coulomb potential for H_2^+ independently in order to reproduce the exact $1s\sigma_g$ curve and, at the same time, to yield a reasonable agreement for $2p\sigma_u$. This modified SC Coulomb potential is given by

$$V_{\mathrm{SCmod}}(z)=\frac{-Q}{1/a-a/b+\sqrt{z^2+(a/b)^2}}, \quad (8)$$

with two parameters a and b. For small z we find

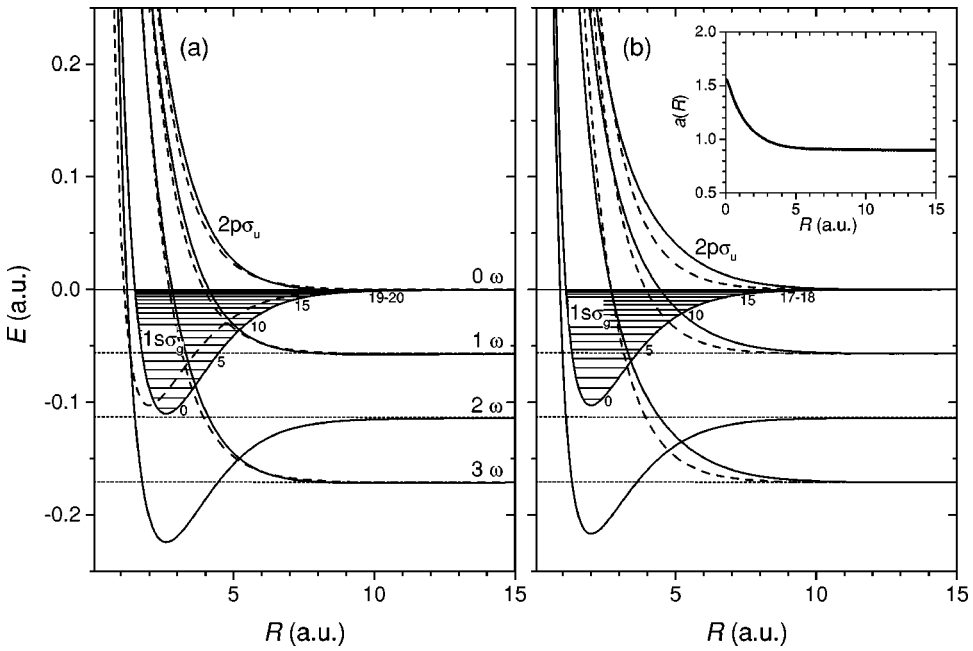

FIG. 1. Dressed $n\omega$ ($n=0,\ldots,3$) Floquet potential curves and vibrational energy levels for the two lowest electronic states $1s\sigma_g$ and $2p\sigma_u$ of H_2^+. Solid curves, 1D model molecule; dashed curves, full 3D result. (a) Model by Kulander, Mies, and Schafer [3] using the SC Coulomb potential (6) with a fixed softening parameter $a=1$. (b) Improved model (this work) based on the modified SC Coulomb potential (8) with the softening function $a(R)$ (shown in the inset).

$V_{\mathrm{SCmod}}(z)\approx -Q(a-\frac{1}{2}bz^2)$, whereas for large z the asymptotic behavior $-Q/z$ is unchanged. Using V_{SCmod}, the two-center model potential in Eq. (4) for H_2^+ ($Q=1$) takes the form

$$V_{en}(z,R)=\frac{-1}{1/a(R)-a(R)/b+\sqrt{z_-^2+[a(R)/b]^2}}+\frac{-1}{1/a(R)-a(R)/b+\sqrt{z_+^2+[a(R)/b]^2}},$$

$$z_\pm=z\pm R/2. \tag{9}$$

For a given value of b, the function $a(R)$ is adjusted to *exactly* reproduce the 3D potential curve of $1s\sigma_g$. b is a fixed parameter which determines the shape of the repulsive $2p\sigma_u$ curve. The result for $b=5$ in comparison with the 3D curves is shown in Fig. 1(b) with the function $a(R)$ given as an inset. There is still some difference between our 1D and the full 3D models for the $2p\sigma_u$ potential curve. A better agreement can be achieved for larger values of b but this makes the potential more and more cusplike at the position of the nuclei. This limits the value of b since for practicable grid spacings the numerical grid cannot resolve a very narrow potential cusp. We found that $b=5$ models the repulsive $2p\sigma_u$ potential curve well without causing spurious effects in the numerical propagation on the grid. Based on our modified SC Coulomb potential (9), we calculated the properties of our 1D model molecule. In comparison with the 1D SC Coulomb potential from Ref. [3], our results are in better agreement with the 3D data (see Fig. 1 and Table I). In

TABLE I. Properties of the 1D model molecule compared with the real 3D molecule (atomic units). R_0, equilibrium internuclear distance; D_e, dissociation energy; ω_e, ground-state frequency; $\omega_e x_e$, anharmonicity constant; I_p, ionization potential.

			1D model	
		3D result[a]	[3]	This work
R_0		2.0	2.6	2.0
D_e		0.103	0.11	0.103
ω_e		1.06×10^{-2}	9.93×10^{-3}	1.06×10^{-2}
$\omega_e x_e$		3.02×10^{-4}	2.02×10^{-4}	3.02×10^{-4}
$I_p(R_0)$		1.1	1.154	1.1
Number of bound states		19	21	19
1ω crossing	R	4.8	5.2	5.2
	v	9	9	10
3ω crossing	R	3.3	3.6	3.4
	v	3	2	4
1ω threshold		$v\geqslant5$	$v\geqslant6$	$v\geqslant5$

[a]Molecular constants from Ref. [28].

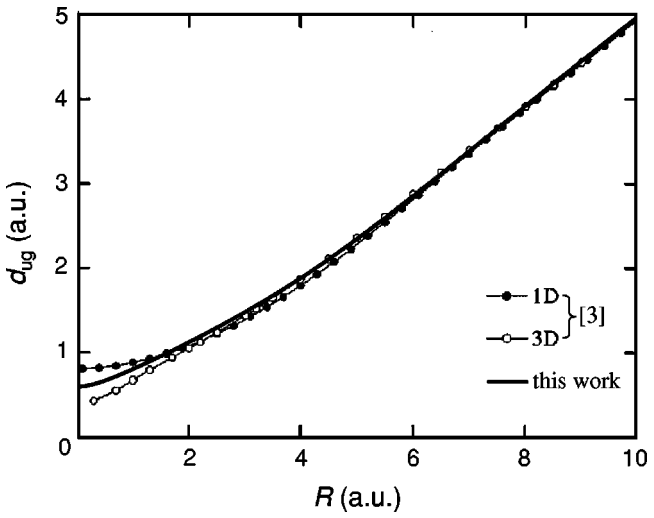

FIG. 2. Dipole coupling matrix element $d_{ug}=\langle 2p\sigma_u|z|1s\sigma_g\rangle$ for the lowest electronic sates of H_2^+. One-dimensional model calculation of this work compared with the former result (1D model and full 3D calculation) from Ref. [3].

addition, the dipole moment d_{ug} is slightly better reproduced than by the simple SC Coulomb potential (Fig. 2).

We note that by adjusting a softening function $a(R)$ only in a model potential $V(z,R)=-Q/\sqrt{z^2+a(R)^2}$, the $1s\sigma_g$ potential curve can also be exactly reproduced. However, the shape of the corresponding repulsive $2p\sigma_u$ curve is in quite poor agreement with the 3D result. This led us to introduce a second free parameter b in Eqs. (8) and (9).

C. Numerical propagation scheme

Our numerical grid extends from 0.05 to 30 in R with a spacing of 0.05 and from -45 to 45 in z with a spacing of 0.2. Absorbing regions using an optical potential are introduced in order to prevent the reflection of the outgoing wave packets at the border of the grid. We implemented this absorber as fourth-order optical potentials in z and R:

$$V_{\rm opt}(z,R)=-i[V_z(z)+V_R(R)], \tag{10a}$$

$$V_z(z)=\begin{cases}5[(-25-z)/20]^4, & z\leqslant -25\\ 5[(z-25)/20]^4, & z\geqslant 25\\ 0 & \text{otherwise,}\end{cases} \tag{10b}$$

$$V_R(R)=\begin{cases}0.05[(R-20)/10]^4, & R\geqslant 20\\ 0 & \text{otherwise.}\end{cases} \tag{10c}$$

The number of time steps per optical cycle is 1100. For each time step the norm of the total wave function within $0.05\leqslant R\leqslant 20$, $-25\leqslant z\leqslant 25$ is calculated. The outgoing current flux through the borders $z_{vd}=\pm 25$, $R_{vd}=20$ of this inner part of the grid is used to obtain differential and integrated data on the fragmentation process. If we write the outgoing wave packet in terms of a real amplitude A and a real phase ϕ,

$$\Psi(z,R,t)=A(z,R,t)\exp[i\phi(z,R,t)], \tag{11}$$

we find the current density

$$\mathbf{j}(z,R,t)=\frac{|A(z,R,t)|^2}{m}\nabla\phi(z,R,t). \tag{12}$$

Here, m is the mass of the particle. The dissociation yield D into the fragmentation channel (1) is given by the time-integrated nuclear flux in the R direction at R_{vd},

$$D(t)=\int_0^t dt'\int_{-z_{vd}}^{+z_{vd}} dz\, j_R(z,R_{vd},t'). \tag{13}$$

Removal of the electron leads to CE, the yield of which is given by the time-integrated electronic flux in the z direction at $z=\pm z_{vd}$,

$$\mathrm{C}(t)=\int_0^t dt'\int_{0.05}^{R_{vd}} dR\, j_z(z_{vd},R,t'). \tag{14}$$

We derive the nuclear momentum distribution for dissociation using the ''virtual detector'' method [26] and imagine virtual detectors for the nuclear and electronic flux at the positions R_{vd} and $\pm z_{vd}$ indicated above. At each time step t_i, we numerically calculate the gradient of ϕ at R_{vd} using a five-point formula for the momentum,

$$p_R^{(D)}(z,t_i)=\left.\frac{\partial}{\partial R}\right|_{R_{vd}}\phi(z,R,t_i). \tag{15}$$

Integration over z and binning of the momentum values for all times t_i yield the momentum distribution for dissociation.

The CE momentum spectra are obtained by first computing the ionization rate as the outgoing electron flux through $\pm z_{vd}$ at a given internuclear distance R. During the (fast) ionization of the electron we treat the (slow) nuclei as ''frozen.'' For each R, the Coulomb energy $1/R$ is released. In order to take the initial (dissociative) momentum

$$p_{\rm init}(R,t_i)=\left.\frac{\partial}{\partial R}\right|_{z_{vd}}\phi(z,R,t_i) \tag{16}$$

of the nuclei into account, we add the Coulomb energy and the initial kinetic energy of the nuclei at the ionization time and obtain the final momentum

$$p_R^{(\rm CE)}(R,t_i)=\sqrt{p_{\rm init}^2(R,t_i)+2\mu/R} \tag{17}$$

of the released fragments. Here, μ is the reduced mass of the nuclei. Analogous to the dissociation, integration over R and binning of the nuclear momentum values for all times t_i give the momentum distribution for CE.

III. RESULTS

Before we discus the vibrational-state dependence of the fragmentation of H_2^+ in a 25-fs laser pulse, we consider the intensity dependence for two selected vibrational states $|v=3\rangle$ and $|v=6\rangle$. The main difference between these states is the fact that $|v=3\rangle$ lies below the threshold for the 1ω

Floquet channel whereas states $|v=5\rangle$ or higher can decay into the 1ω as well as into the 2ω [29] channel that is open for all v states (see Fig. 1). Thus, lower v initial states need excited-state contributions $|v\geqslant 5\rangle$ in order to decay into the 1ω dissociation channel.

Vibrational excitation is likely in sufficiently short and intense laser pulses if the electric-field envelope changes significantly on the time scale of the vibrational motion. In this case, the time dependence of the dressed (Floquet) potential curves leads to nonadiabatic transitions between vibrational states. The influence of the pulse duration on the kinetic-energy spectra has been demonstrated by Frasinski *et al.* [18]. We note that these transitions are mediated by the interaction of the electron cloud with the laser field, since the nuclei cannot absorb photons directly. For all calculations, we used $\sin^2$ shaped 25-fs full width at half maximum pulses of 800-nm wavelength.

A. Fragmentation of H_2^+ ($v=3$) in a 25-fs laser pulse: Intensity dependence

Figure 3(a) shows the time-dependent norm

$$N(t)=\int_{0.05}^{R_{vd}} dR \int_{-z_{vd}}^{+z_{vd}} dz |\Psi(z,R,t)|^2 \tag{18}$$

and the probabilities for dissociation $D(t)$ and Coulomb explosion $C(t)$ for H_2^+ ($v=3$) interacting with a 25-fs laser pulse of intensity $I=0.2$ PW/cm^2. We find 20% probability for dissociation and 70% for CE. The time evolution of the nuclear probability density

$$P(R,t)=\int_{-z_{vd}}^{+z_{vd}} dz |\Psi(z,R,t)|^2 \tag{19}$$

is illustrated in Fig. 3(b) with contour lines indicating the electronic ionization rate due to CREI. In the density plot, the dissociation appears as a threefold jetlike structure. This structure can be associated with distinct peaks in the dissociation kinetic-energy spectrum shown as a solid line in Fig. 3(c) for intensities in the range from 0.05 to 0.5 PW/cm^2. The kinetic-energy range for one- and two-photon absorption into Floquet channels for all vibrational states is given by the shaded areas. For 0.1 PW/cm^2, we find the strongest dissociation. With increasing intensities, Coulomb explosion (dashed line) becomes dominant and results in the reduction of the final dissociation probability. At 0.2 PW/cm^2, the CE spectrum forms a broad peak between 4 and 8 eV corresponding to internuclear distances in the CREI region in Fig. 3(b) at $3.5\leqslant R\leqslant 7$. The CE peak is shifted towards higher kinetic energies for 0.5 PW/cm^2, showing a substructure which reflects the nodes of the initial wave function.

B. Fragmentation of H_2^+ ($v=6$) in a 25-fs laser pulse: Intensity dependence

Figure 4 shows the fragmentation dynamics of the $|v=6\rangle$ initial state. Compared to $v=3$, at 0.2 PW/cm^2 the dissociation probability is reduced to 10% and the CE enhanced to 88%. For the lower intensities, dissociation is much stronger than for the $|v=3\rangle$ initial state, mainly due to the opening of the 1ω channel [note the different scale in the upper row of Fig. 4(c)]. The CE spectra behave similarly to the $v=3$ case but with a generally higher ionization probability. The intensity dependence of the fragmentation (dissociation and CE) probabilities for the $|v=3\rangle$ and $|v=6\rangle$ initial states is summarized in Fig. 5. For $|v=3\rangle$, the dissociation channel shows a maximum of 37% around 0.1 PW/cm^2 whereas for $|v=6\rangle$ the dissociation probability increases further with decreasing intensity up to 73% at 0.05 PW/cm^2. The ionization (CE) probability reaches saturation for both initial states at 0.5 PW/cm^2.

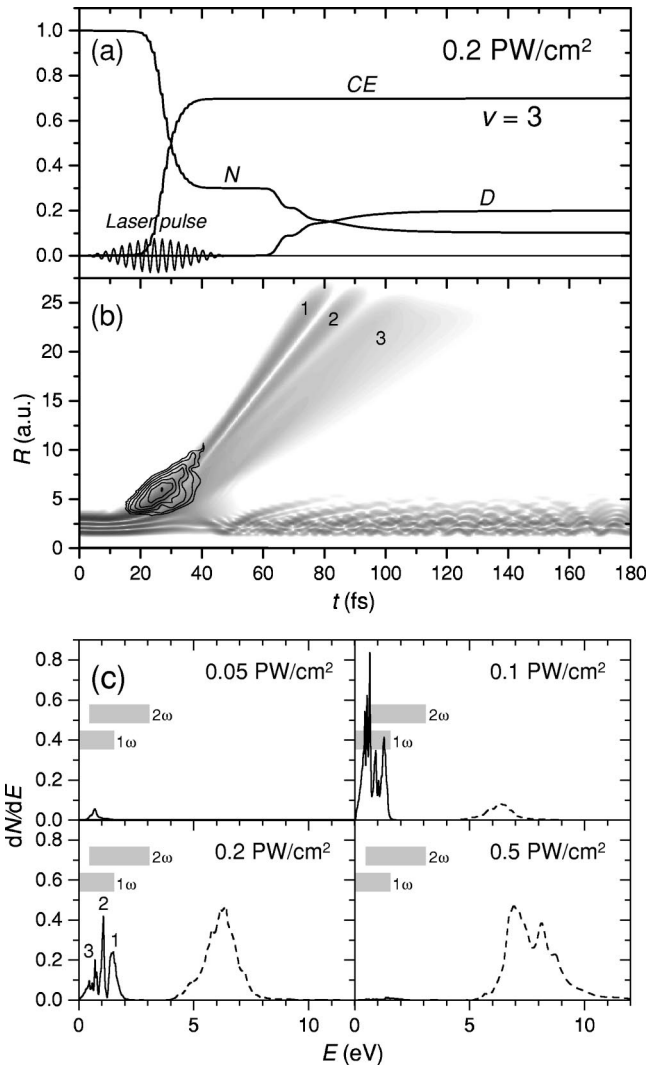

FIG. 3. Fragmentation of H_2^+ ($v=3$) in a 25-fs laser pulse. (a) Time-dependent norm (N) and probabilities for Coulomb explosion (CE) and dissociation (D) at $I=0.2$ PW/cm^2. (b) Corresponding probability density $P(R,t)$ (logarithmic gray scale) and ionization rates (contour lines). (c) Kinetic-energy spectra for dissociation (solid lines) and CE (dashed lines) for intensities in the range from 0.05 to 0.5 PW/cm^2.

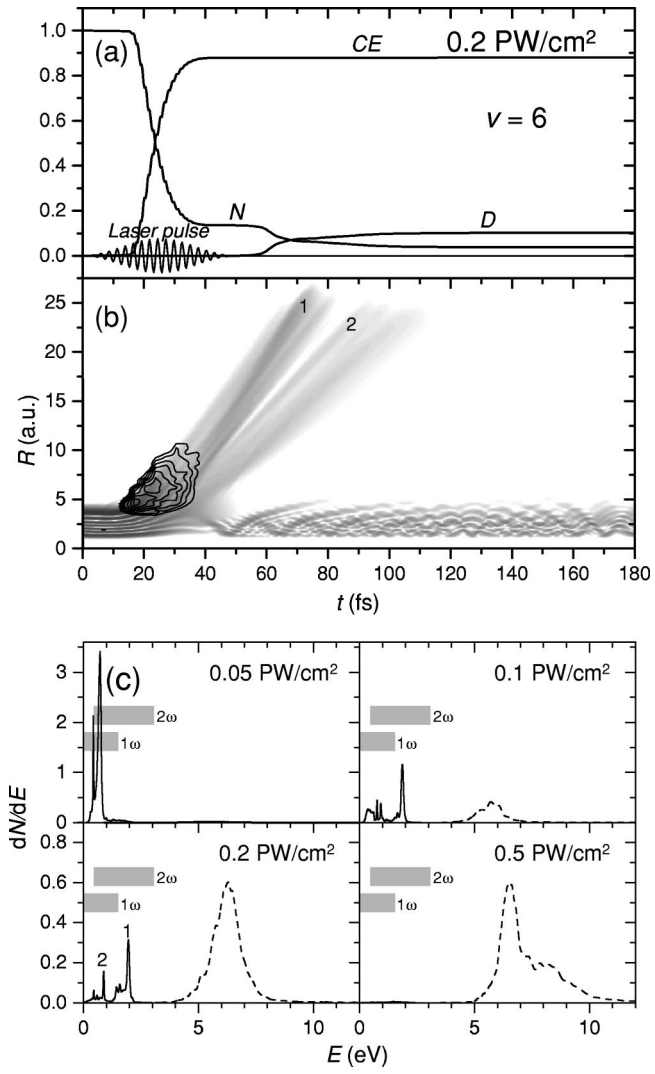

FIG. 4. Same as Fig. 3 but with $|v=6\rangle$ as initial state.

C. Fragmentation of H_2^+ in a 25-fs 0.2-P W/cm^2 laser pulse: Vibrational-state dependence

As mentioned above, for 25-fs pulses we have a competition of dissociation and CREI at an intensity of $\approx$0.2 PW/cm^2. Figure 6 shows the fragment kinetic-energy spectra for the initial states $|v\rangle$, $v=0-2$, 4, 5, 7–9 [for $v=3$, 6, see Figs. 3(c) and 4(c)]. These states significantly contribute to a Franck-Condon distribution one would expect for H_2^+ created in an ion source [24] (see Franck-Condon factors in Fig. 7). We find the vibrational ground state being almost stable against fragmentation. With increasing v, first dissociation dominates with a maximum probability of 33% for $|v=2\rangle$. Then CREI becomes more and more favorable at the expense of dissociation with ionization probabilities $>$90% for $|v=7\rangle$ and higher (see Fig. 7). There is also a noticeable shift in the dissociation spectra from the 1ω to the 2ω region (indicated by the shaded areas).

The v-dependent behavior of the ionization probability can be explained in the following way. For the low v states, we have first an expansion of the molecule due to bond softening. Once R reaches the ''critical'' region of 5–10, CREI becomes likely. With increasing v the overlap of the initial wave function with the CREI region becomes larger. In addition, these states are more sensitive to the bond softening. The increasing overlap of the initial states with the CREI

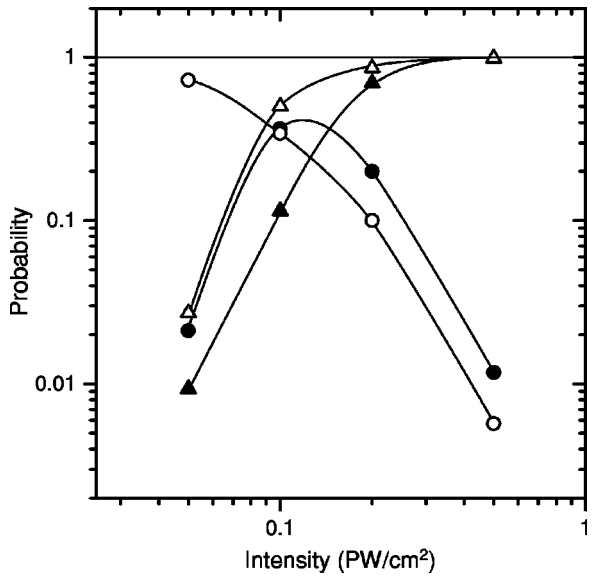

FIG. 5. Intensity dependence of the fragmentation probabilities. $|v=3\rangle$ initial state: ●, dissociation; ▲, CE. $|v=6\rangle$ initial state: ○, dissociation; △, CE. The curves joining the points only serve to guide the eye.

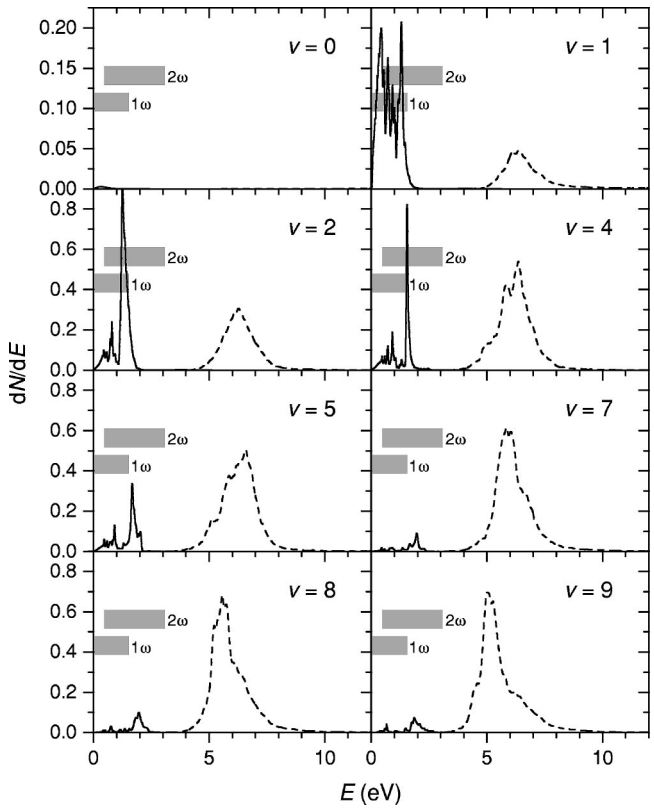

FIG. 6. Fragmentation of H_2^+ in a 25-fs laser pulse at $I=0.2$ PW/cm^2. Kinetic-energy spectra for dissociation (solid lines) and CE (dashed lines) for initial vibrational states $|v\rangle$, $v=0-2$, 4, 5, 7–9 [for $v=3$, 6 see Figs. 3(c) and 4(c)].

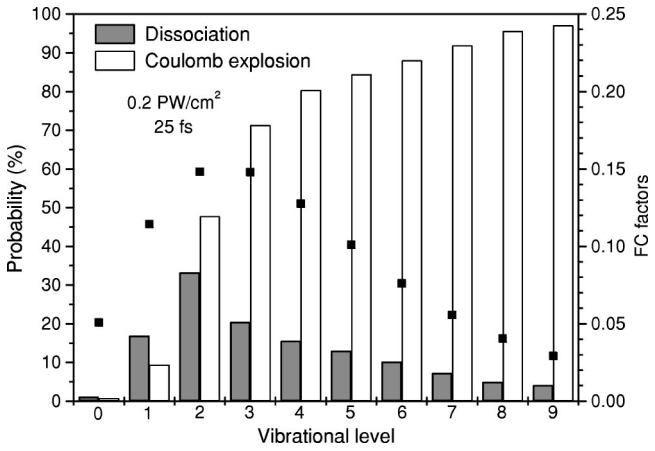

FIG. 7. Fragmentation of H_2^+ in a 25-fs laser pulse at $I = 0.2$ PW/cm^2. Initial-vibrational-state dependence of the probabilities for dissociation and CE. The black squares show the Franck-Condon factors (right scale) $|\langle H_2^+, v|H_2, v=0\rangle|^2$.

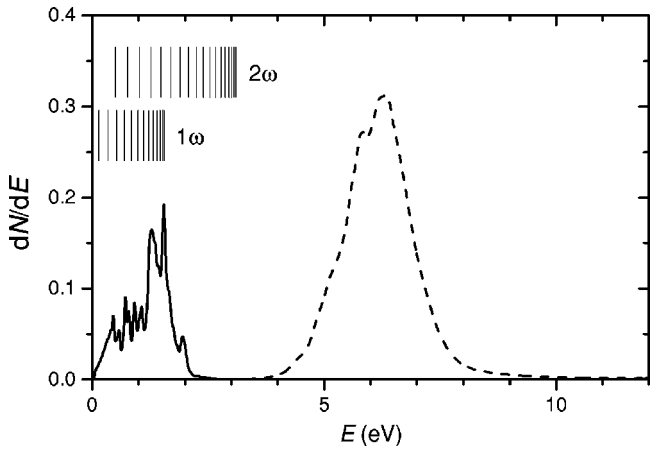

FIG. 8. Fragmentation of H_2^+ in a 25-fs laser pulse at $I = 0.2$ PW/cm^2. Kinetic-energy spectra for dissociation (solid lines) and CE (dashed lines) for a statistical (Franck-Condon) mixture of initial vibrational states.

region shifts the range where ionization occurs towards larger R. This results in lower Coulomb energy release, i.e., in a slight shift of the CREI peak in the spectrum from 6.5 eV ($v=1$) to 5 eV ($v=9$).

So far no experiment with selected pure initial vibrational states has been done due to technical difficulties. Ion sources usually provide a broad distribution of $|v\rangle$ states. The kinetic-energy spectrum for this kind of ensemble is shown in Fig. 8 for a 25-fs, 0.2-PW/cm^2 pulse. Here, we added the spectra for all significant states ($v=0,\ldots,9$), weighted with the Franck-Condon factors. As a result of this summation, much of the interesting v dependence is lost. An alternative to the preparation of pure states is the use of not too intense, ''long'' (>100 fs) pulses, which avoid nonadiabatic vibrational excitations. In this case, high-resolution spectroscopy allows the identification of individual $|v\rangle$ states in the 1ω and 2ω dissociation spectrum, as it has been done in the recent experiment by Sändig, Figger, and Hänsch [23].

IV. CONCLUSION

Using wave-packet propagation calculations within a collinear reduced-dimensionality model, we investigated the fragmentation of the H_2^+ molecular ion in 25-fs, 800-nm laser pulses in the intensity range 0.05–0.5 PW/cm^2. Our model represents both the nuclear and electronic motion by one degree of freedom including non-Born-Oppenheimer couplings. By introduction of a modified soft-core Coulomb potential for the electron-nucleus interaction with a softening function that depends on the internuclear distance, we were able to reproduce accurately essential properties of the ''real'' 3D molecule. We calculated the probabilities and kinetic-energy spectra for dissociation and CE of the molecule for various intensities and initial vibrational states. For the initial vibrational states $|v=3\rangle$ and $|v=6\rangle$ and different intensities, we demonstrated the effect of the threshold ($v \geqslant 5$) for the 1ω Floquet channel. For 0.2 PW/cm^2, our calculation revealed a strong vibrational-state dependence of the branching ratio between dissociation and CE. We found that dissociation dominates for molecular ions that are prepared in the two lowest vibrational states only, while CE becomes more and more dominant for higher vibrational states. The latter is caused by the increasing overlap of the initial nuclear wave function with the region of internuclear distances where CREI leads to high ionization probabilities. We also considered an incoherent (Franck-Condon) mixture of vibrational states, e.g., a beam of molecular ions created in an ion source. In contrast to a coherent superposition of vibrational states, the time dependence of which could be studied in a two-pulse pump-probe experiment [6], some of the interesting v dependence is lost after averaging over the Franck-Condon distribution. We hope that our work stimulates challenging future experimental investigations including the preparation of selected vibrational states.

ACKNOWLEDGMENTS

This work was supported in part by the National Science Foundation (Grant No. PHY-0071035) and the Division of Chemical Sciences, Office of Basic Energy Sciences, Office of Energy Research, U.S. Department of Energy. B.F. acknowledges the financial support from the Deutsche Forschungsgemeinschaft.

[1] M. R. Hermann and J. A. Fleck, Jr., Phys. Rev. A **38**, 6000 (1988).
[2] R. Kosloff, Annu. Rev. Phys. Chem. **45**, 145 (1994).
[3] K. C. Kulander, F. H. Mies, and K. J. Schafer, Phys. Rev. A **53**, 2562 (1996).
[4] S. Chelkowski, A. Conjusteau, T. Zuo, and A. D. Bandrauk, Phys. Rev. A **54**, 3235 (1996).
[5] A. G. Borisov, A. K. Kazansky, and J. P. Gauyacq, Phys. Rev.

B **59**, 10 935 (1999).
[6] B. Feuerstein and U. Thumm, Phys. Rev. A (to be published).
[7] U. Thumm, in *XXII International Conference on the Physics of Photonic, Electronic and Atomic Collisions, Santa Fe, New Mexico*, edited by S. Datz *et al.* (Rinton, Princeton, NJ, 2002), p. 592.
[8] T. Seideman, M. Y. Ivanov, and P. B. Corkum, Phys. Rev. Lett. **75**, 2819 (1995).
[9] T. Zuo and A. D. Bandrauk, Phys. Rev. A **52**, R2511 (1995).
[10] M. Plummer and J. F. McCann, J. Phys. B **29**, 4625 (1996).
[11] T. D. G. Walsh, F. A. Ilkov, S. L. Chin, F. Châteauneuf, T. T. Nguyen-Dang, S. Chelkowski, A. D. Bandrauk, and O. Atabek, Phys. Rev. A **58**, 3922 (1998).
[12] I. Kawata, H. Kono, and Y. Fujimura, J. Chem. Phys. **110**, 11152 (1999).
[13] D. Dundas, J. F. McCann, J. S. Parker, and K. T. Taylor, J. Phys. B **33**, 3261 (2000).
[14] Y. Duan, W.-K. Liu, and J.-M. Yuan, Phys. Rev. A **61**, 053403 (2000).
[15] M. E. Sukharev and V. P. Krainov, Phys. Rev. A **62**, 033404 (2000).
[16] G. N. Gibson, M. Li, C. Guo, and J. Neira, Phys. Rev. Lett. **79**, 2022 (1997).
[17] T. D. G. Walsh, F. A. Ilkov, and S. L. Chin, J. Phys. B **30**, 2167 (1997).
[18] L. J. Frasinski, J. H. Posthumus, J. Plumridge, K. Codling, P. F. Taday, and A. J. Langley, Phys. Rev. Lett. **83**, 3625 (1999).
[19] J. H. Posthumus, J. Plumridge, P. F. Taday, J. H. Sanderson, A. J. Langley, K. Codling, and W. A. Bryan, J. Phys. B **32**, L93 (1999).
[20] C. Trump, H. Rottke, and W. Sandner, Phys. Rev. A **59**, 2858 (1999); **60**, 3924 (1999).
[21] A. Staudte, C. L. Cocke, M. H. Prior, A. Belkacem, C. Ray, H. W. Chong, T. E. Glover, R. W. Schoenlein, and U. Saalmann, Phys. Rev. A **65**, 020703 (2002).
[22] H. Rottke, C. Trump, M. Wittmann, G. Korn, W. Sandner, R. Moshammer, A. Dorn, C. D. Schröter, D. Fischer, J. R. Crespo Lopez-Urrutia, P. Neumayer, J. Deipenwisch, C. Höhr, B. Feuerstein, and J. Ullrich, Phys. Rev. Lett. **89**, 013001 (2002).
[23] K. Sändig, H. Figger, and T. W. Hänsch, Phys. Rev. Lett. **85**, 4876 (2000).
[24] I. D. Williams, P. McKenna, B. Srigengan, I. M. G. Johnston, W. A. Bryan, J. H. Sanderson, A. El-Zein, T. R. J. Goodworth, W. R. Newell, P. F. Taday, and A. J. Langley, J. Phys. B **33**, 2743 (2000).
[25] Q. Su and J. H. Eberly, Phys. Rev. A **44**, 5997 (1991).
[26] B. Feuerstein and U. Thumm, J. Phys. B **36**, 707 (2003).
[27] W. H. Press, S. A. Teukolsky, W. T. Vetterling, and B. F. Flannery, *Numerical Recipes* (Cambridge University Press, Cambridge, 1992), p. 842.
[28] K. P. Huber and G. Herzberg, *Molecular Structure and Molecular Spectra IV. Constants of Diatomic Molecules* (Van Nostrand Reinhold, New York, 1979).
[29] We note that this channel corresponds to a *net* absorption of two photons. In fact, this channel exhibits first an absorption of three photons at the ''3ω'' crossing followed by a reemission of one photon at the subsequent ''1ω'' crossing (see also Fig. 1).

Mapping of coherent and decohering nuclear wave-packet dynamics in D_2^+ with ultrashort laser pulses

Bernold Feuerstein and Uwe Thumm
Department of Physics, Kansas State University, Manhattan, Kansas 66506, USA
(Received 11 November 2002; published 26 June 2003)

Fast ionization of D_2 leads to the coherent population of many vibrational states of D_2^+. Usually, only the squared absolute values of the vibrational state amplitudes, known as Franck-Condon factors, are observed since insufficient experimental time resolution averages out all coherence effects. We propose a Coulomb explosion imaging method to visualize the coherent motion of bound wave packets using ultrashort (5 fs), intense pump-probe laser pulses. With this type of experiment decoherence times in the fs to ps range may become directly observable and provide essential information for coherent control.

DOI: 10.1103/PhysRevA.67.063408 PACS number(s): 33.80.Rv, 33.90.+h, 34.50.Gb, 03.65.Yz

The H_2^+ (D_2^+) molecular ion is of fundamental interest in atomic and molecular physics. Together with its atomic counterparts (H^- and He), this simplest molecule represents a bound three-body Coulomb system. In contrast to the atomic systems, the molecule exhibits (if we neglect rotation) two timescales, the fast electronic motion (as scale) and the vibrational motion of the nuclei (fs scale). The interaction of these smallest molecules with strong fs laser pulses is of particular interest, since the pulse duration is comparable to the vibrational period [14 fs for H_2^+ ($\nu=0$)]. For homonuclear systems, the nuclei do not couple directly to the laser field due to the lack of a permanent electric dipole moment. Thus, the dynamics in the laser field is dominated by the interaction of the electron with the field, which acts only indirectly back on the nuclei via non-Born–Oppenheimer couplings.

Numerous theoretical investigations on H_2^+ in strong laser fields have been done so far emphasizing the influence of the two-center nature of the electronic potential on strong-field ionization [1–10]. Here, the laser-induced coupling of the lowest electronic states leads to an oscillating localization of the electron near one of the nuclei. This gives rise to dissociation of the molecule and to ''charge resonance enhanced ionization'' at intermediate internuclear distances R between 5 and 10 a.u. [2,4]. Experimentally, the situation is more challenging, since mostly neutral H_2 (D_2) targets are available [1,11–18], such that the production and fragmentation of the molecular ion occurring in the same laser pulse are difficult to separate. It was shown that for 50 fs pulses, saturation of H_2^+ is never reached at any intensity [14]. Moreover, a recent kinematically complete study for all ionization and fragmentation channels of H_2 revealed the breakdown of the simple two-step model of production and fragmentation of H_2^+ [18], i.e., the correlation of the two electrons has to be taken into account. To overcome this problem, attempts have been made to get either more detailed information on the time evolution of the molecule during the laser pulse [14,15] or to use a molecular ion beam as the target [19].

Due to advances in ultrashort pulse technology, pulse durations down to 5 fs are now available [20], and Coulomb explosion (CE) imaging of bound and moving nuclear wave packets [21] should become feasible even for light molecules such as H_2. Further, ultrashort pulses enable pump-probe experiments that separate the production and fragmentation of the molecular ion. The time-resolved observation of the nuclear motion will reveal coherence effects, which we describe within the density matrix formalism, starting with a coherent superposition of vibrational eigenstates φ_k,

$$\Phi(R,t)=\sum_k a_k \exp(-i\omega_k t)\varphi_k(R). \tag{1}$$

The probability density of this state can be expressed in terms of the time-dependent density matrix $\rho_{km}=a_k a_m^* \exp(-i\omega_{km}t)$ with $\omega_{km}=\omega_k-\omega_m$,

$$|\Phi(R,t)|^2=\sum_k \rho_{kk}|\varphi_k|^2+\sum_{k\neq m}\rho_{km}(t)\varphi_k\varphi_m^*. \tag{2}$$

Averaging over a time T results in

$$\overline{|\Phi(R,T)|^2}=\sum_k \rho_{kk}|\varphi_k|^2 - \sum_{k\neq m} a_k a_m^* \varphi_k\varphi_m^* \frac{\exp(-i\omega_{km}T)-1}{i\omega_{km}T}. \tag{3}$$

The first sum, containing only diagonal elements of the density matrix, corresponds to an incoherent mixture of eigenstates. The coherence—expressed by the off-diagonal elements in the second term—vanishes for a sufficiently large averaging time $T\gg\omega_{km}^{-1}$. Then, the time average is equivalent to an ensemble average. In two recent experiments [19], the H_2^+ ions have been prepared in an ion source. The uncertainty in the time delay between production of the molecular ions and the interaction with the laser pulse is of the order of μs. Thus, coherence effects on the fs timescale are averaged out according to Eq. (3). Similarly, environment-induced decoherence [22] should yield a stationary probability distribution after a sufficiently long time T. Information about decoherence times is of great importance for the coherent control of quantum systems.

The aim of this paper is twofold. First, we model the fragmentation of D_2^+ out of the vibrational ground state (ν

$=0$) in a two-pulse laser field. We consider D_2^+ rather than H_2^+ in order to take advantage of the slower nuclear motion. Our numerical results will be compared with a recent experiment [15]. Second, we propose a pump-probe experiment for the neutral D_2 molecule in order to image the coherent nuclear wave packet dynamics. We use atomic units, except where otherwise indicated.

The molecular ion is described in a reduced-dimensionality collinear model in terms of the electronic coordinate z relative to the center of mass of the nuclei and the internuclear distance R. The model-inherent alignment of the molecule along the polarization axis of the laser electric field $F(t)$ is not a serious problem since in a kinematically complete experiment fragmentation along this axis can be selected. Further, for linearly polarized nonrelativistic laser fields considered here, only the coordinates parallel to the electric field vector play an important role. Our model includes the (non-Born–Oppenheimer) coupling between the electronic and nuclear motion. The Hamiltonian is given by

$$H = T_n + 1/R + T_e + V_{en} - zF(t), \tag{4a}$$

$$V_{en} = -1/\sqrt{z_-^2 + a(R)^2} - 1/\sqrt{z_+^2 + a(R)^2}, \tag{4b}$$

with $z_\pm = z \pm R/2$. T_n and T_e are the kinetic energies for the nuclei and the electron, respectively. Softcore Coulomb potentials [23] are used for the electron-nucleus interaction with an R-dependent softening function $a(R)$, which is adjusted to exactly reproduce the electronic ground-state potential curve [24]. We solve the time-dependent Schrödinger equation numerically on a grid using the Crank-Nicholson split-operator method [25]. The grid extends from 0.05 to 30 in R with a spacing of 0.05 and from -45 to 45 in z with a spacing of 0.2. Absorbing regions using an optical potential are introduced over the last 200 (in R) and 100 (in z) grid points in order to prevent a reflection of the outgoing wave packets by the border of the grid. The number of time steps per optical cycle is 1100. Each time step the norm of the total wave function within $0.05 \leqslant R \leqslant 20$, $-25 \leqslant z \leqslant 25$ is calculated. The outgoing flux through the borders of this inner part of the grid can be used to obtain differential and integrated data on the fragmentation process. The dissociation yield into the $D^+ + D$ fragmentation channel is given by the time-integrated flux in the R direction at $R=20$. Removal of the electron leads to CE (into $D^+ + D^+ + e^-$), the yield of which is given by the time-integrated electronic flux in the z direction at $z = \pm 25$. From the time-dependent phase of the outgoing nuclear wave packets at $R=20$, we derive the nuclear momentum distribution for dissociation using the ''virtual detector'' method [26]. The CE spectra are obtained by first computing the ionization rate as the outgoing electron flux at a given position R. During the (fast) ionization of the electron we treat the (slow) nuclei as ''frozen.'' For each position R, the Coulomb energy $1/R$ is released. In order to take the initial (dissociative) velocity of the nuclei into account, we add the Coulomb energy and the initial kinetic energy $E_{\mathrm{init}}(R)$ of the nuclei at the ionization time and obtain the final kinetic energy of the fragments,

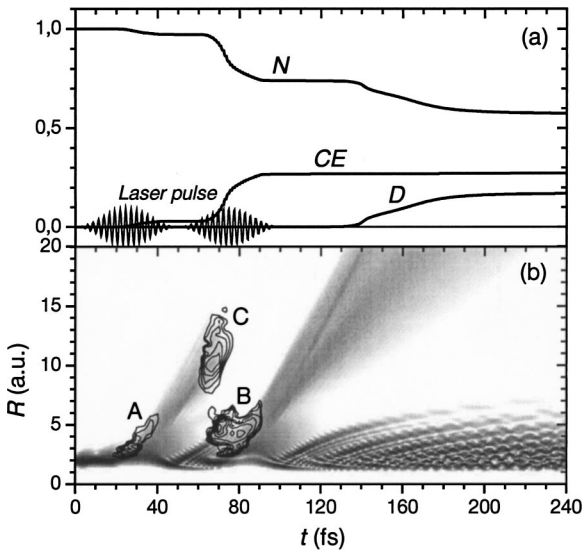

FIG. 1. (a) Time-dependent norm (N) and probabilities for Coulomb explosion (CE) and dissociation (D) of D_2^+ ($\nu=0$) in a two-pulse laser field (25 fs, 0.3 PW/cm^2, 50 fs delay). (b) Corresponding probability density $|\Phi(R,t)|^2$ (logarithmic gray scale) and ionization rates (contour lines).

$$E_{\mathrm{kin}} = 1/R + E_{\mathrm{init}}(R). \tag{5}$$

Figure 1(a) shows the time-dependent norm N and the yield for dissociation D and CE for D_2^+ ($\nu=0$) and two 25 fs laser pulses of 0.3 PW/cm^2 intensity and a delay $\tau = 50$ fs. The time evolution of the probability density $P(R,t) = |\Phi(R,t)|^2$ is shown in Fig. 1(b) with contour lines indicating the electronic ionization rate. Three different ionization regions can be distinguished: ionization from bound vibrational states during the first (A) and second (B) laser pulse and delayed ionization of the dissociating wave packet (C). Figure 2 shows the corresponding total fragment kinetic energy spectra for delays of 30, 50, and 70 fs. The low-energy part of the spectrum is due to dissociation via the Floquet one- and two-photon channels [11]. The CE spectra map ionization events in regions A, B, and C. The broad peak A (5–13 eV) shows no delay dependence. Its large width complies with the ionization rates in Fig. 1(b) and Eq. (5). Besides ionization, the first pulse induces dissociation and excitation into a coherent superposition of bound vibrational states. During the second pulse we find ionization of the bound part (peak B) and delayed ionization of the continuum part of the wave packet (peak C). Peak B is delay dependent due to the coherent motion of the bound wave packet. Peak C moves towards lower kinetic energies with increasing τ and finally merges with the dissociation peaks for large τ, since the energy due to CE becomes small at large R. This kind of imaging has been recently reported for D_2^+ [15]. The experiment used a D_2 target and 80 fs laser pulses and revealed a delay-dependent peak in the kinetic energy spectra (Fig. 2 of [15]), which shows the same delay dependence as peak C in our model.

The behavior of peak B reflects the coherent motion of the bound wave packet and suggests a pump-probe study of the

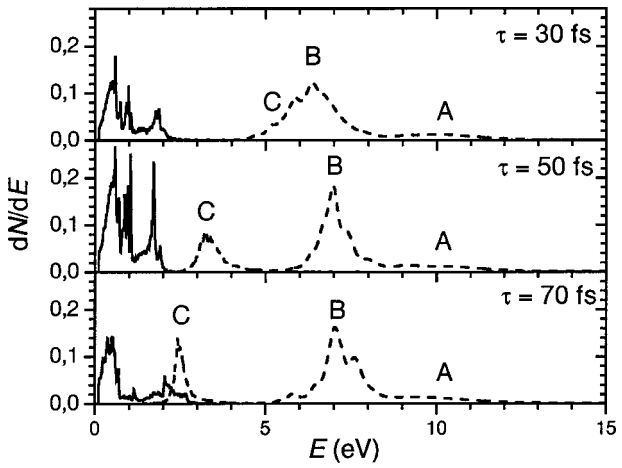

FIG. 2. Kinetic energy spectra for dissociation (solid lines) and Coulomb explosion (dashed lines) of D_2^+ ($\nu=0$) in a two-pulse laser field (25 fs, 0.3 PW/cm^2) with variable delay τ. The features $A-C$ correspond to the ionization regions in Fig. 1(b).

neutral molecule using ultrashort (<10 fs) laser pulses. For neutral targets and pulse durations >50 fs, production and fragmentation of D_2^+ cannot be easily separated. On the other hand, molecular ion beams cannot reveal coherence since the ions have to be treated as a statistical ensemble. We therefore propose to first (almost) completely ionize D_2 with an ultrashort (5 fs), intense (1 PW/cm^2) pulse within less than 2 fs near the pulse maximum [21]. The ionization time is short compared to the classical oscillation time for the D_2 ($\nu=0$) state of 20 fs. Hence, the ionization can be treated as a vertical (Franck-Condon) transition where the D_2 ($\nu=0$) initial wave function is projected onto the D_2^+ potential curve. We start the calculation in the center of the first pulse. Since the assumed intensity of the 5 fs pump pulse is high enough to saturate the D_2^+ production, the ionization probability does not depend on R.

Our calculation shows D_2^+ ions that are prepared at the center of a 1-PW/cm^2 5 fs pulse and survive with a high probability the remaining half pulse. Thus, these pulse parameters are suitable for experimental studies and avoid double ionization contributions from the first pulse. The dissociation (ionization) yield due to the half pulse is 2% (1.7%). For H_2^+, we find 11% (4%). The higher stability of D_2^+ originates in the slower nuclear motion. Figure 3(a) illustrates the coherent nuclear wave packet dynamics of D_2^+ following the vertical transition from D_2 ($\nu=0$). The expectation value $\langle R\rangle$ starts at the equilibrium distance of D_2 ($\nu=0$), $R_0=1.4$. After a few oscillations, the anharmonicity of the potential curve, i.e., the nonequal spacing of the vibrational levels, leads to the ''collapse'' of the wave packet. For $t\approx 580$ fs, we find a partial revival of the wave packet. A measure for the collapse and revival is the autocorrelation function $|\langle\Phi(t=0)|\Phi(t)\rangle|^2$ [Fig. 3(b)].

A second laser pulse, strong enough to ensure complete ionization of D_2^+, can probe the time evolution of the wave packet. In this case CE allows a mapping of $P(R,t)=|\Phi(R,t)|^2$. The measured kinetic energy distribution

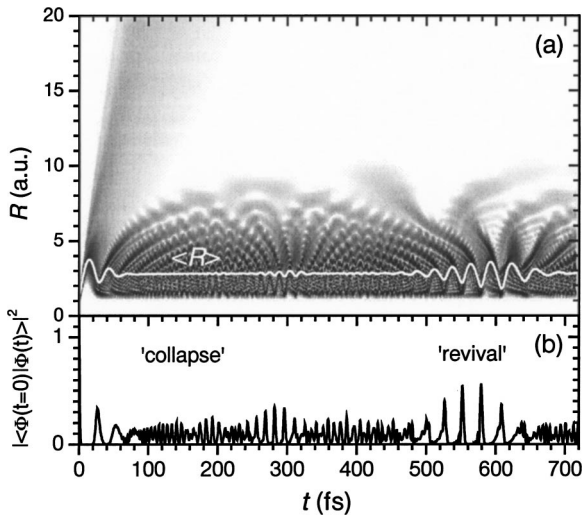

FIG. 3. Coherent motion of the D_2^+ nuclear wave packet following ionization of D_2 ($\nu=0$) in a 5-fs, 1-PW/cm^2 laser pulse. (a) Probability density $|\Phi(R,t)|^2$ (logarithmic gray scale) and expectation value $\langle R\rangle$. (b) Autocorrelation function.

$\mathrm{KE}(E,\tau)$ for a given τ of the probe pulse is then transformed to the reconstructed probability density

$$P'(R,\tau)=\mathrm{KE}(E_C(R),\tau)/R^2. \tag{6}$$

This transformation neglects the kinetic energy of the nuclear motion at the ionization time τ [21]. In general, the accuracy of this imaging method is limited by (1) the finite ionization time during the probe pulse (<2 fs), (2) the initial average

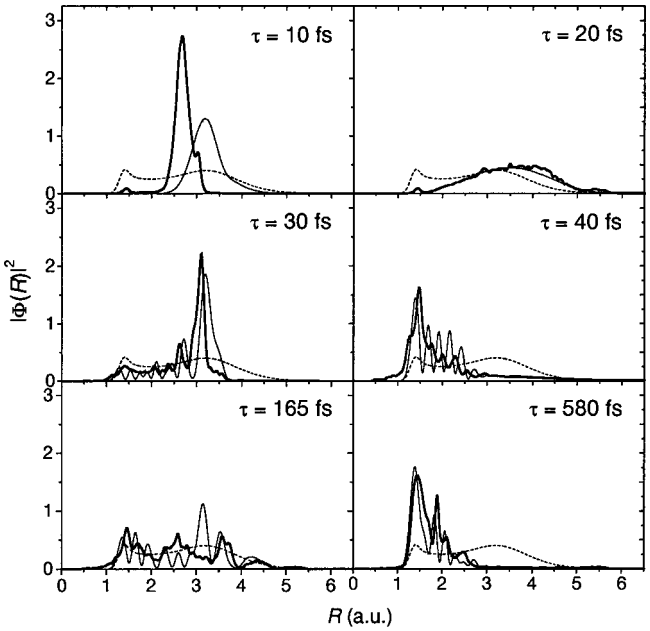

FIG. 4. Snapshots of the coherent nuclear motion in D_2^+ following ionization of D_2 ($\nu=0$) in a 5-fs, 1-PW/cm^2 laser pulse for various delays τ of the probe pulse. Thick solid line: reconstructed probability density $P'(R)$. Thin solid line: original density $|\Phi(R,\tau)|^2$. The incoherent Franck-Condon distribution is given by the dashed lines.

(group) velocity of the wave packet, and (3) the *inherent* momentum spread due to the uncertainty principle. (1) and (3) are similar to the photographic blurring effect for a finite exposure time. (2) leads to a shift of $P'(R,\tau)$ towards smaller R (i.e., larger kinetic energy release). In contrast to (1), the effect (3) remains, even in the limit of an instant ionization. An upper limit for the influence of (3) is obtained from the initial width of the wave packet, $\Delta R_{\mathrm{WP}} \geqslant 0.2$, which leads to a finite image resolution of $\Delta R_{\mathrm{image}} \leqslant 0.1$.

Figure 4 shows $P'(R,\tau)$ compared with the original probability density $P(R,\tau)=|\Phi(R,\tau)|^2$ for selected τ values. The intensity of the 5 fs probe pulse is 2 PW/cm^2. For $\tau = 10$ fs, the shift of the reconstructed distribution towards smaller R due to the kinetic energy of the wave packet becomes obvious. This effect is less important close to the turning point of the oscillating wave packet at $\tau = 20$ fs. The partial revival at $\tau = 580$ fs shows the wave packet with its maximum close to the equilibrium distance of D_2. In the region of the ''collapse'' of the wave packet, the interference structures are partially shifted and partially averaged out due to the effects (1) and (3). However, if coherence is preserved, the time-dependent nuclear motion should be observable in CE imaging. Further, if decoherence occurs due to coupling to other degrees of freedom (e.g., rotation) or to a thermal background, it should manifest itself in a breakdown of the time dependence. Thus, after a ''decoherence time'' the CE spectra become independent of τ, and the reconstructed wave packet merges into an incoherent Franck-Condon distribution. This offers, in principle, a direct measure of decoherence times of a quantum system. Since the direct coupling of the homonuclear D_2^+ to the thermal radiation is very weak due to the lack of a permanent electric dipole moment, an experimental study with HD^+ could demonstrate the influence of coupling strengths on the decoherence time.

In conclusion, the development of ultrashort (5 fs), intense laser pulses enables pump-probe studies of the nuclear wave packet dynamics even for light molecular systems such as H_2^+ or D_2^+. Dissociating wave packets as well as the coherent motion of bound states can be probed on a fs time scale. This method should enable the direct measurement of decoherence times on a fs to ps time scale and, thus, provide important information for the coherent control of quantum systems.

This work was supported by the Division of Chemical Sciences, Office of Basic Energy Sciences, Office of Energy Research, U.S. DOE, and NSF Grant No. PHY-0071035. B.F. acknowledges a research scholarship from the DFG (Germany).

[1] A. Giusti-Suzor, F. H. Mies, L. F. DiMauro, E. Charron, and Y. Yang, J. Phys. B **28**, 309 (1995).
[2] T. Seidemann, M. Yu Ivanov, and P. B. Corkum, Phys. Rev. Lett. **75**, 2819 (1995); T. Zuo and A. D. Bandrauk, Phys. Rev. A **52**, R2511 (1995).
[3] K. C. Kulander, F. H. Mies, and K. J. Schafer, Phys. Rev. A **53**, 2562 (1996).
[4] S. Chelkowski, A. Conjusteau, T. Zou, and A. D. Bandrauk, Phys. Rev. A **54**, 3525 (1996).
[5] M. Plummer and J. F. McCann, J. Phys. B **29**, 4625 (1996).
[6] T. D. G. Walsh *et al.*, Phys. Rev. A **58**, 3922 (1998).
[7] I. Kawata, H. Kono, and Y. Fujimura, J. Chem. Phys. **110**, 11152 (1999).
[8] D. Dundas, J. F. McCann, J. S. Parker, and K. T. Taylor, J. Phys. B **33**, 3261 (2000).
[9] Y. Duan, W.-K. Liu, and J.-M. Yuan, Phys. Rev. A **61**, 053403 (2000).
[10] M. E. Sukharev and V. P. Krainov, Phys. Rev. A **62**, 033404 (2000).
[11] G. N. Gibson, M. Li, C. Guo, and J. Neira, Phys. Rev. Lett. **79**, 2022 (1997).
[12] T. D. G. Walsh, F. A. Ilkov, and S. L. Chin, J. Phys. B **30**, 2167 (1997).
[13] L. J. Frasinski *et al.*, Phys. Rev. Lett. **83**, 3625 (1999).
[14] J. H. Posthumus *et al.*, J. Phys. B **32**, L93 (1999).
[15] C. Trump, H. Rottke, and W. Sandner, Phys. Rev. A **59**, 2858 (1999).
[16] C. Trump, H. Rottke, and W. Sandner, Phys. Rev. A **60**, 3924 (1999); C. Trump *et al.*, *ibid.* **62**, 063402 (2000).
[17] A. Staudte *et al.*, Phys. Rev. A **65**, 020703 (2002).
[18] H. Rottke *et al.*, Phys. Rev. Lett. **89**, 013001 (2002).
[19] K. Sändig, H. Figger, and T. W. Hänsch, Phys. Rev. Lett. **85**, 4876 (2000); I. D. Williams *et al.*, J. Phys. B **33**, 2743 (2000).
[20] T. Brabec and F. Krausz, Rev. Mod. Phys. **72**, 545 (2000); Q. Apolonski *et al.*, Phys. Rev. Lett. **85**, 470 (2000); C. Spielmann *et al.*, Science (Washington, DC, U.S.) **278**, 661 (1997).
[21] S. Chelkowski, P. B. Corkum, and A. D. Bandrauk, Phys. Rev. Lett. **82**, 3416 (1999); S. Chelkowski and A. D. Bandrauk, Phys. Rev. A **65**, 023403 (2002).
[22] F. B. J. Buchkremer, R. Dumke, H. Levsen, G. Birkl, and W. Ertmer, Phys. Rev. Lett. **85**, 3121 (2000); S. Wallentowitz, I. A. Walmsley, L. J. Waxer, and Th. Richter, J. Phys. B **35**, 1967 (2002).
[23] Q. Su and J. H. Eberly, Phys. Rev. A **44**, 5997 (1991).
[24] B. Feuerstein and U. Thumm, Phys. Rev. A **67**, 043405 (2003).
[25] W. H. Press, S. A. Teukolsky, W. T. Vetterling, and B. F. Flannery, *Numerical Recipes* (Cambridge University Press, Cambridge, 1992), p. 842.
[26] B. Feuerstein and U. Thumm, J. Phys. B **36**, 707 (2003).

INSTITUTE OF PHYSICS PUBLISHING JOURNAL OF PHYSICS B: ATOMIC, MOLECULAR AND OPTICAL PHYSICS

J. Phys. B: At. Mol. Opt. Phys. **37** (2004) L161–L167 PII: S0953-4075(04)74513-7

LETTER TO THE EDITOR

Atomic structure dependence of nonsequential double ionization of He, Ne and Ar in strong laser pulses

V L B de Jesus, B Feuerstein, K Zrost, D Fischer, A Rudenko, F Afaneh, C D Schröter, R Moshammer and J Ullrich

Max-Planck-Institut für Kernphysik, D-69029 Heidelberg, Germany

Received 7 January 2004
Published 1 April 2004
Online at stacks.iop.org/JPhysB/37/L161 (DOI: 10.1088/0953-4075/37/8/L03)

Abstract

The ion momentum spectra for nonsequential double ionization of rare gases (He, Ne and Ar) in 23 fs 795 nm laser pulses were measured in the intensity range 0.075–1.25 PW cm^{-2}. In the studies published, confusing differences in the shape of momentum distributions among different targets are consistently explained within a recollision scenario: excitation during recollision plus subsequent field ionization, not implemented in most theoretical approaches, evidently plays a decisive role for He and Ar nonsequential double ionization whereas it plays only a minor role for Ne.

Many-electron dynamics in intense laser fields has been the subject of a large number of theoretical and experimental investigations. In particular, strong field double ionization is a fundamental process and, at the same time, one of the most challenging problems in atomic and optical physics, theoretically as well as experimentally. Whereas single ionization is considered to be well understood within the 'single active electron' (SAE) model, the observed yields of double ionization in linearly polarized laser pulses exceed those predicted by the SAE model assuming a sequence of individual single ionization events by many orders of magnitude. Although the underlying mechanism of this 'nonsequential' (NS) double ionization remained unclear for many years, it was agreed that the NS double ionization has to incorporate the correlated two-electron dynamics in intense laser fields (for reviews see [1, 2]).

Experiments using circularly polarized light as well as recent results exploiting advanced experimental imaging techniques [3, 4] in agreement with most quantum [5–9] and classical calculations [10, 11] provided widely accepted evidence that the so-called rescattering or recollision scenario [12] is the dominating mechanism for NS double ionization. Here, the first (tunnel-)ionized electron is driven back by the oscillating laser field to its parent ion causing ionization of a second electron in an (e, 2e)-like process. It was shown that the kinematics of this dynamical process is the only one that can explain the 'double-hump' structure of ion momentum distributions along the laser polarization direction [13], clearly observed exclusively for Ne^{2+} and Ne^{3+} ions in the NS intensity regime [4]. However, summarizing the results of published experimental data as well as theoretical predictions for

NS double ionization of He, Ne and Ar atoms, one finds quite a confusing situation indicating that the underlying mechanisms are by far not understood.

Singly differential momentum spectra for He^{2+} ions have been measured so far in the intensity range 0.29–0.66 PW cm^{-2}. Here, indications of a double-hump structure have been observed only at the highest intensity. Compared to Ne this characteristic feature is much less pronounced and hardly visible at all. In contrast, as summarized in figure 9 of [2], most of the theoretical models predict a very clear double-hump shape with a deep minimum at zero momentum not consistent with experiment. Moreover, and even more surprising, the apparently most complete approach, namely the numerical solution of the time-dependent Schrödinger equation for two correlated electrons in a one-dimensional model [7] predicts just the opposite behaviour, i.e. a single maximum at zero momentum, which also does not agree with the experimental findings. Recent calculations by van der Hart [14] revealed that excitation of He^{+} during recollision followed by subsequent field ionization of the excited electron contributes decisively to double ionization. This mechanism was not considered in previous theoretical models, which actually predict the double-hump behaviour. Some of them even correctly reproduce the total rates for multiple ionization without taking this mechanism into account. Finally, a systematic study on the intensity dependence of ion momentum spectra for Ar^{2+} did not reveal a double-hump structure for any intensity [15]. Such behaviour for Ar was recently explained by the recollision–excitation mechanism mentioned above, by inspecting correlated electron spectra where the momenta of both emitted electrons are measured in coincidence [16]. In contrast to Ne [17], the majority of the correlated events violate the kinematical constraints set by conservation of energy and momentum in the recollision–ionization scenario [16], whereas these data were found to be consistent with the kinematics of recollision–excitation with subsequent field ionization. Due to its sequential nature, this mechanism leads to small drift momenta of one of the electrons, and thus fills the 'valley' in the ion momentum distribution as observed for He [3] and Ar [15, 16]. Note that other effects of electron correlation, such as the so-called 'shake-off' mechanism, have recently been shown to contribute negligibly to NS strong field ionization [5]. Other many-body effects in tunnelling (including core excitations) as discussed recently in [18] concern mainly the multiple ionization of atoms by circularly polarized light. In our case of linear polarization, the nonsequential recollision mechanism is by far the dominating one for double ionization.

Consequently, inspecting all available data, severe questions arise: whether the atomic structure can influence the dynamics of NS double ionization, whether such a potential structure dependence can explain the experimental results for different targets and what really is then the dominant NS double ionization mechanism for the various atomic species. These questions become even more pressing since it is frequently doubted if at such high intensities the atomic structure plays any role at all.

In order to clarify this situation we present the first comprehensive experimental study on the ion momentum distributions of He^{2+}, Ne^{2+} and Ar^{2+} ions using a novel method for the *in situ* calibration of the intensity in the range 0.075–1.25 PW cm^{-2}. On the basis of a consistent model calculation for the relative contributions of direct (e, 2e) ionization and excitation during recollision followed by subsequent field ionization, we demonstrate a strong target structure dependence of NS double ionization as well as the decisive importance of recollision–excitation. Indeed, we provide convincing evidence that for He and Ar this is the dominant NS ionization mechanism over a wide intensity range. Atomic units are used in the following except where indicated otherwise.

For our experiment, we use a Kerr-lens mode locked Ti:sapphire laser at 795 nm wavelength amplified to pulse energies up to 350 μJ at 3 kHz repetition rate. The width

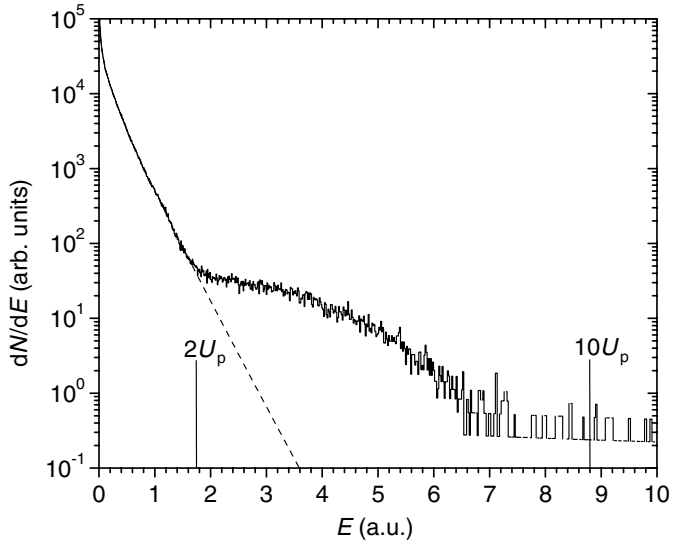

Figure 1. Longitudinal electron kinetic energy spectrum for single ionization of Ne. The spectrum shows a change in slope close to the kinetic energy of $2U_p$ indicating the transition from direct to rescattered electrons. A Gaussian fit (dashed curve) according to the tunnelling theory can, in an indirect way, determine the laser intensity (see text for details).

of the amplified pulses is 23 fs. After compensation of astigmatism by means of a spherical mirror telescope, the laser beam is focused by a spherical on-axis mirror ($f = 100$ mm) to a spot size of 6.5(8) μm on a supersonic gas jet target in an ultra-high vacuum chamber (8×10^{-10} mbar). The focus diameter has been determined from measured optical parameters of the laser beam. Vector momenta of recoil ions emerging from the source volume are recorded using a 'reaction microscope' which has been described in detail before [19]. The polarization direction of the laser is parallel to the time-of-flight axis of the spectrometer. Along this axis (which is perpendicular to the jet axis) an ion momentum resolution of 0.1 au is achieved due to collimation of the gas jet. In addition to the conventional method, we determined the laser intensity '*in situ*' by simultaneously measuring the electron kinetic energy spectra along the laser polarization axis for single ionization. Figure 1 shows such a longitudinal (i.e. parallel to the laser polarization direction) kinetic energy spectrum (log scale) of the electron for single ionization of Ne along with a Gaussian according to the tunnelling theory [20] fitted to the distribution in the region of direct electrons: $w_{\mathrm{ADK}}(p_\parallel) = w(0) \exp\left[\frac{1}{3} p_\parallel^2 \omega^2 (2I_p/I)^{3/2}\right]$. Here, w is the Ammosov–Delone–Krainov (ADK) tunnelling rate for a final longitudinal momentum $p_\parallel$ of the electron, ω is the laser frequency and I_p is the ionization potential. Since the width of the electron spectrum sensitively depends on the intensity I, the fit yields in indirect, online and accurate determination of $I = 0.40(5)$ PW cm^{-2} for the spectrum in figure 1. Moreover, as is well known, the spectrum shows a distinct change in slope occurring close to the kinetic energy of $2U_p$ (ponderomotive potential $U_p = I/4\omega^2$) indicating the transition from direct and rescattered electrons dominating electron production. At higher energies a 'plateau' of rescattered electrons extends up to $\sim 10U_p$ [21]. The intensity derived from the fit results in a focus diameter of 5.5(5) μm, which agrees well with the value given above. We estimate the accuracy of this method for absolute intensity calibration to be better than 15%. The relative intensities are derived from the pulse energies measured with <5% accuracy, which is—at the same time—the stability of the laser.

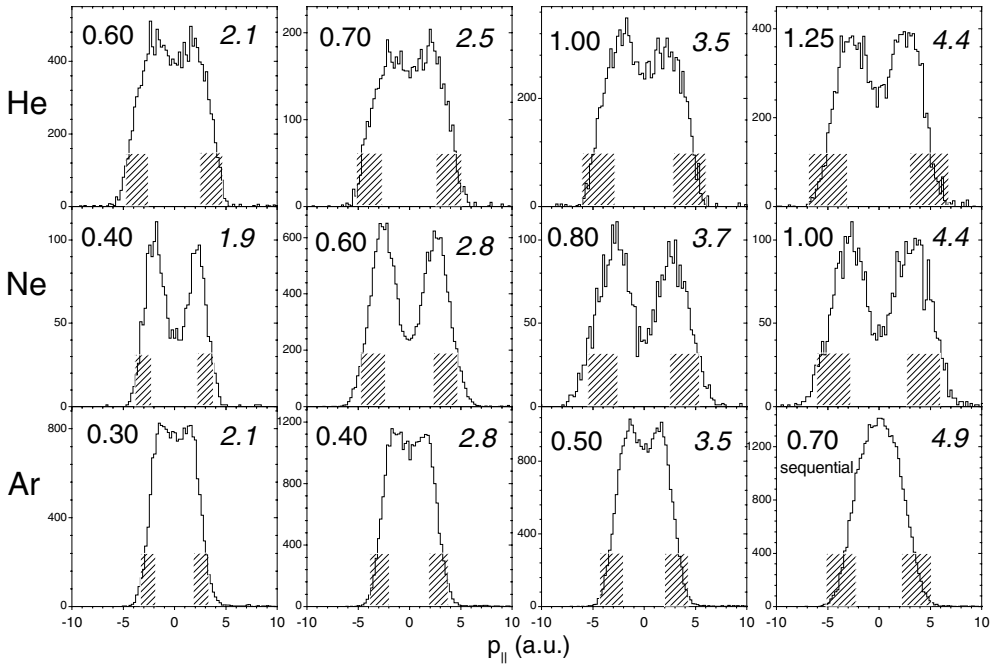

Figure 2. Ion longitudinal momentum spectra for He^{2+}, Ne^{2+} and Ar^{2+}. The spectra are shown in four columns comparing the three species at intensities (numbers on the left) corresponding to approximately the same maximum recollision energy in units of the ionization potential I_p^+ of the singly charged ion $3.17U_p/I_p^+$ (italic numbers on the right). The shaded areas indicate the kinematically favoured regions based on the recollision (e, 2e) model (see equation (9) in [13]). Note that in the last spectrum for Ar (0.7 PW cm^{-2}) the sequential regime is already achieved.

Figure 2 summarizes the measured longitudinal ion momentum spectra for He^{2+}, Ne^{2+} and Ar^{2+}. We compare the three species at intensities corresponding to the same maximum recollision energy in units of the ionization potential I_p of the singly charged ion $3.17U_p/I_p$. Whereas the shape of the spectra for Ne only shows a weak intensity dependence with a clear double-hump structure everywhere, a distinct transition from a single maximum to a broad structure is observed for Ar and He. At the highest intensity (1.25 PW cm^{-2}) for He we find for the first time a pronounced minimum at zero momentum. For Ar such behaviour cannot be observed at all, presumably since the regime of sequential double ionization is already reached at 0.7 PW cm^{-2}. The shaded areas indicate the kinematically favoured regions based on the recollision (e, 2e) model (see equation (9) in [13]). Obviously, for He and Ar another mechanism besides (e, 2e)—most likely a sequential excitation tunnelling process—plays a crucial role in the doubly charged ion formation.

In order to calculate the relative contributions of direct ionization and excitation tunnelling, we use the following semiclassical model within the recollision scenario. In a first step one electron is field-ionized via tunnelling at a phase ωt_0 of the oscillating, linearly polarized electric field $F(t) = F_0 \sin(\omega t)$. Depending on the initial phase the electron may be driven back to its parent ion at a phase ωt_1 with a classical recollision energy $E_{\mathrm{rec}} = 0.5F_0^2\omega^{-2}[\cos(\omega t_0) - \cos(\omega t_1)]^2$. Here, in a second step electron impact ionization or excitation takes place. In the first case, the second electron is directly ionized in an (e, 2e) process, whereas the excitation is followed by subsequent tunnelling of the excited electron.

In the intensity range considered here, this tunnelling occurs with almost 100% probability. Thus, for the calculation of the relative contribution of these two mechanisms, we only need to calculate the ratio of the effective (phase averaged) yields $Y_{\mathrm{ion,exc}}$ for ionization and excitation

$$R = \frac{Y_{\mathrm{ion}}}{Y_{\mathrm{exc}}}, \qquad Y_{\mathrm{ion,exc}} = \int_{\pi/2}^{\pi} W_{\mathrm{ADK}}(t_0)\sigma_{\mathrm{ion,exc}}(E_{\mathrm{rec}}(t_0))\,\mathrm{d}(\omega t_0). \tag{1}$$

Here, $W(\omega t_0)$ is the ADK [20] static-field tunnelling rate. The electron impact cross-sections $\sigma_{\mathrm{ion,exc}}$ are derived using general, simplified (field-free) expressions. In the case of ionization we use the following formula [22]:

$$\sigma_{\mathrm{ion}}(E_{\mathrm{rec}}) = \sum_{\ell k} C_\ell \left(\frac{0.5}{I_p^{+(k)}}\right)^{2-\delta_\ell} \xi_\ell b_k \frac{\ln\left[1 + \left(E_{\mathrm{rec}} - \tilde{I}_p^{+(k)}\right)\big/ I_p^{+(k)}\right]}{E_{\mathrm{rec}}\big/ I_p^{+(k)}}. \tag{2}$$

The coefficients C_ℓ, δ_ℓ can be found in [22]. ξ_ℓ is the number of equivalent electrons in the initial subshell ℓ and b_k is the branching ratio for ionization into a specific term k of the final state. For Ne^+ (Ar^+) we included ionization from the 2p (3p) and 2s (3s) subshells. In order to take into account the effect of barrier suppression due to a finite field at the recollision time t_1, we introduce the suppressed ionization potential of the ion [23] $\tilde{I}_p^+ = I_p^+ - 2\sqrt{2F(t_1)}$.

The $1s \rightarrow 2\ell$ excitation cross-sections for He^+ are taken from a convergent close-coupling calculation [24]. We extrapolate the cross-sections for higher-lying He^+ levels by scaling with known transition strengths [25]. Since comprehensive data on excitation cross-section for Ne^+ and Ar^+ are not available, we use the van Regemorter formula [26] for transitions $i \rightarrow k$

$$\sigma_{\mathrm{exc}}^{(ik)}(x) = \frac{2\pi^2 f_{ik}}{\sqrt{3}E_{ik}^2}\frac{G(x)}{x}, \qquad x = E_{\mathrm{rec}}/E_{ik}, \tag{3a}$$

$$\sigma_{\mathrm{exc}}(x) = \sum_{ik} \sigma_{\mathrm{exc}}^{(ik)}(x), \tag{3b}$$

with the Gaunt factor $G(x) = 0.349 \ln x + 0.0988 + 0.455x^{-1}$ [24], E_{ik} is the excitation energy and f_{ik} is the absorption oscillator strength (values from [25]). Figure 3 shows the total cross-sections for He^+, Ne^+ and Ar^+ as a function of the electron impact energy in units of I_p. As expected from the atomic structure (3p–3d transitions) excitation is much stronger in Ar^+ than in Ne^+. The structure of He^+ is hydrogen-like which results in a reduced ionization cross-section compared to excitation since the latter consumes a large amount of the total oscillator strength. The result for the phase-integrated ratio R as a function of the laser intensity is shown in figure 4. Again, we find a much stronger excitation contribution for He and Ar compared to Ne. This qualitatively explains the different shape of the ion momentum spectra for NS double ionization. For Ar, we can directly compare the calculated ratio $R_{\mathrm{cal}} = 0.37$ at 0.25 PW cm^{-2} with the experimental result from [16], $R_{\mathrm{exp}} = 0.37(6)$ at 0.25(5) PW cm^{-2} which is found to be well reproduced by our model.

To conclude, we have presented the first comprehensive study on nonsequential double ionization of the noble gases He, Ne and Ar. We used a novel technique for intensity calibration based on the well-established ADK tunnelling theory for single ionization electron spectra, the result of which agrees well with the intensity derived from the laser beam parameters. A qualitative difference in shape and intensity dependence of the longitudinal momentum spectra of the doubly charged ions is observed for Ne compared to He and Ar, which behave similarly. For the first time a clear double-hump structure in the He^{2+} momentum distribution is observed. We developed a consistent model calculation within the recollision scenario including both (e, 2e) and excitation tunnelling mechanisms which can—at least qualitatively—explain the

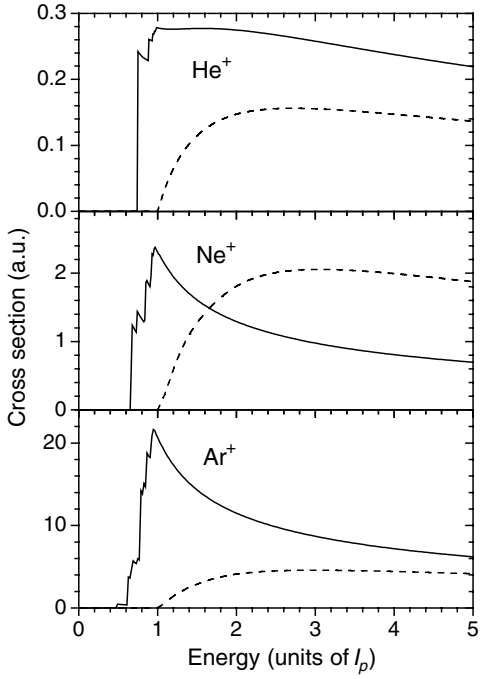

Figure 3. Total excitation (solid lines) and ionization (dashed lines) cross-sections for He^+, Ne^+ and Ar^+ as a function of the electron impact energy in units of ionization potential I_p^+.

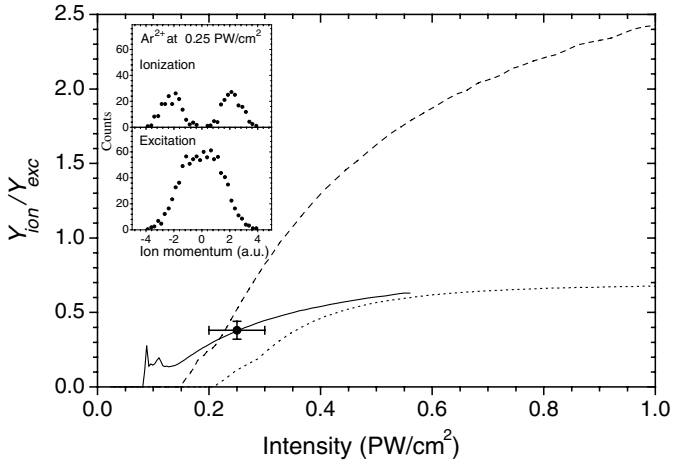

Figure 4. Ratio of the double ionization yield for ionization and excitation according to equation (1) based on the cross-sections shown in figure 3 as a function of the laser intensity. At 0.58 PW cm^{-2} the suppressed I_p^+ is zero for Ar and, thus, beyond this value the calculation is no longer valid. The experimental result for Ar from [16] $R_{\mathrm{exp}} = 0.37(6)$ at 0.25(5) PW cm^{-2} (the Ar^{2+} spectra are depicted on the top) is also shown in the figure.

substantially different behaviour of He/Ar versus Ne due to differences in the excitation cross-sections, caused by the atomic structure. This might be quite surprising considering the fact

that we used field-free cross-sections; the atomic structure seems to be well preserved even in considerably perturbed systems. However, at the phases where recollision occurs, the laser field strength is typically small [12]. In order to obtain more insight into the mechanisms of nonsequential double ionization, more kinematically complete studies are planned, in particular for He since this is the only case where an *ab initio* theoretical description might become available in the future.

Acknowledgments

This work was supported by the Leibniz-Program of the Deutsche Forschungsgemeinschaft. We are grateful to Tom Kirchner for fruitful discussions.

References

[1] Protopapas M, Keitel C H and Knight P L 1997 *Rep. Prog. Phys.* **60** 389
[2] Dörner R, Weber Th, Weckenbrock M, Staudte A, Hattass M, Schmidt-Böcking H, Moshammer R and Ullrich J 2002 *Adv. At. Mol. Opt. Phys.* **48** 1
[3] Weber Th, Weckenbrock M, Staudte A, Spielberger L, Jagutzki O, Mergel V, Afaneh F, Urbasch G, Vollmer M, Giessen H and Dörner R 2000 *Phys. Rev. Lett.* **84** 443
[4] Moshammer R *et al* 2000 *Phys. Rev. Lett.* **84** 447
[5] Becker A and Faisal F H M 2000 *Phys. Rev. Lett.* **84** 3546
Becker A and Faisal F H M 2002 *Phys. Rev. Lett.* **89** 193003
[6] Kopold R, Becker W, Rottke H and Sandner W 2000 *Phys. Rev. Lett.* **85** 3781
[7] Lein M, Gross E K U and Engel V 2000 *Phys. Rev. Lett.* **85** 4707
[8] Parker J S, Moore L R, Meharg K J, Dundas D and Taylor K T 2001 *J. Phys. B: At. Mol. Opt. Phys.* **33** L691
[9] Goreslavskii S P, Popruzhenko S V, Kopold R and Becker W 2001 *Phys. Rev.* A **64** 053402
[10] Sacha K and Eckhardt B 2001 *Phys. Rev.* A **63** 043414
[11] Fu L B, Liu J and Chen S G 2002 *Phys. Rev.* A **65** 021406
[12] Corkum P B 1993 *Phys. Rev. Lett.* **71** 1994
[13] Feuerstein B, Moshammer R and Ullrich J 2000 *J. Phys. B: At. Mol. Opt. Phys.* **33** L823
[14] van der Hart H 2000 *J. Phys. B: At. Mol. Opt. Phys.* **33** L699
[15] Weber Th, Weckenbrock M, Staudte A, Spielberger L, Jagutzki O, Mergel V, Afaneh F, Urbasch G, Vollmer M, Giessen H and Dörner R 2000 *J. Phys. B: At. Mol. Opt. Phys.* **33** L127
[16] Feuerstein B *et al* 2001 *Phys. Rev. Lett.* **87** 043003
[17] Moshammer R *et al* 2003 *J. Phys. B: At. Mol. Opt. Phys.* **36** L113
[18] Kornev A S, Tulenko E B and Zon B A 2003 *Phys. Rev.* A **68** 043414
[19] Ullrich J *et al* 1997 *J. Phys. B: At. Mol. Opt. Phys.* **30** 2917
[20] Delone N B and Krainov V P 1998 *Phys.-Usp.* **41** 469
[21] Paulus G G, Nicklich W, Xu H, Lambropoulos P and Walther H 1994 *Phys. Rev. Lett.* **72** 2851
[22] Bernshtam V A, Ralchenko Yu V and Maron Y 2000 *J. Phys. B: At. Mol. Opt. Phys.* **33** 5025
[23] van der Hart H W and Burnett K 2000 *Phys. Rev.* A **62** 013407
[24] Fisher V I, Ralchenko Yu V, Bernshtam V A, Goldgirsh A, Maron Y, Vainshtein L A, Bray I and Golten H 1997 *Phys. Rev.* A **55** 329
[25] Verner D A, Verner E M and Ferland G J 1996 *At. Data Nucl. Data Tables* **64** 1
[26] van Regemorter H 1962 *Astrophys. J.* **136** 906

Circular dichroism in laser-assisted proton-hydrogen collisions

Thomas Niederhausen*
James R. MacDonald Laboratory, Kansas State University, Manhattan, Kansas 66506-2604, USA

Bernold Feuerstein†
Max-Planck-Institut für Kernphysik, Heidelberg, Germany

Uwe Thumm‡
James R. MacDonald Laboratory, Kansas State University, Manhattan, Kansas 66506-2604, USA
(Received 20 April 2004; published 19 August 2004)

We investigate the effects of a strong laser field on the dynamics of electron capture and emission in ion-atom collisions within a reduced dimensionality model of the scattering system in which the motion of the active electron and the laser electric field vector are confined to the scattering plane. We examine the probabilities for electron capture and ionization as a function of the laser intensity, the projectile impact parameter b, and the laser phase ϕ that determines the orientation of the laser electric field with respect to the internuclear axis at the time of closest approach between target and projectile. Our results for the b-dependent ionization and capture probabilities show a strong dependence on both ϕ and the helicity of the circularly polarized laser light. For intensities above 5×10^{12} W/cm^2 our model predicts a noticeable circular dichroism in the capture probability for slow proton-hydrogen collisions, which persists after averaging over ϕ. Capture and electron emission probabilities defer significantly from results for laser-unassisted collisions. Furthermore, we find evidence for a charge-resonance-enhanced ionization mechanism that may enable the measurement of the absolute laser phase ϕ.

DOI: 10.1103/PhysRevA.70.023408 PACS number(s): 34.50.Rk, 34.70.+e, 32.80.Qk

I. INTRODUCTION

The study of charge exchange in ion-atom collisions dates back to the beginning of the last century, when Henderson [1] experimentally discovered electron capture by α particles passing through matter and was pursued actively over many decades [2]. More recently, the COLTRIMS technique [3,4] has allowed for the investigation of the electron dynamics in ion-atom collisions with unprecedented resolution in energy and momentum of the interacting electrons and nuclei. Independently, the interaction of strong laser fields with atoms, ions, or molecules has been addressed in a large number of experimental and theoretical investigations [5,6] over the past two decades. Even though the detailed investigation of laser-assisted heavy-particle collisions may ultimately help in steering chemical reactions into specific reaction channels by adjusting laser parameters (intensity, wavelength, and pulse shape), the promising combination of the two research areas—laser-matter interactions and heavy-particle collisions—has been the subject of only a few experiments with crossed heavy-particle and laser beams. For example, Débarre and Cahuzac [7] observed laser-induced charge exchange between Sr^+ and Ba in a mixture of strontium and barium vapors using Nd-YAG lasers with relatively very low intensities up to 5×10^8 W/cm^2. Grosser *et al.* [8] used a continuous beam of Na atoms, a pulsed beam of Kr atoms, and two pulsed (pump and probe) laser beams and crossed all beams in a small interaction volume. They explained an oscillatory structure in the angular distribution of excited Na projectiles after laser-assisted collisions with Kr atoms in terms of optical molecular transitions in the transient NaKr complex.

So far, technical challenges in the generation of sufficiently long and intense laser pulses and the synchronization of laser pulses within the interaction time interval (typically not more than 10^{-13} s in slow ion-atom collisions) have prevented a more detailed experimental investigation of laser-assisted or laser-controlled charge-exchange reactions in heavy-particle collisions. With the increasing availability of energetic lasers in atomic collision laboratories [4,9], we expect laser-induced effects in laser-assisted heavy-particle collisions to become observable. High laser intensities, focused on relatively large areas and long laser pulse durations, will significantly improve the statistics in laser-assisted collision experiments and are expected to soon open the door towards more detailed experimental studies that may contribute substantially to our understanding of laser-controlled chemical reactions.

On the theoretical side, a variety of methods have been applied to the calculation of charge exchange and electron emission in laser-assisted heavy-particle collisions. Li *et al.* [10,11] predicted, within lowest-order perturbation theory in the electron nucleus interaction, that the dressing of atomic levels in an intense laser field leads to a significant modification of capture and ionization cross sections in fast proton-hydrogen collisions. Voitkiv and Ullrich [12] found, also within lowest-order perturbation theory in the electron-projectile interaction, that a linearly polarized laser field can

*Electronic address: esdimax@phys.ksu.edu
†Electronic address: Bernold.Feuerstein@mpi-hd.mpg.de
‡Electronic address: thumm@phys.ksu.edu

substantially influence the binary-encounter electron emission process in fast collisions of α particles with hydrogen atoms. Close-coupling calculations for heavy-particle collisions, taking place in a strong laser pulse, were recently performed by Madsen *et al.* [13] and Kirchner [14]. Madsen *et al.* predicted a strong laser-induced modification of the *s-p* excitation probability in laser-assisted proton-H(1*s*) and proton-Na(3*s*) collisions. Kirchner found a strong influence of the electron capture and loss probabilities in laser-assisted He^{2+}-H collisions on the laser wavelength and the initial phase of the laser electric field. Lattice calculations on a three-dimensional Cartesian grid for laser-assisted proton collisions with lithium atoms in ground and excited states by Pindzola *et al.* [15] show a significant modification of the charge-transfer process for moderate laser intensities of 10^{12} W/cm^2. Lein and Rost [16] applied a reduced dimensionality model, solved the Schrödinger equation on a two-dimensional Cartesian grid, and predicted the generation of ultrahigh harmonics in laser-assisted collisions of 2 keV protons with hydrogen atoms in linearly polarized laser pulses with 16 optical cycles, a wavelength of 800 nm, and 10^{14} W/cm^2 intensity.

More work, both experimental and theoretical, has been done for laser-assisted electron scattering, but even a structureless projectile constitutes a serious challenge to present theories [17–19]. The early theory of Kroll and Watson [20] which only retained terms to first order in the photon frequency disagrees with the experimental results of Wallbank and Holmes [21]. This discrepancy between theory and experiment was traced to off-shell effects in the long-range polarization part of the electron-atom scattering potential [22]. Joachain, Dörr, and Kylstra [18] introduced the nonperturbative *R*-matrix Floquet method which was subsequently applied to multiphoton ionization, higher-harmonic generation, and laser-assisted electron atom collisions. Electron-ion collisions have recently attracted considerable interest as an integral part of the rescattering process, in which nonsequential double ionization of an atom or molecule is explained in terms of electron impact ionization of one electron by the laser-driven and rescattered other electron [9,23].

To the best of our knowledge, laser-assisted ion-atom collisions in circularly polarized light have not yet been investigated. In this paper we numerically solve the Schrödinger equation on a two-dimensional grid. Within this reduced dimensionality model, the electronic motion and the rotating laser electric field are confined to the scattering plane. For projectiles (protons) on a classical straight-line trajectory, we study the dependence of the probabilities for electron loss, capture, and emission on the intensity and helicity of the laser electric field. Even though experimental results are expected to differ slightly from the predictions of our two-dimensional calculations, we expect our results to be of sufficient accuracy to provide useful estimates for optimized laser and collision parameters that most clearly display the effects of a laser pulse on the electronic dynamics in heavy-particle collisions. Our numerical results show the strongest influence of the laser electric field on the capture probability at a laser intensity of 0.0014 a.u. (5.0×10^{13} W/cm^2)—i.e., when the laser electric force equals a few percent of the electrostatic Coulomb force exerted on the active electron by the target nucleus.

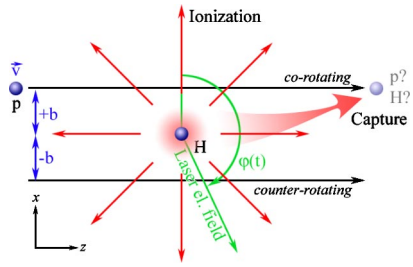

FIG. 1. (Color online) Collision scenario for a proton on a straight-line trajectory with impact parameter b and velocity v colliding with an atomic hydrogen target. The rotating laser electric field breaks the azimuthal symmetry: For positive impact parameters, the projectile follows the rotating laser field (corotating case); for negative impact parameters, the projectile moves against the rotating electric field (counterrotating case).

II. THEORY

A. Potentials

Unless indicated otherwise we will use atomic units ($\hbar = m_e = e = 1$) throughout this paper. For the impact energies considered in this work, we may neglect the nucleus-nucleus interaction and assume that the projectile ion of mass m_P moves along a straight-line trajectory in the z direction,

$$\vec{R}(t) = b\vec{e}_x + v(t - t_0)\vec{e}_z, \tag{1}$$

which is characterized by the impact parameter b, the constant velocity v, and the time of closest approach t_0 (Fig. 1).

Taking the location of the target as the coordinate origin, we employ two-dimensional soft-core Coulomb potentials

$$V_T^{e^-} = -\frac{1}{\sqrt{x^2 + z^2 + a}} \tag{2}$$

and

$$V_P^{e^-}(t) = -\frac{1}{\sqrt{(x-b)^2 + [z - v(t - t_0)]^2 + a}} \tag{3}$$

to represent the electronic interaction with the target and projectile nucleus, respectively. The "softening" parameter $a = 0.641$ regularizes the potentials at the location of the nuclei and is adjusted to reproduce the ground-state binding energy of atomic hydrogen.

In the dipole approximation, the interaction between the active electron and a monochromatic laser electric field of angular frequency ω,

$$E_x(t) = E_0(t)\cos[\omega(t - t_0) + \phi], \tag{4}$$

$$E_z(t) = E_0(t)\epsilon \sin[\omega(t - t_0) + \phi], \tag{5}$$

is given by the potential

$$V_L(x,z,t) = E_x(t)x + E_z(t)z \tag{6}$$

(Figs. 1 and 2). Here $\epsilon \in [-1,1]$ denotes the ellipticity of the laser light. The laser phase ϕ determines the direction of the laser electric field at the time of closest approach $t = t_0$ between the projectile and target.

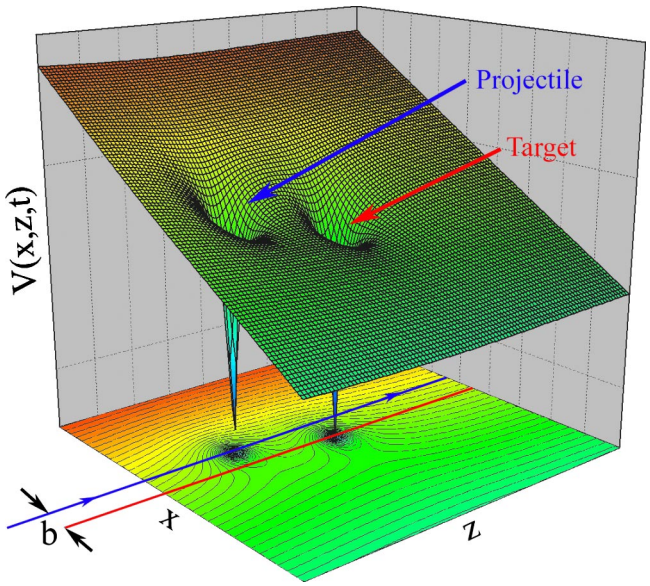

FIG. 2. (Color online) Snapshot of the electronic potential. For negative helicity, the laser electric field causes a clockwise rotation of the inclined potential plane about the target while the projectile moves toward the right-rear end along a straight line.

For the numerical applications in this work, we assume circularly polarized light of positive helicity ($\epsilon=1$), corresponding to clockwise rotation of the laser electric field vector in the zx plane (Fig. 1). The wave vector of the incident laser light is directed into the collision plane in Fig. 1. The envelope function $E_0(t)$ of the laser electric field turns the laser smoothly on during the time τ and then remains constant, once it has reached the maximum field strength E_0:

$$E_0(t) = \begin{cases} E_0 \sin^2\left(\dfrac{\pi}{2}\dfrac{t}{\tau}\right), & 0 \leqslant t \leqslant \tau, \\ E_0 & t > \tau. \end{cases} \tag{7}$$

We assume $\tau \ll t_0$, such that the oscillating electric field is fully turned on before the collision. At the time of closest approach, the electric field is given by

$$E_x = E_0 \cos\phi, \quad E_z = E_0 \sin\phi. \tag{8}$$

The sign of the projectile angular momentum relative to the target center of mass, $\vec{L}=\vec{R}\times m_P\vec{v}$, depends on the sign of the impact parameter. $\vec{L}$ can be either parallel or antiparallel to the laser helicity vector. In the first case the projectile moves in the same direction around the target as the laser electric field. We will address this situation as *corotating* scenario. Similarly, for the *counterrotating* scenario $\vec{L}$ and the helicity vector are antiparallel.

The collision process in the laser field is symmetrical with respect to the simultaneous change in sign of helicity and impact parameter. We can therefore limit our calculations to a given helicity while allowing for both positive and negative impact parameters. In all calculations we will assume a clockwise rotating laser electric field (positive helicity—i.e., $\epsilon=1$). For the coordinate system given in Fig. 1 and for the laser light propagating into the plane of the figure co (counter) rotating collisions occur for positive (negative) impact parameters.

In order to suppress unphysical reflections of the electronic probability density at the boundaries of our rectangular numerical grid, we employ absorbing boundaries [24]. For example, for absorption beyond x_0 in the $+\vec{x}$ direction, this is achieved by adjusting the absorber strength s and absorber width x_a in the negative imaginary potential

$$V_A(x) = \begin{cases} -is\left(\dfrac{x-x_0}{x_0}\right)^2, & x_0 < x < x_0 + x_a, \\ 0, & \text{otherwise}, \end{cases} \tag{9}$$

so that the reflected probability flux becomes negligible. The net electronic potential to be used in wave function propagation is thus given

$$V(x,z,t) = V_T(x,z) + V_P(x,z,t) + V_L(x,z,t) + V_A(x,z), \tag{10}$$

where $V_A(x,z)$ models the absorption in all directions in obvious two-dimensional generalization of $V_A(x)$.

B. Dynamics

The solution of the time-dependent Schrödinger equation (TDSE) $i\partial_t|\Psi(t)\rangle = H(t)|\Psi(t)\rangle$ is formally given by the evolution of the initial wave function $\Psi(x,z,t=0)$,

$$\Psi(x,z,t) = \hat{T}\exp\left[-i\int_0^t dt' H(x,z,t')\right]\Psi(x,z,0), \tag{11}$$

with the time-ordering operator $\hat{T}$ and the Hamiltonian

$$H(t) = T_x + T_z + V(x,z,t). \tag{12}$$

T_x and T_z are the electronic kinetic energy operators. The numerical propagation of the TDSE (11) is carried out on a numerical grid using the unconditional stable Crank-Nicholson split-operator method [25,26]. For a time step Δt the wave function (11) at time $t+\Delta t$ is recursively given in terms of $\Psi(t)$ by

$$\Psi(t+\Delta t) \approx \exp\left[-iT_x\frac{\Delta t}{2}\right] \times \exp\{-i[T_z + V(x,z,t)]\Delta t\} \times \exp\left[-iT_x\frac{\Delta t}{2}\right]\Psi(t). \tag{13}$$

We choose equal grid spacings in x and z direction of $\Delta x = \Delta z = 0.2$. Our grid covers 120 a.u. along the projectile trajectory (z direction) and has a variable length in the x direction, depending on the impact parameter, given by $80+|b|$. We implemented absorbing boundaries of widths $x_a = z_a = 20$ inside the grid boundaries with an absorption strength of $s = 0.01$. These absorber parameters produce converged results that do not differ from those obtained with altered absorbers of twice the absorption width or strength and show no signs of unphysical reflections at the grid edges.

The laser frequency was chosen in the near infrared with $\omega = 0.0428$, which corresponds to a wavelength of 1064 nm

available from common Nd:YAG lasers. After a initial ramping time $\tau=450=10.9$ fs we propagate the electronic wave function in the laser field for 550 a.u.=13.2 fs. A total propagation time in the laser field of $t_{max}=1450=35.1$ fs leads to converged results for capture and ionization probabilities for all relevant values of b and ϕ and for laser intensities between $2.85\times10^{-5}=1\times10^{12}$ W/cm^2 and $2.85\times10^{-3}=1\times10^{14}$ W/cm^2. Time steps of $\Delta t=0.1$ were found small enough to guarantee the long-term accuracy of the propagation scheme.

At each time step we integrate the probability density over two square boxes of length 20 a.u., centered on the projectile ion and target. For larger internuclear distances, we interpret these integrals $N_T(t)$ and $N_P(t)$ as as instantaneous electronic charge states on the projectile and target, respectively. At the end of the numerical propagation, at time $t=t_{max}$, they serve as approximations for the capture and ionization probabilities:

$$P^{\pm}_{cap}(b,\phi)=N_P(t=t_{max}), \tag{14}$$

$$P^{\pm}_{ion}(b,\phi)=[1-N_P(t=t_{max})-N_T(t=t_{max})]. \tag{15}$$

The superscripts $\pm$ distinguish between co $(+)$ and counter $(-)$ rotating collisions. Since the laser phase ϕ is currently not observable or experimentally controllable, we average over ϕ:

$$P^{\pm}_{cap}(b)=\frac{1}{2\pi}\int_0^{2\pi}d\phi P^{\pm}_{cap}(b,\phi), \tag{16}$$

$$P^{\pm}_{ion}(b)=\frac{1}{2\pi}\int_0^{2\pi}d\phi P^{\pm}_{ion}(b,\phi). \tag{17}$$

We found that it is sufficient to calculate the capture and ionization probability for eight different laser phases (between 0° and 315° with increments of 45°). Values for $P^{\pm}_{cap}(b,\phi)$ and $P^{\pm}_{ion}(b,\phi)$ at arbitrary values for ϕ are obtained by spline interpolation. Test calculations using 36 different phases with increments of 10° showed no relevant change in the interpolated probabilities.

Finally, we integrate over b in order to obtain total cross sections for capture and ionization:

$$\sigma^{\pm}_{cap}=2\pi\int_0^{\infty}dbbP^{\pm}_{cap}(b), \tag{18}$$

$$\sigma^{\pm}_{ion}=2\pi\int_0^{\infty}dbbP^{\pm}_{ion}(b). \tag{19}$$

We note that $P^{\pm}_{cap}(b,\phi)$ and $P^{\pm}_{ion}(b,\phi)$ are calculated within a two-dimensional model and that effects due to the reduced dimensionality are disregarded in the integration over b in $\sigma^{\pm}_{cap}$ and $\sigma^{\pm}_{ion}$.

III. NUMERICAL RESULTS

A. Field-free results

Reduced-dimensionality numerical capture probabilities for field-free proton-hydrogen collisions have been published by Lein and Rost [16]. Their results are almost identical with our field-free capture probabilities (Fig. 3). Total capture cross sections for collisions of 1–2 keV protons with atomic hydrogen have been measured by Gealy and Van Zyl [27]. For 2 keV incident kinetic energy, our calculated capture cross section is 44% larger than the experimental value. For 1 keV protons it is 34% larger (Table I).

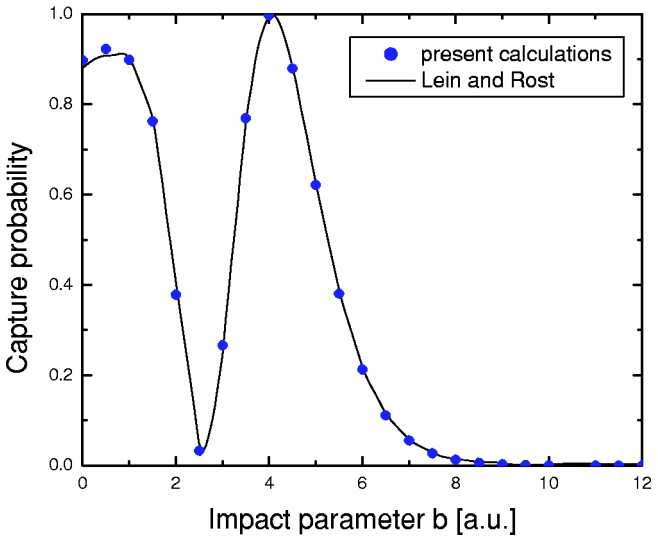

FIG. 3. (Color online) Capture probability as a function of the impact parameter for field-free collisions of 2 keV protons with hydrogen atoms. Results from independent two-dimensional wave function propagation calculations: Lein and Rost [16] (solid curve), present results (dots).

The difference between the measured and calculated cross sections can be understood in terms of a simple overlap argument. Compared to experiment or full-dimensionality calculations, the smaller phase space inherent in reduced-dimensionality calculations increases the wave function overlap between the interacting projectile and target, thus resulting in larger calculated cross sections (Table I). However, we do not expect that the main conclusions from our numerical results for laser-assisted collisions (see below) are significantly influenced by reducing the dimensionality from 3 to 2. In particular, reduced-dimensionality results that indicate a strong relative difference in the capture or ionization cross sections between corotating and counterrotating laser-assisted collisions are expected to be observable.

B. Circular polarization

The presence of the laser radiation during the collision process results in an additional dependence of the electronic

TABLE I. Comparison of the calculated (reduced dimensionality) total capture cross sections for field-free collisions with the experiment of Gealy and Van Zyl [27].

Energy (keV)	Electron capture cross section σ^{theor}_{cap} (10^{-16} cm^2)	σ^{expt}_{cap} (10^{-16} cm^2)	Difference
1	21.87	16.3±18%	34%
2	20.04	13.9±17%	44%

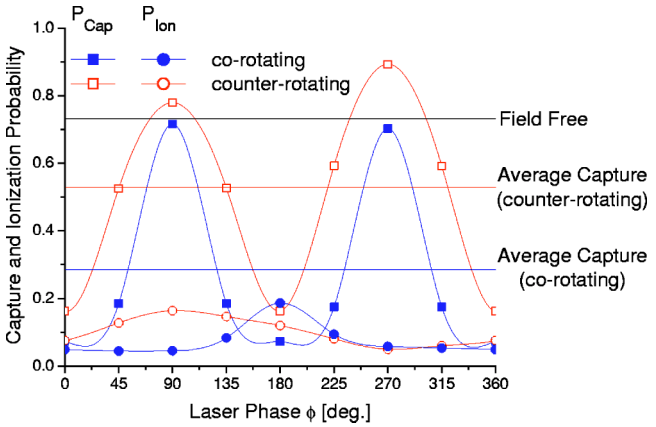

FIG. 4. (Color online) Capture and ionization probability as a function of the laser phase ϕ at the time of closest approach between projectile and target for 1.21-keV p-H collisions. The impact parameter is $b=\pm 4$ a.u. and the laser intensity 5×10^{13} W/cm^2. Phase-averaged results for the capture probability differ significantly for corotating and counterrotating laser-assisted collisions.

dynamics on the laser phase ϕ at the time of closest approach. Our results for a fixed impact parameter $b=\pm 4$ and laser intensity 5×10^{13} W/cm^2 for the capture probability as a function of ϕ show large amplitude oscillations and differ from the field-free results most strikingly for $\phi=0°$ and 180° (Fig. 4). They also display a strong dichroism effect—i.e., a substantial difference in the electron capture probability for positive and negative impact parameters or, equivalently, for corotating as compared to counterrotating collisions.

In comparison to the phase-averaged results for the field-free case, we find that the capture probabilities in both corotating and counterrotating collisions are considerably reduced. The ionization probabilities depend less sensitively on ϕ, and their phase averages (not shown in Fig. 4) differ much less for corotating and counterrotating collisions (positive and negative impact parameters) than the phase-averaged capture probabilities. This tendency of weak dichroism in the ionization probability extends to other impact parameters, as will be discussed below. In the following discussion, we will first focus on the strong dichroism apparent in the capture probability, followed by an analysis of the ionization process.

1. Electron capture

Figure 5(a), shows the electron capture probability as a function of the impact parameter and the laser phase ϕ for a laser intensity of $I=5\times 10^{13}$ W/cm^2. The electron capture probability shows maxima at impact parameters $b=\pm 2$ and $b\approx\pm 4.0$. Similar structures appear for the field-free capture probability (Fig. 3). They originate in the large wave function overlap of the corresponding target and projectile states near the point of closest approach.

With regard to the dependence on the phase of the rotating laser field, the capture probability shows a strong enhancement at $\phi=90°$ and 270°, when the force exerted by the laser electric field on the electron at the time t_0 of closest approach is either antiparallel or parallel to the direction of the projectile motion, respectively (see Fig. 1 and note that force and electric field point in opposite directions). For these particular phases, the field-modified Coulomb potentials of target and projectile are identical at t_0, and the internuclear axis is momentarily perpendicular to the laser electric field. This implies perfect level matching of field-dressed projectile and target states and explains the large capture probabilities for $\phi=90°$ and 270° in Fig. 5(a).

To support this interpretation further, we also calculated the electron capture probability for a *constant* electric field, corresponding in direction and magnitude to the laser electric field at time t_0, with otherwise identical parameters [Fig. 5(d)]. In this calculation, ϕ parametrizes the direction of the stationary electric field. We note that this scenario is somewhat unrealistic, since a constant electric field would deflect the projectile ion and invalidate our assumption of a straight-line projectile trajectory. Interestingly, however, the dependence on the laser electric field direction of the capture probability in Fig. 5(d) compares well with the ϕ dependence in Fig. 5(a), thus adding credibility to the importance of energy-level matching between projectile and target states at time t_0.

For the laser phases $\phi=0°$ and 180° and positive impact parameters, the laser force on the electron at time t_0 points to the target or to the projectile, respectively (vice versa for negative impact parameters). The mismatch of the field-dressed hydrogen energy levels is largest at the time of closest approach, thus strongly suppressing electron capture in favor of enhanced ionization for $\phi=180°$ at positive impact parameters and for $\phi=0°$ at negative impact parameters [Fig. 5(b)].

Compared to the laser phase of 270°, Figs. 5(a) and 5(d) show a slightly reduced capture probability at $\phi=90°$, when the laser electric force on the electron at t_0 is antiparallel to the projectile velocity. The target electron loss probability [Figs. 5(c) and 5(d)] does not show this asymmetry, and the slightly larger capture probability for $\phi=270°$ appears to be due to the "extra push" the electron receives by the laser force at t_0 in direction of the projectile motion. In contrast, for $\phi=90°$, the electron is accelerated in the opposite direction by the laser force and is a little more likely to ionize.

Overall, Fig. 5(a) displays a strong enhancement of the electron capture probability for negative impact parameters (counterrotating collisions) in comparison with for positive impact parameters (corotating collisions), with much broader peaks at $\phi=90°$ and 270° for the counterrotating case.

If the laser electric field is oriented perpendicular to the internuclear axis, both Coulomb potentials are identical and electron transfer is most likely. For corotating collisions, the relative orientation of the laser electric field and internuclear axis changes much less rapidly during the collision time than for counterrotating collisions. At appropriate impact energies and impact parameters, this relative orientation is maintained throughout the projectile-target interaction for corotating collisions. During the interaction time, which is of the order of one laser cycle, the projectile and target will then form a short-lived quasimolecule. Thus, in conclusion, electron capture is expected to depend sensitively on the laser phase for corotating collisions.

In contrast, for counterrotating collisions, the angle between the rotating electric field of the laser light and the internuclear axis changes rapidly, irrespective of the value of

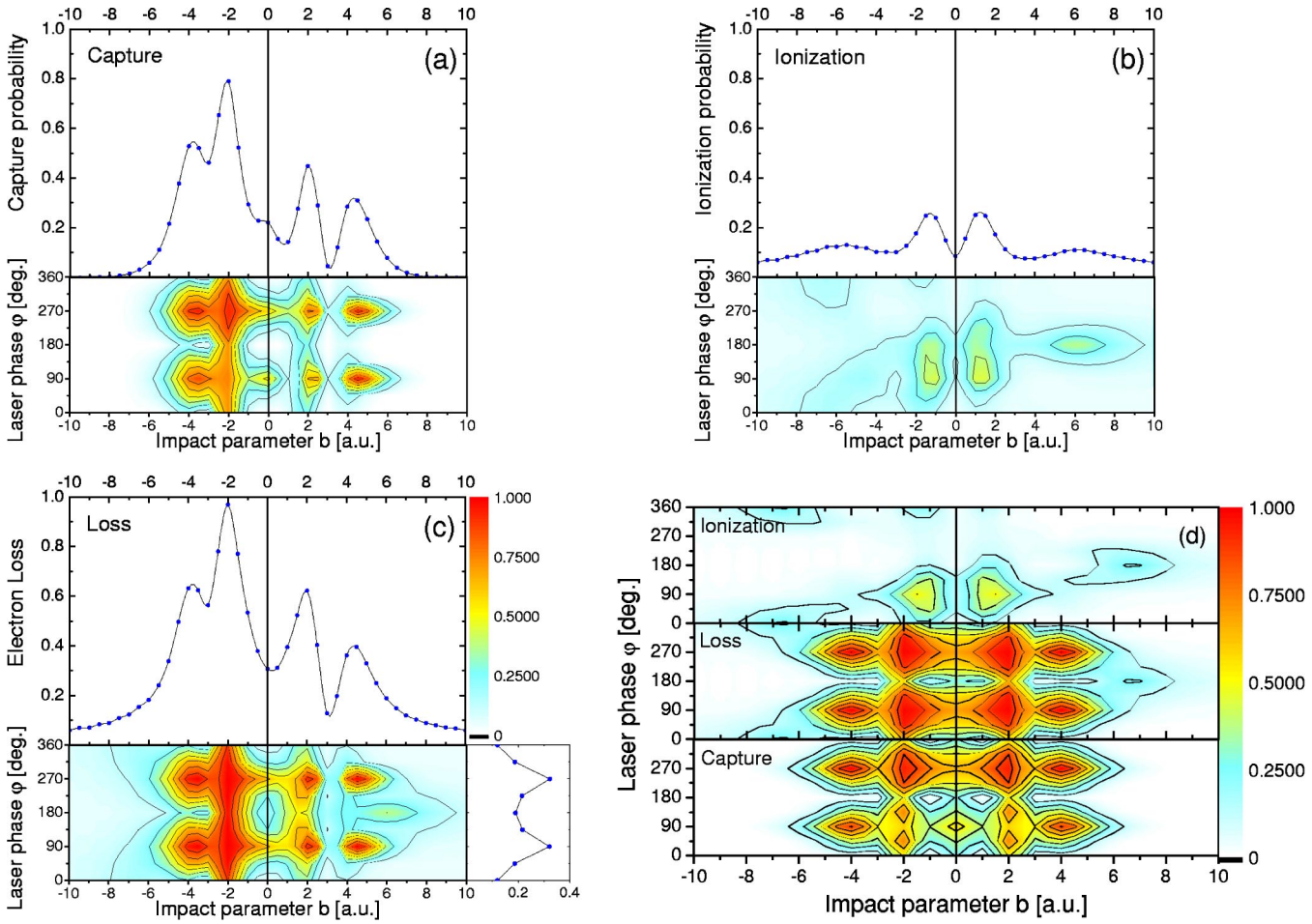

FIG. 5. (Color online) Electron capture (a), ionization (b), and target electron loss probability (c) in laser-assisted 1.21-keV p-H collisions for a laser intensity of $I=5\times10^{13}$ W/cm^2. The contour plots show the probabilities as a function of the impact parameter b and the laser phase ϕ. The probability difference between consecutive contour lines is 0.125. The top panels in (a), (b), and (c) show phase averaged results. The side panel in (c) shows the impact-parameter average as a function of the laser phase. Capture, ionization, and loss probabilities as a function of the impact parameter and the laser phase for the case of a *static* electric field, corresponding in the direction and magnitude to the laser electric field at the distance of closest approach in (a), (b), and (c), are shown in (d) for comparison.

ϕ. Level matching of projectile and target states occurs for a wide range of laser phases, but only for a small fraction of the interaction time. However, since the time scale of the electronic motion (1 a.u.) is about two orders of magnitude faster than a laser cycle (146.7 a.u.), the transient reflection symmetry of both Coulomb potentials still lasts long enough to enable noticeable electron transfer. In particular, at the chosen projectile velocity ($v=0.22$) electron transfer to the projectile is relatively likely, while recapture by the target is suppressed by the rapidly increasing asymmetry between the two laser-modified Coulomb potentials.

For the given projectile speed, this explains the enhancement of capture in counterrotating collisions. For corotating collisions, the relative orientation of the laser electric field and the internuclear axis is maintained for approximately half a laser cycle, and the formation of a transient molecule decreases the probability for the electron to remain in a projectile state. In agreement with this explanation, a numerical test has shown that the capture probability in corotating collisions is reduced, and the difference between corotating and counterrotating electron capture becomes much less pronounced projectiles if we double the impact velocity ($E_{kin}=4.83$ keV).

As mentioned earlier, the ϕ dependence in laser-assisted capture cross sections is difficult to resolve experimentally. Interestingly, however, the clear enhancement of the capture probability in counterrotating over corotating collisions remains after averaging over ϕ [top panel of Fig. 5(a)] and may be probed in angle-differential collision experiments, at appropriate projectile velocities.

2. Ionization

The ionization probabilities in Figs. 5(b) and 5(d) show a broad enhancement near $\phi=90°$ when the laser electric force on the electron opposes the projectile motion and for impact parameters around $b=\pm1.5$. A less pronounced enhancement in the ionization probability occurs at $b\sim\pm6$ [Fig. 5(b)].

For corotating collisions (positive b) and larger impact parameters, ionization is enhanced at a laser phase of 180°, while in the counterrotating case a much broader and weaker

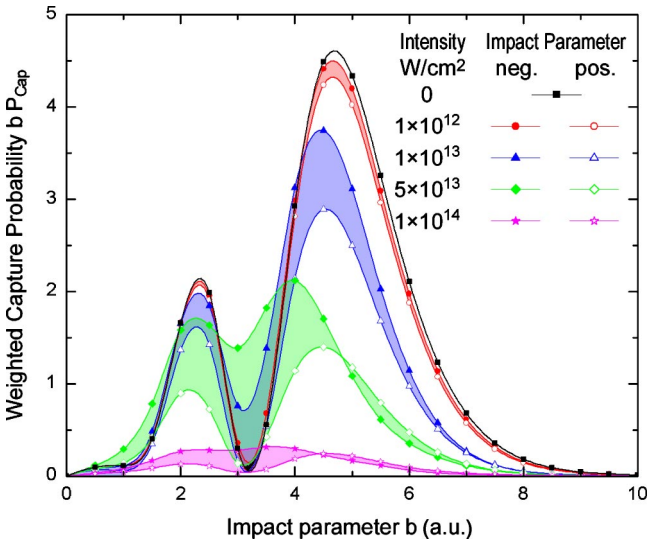

FIG. 6. (Color online) bP_{cap}, averaged over the laser phase, at different laser intensities for corotating (positive impact parameter) and counterrotating (negative impact parameters) collisions.

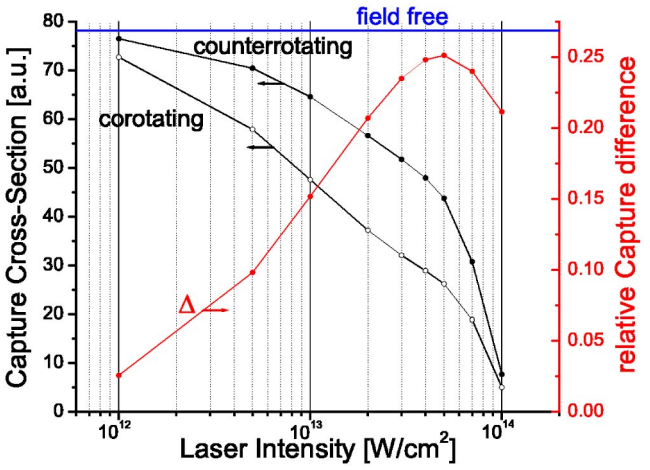

FIG. 7. (Color online) Total electron capture cross sections as a function of the laser intensity for corotating and counterrotating collisions. Also shown is the relative difference Δ, which is largest at a laser intensity of 5×10^{13} W/cm^2.

peek occurs near $\phi=0°$. In both cases the laser force on the electron points towards the projectile at the time of closest approach. This explains the signature of enhanced ionization in Fig. 5(b) at $\phi=0°$ and 180°. This enhancement corresponds to the well-known charge-resonance-enhanced ionization (CREI) during the fragmentation of diatomic molecules in strong laser fields at larger internuclear distances [28].

The broadening of the ionization peak for counterrotating collisions (negative b) is identical to the corresponding feature in the capture probability discussed earlier. In the corotating scenario, while near the target, the projectile moves along with the laser electric field vector. The Coulomb and laser electric forces then add to their maximal possible magnitude for a relatively long time. The time during which a maximal force is exerted on the electron is much smaller for the counterrotating case. Therefore, for counterrotating collisions, the CREI peak around $\phi=0°$ is weaker and less compressed than the CREI peak in corotating collisions at $\phi=180°$ [Fig. 5(b)]. The distinctive CREI peak might allow for the determination of the actual laser phase in future phase-locked experiments. Averaging over all laser phases ϕ removes the dichroism effect almost entirely [top panel in Fig. 5(b)].

3. Laser intensity dependence

Figure 6 shows the laser phase-averaged results for the weighted electron capture probability bP_{cap} at different laser intensities for corotating and counterrotating collisions. Noticeable differences between corotation and counterrotation appear above laser intensities of 5×10^{12} W/cm^2. The capture probability rapidly decreases for laser intensities above 1×10^{14} W/cm^2, when ionization begins to be the dominate. It is for all intensities smaller than for field-free collisions. The relative difference

$$\Delta=\frac{|\sigma_{cap}^{+}-\sigma_{cap}^{-}|}{\sigma_{cap}^{+}+\sigma_{cap}^{-}|} \tag{20}$$

in the total electron capture cross section as a function of the laser intensity is shown in Fig. 7. The difference in the capture cross section or corotating and counterrotating collisions amounts to up to 40% at a laser intensity of 5×10^{13} W/cm^2 (Table II). We consider these differences as upper limits for the dichroism effect and expect them to decrease slightly in full three-dimensional calculations, since an added degree of freedom no longer limits the electronic motion to the plane in which the laser field rotates.

The results in Fig. 7 relate to *total* cross section only. Experimentally, *scattering-angle differential* cross sections [and $P(b)$] can be measured either directly by detecting the projectile scattering angle or indirectly by observing the recoil direction of the target. For scattering angles that correspond to impact parameters with the largest circular dichroism in $P(b)$, the dichroism effect is more pronounced in differential cross sections than in total cross sections (cf. Fig. 5).

TABLE II. Comparison of the total capture cross section for corotating and counterrotating collisions at different laser intensities.

Intensity (W/cm^2)	Electron capture cross section	
	Corotating	Counterrotating
0	78.08	78.08
1×10^{12}	72.67	76.47
5×10^{12}	57.85	70.41
1×10^{13}	47.53	64.52
5×10^{13}	26.18	43.74
1×10^{14}	4.97	7.63

IV. CONCLUSION

We have shown by numerically solving the Schrödinger equation within a two-dimensional model that a significant difference in the electron capture probabilities $P_{cap}^{\pm}(b)$ in corotating and counterrotating laser-assisted *p*-H collisions is due to a energy-level matching effect between the target and projectile states at relevant impact parameters. We thus predict a strong circular dichroism; i.e., we find that capture (and to a lesser extent ionization) probabilities are different for parallel and antiparallel laser helicity and projectile angular momentum.

Laser pulses with lengths of a few nanoseconds and intensities of about 5×10^{12} W/cm^2 and higher should allow for the experimental verification of the predicted dichroism in the capture probability. In addition, we found evidence for the charge-resonant-enhanced ionization mechanism in laser-assisted ionization. In conjunction with phase-locked lasers, this effect may be used in angle-differential laser-assisted collision experiments in order to select a specific orientation of the laser electric field at the time of closest approach between projectile and target.

We hope that this work will stimulate the challenging experimental test of the predicted effects, electron capture dichroism, and CREI in laser-assisted collisions. In the long run, this may lead to new and more efficient schemes for the control of chemical reactions with intense laser radiation.

ACKNOWLEDGMENTS

This work is supported by the NSF (Grant No. PHY-0071035) and the Division of Chemical Sciences, Office of Basic Energy Sciences, Office of Energy Research, U.S. DOE.

[1] G. H. Henderson, Proc. R. Soc. London, Ser. A **102**, 496 (1923).
[2] B. H. Bransden and M. R. C. McDowell, *Charge Exchange in the Theory of Ion-Atom Collisions* (Clarendon Press, Oxford, 1992).
[3] R. Dörner, V. Mergel, O. Jagutzki, L. Spielberger, J. Ullrich, R. Moshammer, and H. Schmidt-Böcking, Phys. Rep. **330**, 95 (2000).
[4] J. Ullrich, R. Moshammer, A. Dorn, R. Dörner, L. P. H. Schmidt, and H. Schmidt-Böcking, Rep. Prog. Phys. **66**, 1463 (2003).
[5] M. Protopapas, C. H. Keitel, and P. L. Knight, Rep. Prog. Phys. **60**, 389 (1997).
[6] B. Feuerstein and U. Thumm, Phys. Rev. A **67**, 043405 (2003).
[7] A. Débarre and P. Cahuzac, J. Phys. B **19**, 3965 (1986).
[8] J. Grosser, D. Hohmeiser, and S. Klose, J. Phys. B **29**, 299 (1996).
[9] A. S. Alnaser, T. Osipov, E. P. Benis, A. Wech, B. Shan, C. L. Cocke, X. M. Tong, and C. D. Lin, Phys. Rev. Lett. **91**, 163002 (2003).
[10] S.-M. Li, Y.-G. Miao, Z.-F. Zhou, J. Chen, and Y.-Y. Kiu, Z. Phys. D: At., Mol. Clusters **39**, 29 (1997).
[11] S.-M. Li, J. Chen, and Z.-F. Zhou, J. Phys. B **35**, 557 (2002).
[12] A. B. Voitkiv and J. Ullrich, J. Phys. B **34**, 1673 (2001).
[13] L. B. Madsen, J. P. Hansen, and L. Kocbach, Phys. Rev. Lett. **89**, 093202 (2002).
[14] T. Kirchner, Phys. Rev. Lett. **89**, 093203 (2002).
[15] M. S. Pindzola, T. Minami, and D. R. Schultz, Phys. Rev. A **68**, 013404 (2003).
[16] M. Lein and J. M. Rost, Phys. Rev. Lett. **91**, 243901 (2003).
[17] H. J. Mason, Rep. Prog. Phys. **56**, 1275 (1993).
[18] C. J. Joachain, M. Dörr, and N. Kylstra, Adv. At., Mol., Opt. Phys. **42**, 225 (2000).
[19] A. Cionga, F. Ehlotzky, and G. Zloh, J. Biol. Phys. **34**, 2057 (2001).
[20] N. M. Kroll and K. M. Watson, Phys. Rev. A **8**, 804 (1973).
[21] B. Wallbank and J. K. Holmes, J. Phys. B **27**, 1221 (1994); **27**, 5405 (1994).
[22] A. Jarón and J. Z. Kamiński, Phys. Rev. A **56**, R4393 (1997).
[23] R. Moshammer, B. Feuerstein, J. CrespoLopez-Urrutia, J. Deipenwisch, A. Dorn, D. Fischer, C. Höhr, P. Neumayer, C. D. Schröter, J. Ullrich, H. Rottke, C. Trump, M. Wittmann, G. Korn, and W. Sandner, Phys. Rev. A **65**, 035401 (2002).
[24] Himadri. S. Chakraborty, Thomas Niederhausen, and Uwe Thumm, Phys. Rev. A **69**, 052901 (2004).
[25] W. H. Press, B. P. Flannery, S. A. Teukolsky, and W. T. Vetterling, *Numerical Recipes in FORTRAN 77*, (Cambridge University Press, Cambridge, England, 1992), p. 842.
[26] U. Thumm, in *Book of Invited Papers, XXII ICPEAC, Santa Fe, NM*, edited by S. Datz *et al.* (Rinton Press, Princeton, NJ, 2002), p. 592.
[27] M. W. Gealy and B. Van Zyl, Phys. Rev. A **36**, 3091 (1987).
[28] A. D. Bandrauk and J. Ruel, Phys. Rev. A **59**, 2153 (1999).

INSTITUTE OF PHYSICS PUBLISHING JOURNAL OF PHYSICS B: ATOMIC, MOLECULAR AND OPTICAL PHYSICS

J. Phys. B: At. Mol. Opt. Phys. **38** (2005) 487–501 doi:10.1088/0953-4075/38/5/002

Fragmentation dynamics of molecular hydrogen in strong ultrashort laser pulses

A Rudenko, B Feuerstein, K Zrost, V L B de Jesus[1], T Ergler, C Dimopoulou, C D Schröter, R Moshammer and J Ullrich

Max-Planck-Institut für Kernphysik, D-69029 Heidelberg, Germany

Received 8 October 2004
Published 21 February 2005
Online at stacks.iop.org/JPhysB/38/487

Abstract

We present the results of a systematic experimental study of dissociation and Coulomb explosion of molecular hydrogen induced by intense ultrashort (7–25 fs) laser pulses. Using coincident recoil-ion momentum spectroscopy we can distinguish the contributions from dissociation and double ionization even if they result in the same kinetic energies of the fragments. The dynamics of all fragmentation channels drastically depends on the pulse duration, and for 7 fs pulses becomes extremely sensitive to the pulse shape.

(Some figures in this article are in colour only in the electronic version)

1. Introduction

The fragmentation of the two simplest molecules H_2 and H_2^+ (or alternatively D_2/D_2^+) in intense optical fields has been extensively studied both theoretically and experimentally. In contrast to the atomic case, the molecule exhibits three timescales, the fast electronic motion (as scale), the vibrational (fs scale) and rotational (ps scale) nuclear motion. The vibrational degree of freedom is of particular interest since its timescale matches the duration of state-of-the-art optical laser pulses. Considerable theoretical work has been done for the neutral hydrogen molecule (see, e.g., Yu *et al* (1996), Walsh *et al* (1998), Harumiya *et al* (2002), Saenz (2002a, 2002b)) and for the molecular ion (see, e.g., Zuo and Bandrauk (1995), Chelkovski *et al* (1996, 1999), Numico *et al* (1997), Dundas *et al* (2000), Bandrauk and Shon (2002), Feuerstein and Thumm (2003)). Some specific properties make the latter a model laboratory system for laser–matter interactions. First, there exists only one bound potential curve, i.e. the electronic ground state—all other electronically excited states are purely repulsive and converge towards the Coulombic $1/R$ curve, where R is the internuclear distance (see figure 1). Second, the degeneracy of the two lowest electronic states $1s\sigma_g$ and $2p\sigma_u$ at large internuclear distances leads to a strong dipole interaction of these levels in the presence of

[1] Present address: Centro Federal de Educação Tecnológica de Química de Nilópolis/RJ, Rua Lucio Tavares 1045, Centro, Nilópolis, 26530-060, Rio de Janeiro, Brazil.

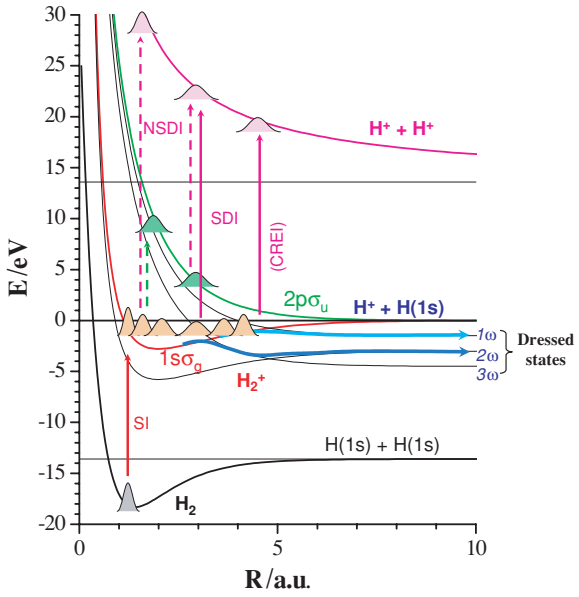

Figure 1. Potential curves of two lowest electronic states of H_2^+ dressed with n ($n = 1, 2, 3$) photons. Arrows indicate different fragmentation pathways. SI: single ionization; SDI: sequential double ionization; NSDI: non-sequential double ionization; CREI: charge resonance enhanced ionization.

external electrical fields, which is essential for the coupling of the system to laser radiation. Third, the quite large difference in the ionization energies of H_2 (15.2 eV) and H_2^+ (29.9 eV) is the basis of a two-step treatment. Starting with the neutral molecule in a strong laser pulse the first electron will be easily removed creating the ionic state which will subsequently undergo further fragmentation processes. Most experiments have used the neutral molecule as a target (Zavriyev *et al* 1993, Walsh *et al* 1997, Thomson *et al* 1997, Gibson *et al* 1997, Frasinski *et al* 1999, Posthumus *et al* 2000, Rottke *et al* 2002). However, the formation and fragmentation of H_2^+ occur in the same laser pulse and, thus, cannot be completely disentangled (Walsh *et al* 1998).

Hence, there is a growing interest in using molecular ions as targets (Williams *et al* 2000, Sändig *et al* 2000, Schellhammer *et al* 2000) or in getting better insight into the time dependence of the fragmentation dynamics. The latter is not least stimulated by the fact that in contrast to the ionic case, using a neutral molecule as a target opens an additional possibility of probing the dynamics of the nuclear motion. Recently, the pioneering concept of a 'molecular clock' (Niikura *et al* 2002, 2003, Alnaser *et al* 2003) was introduced. The idea is based on the so-called recollision model (Corkum 1993). Here, one considers the combined propagation of the nuclear and electronic wave packets, which is started by the first ionization step. The emitted electron is driven back and forth by the oscillating laser field and may recollide after a well-defined time with its parent ion, while the nuclei have moved apart according to their motion on the new H_2^+ potential curve. Emission of the second electron induced by the recollision leads to Coulomb explosion (CE) of the molecule, which provides a mapping of the nuclear wave packet at the time of recollision via the relation of the kinetic energy release (KER) of the fragments $E_{\mathrm{kin}} = 1/R$. However, to read the molecular clock one has to know via which channel the fragmentation takes place. This requires a detailed

and comprehensive modelling of the recollision process. Very recently, a good agreement of theory and experiment has been achieved (Alnaser *et al* 2003, Tong *et al* 2003). However, there are still open questions remaining. In particular, there is an ongoing debate whether recollision-induced dissociation contributes to the fragments detected in the molecular clock scheme.

The present work focuses on the influence of the temporal structure of short and ultrashort (<10 fs) laser pulses on the fragmentation dynamics of H_2 and on the problem of reliably distinguishing between the contributions from the dissociation and Coulomb explosion for the cases where they lead to fragments with similar kinetic energies. The paper is structured as follows: in section 2 a brief description of the experimental set-up is given, followed by an overview of the various fragmentation channels and the driving mechanisms in section 3. The experimental results are presented and discussed in section 4, and conclusions are given in section 5. Atomic units (au) are used if not stated otherwise.

2. Experimental set-up

The measurements were performed using a new 'reaction microscope' (Ullrich *et al* 2003) designed to meet the specific requirement of the experiments with high-intensity lasers (see de Jesus *et al* (2004b) for details). We used linearly polarized radiation of a Kerr-lens mode-locked Ti:sapphire laser at 795 nm wavelength with 25 fs pulse width (FWHM). To generate few-cycle pulses, they were spectrally broadened in a gas-filled hollow fibre and then compressed to 7 fs (FWHM) by chirped mirrors and a prism compressor. Fluctuations of the laser intensity from pulse to pulse were monitored during the experiment and did not exceed 5%. Absolute calibration of the peak intensity was performed using a clear kink in the measured photoelectron momentum distribution, which corresponds to the maximum drift momentum of $2\sqrt{U_p}$ that electrons can gain from the laser field (de Jesus *et al* 2004a).

The laser beam was focused to a spot size of $\sim$7 μm on the collimated supersonic gas jet in the ultrahigh vacuum chamber (2×10^{-11} mbar). Charged reaction fragments were guided to two position-sensitive channel plate detectors by weak electric (2 V cm^{-1}) and magnetic (7 G) fields applied along the laser polarization axis. From the time-of-flight (TOF) and position on the detectors, the full momentum vectors of the recoil ions and electrons were calculated.

A typical TOF spectrum of H_2 fragmentation by 25 fs laser pulse is shown in figure 2(a). The most prominent line at the right side of the spectrum corresponds to H_2^+ ions. H^+ fragments form two groups of peaks nearly mirror symmetric with respect to the full vertical line indicating the TOF of the protons with zero longitudinal (along the polarization direction) momentum. 'Forward' protons are those going directly to the ion detector, while 'backward' ones go first to the opposite hemisphere and then are turned back by the extraction field. Thus, the H^+ peaks corresponding to the various fragmentation channels appear two-fold in the spectrum. Slight asymmetry in the peak positions is due to the fact that the longitudinal momentum is not exactly linear with TOF. Here it should be noted that the heights of the peaks, i.e. the branching ratios of the different channels, depend on the acceptance of the spectrometer, which differs for different fragment energies (see de Jesus *et al* (2004b) for details). Thus only the qualitative changes of these ratios with intensity and pulse duration will be considered here.

Figure 2(b) shows the corresponding energy spectrum for the forward protons, where the same set of peaks can be seen. Fragmentation mechanisms giving rise to these structures are discussed in the next section.

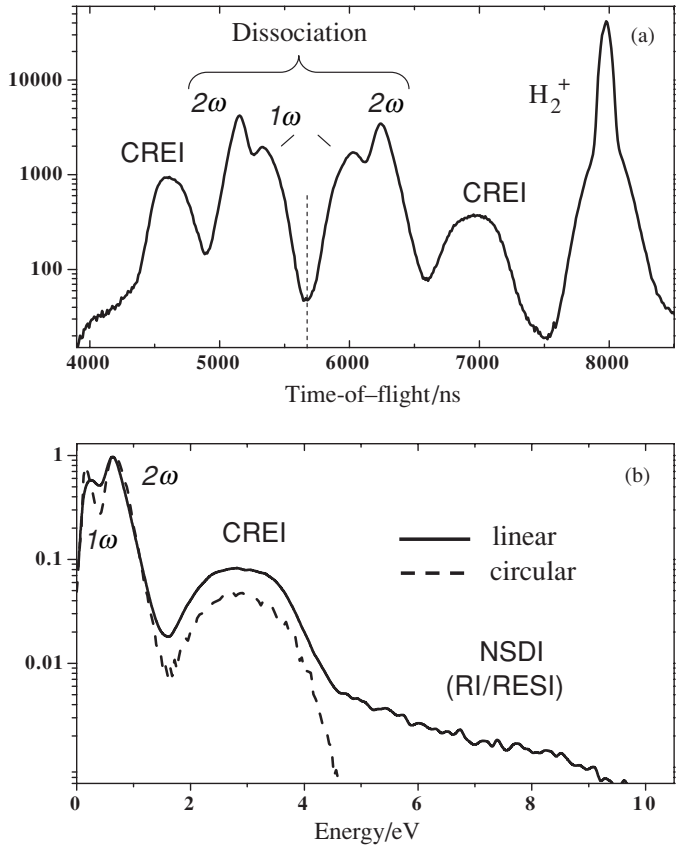

Figure 2. H_2 fragmentation spectra with 25 fs pulses at 0.2 PW cm^{-2}. (a) Typical time-of-flight ion spectra. The dashed vertical line indicates time-of-flight of the protons with zero momentum along the field polarization direction. (b) Solid line: corresponding proton energy spectrum for the forward protons (see text). Dashed line: the data obtained with circularly polarized light. The curve is normalized to fit the 2ω peak for linear polarization. In the circular case the intensity was halved. RI: recollision ionization; RESI: recollision–excitation with subsequent field ionization.

3. Fragmentation channels of H_2 in strong 800 nm laser pulses

Figure 1 shows the different ionization and fragmentation pathways of H_2 in a strong 800 nm laser field in the form of a potential curve diagram. By single ionization of H_2 the initial vibrational ground state is promoted in a vertical transition onto the electronic ground state potential curve $1s\sigma_g$ of H_2^+. Since the wave packet is no longer an eigenstate it will start to propagate on the new potential curve defining a timescale for subsequent fragmentation processes. The molecular ion can either dissociate or be further ionized leading to a pair of protons (Coulomb explosion). Up to now there has been no experimental evidence found for direct molecular dissociation leading to a pair of neutral hydrogen atoms (Posthumus 2004).

3.1. Dissociation

Dissociation is driven by a strong dipole interaction of the two lowest electronic states $1s\sigma_g$ and $2p\sigma_u$ in the presence of a strong field along the molecular axis. In a cycle-averaged

Floquet description (Shirley 1965, Bandrauk and Sink 1981), one finds a series of dressed potential curves spaced by the photon energy. Via avoided crossings the molecular ion can dissociate by a net absorption of one or two photons. In the latter case, absorption of three photons in the first avoided crossing is followed by a re-emission of one photon at the second crossing. Since for each photon the parity of the molecular state must change, there is no direct two-photon process. In the fragment kinetic energy spectrum (see figure 2(b)), these channels manifest themselves as two peaks below 1 eV per proton (1ω and 2ω peaks). A comprehensive discussion on the dynamics and interplay of different dissociation mechanisms referred to as 'bond-softening' (Bucksbaum *et al* 1990), vibrational trapping or 'bond-hardening' (Frasinski *et al* 1999), 'above-threshold' (Giusti-Suzor *et al* 1990), 'below-threshold' (Numico *et al* 1997) or 'zero-photon' (Posthumus *et al* 2000) dissociation can be found in the reviews of Giusti-Suzor *et al* (1995) and Posthumus (2004).

3.2. Sequential double ionization (SDI)

The mechanism of sequential double ionization (SDI) in strong laser fields, which is well known for atoms, becomes more complex in the molecular case since the ionization potential of the molecular ion depends on the internuclear separation R. In addition, at intermediate R an even stronger enhancement of the field ionization rates is observed due to the interaction of the $1s\sigma_g$ and $2p\sigma_u$ states, which causes an oscillating localization of the electron cloud at one of the nuclei. This effect of charge resonance enhanced ionization (CREI) (see, e.g. Zuo and Bandrauk (1995)) gives the largest ionization probabilities for H_2 in a range of internuclear distance from 3.5 to 7 au corresponding to a KER per proton of 2–4 eV (figure 2(b)). Since the dipole interaction occurs along the molecular axis, the corresponding Coulomb explosion contribution is strongly peaked along the laser polarization direction (Posthumus 2004). CREI was found to be a dominant sequential double ionization channel in most of the measurements on H_2 and D_2. However, the results of recent experiments (Légare *et al* 2003, Alnaser *et al* 2004) have shown that if few-cycle laser pulses are used, the 'atomic-like' sequential double ionization, which results in more energetic Coulomb explosion fragments with more isotropic angular distribution, starts to compete with CREI. In Légare *et al* (2003), these two channels were referred to as 'sequential ionization' and 'enhanced ionization'. This should not lead to confusion: both processes are definitely sequential and the essential difference is the extreme R-dependence of the enhanced ionization (CREI). Throughout this paper, we use the term 'sequential' double ionization to denote the processes where two electrons are emitted independently, in contrast to the 'non-sequential' case, where an electron–electron interaction is involved.

3.3. Non-sequential double ionization (NSDI)

In the case of a linearly polarized laser field, the first emitted electron can be driven back and recollide after about three quarters of an optical cycle with its parent ion. The returning electron may either kick out the second electron directly through recollision–ionization (RI) or promote the bound electron into an excited state, which can then be easily field ionized. This mechanism of recollision–excitation followed by subsequent field ionization (RESI) was found to play a decisive role for non-sequential double ionization of atoms (Feuerstein *et al* 2001, de Jesus *et al* 2004a, 2004b). For H_2 the non-sequential double ionization channel has been identified as a high-energy shoulder in the fragment energy spectra for linear polarization, which disappears in the circular case as shown in figure 2(b) since in this case the electron does not recollide with its parent ion (see also Staudte *et al* (2002), Sakai *et al* (2003), Légare

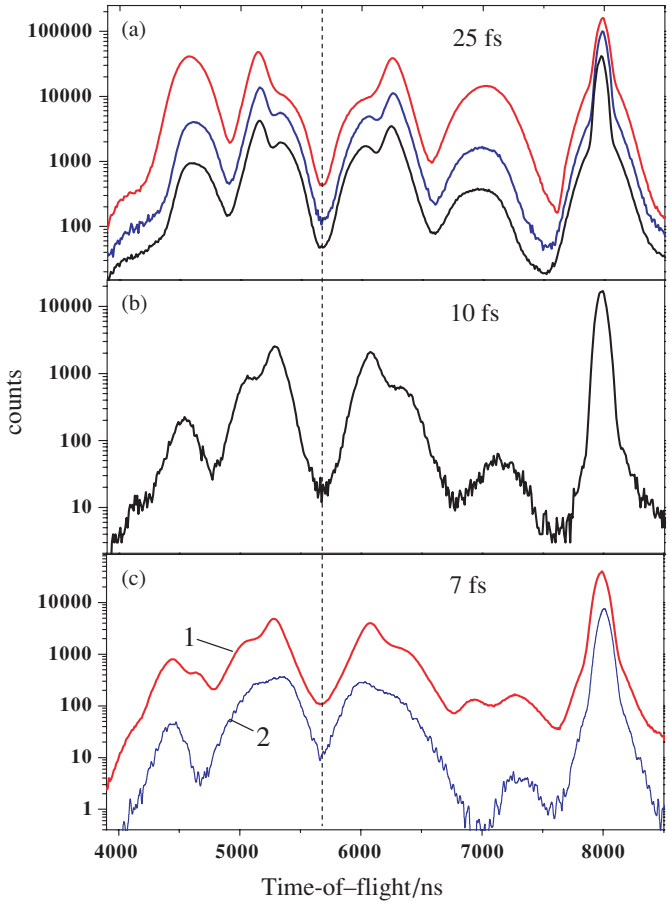

Figure 3. Evolution of the proton time-of-flight spectra with the pulse duration. (a) 25 fs pulses with the intensities of 0.2, 0.3 and 0.5 PW cm^{-2} for the lower, middle and upper curves, respectively. The curves are separated in the vertical direction for visual convenience. (b) 10 fs, 0.5 PW cm^{-2}. (c) 7 fs, 0.8 PW cm^{-2}. Curves 1 and 2 were obtained with pulses of different shape (see text and figure 4).

et al (2003)). Non-sequential double ionization leads to the largest fragment energies since it is a fast process, which for the first electron return gives the nuclei less than one optical cycle to separate. In a recent work based on the molecular clock principle mentioned above, it was shown by comparison of experimental and theoretical results that RESI is the dominating non-sequential double ionization channel (Alnaser *et al* 2003, Tong *et al* 2003).

4. Results and discussion

4.1. From short to ultrashort pulses: influence of the pulse shape

Figure 3 shows the evolution of the TOF spectra of the H_2 fragments with decreasing pulse duration. The spectra for 25 fs pulses at peak intensities of 0.2, 0.3 and 0.5 PW cm^{-2} are shown in figure 3(a). Similar to figure 2(a), with lowest kinetic energy we find the 1ω and 2ω dissociation peaks followed by the broad structure due to CREI. As the intensity is increased,

the branching ratio of the 1ω versus 2ω dissociation becomes smaller and CREI starts to compete with the dissociation channel. A similar intensity dependence of the spectra was observed in previous experiments (Thomson *et al* 1997, Trump *et al* 2000, Staudte *et al* 2002). If we now reduce the pulse duration while keeping the peak intensity approximately fixed, the fragmentation pattern changes significantly (figure 3(b): 10 fs; figure 3(c): 7 fs). We find the branching ratio of 1ω and 2ω dissociation channels reversed and the corresponding peaks broadened, a feature that will be discussed in section 4.3. With decreasing pulse duration, we observe a strong suppression of the Coulomb explosion (CREI) channel compared to dissociation. Intuitively it is comprehensible: when the pulse length becomes shorter than the vibrational period, the pulse may be gone before the molecule extends to the critical internuclear distances corresponding to the region of enhanced ionization.

Figure 3(c) depicts two spectra obtained with pulses of the same temporal width (FWHM) (7 fs) but different shapes. Figure 4 shows the measured frequency spectra, the Fourier limit for the intensity profile and measured second-order autocorrelation for both pulses. Autocorrelation patterns calculated from the spectra are very close to the measured ones. Panels (a)–(c) and (d)–(f) in figure 4 correspond to the curves 1 and 2 in figure 3(c), respectively. For curve 1, similar to the results of Légare *et al* (2003) on D_2, we find a splitting of the Coulomb explosion peak into two components, one corresponding to CREI and one with higher energies, whereas for curve 2 only the outer peak can be observed. In order to elucidate this effect in more detail, we consider the correlated longitudinal (along the field polarization direction) momenta of two protons detected in coincidence as shown in two-dimensional diagrams in figure 5 for 25 fs (a) and 7 fs (b) pulse width, respectively. The true coincidences are found close to the diagonal reflecting almost zero sum momentum. The remaining width is due to the momentum defect carried away by the electron which is not shown here (see de Jesus *et al* (2004b)). All other events are due to random coincidences, mainly with protons from dissociation as can be seen from the projected momentum spectra at the top and on the left-hand side. In figure 5(a), CREI events are found in the broad maximum on this diagonal whereas the events due to recollision form the tail extending to larger momenta. The small peak around ± 9 au consists mainly of false events due to the crossing of two bands of random coincidences. The correlation diagram for the 7 fs pulse, which belongs to the curve 1 of figure 3(c), again reveals the disappearance of the broad CREI peak and, instead, two new peaks in its flanking parts. At lower momenta (± 14 au) a third peak shows up, which is certainly not an artefact since it does not fit a band of random coincidences. Assuming all proton energy to be due to the Coulomb explosion, the internuclear distance R at the time when the second electron was removed can be extracted from the peak positions. Here, we find $R = 3.2$ au and $R = 5.7$ au for the two peaks visible in figure 3(c). The third peak corresponds to $R = 9.4$ au and, hence, the question arises how the nuclear wave packet can reach that distance within the duration of the pulse. This leads us back to figure 3(c) and the dependence on the pulse shape.

As can be seen from figure 4, for those cases where we find in the correlation spectrum a clear splitting of sequential double ionization peak, the pulse shape was affected by quite strong pre- and post-pulses. By optimizing the pulse shape, i.e. suppressing the pre- and post-pulses (figures 4(d)–(f)), two low-energy peaks are suppressed and only the peak with the highest kinetic energy (and consequently shortest delay between removal of the first and the second electron) survives (curve 2 in figure 3(c)). This proves that the pre- and post-pulses were strong enough for a subsequent ionization on a time scale of 15–25 fs, which is much longer than the FWHM of the main peak of the temporal pulse profile. This critical dependence on the pulse shape is due to the fact that the molecular ion becomes more and more sensitive to field ionization as it expands with time and reaches the region of enhanced ionization where

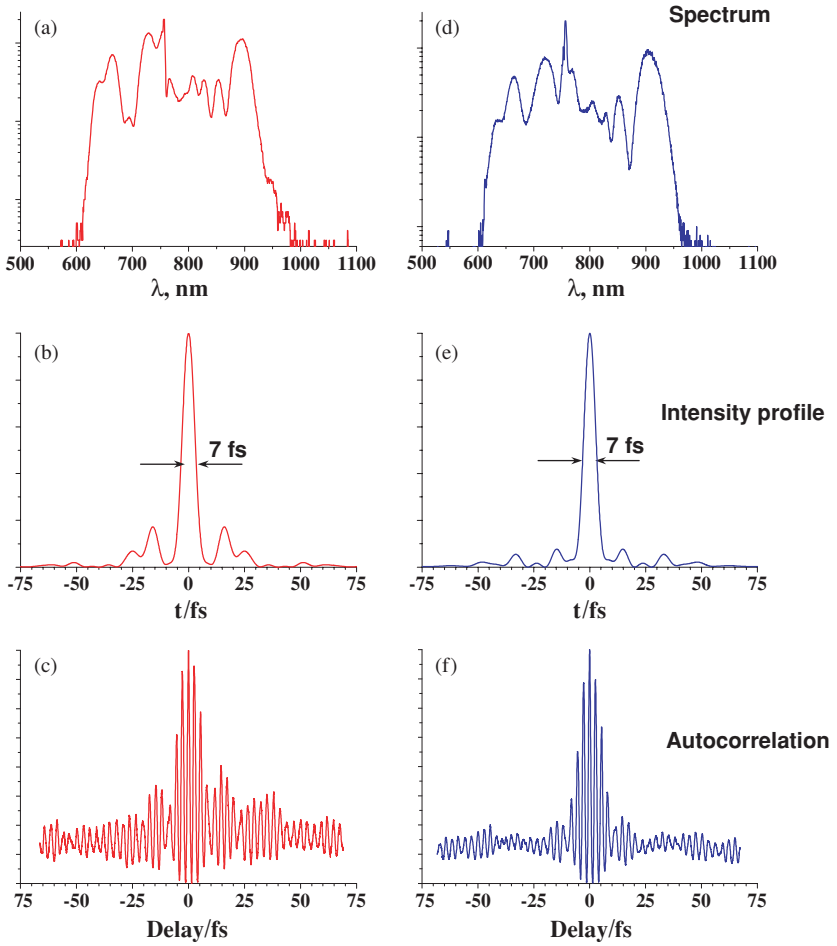

Figure 4. Characteristics of two laser pulses corresponding to the results of figure 3(c). (a), (d) Measured frequency spectra. (b), (e) Fourier limit for the intensity profile. (c), (f) Measured second-order autocorrelation. Panels (a)–(c) and (d)–(f) correspond to the curves 1 and 2 in figure 3(c), respectively.

even a weak post-pulse can remove the second electron. From a more technical point of view, this behaviour makes H_2 a sensitive probe for the quality of ultrashort laser pulses which could be used as a diagnostic tool.

4.2. Sequential double ionization

The intensity dependence of the proton energy spectra for ultrashort pulses with a 'clean' temporal profile, i.e. without significant pre- and post-pulses, is depicted in figure 6. Here only the most energetic sequential double ionization peak, where the second ionization step occurs before the internuclear distance reaches the region of enhanced ionization, can be resolved. However, some residual structures on the position of two low-energy double ionization peaks can still be observed in the coincidence diagrams. This is more pronounced for the highest intensities: indeed, for a peak intensity of PW cm^{-2} the post-pulses on a level as low as 1% can still result in a considerable number of enhanced ionization events.

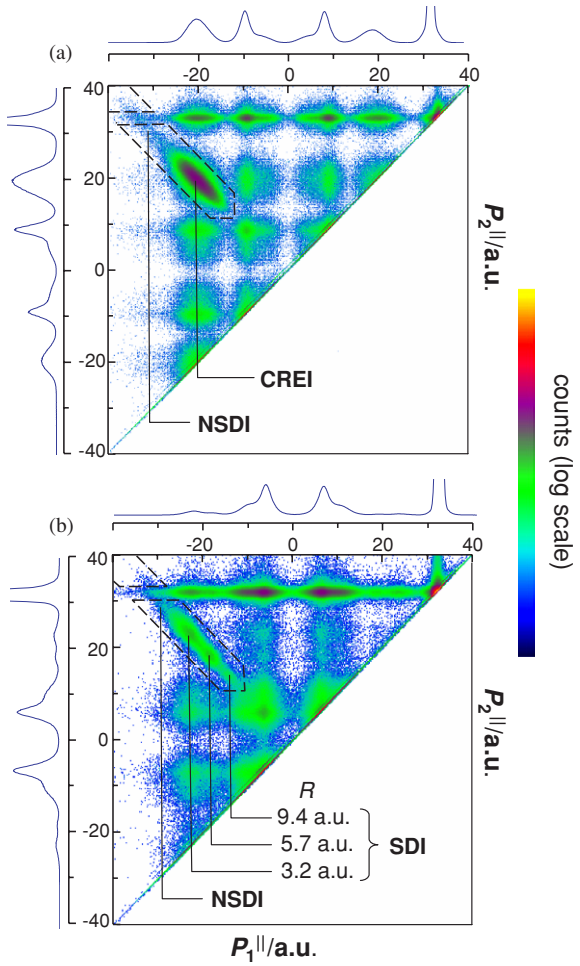

Figure 5. Coincidence diagram of the proton longitudinal momenta. The momentum of the protons detected on the detector as a first hit ($P_1^{\parallel}$) is plotted versus the momentum of the second one ($P_2^{\parallel}$). The momentum distribution is recalculated from the ion time-of-flight and thus contains the contribution of H_2^+ ions (a peak above 30 au) which does not reflect their momenta. The real coincidences lie near the diagonal $P_1^{\parallel} = -P_2^{\parallel}$ due to momentum conservation. (a) 25 fs, 0.5 PW cm^{-2}. (b) 7 fs, 0.8 PW cm^{-2}. The diagram corresponds to curve 1 in figure 3(c) and panels (a)–(c) in figure 4. For discrete Coulomb explosion peaks, the estimated values of the internuclear distances R are indicated.

Over the peak intensity range from 0.2 to 2.0 PW cm^{-2} sequential double ionization starts from almost negligible contribution at the lowest power density and becomes finally comparable with the dissociation channel. The maximum of the sequential double ionization peak shifts from 4.1 eV for 0.2 PW cm^{-2} to 5.2 eV for 2.0 PW cm^{-2}, which corresponds to an internuclear separation of $R = 3.3$ au and $R = 2.6$ au, respectively. This effect has been recently demonstrated theoretically by Tong and Lin (2004). In their simulations for D_2, the peak positions of ∼6.2 eV at 3.2 PW cm^{-2} and ∼5.7 eV at 2.4 PW cm^{-2} are predicted, which are in good qualitative agreement with our results. This shift is due to the fact that for the same pulse duration at higher peak intensities the second ionization step can occur earlier, at smaller values of R, thus resulting in larger Coulomb energies of the fragments. The effect is

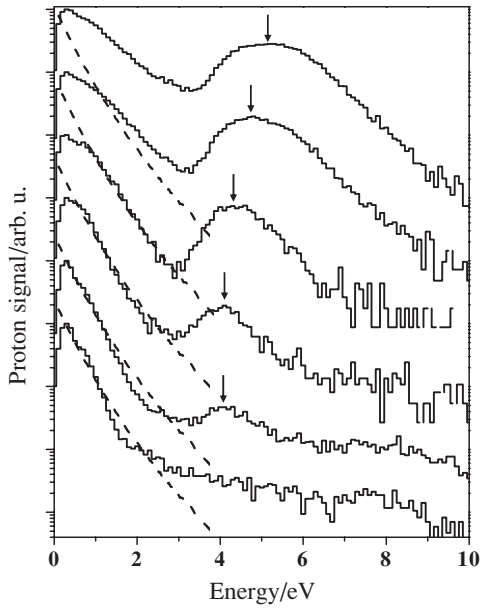

Figure 6. Proton kinetic energy distributions obtained with 7 fs laser pulse. The curves are separated in the vertical direction for visual convenience. The intensities from up to down: 2.0 PW cm^{-2}, 1.4 PW cm^{-2}, 0.8 PW cm^{-2}, 0.5 PW cm^{-2}, 0.3 PW cm^{-2}, 0.2 PW cm^{-2}. The data were obtained with the clean pulses (the curve for 0.8 PW cm^{-2} corresponds to the curve 2 in figure 3(c) and panels (d)–(f) in figure 4). Vertical arrows indicate positions of sequential double ionization maxima. Dashed lines show a Franck–Condon distribution (see text).

less pronounced in the low-intensity regime, most likely due to a stronger R-dependence of the ionization probability (Plummer and McCann 1996). A similar shift is observed for the CREI peak (figure 3(a), see also Walsh *et al* (1997) and Trump *et al* (2000)).

4.3. Recollision-induced double ionization

For non-sequential double ionization of atoms by strong linearly polarized fields, the electron correlation is partly reflected by the sum momentum of the electrons parallel to the laser polarization direction. In the case of an atom, this is identical to the negative recoil momentum of the doubly charged ion. It is known that the ion momentum distributions along the field polarization direction for non-sequential double ionization are significantly broader than for the sequential case (Weber *et al* 2000). It can even exhibit clear maxima at non-zero momenta ('double-hump' structure) in the case of dominance of direct recollision-induced ionization such as, e.g., for Ne (de Jesus *et al* 2004b). If RESI is the dominating mechanism of non-sequential double ionization, one finds a maximum at zero momentum but still a broader distribution compared to sequential ionization (Feuerstein *et al* 2001). In the case of H_2, one has to consider the sum (or centre-of-mass) momentum of the two protons which plays the role of the recoil-ion momentum in the atomic case and balances the sum momentum of the electrons. Figure 7 shows the protons sum momentum distributions for the CREI and non-sequential double ionization channels for 25 fs and 7 fs laser pulses. In both cases one finds a significantly broader distribution for non-sequential double ionization compared to CREI. A double-hump structure is not found in the recollision case providing additional evidence that RESI is the dominating mechanism as has been recently discussed by Tong *et al* (2003).

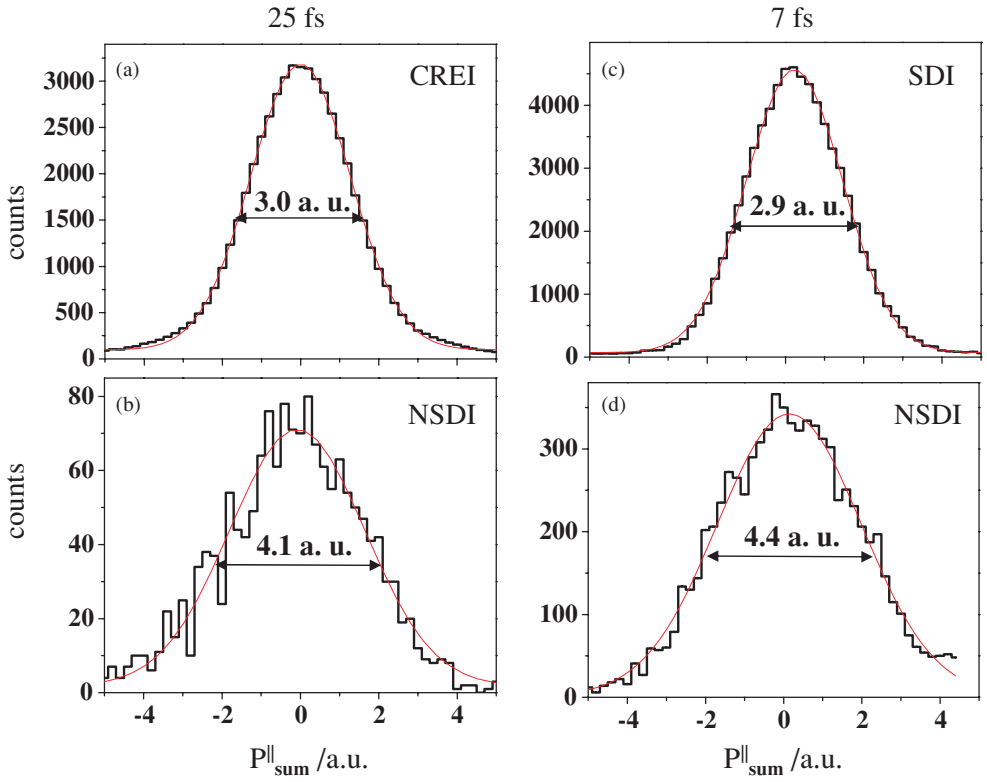

Figure 7. Sum longitudinal momentum of two coincident protons created by sequential (a), (c) and non-sequential (b), (d) double ionization of H_2 at 0.5 PW cm^{-2}. (a), (b) 25 fs. (c), (d) 7 fs. The width (FWHM) is shown for each spectrum.

It can be noted that the non-sequential double ionization momentum distribution is slightly broadened for a few-cycle pulse, while the sequential double ionization spectra have almost the same width. Low statistics does not allow us to draw a conclusion whether this broadening indeed reflects some changes in the recollision dynamics. To clarify this point, kinematically complete experiments on rescattering double ionization of H_2 are under way.

4.4. Dissociation in ultrashort pulses

When the laser pulse duration is decreased from 25 to 10 fs, the most remarkable change in the low-energy part of the proton spectrum is the reversed branching ratio of 1ω and 2ω dissociation channels (figures 3(a) and (b)). Enhancement of the 1ω peak for pulses with very short rise-times was discussed by Numico *et al* (1997) in terms of below-threshold dissociation. Later, Frasinski *et al* (1999) experimentally observed the dynamical shift of this structure to higher energies with decreasing pulse duration, which was associated with the different speed of the release of the trapped wave packet at the falling edge of the pulse. For 10 and 7 fs pulses, we also observe a slight shift of the position of the 1ω peak compared to 25 fs. However, it is not clear to what extent effects such as vibrational trapping or below-threshold dissociation can contribute in our case of high intensities. In general, with decreasing temporal width of the pulse the shape of the dissociation part of the spectrum deviates more and more from the two-peak structure corresponding to the 1ω and 2ω dissociation channels (see curve 2 in

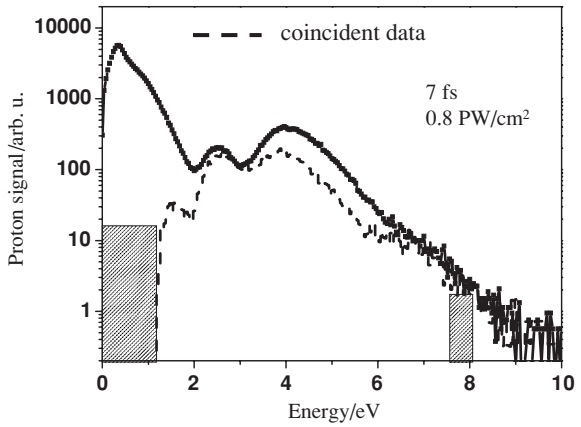

Figure 8. Kinetic energy spectra of coincident and non-coincident protons. The set of data is the same as for the figure 5(b) and curve 1 in figure 3(c). Solid line: all events. Dashed line: events detected in coincidence. Shaded areas mark the regions where false coincidences cannot be excluded.

figure 3(c)). The reason for this, apart from the broadening of the photon spectrum, is the breakdown of the Floquet model for the dissociation which assumes a quasi-CW laser field. The propagation of the wavepackets on the light-induced potential curves via avoided crossings (see figure 1) into the dissociation continuum needs time. If the pulse duration becomes shorter than the time required to reach the level crossings, this mechanism does not work anymore, similar to the suppression of CREI discussed above. However, even in the limit of an infinitely short 'δ-like' pulse the molecule will still have a finite probability of dissociating, since the vertical (Franck–Condon) transition from H_2 to H_2^+ in the preceding single ionization gives rise to a small overlap of the initial nuclear wavefunction with the dissociation continuum wavefunction of H_2^+. The corresponding fragment energy distribution is compared to the experimental result for a 7 fs pulse in figure 6. The best agreement is found for 0.8 PW cm^{-2} with a residual deviation most likely due to the finite pulse duration. This difference becomes stronger at higher intensities in the form of a partial reappearance of the two light-induced dissociation peaks since even weak post-pulses may be strong enough to open the dissociation paths through the avoided crossings. (This can be confirmed by comparison of the curves 1 and 2 in figure 3(c).) The lower intensity shows a remarkable lack of higher dissociation energies compared to the Franck–Condon distribution. This is most likely caused by the R-dependent ionization potential of H_2, which leads to a considerable reduction of the ionization probability at small R. As a consequence, the Franck–Condon distribution is shifted to larger R which reduces the number of more energetic fragments. Such an effect has been demonstrated in a recent joint experimental and theoretical work (Urbain *et al* 2004) for the population of vibrational states of H_2^+ in strong-field single ionization of H_2.

The question remains whether all dissociation products are restricted to the low-energy region. Figure 8 displays the proton energy spectra corresponding to the coincidence diagram in figure 5(b) and curve 1 in figure 3(c). The dashed line shows the energy distribution for the events where two protons are detected in coincidence and momentum conservation is fulfilled. This makes the separation of double ionization and dissociation events more reliable. The spectra are scaled in order to match the number of single proton events in the CREI region. Regions of the spectrum where random coincidences cannot be excluded are marked by shaded areas. We find a significant deficit of coincident events around 3–6 eV, i.e. in the region of sequential double ionization. This indicates indirectly a contribution of

dissociation since neutral fragments are not detected. The origin of these energetic dissociation fragments remains unclear. One possible contribution can be given by the RESI mechanism for non-sequential double ionization. In its second step, the electron in the recollision-induced excited state is field-ionized. If the laser pulse duration is short enough even at high peak intensities, some population in excited states may survive. Since all corresponding potential curves are repulsive, the electronically excited molecule will dissociate. Figure 1 shows that, for example, recollision population of the first excited state $2p\sigma_u$ will lead to a total KER of 5–12 eV (i.e. 3–6 eV per proton), which is in good accordance with our experimental findings. Similar values are expected for the $2p\pi_u$ state. There is an ongoing debate whether dissociation or Coulomb explosion is the dominating channel in the molecular clock scheme. Niikura *et al* (2003) attributed the main feature in the fragment spectrum around 6 eV to the dissociation of recollision-excited molecular ions. However, their non-coincident experiment could not distinguish reliably between dissociation and Coulomb explosion. More recently, Tong *et al* (2003) demonstrated that both channels contribute and discussed in detail the non-coincident and coincident (Alnaser *et al* 2003) spectra. For the dissociation fragments, a KER per particle of 2–7 eV is calculated, which is in reasonable agreement with our results. However, it seems unlikely that in our case recollision-induced dissociation is the dominant source of the high-energy dissociated protons since we do not restrict the solid angle in order to select the recollision contribution, as was done in the experiment of Alnaser *et al* (2003).

5. Conclusions and outlook

We have studied the dynamics of molecular hydrogen fragmentation by intense laser pulses of different durations. For 25 fs pulses we observed the spectra well known from previous studies, with 1ω and 2ω dissociation peaks, a broad CREI structure and high-energy tail due to recollision-induced Coulomb explosion. When the pulse width is reduced, the two-peak dissociation structure in the proton kinetic energy spectra is smeared out, and for 7 fs becomes closer to the Franck–Condon distribution. The Coulomb explosion (CREI) contribution is suppressed, and the atomic-like sequential double ionization which results in the production of protons with higher kinetic energies starts to be distinguishable. The intensity dependence of this sequential double ionization is in a good qualitative agreement with the recent theoretical results (Tong and Lin 2004). Coincident measurements revealed the existence of a low-energy Coulomb explosion peak which for non-coincident data is hidden in the dissociation part. Experiments with different pulse shapes showed that this structure is most likely due to delayed ionization caused by the post-pulses at large internuclear distances. This low-energy structure, as well as residual CREI contribution, can be enhanced (see curve 1 in figures 3(c), 5(b) and 8), if 7 fs pulses with higher pre- and post-pulses are used.

There are several questions that remain open. The low-energy Coulomb explosion peak seems to be well-localized. An interesting point is whether two double ionization peaks in figure 8 (at $\sim$1.5 and 2.5 eV) reflect two maxima in the R-dependence of the probability of enhanced ionization, which were predicted theoretically (see, e.g., Zuo and Bandrauk (1995)) but never observed experimentally. To answer this question, pump–probe experiments with few-cycle pulses are planned. Another problem concerns the observed deficit of coincidence events for proton kinetic energies of 3–6 eV. To clarify this point, more detailed coincident measurements with 'clean' 7 fs pulses together with reliable time-dependent description of the fragmentation process are required. And, of course more information on the dynamics of different fragmentation channels can be obtained from the coincident electron spectra. First, results for 30 fs were reported earlier (Rottke *et al* 2002), and the experiments with few-cycle pulses are under way.

Acknowledgments

The authors are grateful to H Rottke and A Voitkiv for valuable discussions.

References

Alnaser A S, Osipov T, Benis E P, Wech A, Shan B, Cocke C L, Tong X M and Lin C D 2003 *Phys. Rev. Lett.* **91** 163002

Alnaser A S, Tong X M, Osipov T, Voss S, Maharjan C M, Ranitovic P, Ullrich B, Shan B, Chang Z, Lin C D and Cocke C L 2004 *Phys. Rev. Lett.* **93** 183202

Bandrauk A D and Shon M H 2002 *Phys. Rev.* A **66** 031401

Bandrauk A D and Sink M L 1981 *J. Chem. Phys.* **74** 1110

Bucksbaum P H, Zavriyev A, Muller H G and Schumacher D W 1990 *Phys. Rev. Lett.* **64** 1883

Chelkovski S, Conjusteau A, Zuo T and Bandrauk A 1996 *Phys. Rev.* A **54** 3235

Chelkovski S, Corkum P B and Bandrauk A 1999 *Phys. Rev. Lett.* **82** 3416

Corkum P B 1993 *Phys. Rev. Lett.* **71** 1994

de Jesus V L B, Feuerstein B, Zrost K, Fischer D, Rudenko A, Afaneh F, Schröter C D, Moshammer R and Ullrich J 2004b *J. Phys. B: At. Mol. Opt. Phys.* **37** L161

de Jesus V L B, Rudenko A, Feuerstein B, Zrost K, Schröter C D, Moshammer R and Ullrich J 2004a *J. Electron Spectrosc. Relat. Phenom.* **141** 127

Dundas D, McCann J F, Parker J S and Taylor K T 2000 *J. Phys. B: At. Mol. Opt. Phys.* **33** 3261

Feuerstein B and Thumm U 2003 *Phys. Rev.* A **67** 043405

Feuerstein B *et al* 2001 *Phys. Rev. Lett.* **87** 043003

Frasinski L J, Posthumus J H, Plumridge J, Codling K, Taday P F and Langley A J 1999 *Phys. Rev. Lett.* **83** 3625

Gibson G N, Li M, Guo C and Neira J 1997 *Phys. Rev. Lett.* **79** 2022

Giusti-Suzor A, He X, Atabek O and Mies F H 1990 *Phys. Rev. Lett.* **64** 515

Giusti-Suzor A, Mies F H, DiMauro L F, Charron E and Yang B 1995 *J. Phys. B: At. Mol. Opt. Phys.* **28** 309

Harumiya K, Kono H, Fujimura Y, Kawata I and Bandrauk A 2002 *Phys. Rev.* A **66** 043403

Légare F, Litvinyuk I V, Dooley P W, Quéré F, Bandrauk A D, Villeneuve D M and Corkum P B 2003 *Phys. Rev. Lett.* **91** 093002

Niikura H, Légaré F, Hasbani R, Bandrauk A D, Ivanov M Y, Villeneuve D M and Corkum P B 2002 *Nature* **417** 917

Niikura H, Légaré F, Hasbani R, Ivanov M Y, Villeneuve D M and Corkum P B 2003 *Nature* **421** 826

Numico R, Keller A and Atabek O 1997 *Phys. Rev.* A **56** 772

Plummer M and McCann J F 1996 *J. Phys. B: At. Mol. Opt. Phys.* **29** 4625

Posthumus J H 2004 *Rep. Prog. Phys.* **67** 623

Posthumus J H, Plumridge J, Frasinski L J, Codling K, Divall E J, Langley A J and Taday P F 2000 *J. Phys. B: At. Mol. Opt. Phys.* **33** L563

Rottke H *et al* 2002 *Phys. Rev. Lett.* **89** 013001

Saenz A 2002a *Phys. Rev.* A **66** 063407

Saenz A 2002b *Phys. Rev.* A **66** 063408

Sakai H, Larsen J J, Wendt-Larsen I, Olesen J, Corkum P B and Stapelfeldt H 2003 *Phys. Rev.* A **67** 063404

Sändig K, Figger H and Hänsch T W 2000 *Phys. Rev. Lett.* **85** 4876

Schellhammer C, Schyja V, Hielscher A and Helm H 2000 *Laser Part. Beams* **18** 443

Shirley J H 1965 *Phys. Rev.* **138** B979

Staudte A, Cocke C L, Prior M H, Belkacem A, Ray C, Chong H W, Glover T E, Schoenlein R W and Saalmann U 2002 *Phys. Rev.* A **65** 020703

Thomson M R, Thomas M K, Taday P F J, Posthumus J H, Langley A, Frasinski L J and Codling K J 1997 *J. Phys. B: At. Mol. Opt. Phys.* **30** 5755

Tong X M and Lin C D 2004 *Phys. Rev.* A **70** 023406

Tong X M, Zhao Z X and Lin C D 2003 *Phys. Rev.* A **68** 043412

Trump C, Rottke H, Wittmann M, Korn G, Sandner W, Lein M and Engel V 2000 *Phys. Rev.* A **70** 023406

Ullrich J, Moshammer R, Dorn A, Dörner R, Schmidt L Ph H and Schmidt-Böcking H 2003 *Rep. Prog. Phys.* **66** 1463

Urbain X, Fabre B, Staicu-Casagrande E M, de Ruette N, Andrianarijaona V M, Jureta J, Posthumus J H, Saenz A, Baldit E and Cornaggia C 2004 *Phys. Rev. Lett.* **92** 163004

Walsh T D G, Ilkow F A and Chin S I 1997 *J. Phys. B: At. Mol. Opt. Phys.* **30** 2167

Walsh T D G, Ilkow F A, Chin S I, Châteauneuf F, Nguyen-Dang T T, Chelkovski S, Bandrauk A and Atabek O 1998 *Phys. Rev.* A **58** 3922

Weber Th, Weckenbrock M, Staudte A, Spielberger L, Jagutzki O, Mergel V, Afaneh F, Urbasch G, Vollmer M, Giessen H and Dörner R 2000 *J. Phys. B: At. Mol. Opt. Phys.* **33** L127

Williams I D, McKenna P, Srigengan B, Johnston I M G, Bryan W A, Sanderson J H, El-Zein A, Goodworth T R J, Newell W R, Taday P F and Langley A J 2000 *J. Phys. B: At. Mol. Opt. Phys.* **33** 2743

Yu H, Zuo T and Bandrauk A 1996 *Phys. Rev.* A **54** 3290

Zavriyev A, Bucksbaum P H, Squier J and Saline F 1993 *Phys. Rev. Lett.* **70** 1077

Zuo T and Bandrauk A 1995 *Phys. Rev.* A **52** R2511